UNIVERSITY OF SOUTHAMPTON

FACULTY OF PHYSICAL SCIENCES AND ENGINEERING

ELECTRONICS AND COMPUTER SCIENCE

NANO RESEARCH GROUP

Shaped apertures enhance the stability of suspended lipid bilayers

by

Sumit Kalsi

Thesis for the degree of Doctor of Philosophy

January 2014

Supervisors: Dr Maurits de Planque
Prof Hywel Morgan

Abstract

A biological membrane not only forms a protective outer boundary for cells and organelles but also houses ion channels that are attractive drug targets. The characterisation of membrane-embedded ion channels hence is of prime importance, but *in vivo* studies have been hindered by the complexity of the natural membranes. Lipid bilayers suspended in apertures have provided a simple and controlled model membrane system for ion channel studies, but short lifetimes and poor mechanical stability of suspended bilayers have limited the experimental throughput of bilayer electrophysiology experiments. Although suspended bilayers are more stable when smaller apertures are used, ion channel incorporation through vesicle fusion with the suspended bilayer becomes increasingly difficult. In this project, in an alternative bilayer stabilization approach, shaped apertures with tapered sidewalls have been fabricated with serial two-photon laser lithography and high-throughput grayscale lithography in photoresist. Bilayers formed at the 2 µm thin tip of the shaped apertures, either with the painting or the folding method, displayed drastically increased lifetimes, typically >20 hours, and mechanical stability, being able to withstand extensive perturbation of the buffer solution, as compared to the control shapes. Single-channel electrical recordings of the peptide Alamethicin, water soluble protein α-Hemolysin and of the proteoliposome-delivered potassium and sodium channels KcsA, hERG and Na_vSp pore domains demonstrate channel conductance with low noise, made possible by the small capacitance of the 50 µm thick resist septum, which is only thinned around the aperture, and unimpeded proteoliposome fusion, enabled by the large aperture diameter of 80 µm. Optically accessible horizontal bilayers in shaped apertures were developed to visualize suspended bilayers and incorporated ion channels. It is anticipated that these shaped apertures with micrometer edge thickness can substantially enhance the throughput of channel characterisation by bilayer lipid membrane electrophysiology, especially in combination with automated parallel bilayer platforms.

Table of Contents

Acknowledgement

Thanks God, the almighty, merciful and the passionate, for being so kind, blessing and forgiving.

First and foremost, I would like to express my sincere and deep appreciation for my supervisor Dr. Maurits de Planque for his invaluable support and guidance throughout this work. He has been extremely motivating and friendly throughout my PhD, thanks for lending an ear and guiding me when I was in trouble either for the project work or in personal front. I am honoured to have the opportunity to work under his supervision. There are no words enough to thanks him. Another person I want to thank is Prof Hywel Morgan who was also a part of my supervisory team. His assistance and valuable time in critical stages of this project has substantially benefitted this project and is greatly appreciated. A big word of thanks to the friends I have made in the last three years in Southampton; Mark, Shilong, Prameen, Hend, Ahmed, Priyanka, Gautum, Jingyao, Shimul, Junjia, Hang, Jinfeng and Chinnu, for their help whenever I needed and being so supportive and encouraging. Also, thanks to Sweta Pherwani for the constant fighting with me all the way from the US to give me a break from work and Sneha, Nipul and Umesh for always bringing optimism. Special thanks to Dr Kian S Kiang for help in designing the grayscale mask and Mr Jiajun Wang for taking the measurements for mechanical stability of the suspended bilayers in shaped apertures fabricated with grayscale. I would also like to express gratitude towards other members in Bio-ECS group and clean room technical team for lending a helpful hand in general.

I would like to thank my parents, grandmother, and my uncles, and aunts, cousins for their endless support and motivational talk, to cheer me up when I am down. I owe whatever I am today to them. My brothers, Vivek and Amit, have been very influential in my life. Thanks guys for listening to all my problems even when you would not understand half of them and giving suggestions, which actually worked. Thanks for having faith in me. Thanks Vivek for getting me started with this PhD before you left Southampton, you have helped me in more ways than you know of. Thanks to my sister, Shweta, for updating me about everything on Skype calls and also doing pep talks to keep me going.

List of Abbreviations and symbols

A	Ampere
B	Bandwidth
C	Capacitance where subscript represent components contributing to the capacitance for e.g. C_m represents capacitance of membrane
CAD	Computer aided design
D	Dielectric loss factor
DOPC	1,2-dioleoyl-sn-glycero-3-phosphocholine
DOPE	1,2-Dioleoyl-sn-Glycero-3-Phosphoethanolamine
DPhPC	Diphytanoylphosphatidylcholine
POPG	1-palmitoyl-2-oleoyl-sn-glycero-3-[phosphor-rac-(1-glycerol)] (POPG/PG)
DOPG	1,2-dioleoyl-*sn*-glycero-3-[phospho-*rac*-(3-lysyl(1-glycerol))]
L:P	Lipid:Protein ratio
MPA	Multiphoton absorption
R_a	Access resistance
S	Noise spectral density where subscript represent components contributing to the noise for e.g. S_{vc} represents spectral noise density from interaction of

	voltage and capacitance.
T	Temperature
e_n	Root mean square (rms) noise voltage in the headstage input
f	Frequency
i	Current
k	Boltzmann constant = 1.38×10^{-23} JK^{-1}

Chapter 1 Introduction

The integrity of a cell, which is achieved by delimiting the internal environment of the cell from the drastically different external medium, is essential for its survival. The encapsulation and compartmentalisation of cells and organelles is achieved by biological membranes, which have a thickness of 4-5 nm [1-3]. These membranes form a vital component of living cells, not only defining boundaries that serve as a margin between life and death for individual cells, but also allowing various cellular processes such as communication and tightly regulated transport across the membrane to occur [3, 4]. Biological membranes contain particular proteins, known as membrane proteins, which serve a specific function [1]. Ion channels, an important and diverse family of membrane proteins, are ubiquitous and are expressed in all tissue and cell types in the human body [5]. They create a gated and water filled pore that facilitates the flow of ions between intracellular and extracellular environments as shown by a cartoon representation in Figure 1 [6, 7]. The controlled flow of ions through these channels establishes and maintains a voltage potential across the cell membranes [6]. Since membrane excitability and neurotransmission as required for the proper functioning of muscles, neurons and cardiac cells is based on the ion flux through these channels [8], it is not surprising that mutations in the genes encoding ion channels can cause cardiac disorders, neurological indications and impaired pain perception, collectively referred to as channelopathies [6, 9]. Given that the mutations in ion channels have been associated with more than 60 channelopathies, and considering the central role that ion channels play in human physiology, they represent attractive targets for drug discovery [6, 10]. The identification of novel ion channels has also been vital in expanding the set of ion channel drug diseases beyond neurological and cardiac disorders to cancer, immune disorders and other diseases [10].

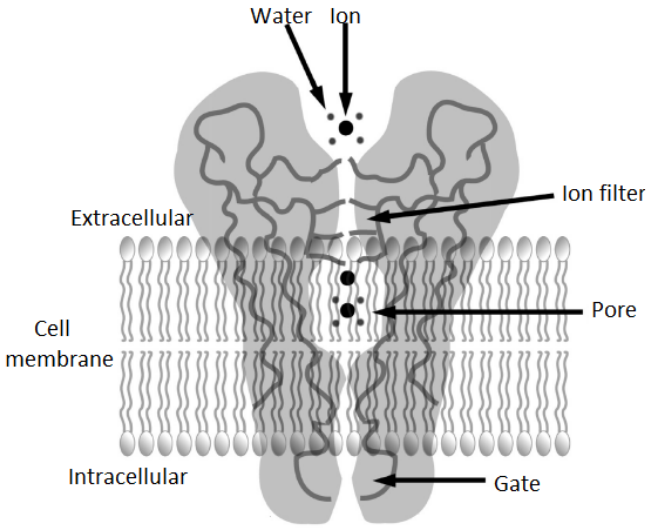

Figure 1: Cartoon representation of an ion channel embedded in a cell membrane. The figure shows structural components of ion channels featuring the pore region that allows passage of ion through the cell membrane, the selectivity filter that regulates which ions are permitted through the pore, and the gating domain that controls opening and closing of the pore, combined with a sensing mechanism that detects and responds to a given stimulus. [6]

The cardiac activation cycle or action potential (PQRST wave) is also dependent on the ion channels: sodium, calcium and potassium ion channel. During depolarisation phase of the action potential, the resting potential across cardiac cell membrane (-80 mV) becomes less negative and activates voltage-gated sodium channels that allow sodium ions to rapidly flow into the cell. This depolarisation of the membrane is maintained by opening of calcium channels that allow influx of calcium ions. The opening of rectifying potassium channel creates equilibrium between efflux of potassium and influx of calcium, causing the cell internal charges to plateau. In the repolarisation phase, the efflux of potassium dominates which brings the membrane potential to negative resting potential. The QT interval in the cardiac activation cycle is a measure of time from the start of the QRS complex to the end of the T wave in the electrical cycle and represents the duration of activation and recovery of ventricular cardiac muscle, or myocardium. During long QT syndrome, repolarisation is delayed thus extending the action potential, which could arise due to increase in depolarising current or decrease in repolarising current. This elongation of the QT interval is a marker of myocardial instability with possible development of ventricular arrhythmia and carries a risk of sudden death[1] [11, 12]. It has been found that non-cardiovascular drugs such as astemizole and cisapride can also cause QT interval prolongation by inhibiting potassium ion channels which causes delayed repolarisation of the ventricular myocardium or cardiac muscle [12, 13]. As a result, the Committee for Proprietary Medicinal Products of the European Union has made assessment of the potential for QT interval prolongation by non-cardiovascular drugs mandatory, which in turn requires potassium ion channel screening against these drugs [12].

[1] Wikipedia and GPnotebook (http://www.gpnotebook.co.uk/simplepage.cfm?ID=288686125). Date accessed 10/5/2012.

More than 50% of pharmacological drugs target membrane proteins [14-16] and 7.9% and 5.5%, respectively, specifically target ligand-gated and voltage-gated ion channels (the classification of ion channels is based on the stimuli and is discussed in Chapter 2) [8]. Drug design requires understanding of ion channel function, as dictated by their three-dimensional structure. Because these proteins require biomembranes to retain their structural, and hence functional, integrity, the study of biomembranes is also crucial for drug design [17]. As the major component of biological membranes, lipid molecules have also been reported to cause abnormalities, highlighting their prominent role in cell membranes [18]. Characterisation of biological membranes in general and of the properties of ion channels in particular is therefore of prime importance. However, because of the complexity of studying biological membranes *in vivo*, much of the information on the physical and chemical characteristics of membranes has been unravelled by artificial model membrane systems. These systems retain the essential lipid bilayer structure of biological membranes but are more suitable for the characterization of individual components [3, 16, 19].

Bimolecular lipid membranes (BLMs) were recognised as a model for biomembranes in the mid twentieth century when the first artificial model membrane system was demonstrated by Mueller *et al.* [20]. The idea of lipid bilayers has been derived from coloured soap films that exhibit spontaneous formation of distinct black regions [21]. This uncanny observation aroused the curiosity of scientists to pursue research in black soap films. Soon enough it was proved that these black regions correspond to ultra-thin regions, with a thickness of just a few nanometers, in the soap film. When free-standing planar lipids films are illuminated and reflected light is analysed, coloured reflections start developing grey-black spot which spreads over the film as the film starts to thin out (discussed in section 2.3.1.1). This is due to the destructive interference of the reflected light from the water/lipid interface and phase-shifted lipid/water interface, which has negligible pathway as compared to the wavelength. Various thermodynamic studies were carried out to gain insight in the formation of black regions at the air-water-air interface, or biface [22]. Following quantitative characterisation of ultra-thin soap films, the concept of the lipid bilayer, which is also few nanometres thin, was put forward and experimentally validated [21, 23]. The thermodynamic study explaining the formation of thin lipid bilayers at the “water-lipid bilayer-water” biface has been discussed in detail in [24-26]. Bimolecular lipid membranes have, over the last 50 years, covered a wide range of application areas, ranging from basic membrane biophysics including transport phenomena, practical AIDS research, and microchip studies, to the conversion of solar energy via photolysis, to biosensor development using supported lipid membranes, to photobiology comprising apoptosis and to photodynamic therapy [21].

1.1 Objective of the work

The small number of pharmacological drugs that target ion channels, in the context of the vast amount of resources invested in the drug discovery market in general, highlights the room for improvement in this field [5]. To date, patch clamp electrophysiology, the measurement of electrical activity of a patch of cell membrane that contains ion channels, has been the gold standard method for characterising ion channel properties and their modulation by drug candidates [12]. While the lipid bilayers are considered to be an inert electrical insulator, electrical phenomena in cell membranes are related to the ion conduction events mediated by ion channels [27]. The study of ion channels using electrophysiological techniques has also allowed the (patho)physiological effect of mutations in channels to be understood in considerable detail [7]. Ionic currents (electrophysiological recordings) can also provide substantial information on the distinctive gating mechanism of the channels such as number of states a channel can enter, time spent in each state and rate of transition between the various states. Although gating has been studied by macroscopic current measurements from a large number of channels through the entire cell membrane (whole cell electrophysiology) [28, 29], single ion channel data provides molecular insights that are nearly unattainable from macroscopic measurements [30, 31]. However, compared to other methods for drug screening such as efflux assays with fluorescent indicator dyes, the experimental throughput of the patch clamp electrophysiology technique is low, presenting a bottleneck in large-scale research programmes [8]. Due to the high importance of membrane proteins in drug discovery and due to complications with their *in vivo* characterisation platform, there is a demand for providing a robust, stable and high throughput platform for the formation of artificial membranes suitable for incorporation and characterisation of functional proteins. Vesicles, microbubbles, Langmuir-Blodgett films, supported phospholipid bilayers and suspended phospholipid bilayers are some of the established artificial membrane systems [32-34]. Various ion channels including potassium channels, sodium channels, acetylcholine receptors and ryanodine receptors have been studied using lipid bilayers that are suspended across an aperture in a hydrophobic septum. This resembles the cell membrane patch at the tip of the glass capillary in patch clamp electrophysiology, but aperture-suspended bilayers suffer from poor stability of the bilayer, resulting in a low experimental throughput. Hence, the objective of this project is to establish a platform for formation of stable aperture-suspended lipid bilayers that can be used for bilayer incorporation and functional characterization of ion channels, including drug screening. Other factors including manufacturability of the apertures for lipid bilayer formation will also be considered.

1.2 Motivation for the work

The availability of a range of platforms for artificial biomembrane formation is an indication that each system has its advantages. A compromise is made while selecting a model for bilayer formation. For example, suspending of bilayer across an aperture makes it fragile but allows the incorporation of active transmembrane proteins, while this situation is reversed in the case of solid-supported lipid bilayers. Thus, the motivation for this project comes from the need for optimisation and refinement of one of these techniques for achieving the objective of this PhD project, which is the development of a platform that contains lipid bilayers that are stable for tens of hours that can be used for the functional characterization of ion channels in the absence and the presence of channel effectors such as drug candidates.

1.3 Challenges for the work

The electrophysiological requirement of a large measurement bandwidth to obtain high temporal resolution of pA current amplitudes puts stringent requirements on the read-out electronics, necessitating the use of low-noise headstage current amplifiers (amplifiers placed as close as possible to the recording electrodes). However, an increase in bandwidth is accompanied by an increase in noise and this limits the sensitivity, i.e. the capability to clearly resolve pA current events. It has been shown that the noise spectrum is dependent on the total capacitance of the bilayer system. Since the artificial bilayers are a major contributor to the total capacitance, it is necessary to reduce the bilayer area in order to minimize the electrical noise in the current recordings [35, 36]. However, reducing the bilayer area makes it more difficult to achieve bilayer insertion of active membrane proteins by proteoliposome fusion, and it is also difficult to achieve high protein density in a smaller bilayer [37, 38].

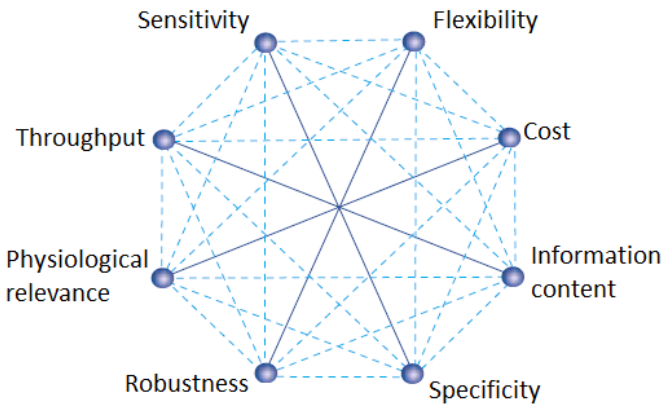

Figure 2: Interdependence of parameters for ion channel assays where solid lines indicate an opposing relation and dotted lines represent positive or negative impacts [39].

One of the major concerns with aperture-suspended lipid bilayers is the fragile nature of the bilayers. It is known that bilayer stability can be increased by reducing the size of the bilayer (i.e. using a smaller aperture) [26] or by changing the geometry of the aperture across which the bilayer is suspended [40], but smaller bilayers limit the proteoliposome fusion area. These arguments highlight the interdependence of the various attributes, with improvement in one aspect coming at the cost of a decreased performance in other aspects of the system. Figure 2 shows inter-relation of attributes of ion channel assays in such a way that change in requirement of one attribute brings positive or negative impact on several other attributes. The attributes placed at the opposite end have a negative impact on each other i.e. attainment of one attribute comes at a sacrifice of the other. Hence, the overall challenge in this PhD project is to improve one parameter while minimally compromising the other important parameters. Specifically, the geometry of the aperture, but not its diameter, will be changed, as shown in Figure 3, to enhance the stability of the aperture-suspended lipid bilayers. These shaped apertures will be fabricated in a hydrophobic septum material with low intrinsic noise, good mechanical and chemical stability.

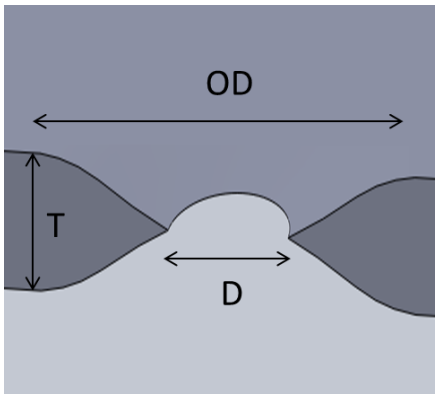

Figure 3: Schematic illustrating of a shaped aperture, with a thin aperture edge that tapers out to the full thickness of the bulk septum. T= thickness of the sheet, D= diameter of the aperture, OD= outer diameter from where the tapering of the edge-wall begins.

1.4 Novelty of the work

As has been discussed in the previous paragraphs, the issue of fragile suspended bilayers can be addressed by the use of shaped apertures without substantially compromising other assay parameters, but the current method mentioned in the literature employs high intrinsic capacitance materials and supports which increases noise. To address this issue, shaped apertures in standalone septum sheets of low intrinsic capacitance and UV-polymerised photoresists will be used. The shaped apertures will be fabricated using two-photon polymerisation technique and a mass production method of grayscale lithography. Although these methods were introduced few decades back, their usability for such application has not been demonstrated. In this work, a systematic study of dependence of bilayer stability on the shape of the aperture will be

undertaken. Moreover, optically accessible lipid bilayers suspended in shaped apertures will be used to demonstrate the applicability of shaped apertures for “protein incorporation into lipid bilayer” studies.

1.5 Structure of the thesis

As this work involves fabrication of apertures for forming stable lipid bilayers and also of the electrical characterization of ion channels, the literature review has been divided into two distinct chapters. Chapter two presents general background on biological membranes and ion channels, together with a discussion of electrophysiological techniques for ion channel studies and an overview of artificial model membrane systems. Chapter three then discusses the technicalities of the role of the septum in which the aperture is made, the size of the aperture, and the use of lithographic techniques for aperture fabrication, and concludes with an overview of existing microfluidic platforms for high throughput electrophysiology. Chapters four and five subsequently present and discuss the fabrication of shaped apertures with, respectively, serial and parallel lithographic techniques. Chapter six describes the results from the lipid bilayer stability experiments in the shaped apertures while Chapter seven contains electrophysiological measurements of sodium and potassium ion channels obtained with bilayers suspended in the fabricated shaped apertures. Chapter eight forms the last experimental chapter of this thesis, presenting preliminary data on optically accessible lipid bilayers in shaped apertures in microfluidic chips, suitable for the observation of fluorescently labelled ion channels. Finally this thesis concludes with a recapitulation of the key findings and a future outlook for shaped apertures that can produce stable lipid bilayers to be used for electrophysiological or optical studies.

Chapter 2 Lipid bilayers and ion channel electrophysiology

2.1 Membranes

Biological membranes form the outer boundary of cells and as such play an essential role in cell protection and transport of molecules into and out of the cell. Biomembranes act as an effective diffusion barrier and as a scaffold for membrane proteins and surface carbohydrates which facilitate communication and transport across cells. Since cell membranes are amongst the most important interfaces in a living organism, the study of membrane structure, properties, and functions has been an attractive research area. Biophysical and biochemical studies have given fundamental insight in processes such as cell metabolism, signal transduction, and the interplay of various membrane components like sterols, lipids and proteins [41]. Biological membranes are composed of a lipid double layer, usually referred to as a bilayer, that has a fluid character [15, 16, 19, 32]. A lipid molecule is amphiphilic in nature as it consists of a hydrophilic head group and hydrophobic tails. The tendency of the hydrophobic domains to pack together and avoid exposure to polar water molecules, in combination with and geometric packing constraints, drives these molecules to self-assemble into lamellar bilayers in aqueous solution [42]. The hydrophobic tails point towards the inside of the bilayer and the polar head groups are situated at the two surfaces

(Figure 4). A membrane that only consists of lipid molecules forms an effective diffusion barrier for most molecules and ions.

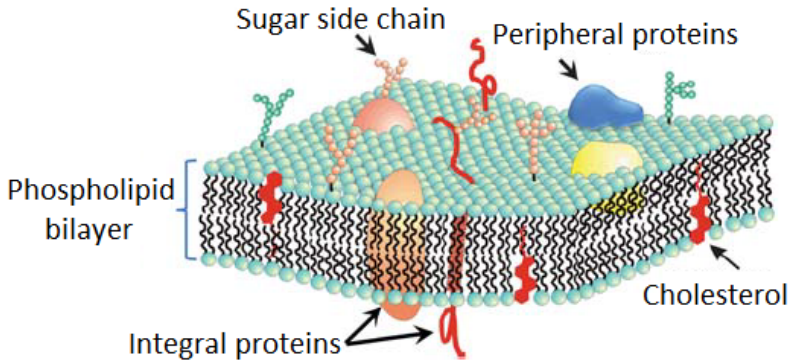

Figure 4: Cartoon illustration of a biomembrane. It consists of a phospholipid bilayer in which the hydrophobic tails of the lipid molecules are buried within the interior while the hydrophilic headgroups are exposed to the aqueous environment. Integral and peripheral membrane proteins provide functionality to membranes by controlling the transport of molecules and ions across the membrane [19].

2.1.1 Membrane proteins

Since biomembranes act as barriers, controlled transport into and out of the cell is facilitated by membrane proteins, which hence form a vital functional component of the membrane. These integral and peripheral proteins are involved in processes such as energy conversion, regulation of transport across the membrane, and signal transduction. Although neutral gases and, to some extent, water can cross a pure-lipid membrane, diffusion of electrolytes such as potassium, sodium or chloride ions through the hydrophobic interior of the membrane is energetically unfavourable in the absence of membrane proteins [32]. Based on the mechanism of translocation of ions or molecules across the membrane, Figure 5 categorises different types of membrane proteins according to the transport mechanism, which can be active or passive. Active transport as facilitated by transporter proteins works against ion concentration gradients and requires metabolic energy. Passive transport as enabled by ion channels and carriers is driven by a concentration gradient and allows molecules to flow towards the side of the membrane with the lower concentration. Due to interaction of molecules or ions with amino acid residues in the path across the membrane, carriers have generally have a much lower translocation efficiency than ion channels [14]. Ion channels can be further categorized according to the stimulus that activates, or opens, the channel. Voltage-gated channels are typically activated by a depolarisation potential and are crucial for neuronal and cardiac excitability as they permit the cells to initiate and propagate action potentials. In ligand-gated channels, the change in conformation of the channel is brought about by the binding of small biomolecules called

ligands, such as neurotransmitters or hormones. Mechanosensitive channels open as a response to a mechanical stimulation, e.g. pressure, and are important regulators in osmotic sensing [14].

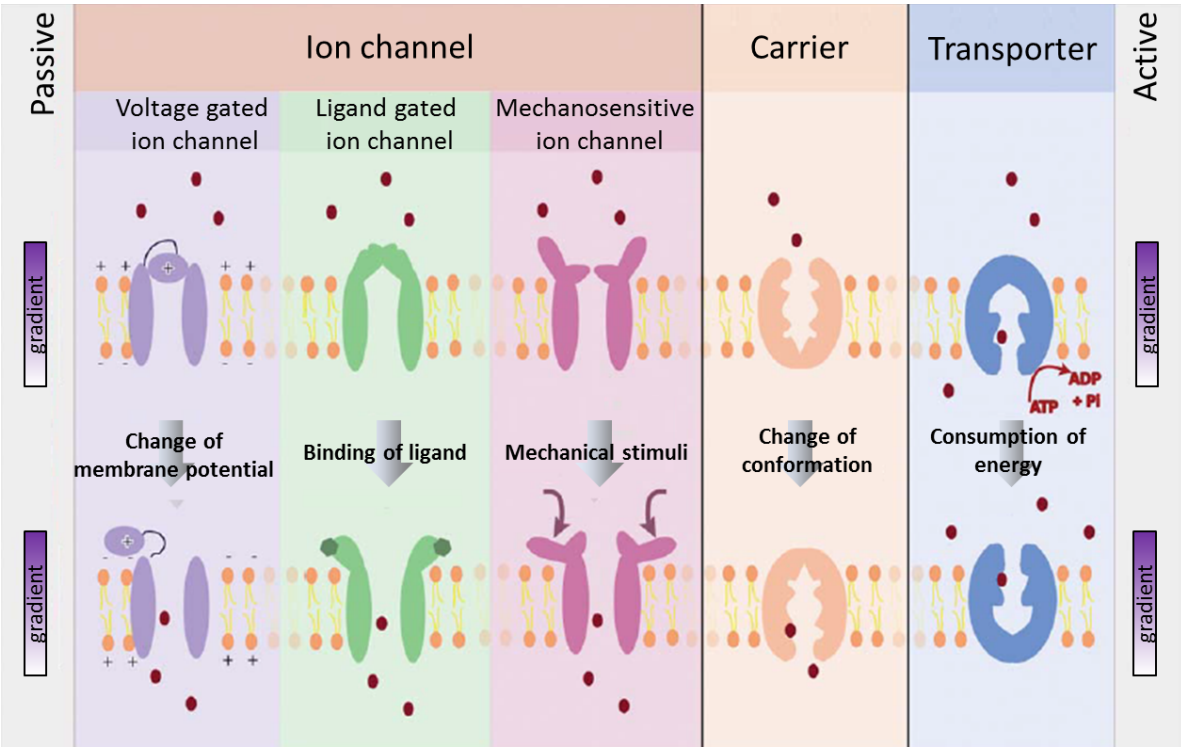

Figure 5: Classification of membrane proteins based on the translocation mechanism of molecules or ions. Active transportation (by transporters proteins) translocates molecules against a concentration gradient, consuming metabolic energy (ATP). Passive transportation (by ion channel and carrier proteins) is along the concentration gradient. Ion channels can be categorized into several types depending on the stimulus which activates or opens the channel. These include voltage change, ligand binding and mechanical stimulus [14].

An ion channel consists of two major functional units, the 'gate' and the 'pore'. The pore provides the pathway for penetrating ions while the gate is a mechanism for switching the ion flux 'off' and 'on'. This opening and closing of the pore is brought about by conformational changes in the protein, known as the 'gating' mechanism [6, 43]. When a channel is in the 'on' or 'open' state, ions pass through the lipid membrane depending on the applied potential and ion concentration across the membrane, at a rate of 10^6 to 10^9 ions per second, producing an electrical current on an order of 10^{-12} to 10^{-10} amperes [6]. The resulting electrical conductance is a measure of ion flux efficiency. Because it is dependent on factors such as pore size, pore length and the dielectric constant in the pore, the conductance is a characteristic property of an ion channel [43]. Each ion channel also has a specific structural arrangement of amino acids at the entrance of the pore, known as the selectivity filter, which imparts characteristic selectivity to the ion channel by favouring a specific ionic species. For example, the filter structure of a potassium ion channel provides a better fit for potassium (K^+) ions than for sodium (Na^+) ions, thus translocating potassium ions 100x more efficiently than sodium ions [44]. However, anions are not passed through the channel due to electrostatic repulsion by negative charges on amino acids of the filter [44].

Since the selective transport of ions across the membrane underlies numerous physiological processes, including heart signalling, nervous signalling, fluid secretion in the lung, hormone secretion, the immune response and tumour cell proliferation [45] and because ion channels are also involved in a wide range of pathologies, covering the majority of therapeutic areas, they are regarded as important drug targets [14]. Moreover, >50% of all current pharmacological drugs target a membrane protein, which makes it essential to characterize properties of membrane proteins in general, also of non-channel proteins, in the context of drug discovery and drug design [41]. However a lipid environment is required to maintain the functionality of membrane proteins, which necessitates careful consideration of the characterisation technique and the measurement setup [17].

2.2 Electrical characterisation of ion channels - Patch clamp electrophysiology

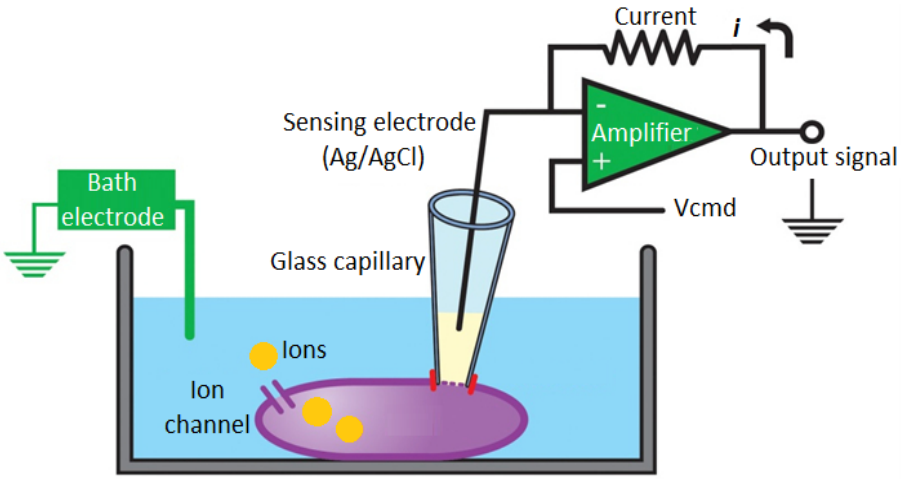

Figure 6: Schematic illustration of an experimental setup for a whole-cell patch clamp to study ionic currents through ion channels in the membrane. A glass pipette is pressed against the surface of a cell in which the ion channel to be studied has been expressed. A sensing electrode, silver-silver chloride (Ag/AgCl), is placed in the electrolyte solution inside the pipette. The electrical circuit is completed by a second electrode, which is grounded, placed in the bath solution. The sensing electrode is connected to a transimpedance amplifier which converts a current signal into a voltage output. *Vcmd* stands for command voltage. [45]

Electrical measurement of ion permeation is the most powerful method to characterize ion channel function, especially at the single-channel level [8, 46]. One of the most widely used methods for studying the currents flowing through the ion channels is patch clamping of cell membranes, following cellular expression and membrane incorporation of the ion channel of interest [47]. The conventional patch clamp technique, developed by Sakmann and Neher, involves pressing of tip of a glass pipette onto the surface of a cell to form a high resistance seal, followed by application of negative pressure to rupture the cell membrane and achieve access to the interior of the cell, enabling recording of the ion channel currents from the whole cell

membrane [48]. A high-resistance seal isolates the current measured across the membrane from the competing noise by allowing the flow of ionic currents only through the pipette and not through the seal [49], and it also provides electrical continuity between the pipette electrode and the inside of cell. The glass pipette is filled with electrolyte and an electrode is placed in it. This electrode is attached to a transimpedance amplifier for converting the detected current into voltage signals. The electric circuit is completed by another electrode, which is grounded, in the bath solution as shown in Figure 6. In this configuration, the electrical current flowing over the entire cell membrane, except for the excised patch, is measured.

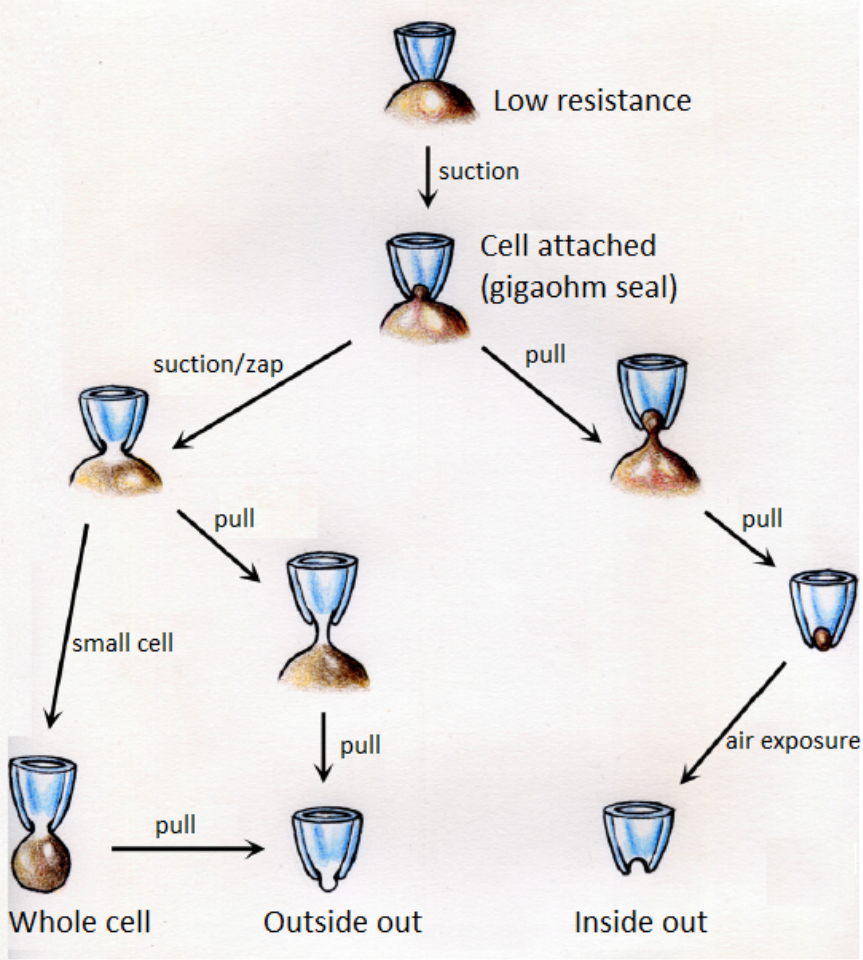

Figure 7: Schematic illustration of configurations of patch clamp electrophysiology techniques- whole cell configuration achieved when the part of the membrane patched by the pipette is ruptured, outside out configuration obtained by pulling the pipette from whole cell mode, and inside out configuration achieved by pulling the pipette away from the cell in cell attached configuration [50].

Patch clamp electrophysiology produces data of unparalleled fidelity and quality, having a high temporal resolution for recording ultra-rapid kinetics, i.e. ion channel gating on a timescale of a few milliseconds, and a high sensitivity to detect channel currents in the pico ampere (pA) range [45]. For the important class of voltage-gated ion channels, it also provides precise control of channel gating by clamping the membrane potential, which is not possible with non-electrophysiological assays [8]. Since the ionic current measured using the whole-cell recording

mode represents the activity of all the ion channels present in the membrane, small changes in ion channel conductance can be easily observed. However, simultaneous gating of a large number of ion channels makes it difficult to resolve the gating kinetics of the channel of interest [5]. Other patch clamp configurations, shown in Figure 7, are used to measure fewer ion channels simultaneously, down to a single channel. Cell-excised configurations (inside out and outside out) are achieved by withdrawing the pipette from the cell after the formation of a stable and tight seal, resulting in a smaller membrane area (only the membrane patch) between the electrodes. At a sufficiently low density of active ion channels, gating of a single ion channel can be observed in this configuration.

2.2.1 High throughput electrophysiology

Screening of a large collection of chemical entities against ion channel targets make a high throughput platform necessary for primary screening of drugs [39]. Although patch clamp electrophysiology provides the desired sensitivity and resolution, it suffers from low throughput due to the technical expertise and manual labour required [45]. On the other hand, non-electrophysiological methods for screening provide higher throughput, but suffer from significant drawbacks such as low temporal resolution (several seconds to minutes) is insufficient for rapid-gating channels), dependence on non-physiological methods for channel activation, and a high frequency of false positive readouts [45]. As such, there has been an increased demand for high throughput patch clamp electrophysiology, which has been the driving force to develop new electrophysiology platforms. A successful approach is the automated planar array patch clamp technique, which combines much, but not all, of the reliability and precision of manual patch clamp with an increase in throughput, attained by automation of manual procedures and parallel recordings, i.e. measuring multiple cells simultaneously [8]. This is achieved by replacing the pipette with a patch plate with a single or multiple planar apertures to trap the cells by suction and to form the electrical seal (Figure 8). These planar aperture chips may or may not have a built-in flow channel for fluid exchange. Over the last decade, several instruments for automated electrophysiological studies have been introduced into the market., which differ from each other in terms of liquid handling systems and patch plate material [8]. Recently introduced commercial products have taken the throughput of automatic patch clamp to newer levels where 384 or 768 cells can be recorded in parallel with 384 amplifiers and pipettes and examples of such recording systems include the Qube from Sophion, Synchropatch 384 PE (can record 768 cells in parallel) from Nanion Technologies, and Ionworks barracuda from Molecular Devices. Although automated patch clamp technology provides a medium to high throughput platform for electrophysiology, it involves recordings in the whole cell mode and is therefore not suitable for studying single ion

channels. Moreover, the challenge regarding the reproducibility with the cells being used is often underestimated, which is the key to success in parallel electrophysiology [8]. It can also be problematic to guide the cells to the recording sites and successfully form a gigaseal as required for low-noise recordings [48].

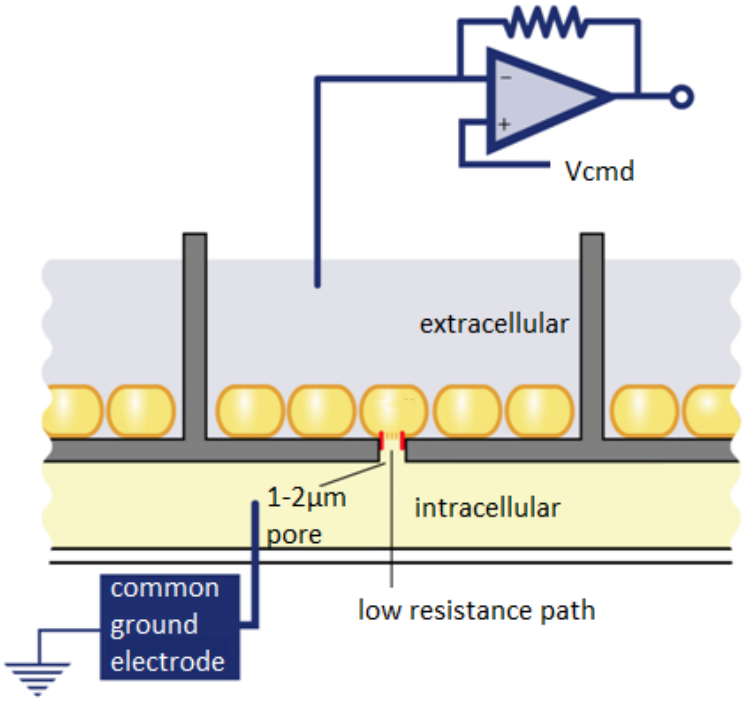

Figure 8: Schematic illustration of an automated patch clamp configuration with no provision for fluid exchange. The patch pipette is replaced by a planar plate, with each well in the plate having a micro-aperture on which a cell becomes trapped by suction, resulting in the formation of an electrical seal [8].

2.3 Biomimetic model membranes

Natural cell membranes are inherently complex multi-component assemblies and this structural complexity limits the scope of their utility [4]. This has led to the development of several biomimetic model membranes for studying properties, structure and processes pertaining to membranes [19, 32]. These *in vitro* membrane systems also enable direct incorporation and electrophysiological studies of membrane proteins, which can potentially revolutionise drug screening technologies [16]. Biomimetic membranes, or artificial model membrane systems, exploit the self-assembly of lipid molecules into lamellar lipid bilayers, either as a suspended lipid bilayer, a supported bilayer, or a tethered supported bilayer [19]. The formation of a lipid bilayer across an aperture and on a suitable support is schematically depicted in Figure 9. For ease of discussion, the following section will be divided into three sub-sections: suspended bilayers, solid-supported bilayers and pore-supported bilayers.

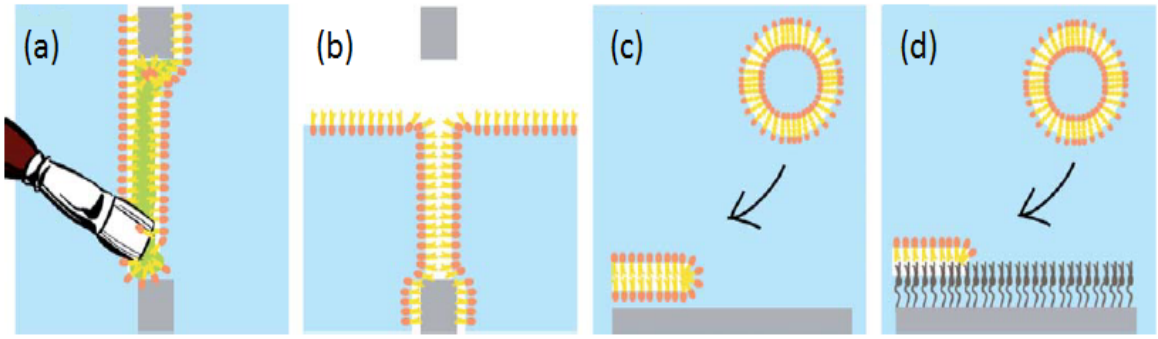

Figure 9: Schematic illustration of preparation methods for biomimetic model membranes. (a) Painted bilayer formed by application of lipid in non-polar solvent across an aperture in a hydrophobic septum. (b) Montal-Mueller (folded) bilayer formed by raising of buffer solution covered by a lipid monolayer over both sides of an aperture in a hydrophobic septum. (c) Solid-supported bilayer formed on a hydrophilic surface by fusion of a vesicle. (d) Supported bilayers tethered via a linker molecule to a solid support, also formed by vesicle fusion. The blue colour represents buffer solution [14].

2.3.1 Suspended bilayers

Aperture-suspended lipid bilayers (see Figure 10) offer the significant advantages of easy access to the solution, and therefore control of the ionic composition, on both sides of the bilayer, formation of a giga seal, and clamping of the voltage across the membrane [51]. But it suffers from an inherent and serious disadvantage of instability, with the membrane typically breaking within a few minutes to a few hours of preparation. Lipid bilayers are conventionally suspended across an aperture with a diameter of several hundred micrometers in a hydrophobic septum by the Mueller-Rudin (‘painting’) method, in which an oil-lipid solution is deposited on the aperture and the bilayer forms when the oil phase (or solvent phase) has thinned to a sufficient extent [20], or by the Montal-Mueller ('folding') method [52], in which an air-water interface with a lipid monolayer is raised over both sides of the aperture, which is typically pretreated with an apolar solvent [53, 54]. Although the folding method involves a substantially smaller amount of solvent than the painting method, both protocols result in a planar bilayer that is connected to the wall of the aperture by a solvent annulus which is also referred to as the Plateau Gibbs border [25, 55-57]. Lipid bilayers formed by the painting method also have sub-microscopic solvent lenses, formed due to separation of excess solvent during bilayer thinning, scattered over the surface [58, 59]. The presence of this extra solvent in painted bilayers may affect ion channel activity, which would be undesirable [55]. The solvent used for the formation of painted bilayers has also been shown to affect bilayer thickness, with shorter alkanes producing thicker and more compressible bilayers [60-63]. Since a change in bilayer thickness can affect ion channel function [64-66], the choice of solvent and lipid species needs to be carefully considered. Lipid bilayers produced with the folding method have a significantly lower solvent content and their formation is more reproducible than painted bilayers [54, 55].

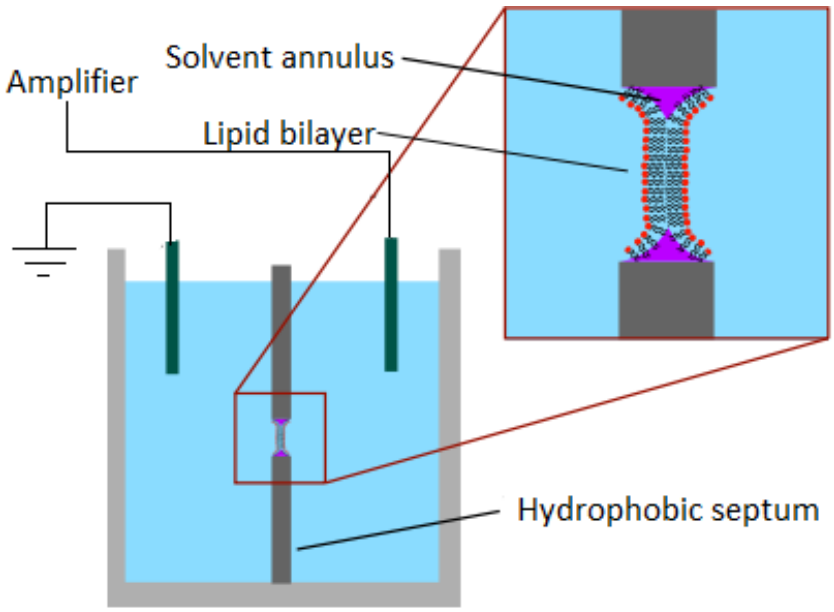

Figure 10: Schematic illustration for ion channel electrophysiology using a lipid bilayer suspended across an aperture in a hydrophobic septum. After the formation of the suspended bilayer the ion channel of interest is incorporated in the bilayer. The bilayer current is recorded using two AG/AgClelectrodes, one of which is connected to the transimpedance amplifier and the other is grounded.

2.3.1.1 Suspended bilayer formation with the painting method

Before the formation of a bilayer at the aperture, a thick solvent-lipid plug blocks the aperture, creating a water-solvent-water biface. Since the septum material is hydrophobic, the non-polar solvent wets the walls of the aperture and excess solvent drains away over the surface of the septum. Under favourable conditions, the solvent-lipid film thins spontaneously to bring two monolayers in close proximity (0.1-1 µm) and the solvent is pushed to the periphery, forming a solvent annulus. A lipid bilayer is not formed readily because the attraction between the two solvent-separated monolayers is negligible for distances >100 Å. The further thinning of the membrane is brought about by the Plateau Gibbs border (PGB) of the solvent annulus [26]. Due to the concave interfaces at the Plateau Gibbs border, it has less pressure compared with the central region of the oil-lipid film. The PGB therefore exerts strong suction on the remaining solvent and causes rapid thinning of the oil-lipid film. An additional cause of thinning is the “zipper like” action contributed by the Van der Waals forces of attraction between the lipid monolayers [26]. Recently, Beerlink *et al.* imaged the Plateau Gibbs border and the process of thinning in an aperture by using X-ray propagation and near field diffraction (Figure 11) [57].

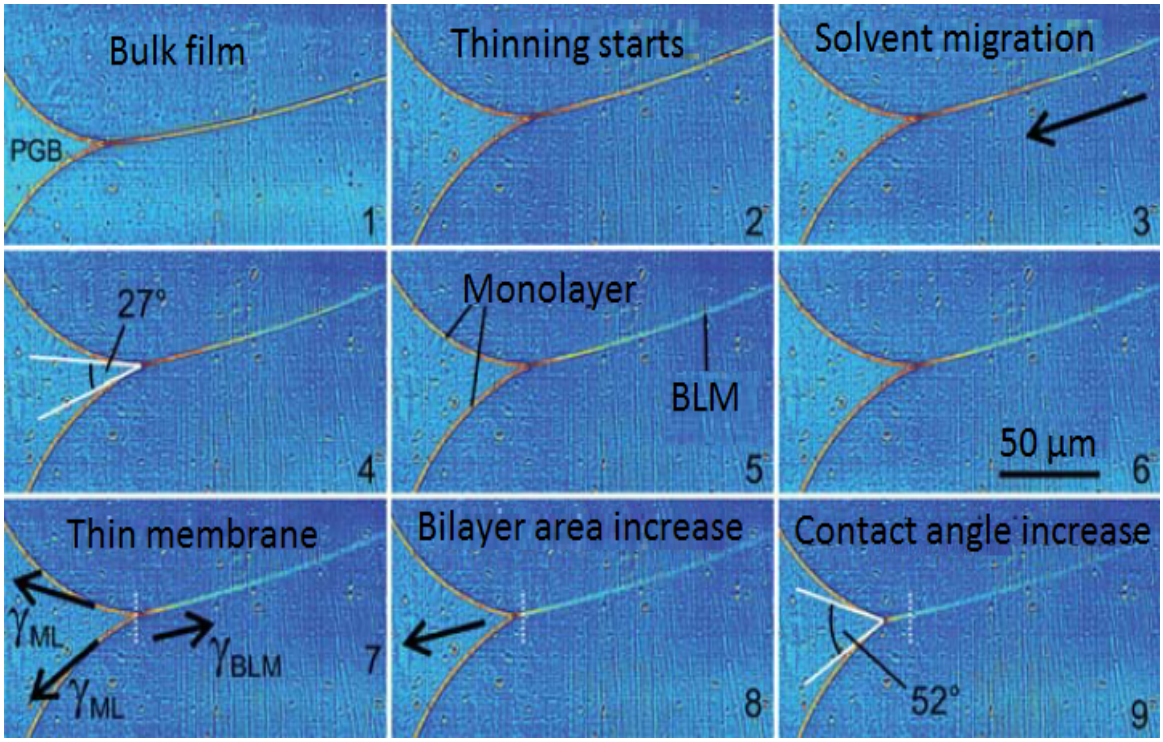

Figure 11: Series of images demonstrating the thinning process of a painted oil-lipid film into lipid bilayer using X-ray propagation imaging. Two monolayers of lipid molecules assemble at the solvent-buffer interfaces. Adhesive forces and van der Waals forces drive the solvent into the Plateau-Gibbs border (PGB). γML represents the interfacial tension of the monolayer and γBLM represents the interfacial tension of the lipid bilayer. Since the tension of BLM (γBLM) is smaller than twice the tension of monolayers (γML), a force is present that expands the bilayer [57].

2.3.1.2 Electrical properties of lipid bilayers

The lipid bilayer is a three-dielectric layer structure, formed by the hydrocarbon interior sandwiched between the two polar head regions [67]. The equivalent electrical circuit of a bilayer consists of a capacitor in parallel with a resistor of several GΩs, with the specific capacitance of the bilayer being determined primarily by the dielectric coefficient and the thickness of the hydrocarbon layer [2, 68]. Consequently, application of a triangular voltage wave to a bilayer produces a square wave by the differentiating action of the bilayer. This method is normally used for electrical validation of bilayer formation in an aperture, although optical microscopy can also be used. However, the presence of a capacitance in the aperture does not necessarily signify the presence of a bilayer. After the application of the lipid-oil solution to the aperture, the following configurations are possible: the aperture may be filled with a lipid-solvent plug, a single suspended bilayer is present, multiple bilayers have formed in the aperture, or a combination of a bilayer and a solvent plug is present (Figure 12). All these configurations have dielectric properties and can give rise to a capacitance. However, the ~5 nm thickness of a single bilayer imposes a minimum capacitance requirement which cannot be achieved by the other configurations.

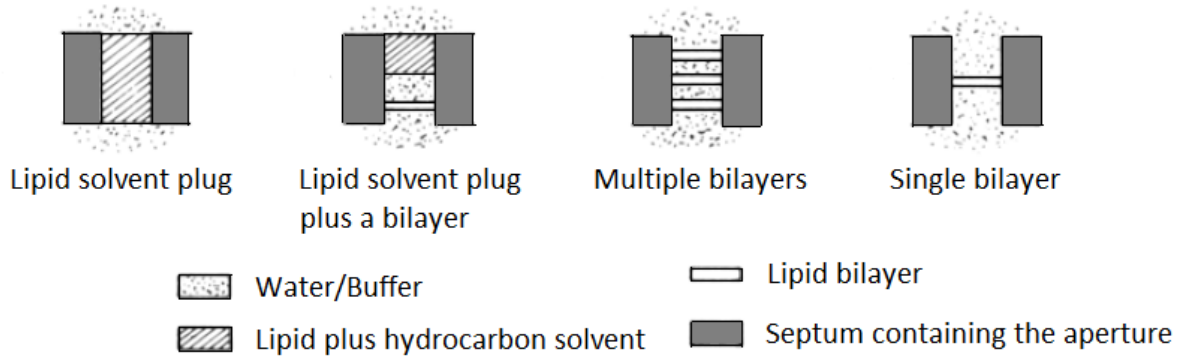

Figure 12: Schematic illustration of possible configurations that a lipid-in-solvent solution can take when applied to a hydrophobic aperture [69].

2.3.2 Solid-supported bilayers

Unlike aperture-suspended bilayers, supported bilayers are quite stable, owing to the attachment to a solid surface which confers mechanical stability [41]. Supported bilayers are obtained by spontaneous rupture of vesicles, or liposomes, on the surface of the solid material, which should be smooth and hydrophilic to promote vesicle adhesion and rupture [38]. Because of their method of formation supported bilayers are free of solvents (Figure 13). However, the increase in stability comes at a cost: incorporation of transmembrane protein becomes difficult due to unfolding of extramembranous protein domains in contact with the solid surface, and the limited volume of the aqueous phase under the lower leaflet of the lipid bilayer makes electrophysiological measurements difficult [16]. The most significant improvement in the field of supported bilayers has come from strategies to decouple the bilayer from the underlying support, by forming a tethered bilayer on spacer molecules [19]. Supported bilayers have been used for detection of ligand binding to membrane proteins by surface plasmon resonance [32].

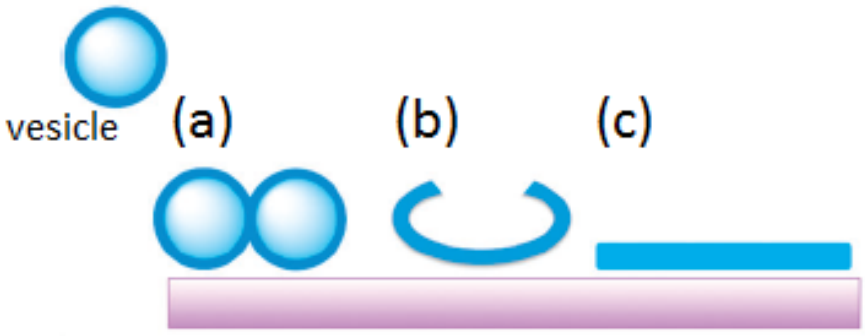

Figure 13: Schematic illustration of supported bilayer formation: (a) adhesion of vesicles to the hydrophilic surface, (b) rupturing of vesicles on the surface, and (c) formation of a continuous supported bilayer by coalescence of smaller bilayer domains [70].

2.3.3 Pore-supported bilayers

A better bilayer platform could be attained by combining the advantages from the aperture-suspended and the solid-supported approaches. Bilayers supported by a porous substrate can provide the advantage of stability as a result of the support on which they are formed and allow ion channel electrophysiology as well because the pores connect to a larger aqueous reservoir [71, 72]. Stable and solvent-free lipid bilayers spanning pores of sub-micrometer diameter fabricated in silicon or silicon-based substrates have been demonstrated that can be used for multiplexed analysis of membranes using fluorescence signal [73-75]. Recently Sugihara *et al.* demonstrated formation of a bilayer formed by vesicle fusion over a single 800 nm aperture (Figure 14) and measured ion channel conductance of a self-inserting peptide with integrated electrodes [71]. However, this approach suffers from issues with leakage current and the use of sub-micron aperture makes the incorporation of protein ion channels delivered by vesicles difficult because of the limited fusion area [37, 38].

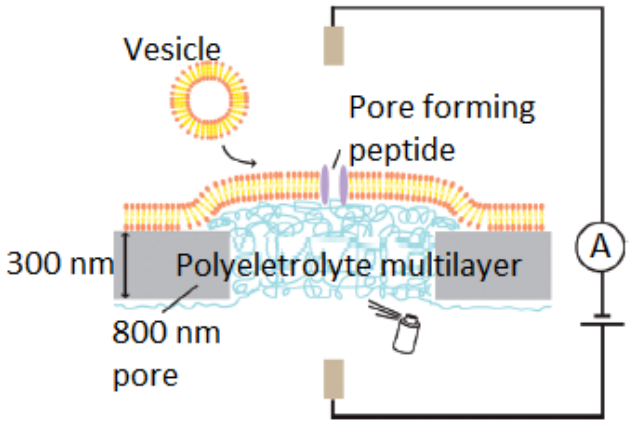

Figure 14: Schematic illustration of a pore-supported lipid bilayer formed by vesicle fusion on a silicon nitride/silicon chip filled with polyelectrolyte multilayers for promoting fusion of vesicles. It combines the advantages of aperture-suspended and solid-supported bilayer platforms: solvent-free stable bilayers with substantial aqueous reservoirs on both sides of the bilayer [71].

2.4 Ion channel incorporation in model membrane systems

Ion channel electrophysiology requires that the channels are present in a membrane but incorporation of the ion channels into model membranes such as aperture-suspended bilayers represents one of the major challenges [76]. While some ion channels (e.g. gramicidin, alamethicin, α-hemolysin and OmpF [14]) can insert directly from the aqueous solution into the bilayer, the vast majority of membrane proteins or transmembrane ion channels are not capable

of self-insertion [16]. Incorporation of such protein ion channels into the bilayer requires the use of detergents or lipid vesicles. Figure 15 illustrates different procedures for ion channel incorporation in free standing lipid bilayers. The first method shows the incorporation of ion channels solubilized with detergent micelles into preformed bilayers. The second method demonstrates the incorporation of ion channels by fusion of vesicles containing the desired protein in the vesicle bilayer, also known as proteoliposomes, with the preformed planar free-standing bilayers. Another approach for studying ion channels in their native membrane environment is to transfer cell membrane fragments onto nano-porous silicon nitride substrates [14]. Nonetheless, the vesicle-mediated ion channel incorporation method is regarded as the most promising approach for protein delivery to pure-lipid bilayers [16]. To facilitate protein incorporation by proteoliposome fusion, osmotic pressure modulation, with or without transient nystatin-ergosterol channels, can be employed [77, 78].

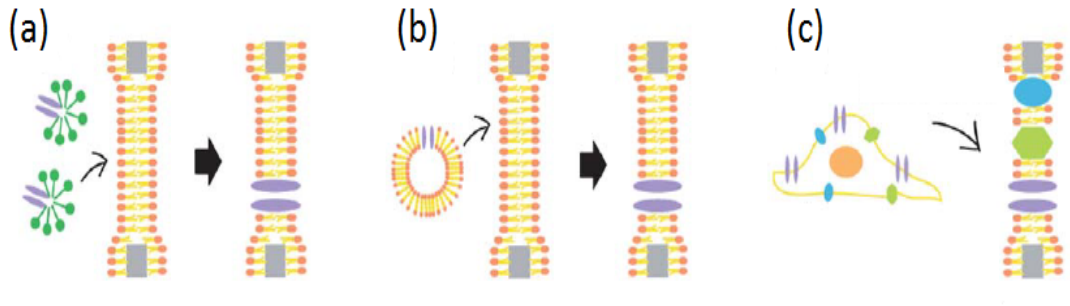

Figure 15: Schematic illustration of ion channel incorporation procedures for free-standing planar lipid bilayers using (a) detergent-solubilized membrane proteins in the form of protein-containing detergent micelles (b) proteoliposomes with proteins incorporated into the vesicular bilayer, and (c) native cell membranes [14]

2.5 Peptide and protein ion channels

Ion channels can be classified into protein ion channels and peptide ion channels. Peptide ion channels are composed of monomers of up to ~50 amino acids and are typically (antimicrobial) toxins [14]. Protein ion channels tend to be (substantially) larger and are usually not water-soluble, unless their biological role is that of a membrane-targeting toxin. The following sections discuss ion channels, from both these categories, which will be used in this project to demonstrate the capability of the bilayers in the developed platforms to support ion channel incorporation and correct ion channel function.

2.5.1 Peptide ion channels

Since most protein ion channels are difficult to express and purify, channel-forming peptides, which mimic the transmembrane domains of larger and more complex channel

proteins, have been used extensively in biophysical membrane studies. These biomolecules are small in size (<50 amino acid residues) and adsorb onto artificial lipid membranes from solution and self-insert into the bilayers to form (multimeric) pores. Even though they are not relevant for drug screening, they provide good models for membrane protein assays and offer the advantages of commercial availability and stability in solution [14].

2.5.1.1 Gramicidin

Due to its easy handling, simple structure and selectivity for monovalent ions, the peptide gramicidin from *Bacillus brevis* serves as an excellent model for transmembrane ion channels [79, 80]. Gramicidin belongs to a family of antibiotics which increase the permeability of the cell membrane to cations [81]. It self-inserts into membranes to form ion channels which are only functional in a suitable lipid bilayer environment [79]. A single gramicidin channel consists of two monomer units, which insert into opposite leaflets of the bilayer. Only when these two monomers units come together is a channel formed for ions to pass through, as shown in Figure 16b. Gramicidin occurs in three natural variants (gramicidin A, B and C) which differ from each other in the amino acid at position 11 in the peptide chain. Most experiments are performed with the natural mixture known as gramicidin D which is predominantly (80%) gramicidin A.

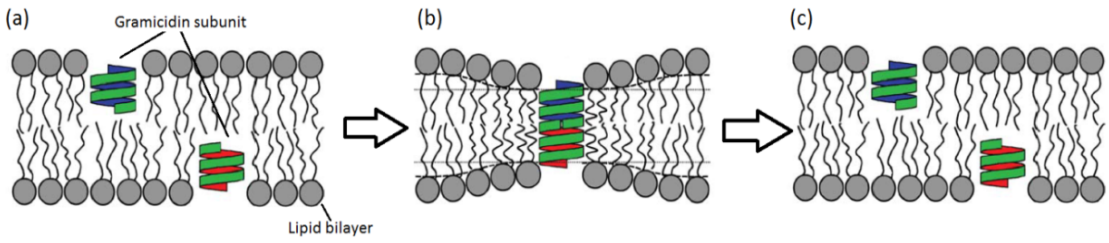

Figure 16: Schematic representation of the formation of a gramicidin channel in a lipid bilayer. The channel is formed by association and dissociation of non-conducting gramicidin monomers. (a) No channel is formed, (b) a channel is formed by dimerization of two opposing monomers, and (c) the channel closes because of monomer dissociation. The channel open time is defined by the lifetime of the conducting dimeric state [81]

Because the hydrophobic amino acids of gramicidin render this peptide insoluble in water, it is dissolved in polar organic solvent in which gramicidin exists in its monomeric form. However, gramicidin has also been shown to exist as a mixture of a non-channel forming dimer in equilibrium with a channel-capable monomeric form when dissolved in alcohols [82]. The current-voltage curve for gramicidin is fairly linear, with a single-channel conductance of about 11 pS in 1 M NaCl (e.g. Figure 17). Although the channel is to some extent voltage-sensitive, there is no voltage at which the channel is closed [83]. Channel conductance events for gramicidin have a lifetime in the order of seconds [83].

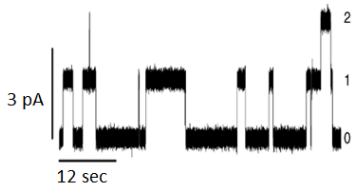

Figure 17: Single-channel current trace of gramicidin A in a lipid bilayer, for 1 M NaCl and an applied potential of 200 mV. ([81]). Each upward current step represents the formation of a gramicidin channel in the bilayer. Number 0, 1, 2 illustrate the presence of no, single and two gramicidin channels.

2.5.1.2 Alamethicin

Alamethicin is an antibiotic peptide from the fungus *Trichoderma viride* that exhibits a voltage-dependent conductance, has multiple non-equidistant single-channel conductance levels and a macroscopic dipole moment [84]. Alamethicin produces macroscopic currents when added to a bilayer which, depending on the lipid composition, can be larger when the potential of the side opposite to that of alamethicin addition is made negative [83]. The conductance of these poorly selective ion channel increases *e*-fold for every 4-5 mV increase in voltage, but is closed at potentials below |60mV|[85]. The conductance of alamethicin channels is also dependent on the non-lamellar phase tendency of the lipids in the bilayer, and on lipid headgroup charge and hence the pH of the solution as well [86, 87]. Figure 18 shows a model for the conducting state of an alamethicin channel formed by eight alamethicin monomers and a typical current trace composed of bursts of discrete multilevel conductances. These channel activity bursts are separated by inactive periods, the duration of which is modulated by the applied voltage [88]. Various models have been proposed to explain several striking features of the electrical properties of alamethicin channels such as a high concentration dependence, multilevel conductances and the magnitude of the apparent gating charge. These models differ considerably in the proposed mechanism of voltage gating but do share some common features [83, 88].

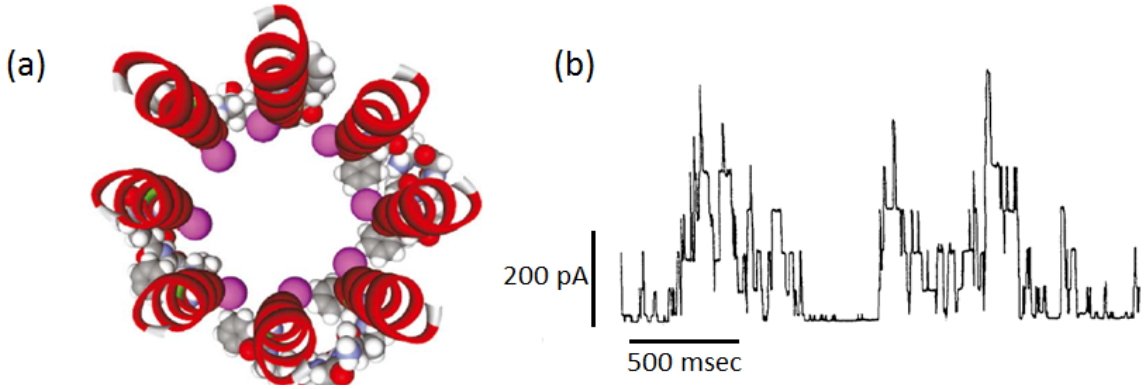

Figure 18: Schematic illustration of a proposed octameric (four dimers) conducting state of an alamethicin channel. The red ribbons represent peptide backbones while the coloured spheres represent amino acids side chains that link the monomers together (b) "Single channel" current trace for bilayer-incorporated alamethicin, for 0.5 M KCl and an applied potential of 125 mV [83].

2.5.2 Protein ion channels

2.5.2.1 α-Hemolysin (α-HL)

α-Hemolysin is a self-assembling toxin secreted from *Staphylococcus aureus* as a water soluble monomer. It has an important virulence factor due to its cytolytic and cytotoxic activity, which is mediated by formation of a wide heptameric channel. α-Hemolysin monomers self-insert into cell membranes and oligomerize to form a heptameric pore of nanometer inner diameter that enables ions, water and low molecular weight molecules to pass through the membrane. This is the primary mechanism of cell damage and death caused by this channel. The α-hemolysin channels display partial rectification, defined as preferred biasing of current flow to either the inward or outward direction, modest anion selectivity, and rapid fluctuation to a higher single channel conductance at acidic pH [89, 90]. α-HL nanopores have also been exploited for translocation of single natural and synthetic macromolecules like nucleic acid segments or polyethyleneglycol (PEG) polymers [91, 92]. The interaction of these molecules with the lumen of the nanopore partially or completely blocks the ion pathway in a specific manner which results in characteristic conductance changes that allow identification of single molecules [93]. Figure 19a shows the mushroom shaped geometry of a heptameric α-HL channel, with cap, rim and stem domains.

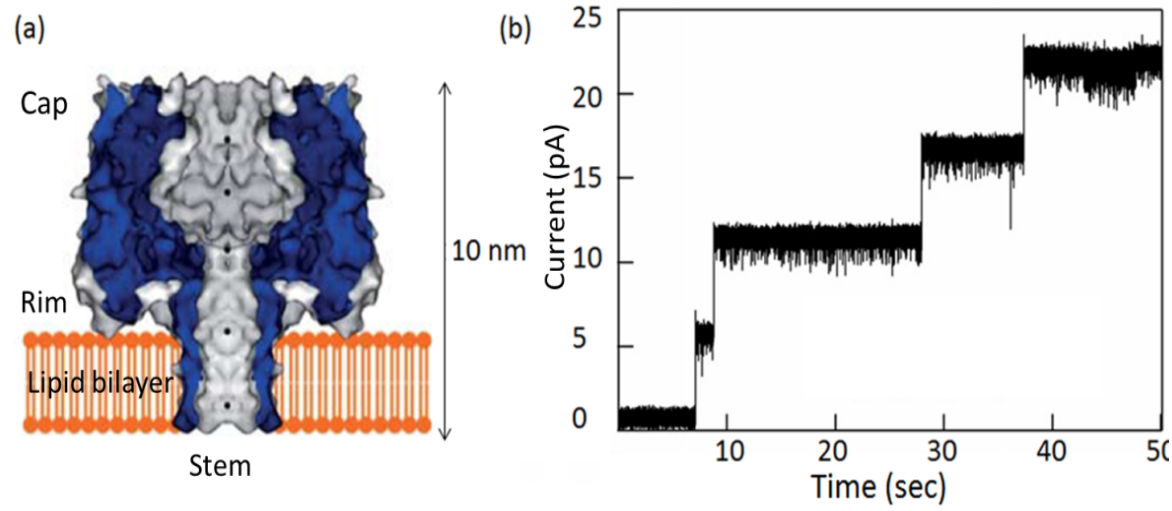

Figure 19: (a) Schematic illustration of the mushroom shaped heptameric pore formed by α-HL monomers [93]. (b) Current trace for α-HL channels in a lipid bilayer, for 100 mM KCl and an applied potential of 40 mV. Each upward current step represents insertion of an additional heptameric pore in the bilayer [94].

2.5.2.2 KcsA potassium ion channel

KcsA, from bacterium *Streptomyces lividans,* is one the best understood protein ion channels and as such has become the experimental model of choice to study ion channel and

transmembrane protein properties in relation to protein-lipid interactions. Thorough investigation of mechanistic aspects of gating and permeation in potassium channels has been possible due to the availability of high resolution crystal structures of KcsA in several conformations: with different ions in the pore and in complex with different blocker molecules and with antibodies . It is a homotetrameric K^+ channel that has high sequence similarity in the pore region with eukaryotic K^+ channels and thus provides practical insight into the pores of all homologous K^+ channels. Also, the ion selectivity for KcsA is similar to other potassium channels ($K^+ > Rb^+ > NH_4^+ >> Na^+ > Li^+$) [95]. Since it is a transmembranous protein, it spans the membrane with extracellular, cytoplasmic and membranous domains. KcsA is a pH-gated channel which opens at acidic pH and closes at neutral pH, as depicted in Figure 20a [95-97]. Figure 20b,c also shows gating transition from the open to the closed state of a KcsA channel incorporated in a suspended lipid bilayer with a representative current trace in suspended lipid bilayer. Because the electrophysiology of KcsA, which includes particular modulation by pH and voltage, is well described, it has become an important channel to validate bilayer platforms [98].

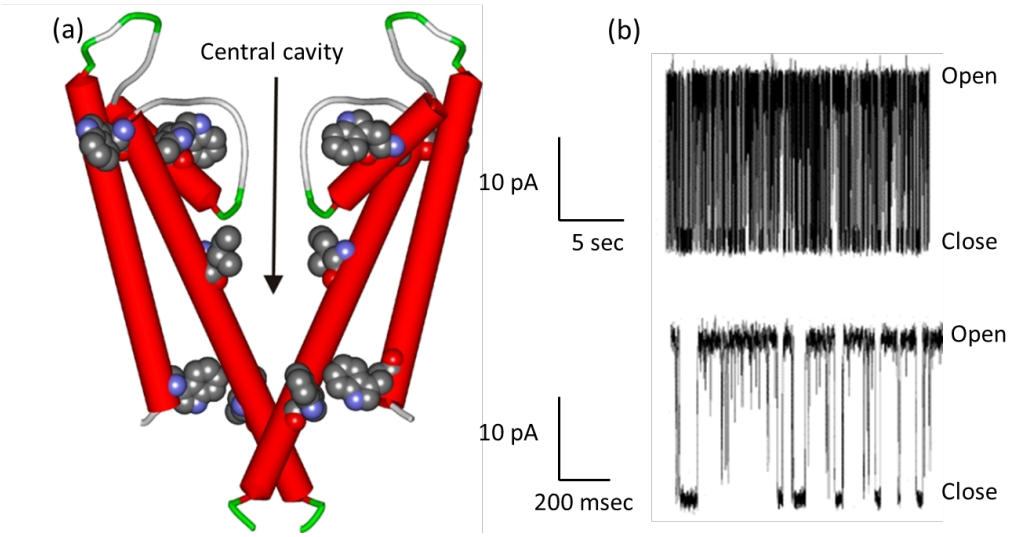

Figure 20: (a) Cross-sectional schematic illustration of KcsA, showing two of the monomers (shown by red colour) that make up the homotetrameric structure [99]. Grey colour shows isoleucine-100 residue and green colour is tryptophan residue (b) Current trace for KcsA in a suspended lipid bilayer, for 150 mM KCl and an applied potential of 100 mV [97]. Open and closed states of the channel are indicated.

2.5.2.3 Na_vSp sodium ion channel pore domain

Voltage-gated sodium channels are involved in electrical signalling, including action potential propagation, in excitable cells in eukaryotic organisms ranging from humans to electric eels and flies. They are targets for a range of pharmaceuticals used for the treatment of pain, epilepsy, cardiovascular diseases, and also breast and prostate cancer [100-102]. Due to the difficulty in expressing and purifying functional eukaryotic channels, several simpler prokaryotic sodium channels such as Na_vSp from *Silicibacter pomeroyi* have been identified, that can be

obtained from *E. coli* cell cultures. These prokaryotic voltage-gated channels are highly selective for Na^+ ions, bind drugs such as mibefradil and nifedipine that block human calcium channels (which are related to the sodium channel family), and exhibit similar activation and inactivation as human voltage-gated sodium channels [100]. The Na_vSp channel is composed of a transmembrane pore domain and a transmembrane voltage sensing domain. The pore domain of Na_vSp, but not the entire Na_vSp protein, can be expressed and purified and it has been demonstrated that it can assemble, fold and function independently in the absence of the voltage sensor subdomain (Figure 21) [100, 102, 103]. Prokaryotic sodium channel pore domains provide an excellent model for to study structural and functional aspects of human voltage-gated sodium channels [102]. Figure 21 shows Na_vSp pore electrical activity obtained by clamping of a giant unilamellar vesicle in which the ion channel pore has been incorporated [102].

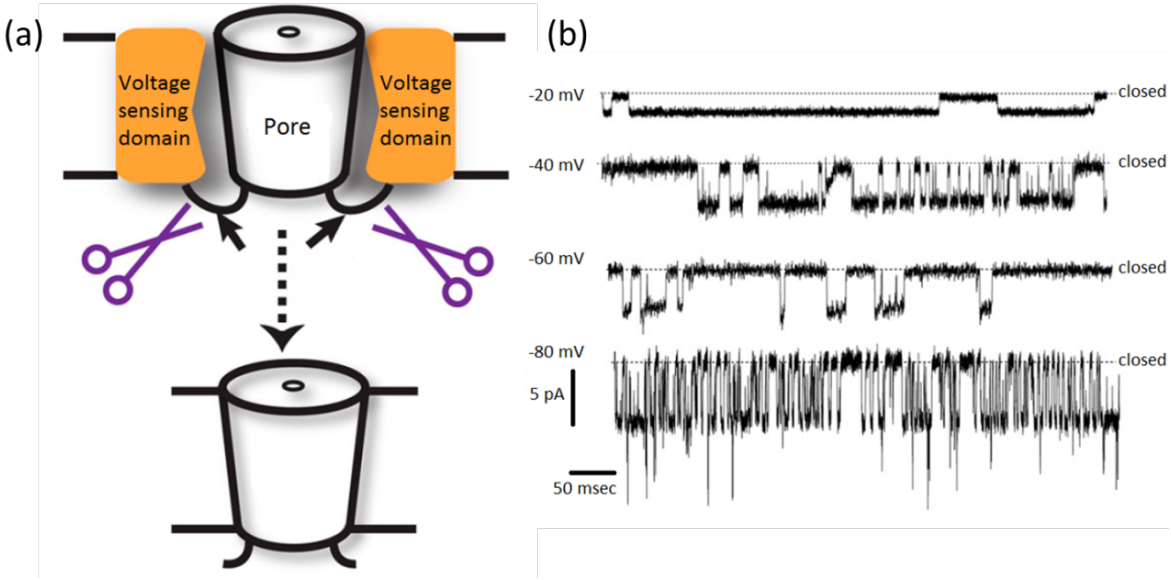

Figure 21: (a) Cartoon illustration depicting the strategy to create a pore domain-only channel by dissecting the voltage sensing domain of the Na_vSp ion channel. (b) Current trace for Na_vsp pore domain channel by clamping of giant unilamellar vesicles with the channel incorporated in the vesicular lipid bilayer, using asymmetric solutions of 110 mM KCl and 200 mM NaCl on either side of the bilayer at the indicated potentials [102]. Open and closed states of the channel are indicated.

2.5.2.4 hERG potassium ion channel pore domain

The hERG (human *ether-a-go-go* related gene) channel belongs to a family of voltage-gated potassium channels and is of critical importance for the function of the heart, where it acts as a molecular brake on the cardiac action potential [104, 105]. Its importance in normal human cardiac activity has become strikingly obvious as its mutation has been related to cause long QT syndrome, a cardiac repolarisation disorder leading to arrhythmias. Since non-cardiac pharmacological drugs can also trigger ventricular arrhythmias, testing of new drug candidates for hERG-channel modulation has become a routine practise known as cardiac safety screening [106]. The hERG channel consists of four monomer subunits but its exact structure is not known as a

crystal structure is not available. However, based on sequence similarities with other channels, the domain organization as depicted in Figure 22 has been proposed. Although unwanted interaction of drugs with hERG channel and mutations that lead to long QT syndrome require biochemical and detailed structural information of the hERG channel, such information is scarce including procedures that provide purified, functional and tetrameric channel [107]. The pore domain, including the selectivity filter, of the hERG channel is the binding site for various drugs that cause long QT syndrome [108]. Surprisingly, only a handful of publications address the single-channel conductance of the hERG channel. Figure 23 shows current traces of the full-length hERG ion channel obtained with the patch clamp method [109] and also with a suspended lipid bilayer platform [110].

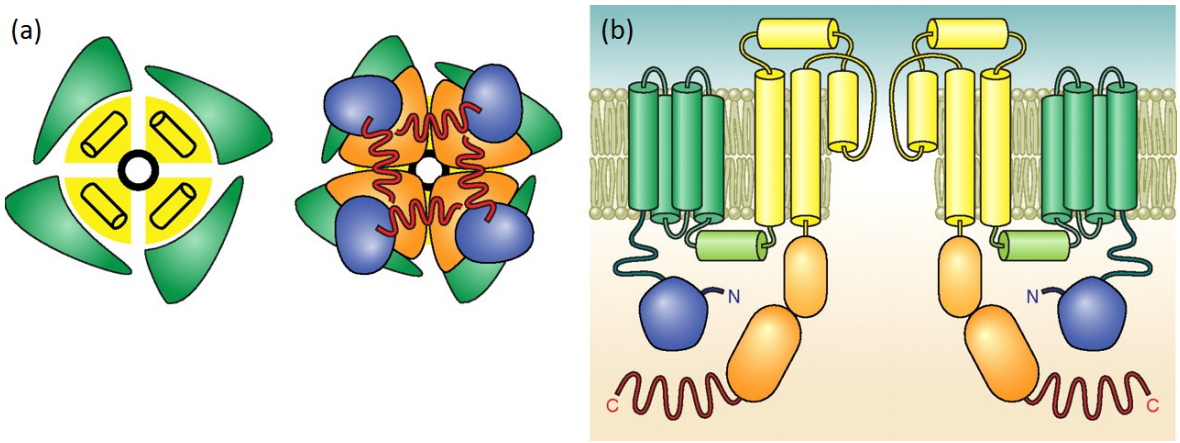

Figure 22: (a) Representation of extracellular (left) and intracellular view (right) of hERG ion channel (b) Topology of two opposing hERG subunit in the cell membrane. Yellow colour represents pore, dark green represents voltage sending domains, blue represents cytoplasmic $–NH_2$ terminal, and orange represents cytoplasmic –COOH terminal [111].

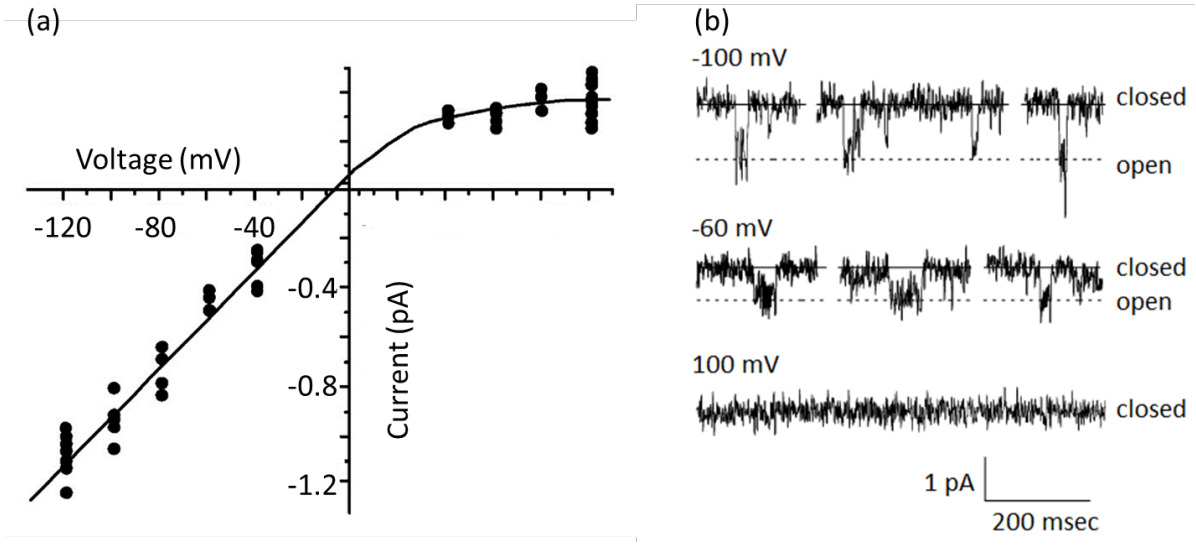

Figure 23: (a) Single channel current-voltage (I-V) plot of hERG channel using patch clamp. The plot is linear in inward direction and rectifies inwardly in outward direction [109] (b) Current trace for hERG ion channel in a lipid bilayer, for 22 mM KCl at the indicated potentials. Open and closed states of the channel are indicated on the plot [110].

2.6 Conclusions

The structural matrix of cell membranes, which define the boundaries in all living cells, is a bilayer of lipid molecules. Membranes form an effective diffusion barrier and maintain concentration gradients of ions and molecules across the cell membrane. The proteins embedded in cell membranes enable and control the selective transport of molecules and ions, playing a central role in many (patho)physiological processes and constituting a prime target for new pharmacological drugs. Patch clamp electrophysiology is the gold standard for ion channel characterisation, including drug screening, and is conventionally performed by patching a whole cell membrane that contains ion channels overexpressed in the cell. However, the complexity of natural cell membranes and the difficulty of working with live cells has motivated research in simpler, membrane mimicking model systems of lipid-only membranes. Methods for incorporation of protein ion channels into these model membranes have been described in this chapter, and some specific peptide and protein ion channels have been briefly introduced. Moreover, in this chapter, various pure-lipid membrane model systems, such as aperture-suspended and solid-supported lipid bilayers have been discussed along with their advantages and disadvantages. Aperture-suspended bilayers are favourable systems for electrophysiology because of large aqueous reservoirs on both sides of the bilayer, unlike solid-supported bilayers, but are quite fragile, which severely limits measurement throughput. The next chapter discusses various methods to improve the stability of aperture-suspended bilayers as well as the techniques described in the literature for fabrication of apertures for bilayer formation.

Chapter 3 Apertures for suspended lipid bilayers and microsystems for bilayers

3.1 Apertures for suspended lipid bilayers

3.1.1 Interdependence of stability of the bilayer, noise in the electrical recording and probability of protein incorporation

Even though suspended lipid bilayers are an established laboratory approach, the method suffers from the major drawback of bilayer instability. Typically the suspended bilayer ruptures, or fails, within a few hours, even with no or minimal perturbation of the aqueous compartments. This hinders long-term ion channel monitoring and makes studies of channel modulators, which involve a change of composition of the aqueous compartment, a very low-throughput procedure [14, 16]. Rupturing of the bilayers is not a process that occurs uniformly over the whole lipid membrane surface, but originates in one or more discreet regions from where it spreads until the bilayer breaks [26, 79]. Hence, the probability of rupturing can be reduced by decreasing the bilayer area by using a smaller aperture. Consequently, stable bilayers that have an improved lifetime of several hours to a few days have been formed across apertures with a diameter of a

few micrometers or of hundreds of nanometers [35, 36, 112-118]. Lithographic techniques have played an important role for the reproducible fabrication of these apertures, with controlled and precise diameters, in conventional microfabrication materials such as silicon, silicon nitride, and glass (see Figure 24). However, a decreased membrane area also reduces the probability of fusion into the bilayer of the vesicles that deliver protein ion channels into the bilayer [37, 38]. Nanoporus substrates have been used to attain an increase in the effective bilayer area while producing stable lipid bilayers [72, 119, 120], however when the support material is porous, it is also a challenge to reliably cover all the sub-micrometer pores in the substrate with a lipid bilayer and to avoid the high leakage currents that affect the ion channel recordings [71]. For aperture-suspended bilayers, any decrease in aperture size should also be accompanied with a decrease in septum thickness in order to avoid creating apertures where the aspect ratio - aperture wall thickness to aperture diameter - is high, because a high aspect ratio causes increased convergence resistance at the opening of the aperture and also unstirred layer effects near the surface of the bilayer in the aperture.

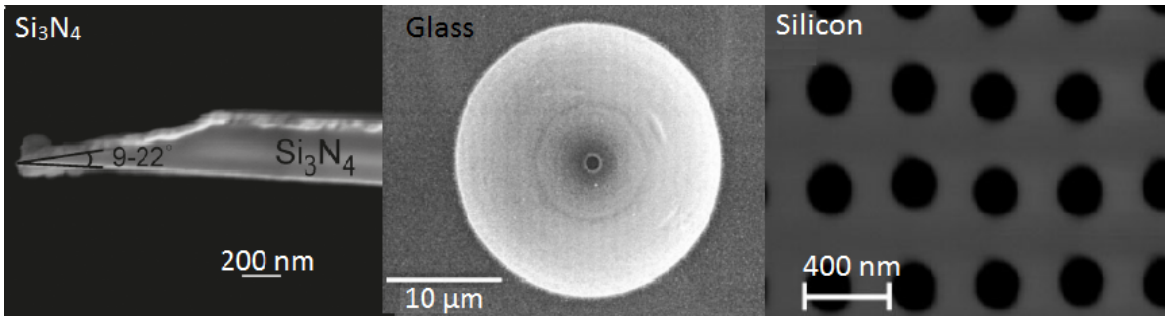

Figure 24: SEM images of apertures in three different type of septum material: (a) Cross-sectional image of a triangle-shaped aperture in silicon nitride (Si_3N_4) [121], and top view of apertures in (b) glass [115] and (c) silicon [118].

The lipid bilayers are suspended across an aperture with a solvent annulus, comprising of an alkane or non-polar solvent, which surrounds it. The septum is a non-polar material (hydrophobic) such as polytetrafluoroethylene (PTFE) that allow its wetting by the lipid solution to get a quasi-equilibrium state where the surface tension of the bilayer film is balanced by tensions in the monolayers (in the annulus). In the absence of solvent annulus, the non-zero tension in the bilayer film is not balanced, which results in collapse of the bilayer. This holds true to all suspended bilayers irrespective of method of their preparation- painting or Montal-Mueller technique [53]. Hence, the surface of the septum and use of solvent is crucial. The analytical analysis, based on variational calculus, done by White *et al.* of annulus surrounding lipid bilayers provides insight into design criteria for the aperture. Based on this analysis that also includes bilayer-to-annulus and annulus-to-septum contact angles, it has been predicted that large-area stable suspended bilayers can be formed when a long cylindrical aperture is used or a very thin septum is utilized or aperture with appropriate edge geometry is used [25]. Although thinner

septums will allow lipid solution to pass over the edge of the aperture to get the correct annulus-to-septum contact angle leading to drainage of the annulus causing bilayer failure, use of "very thin" septum will produce an effect where the wall of the aperture is rotated through an angle of 90 ^{o} to satisfy the angle. While long cylindrical apertures has issues of unstirred layers and increased convergence resistance, the use of a thinner septum, e.g. 1-10 µm thick, increases the contribution of the intrinsic capacitance of the septum to the total capacitance of the system and therefore increases noise in the recordings, effectively reducing the measurement sensitivity, as discussed in later sections. It can thus be concluded that the design of the aperture across which the bilayer is suspended is crucial.

3.1.2 Septum material for apertures

A significantly improved bilayer lifetime of tens of hours, in combination with an increased mechanical stability of the bilayer, has also been demonstrated in a number of studies that use apertures with tapered edge walls. This tapered aperture geometry is also the subject of this thesis. Figure 25a illustrates a fabrication procedure, from Iwata *et al.*, for a tapered edge-wall aperture in silicon nitride, based on a silicon wafer with one side coated with 240 nm of silicon nitride. Silicon dioxide (SiO_2) was deposited on this wafer by thermal oxidation and then by sputtering method on the silicon nitride layer. The first oxide layer was photolithographically patterned and etched in tetramethylammonium hydroxide solution. SiO_2 was then deposited on the surface of the silicon nitride where this was exposed during the etching step. Circular apertures (20-30 µm) were subsequently defined in the nitride layer by photolithography and isotropic etching with phosphoric acid, which gives rise to the tapered side walls of the aperture. Finally the oxide layer underneath the apertures was removed by an hydrofluoric acid etch [121]. In other studies, circular apertures with triangle-shaped side walls have been produced in thin films of photoresists, polyimide or SU8, usually supported on a silicon substrate , which has a high intrinsic capacitance [112, 113, 122]. However, thin films on a support increase the capacitance contribution of the septum to the total capacitance of the system, which in turn increases the noise in the bilayer recording. Oshima *et al.* achieved reduction in the noise by covering silicon nitride films with Teflon, which increases the septum thickness and also renders the surface hydrophobic (Figure 25b) [123]. These studies with bilayers suspended in tapered edge wall apertures have reported ion channel activity of gramicidin, alamethicin, and the vesicle-delivered proteins hERG and nicotinic acetylcholine receptor [110, 113, 121-123].

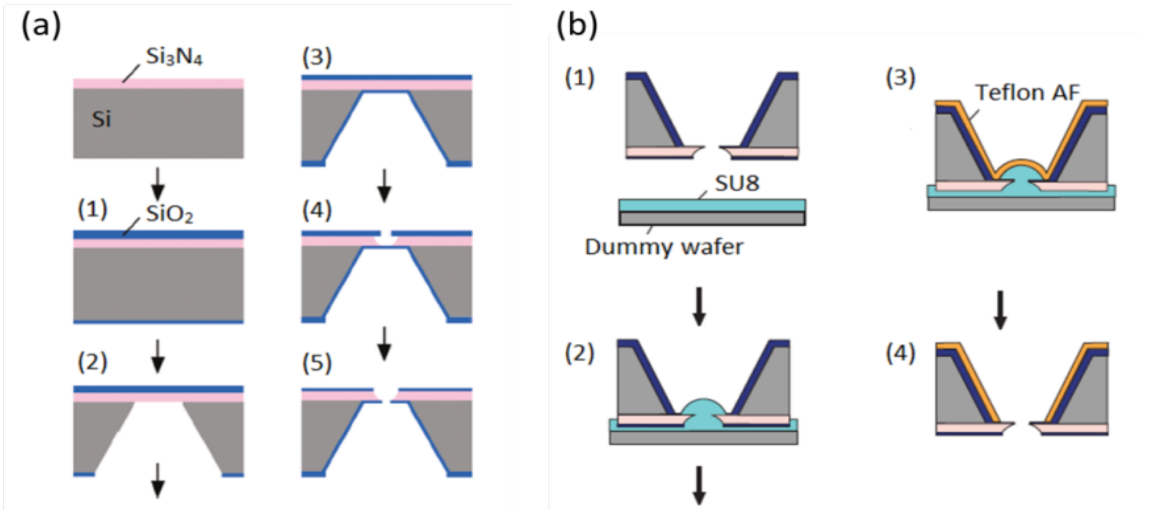

Figure 25: Illustration of fabrications steps for fabrication of shaped apertures in a silicon nitride (Si_3N_4) septum, with and without Teflon coating. (a) (1) Silicon (Si) wafer (100),coated on one side with 240nm of silicon nitride is thermally oxidised and silicon dioxide (SiO_2) is deposited on the wafer; (2) The back side of the wafer is patterned and anisotropically etched; (3) SiO_2 is sputtered; (4) Si_3N_4 is isotropically etched; (5) SiO_2 is removed [121]. (b) Teflon coating on these chips by (1) wet thermal oxidation; (2) positioning the wafer on a layer of SU8-3010 photoresist, (3) spin coating of Teflon-AF, and (4) lift-off of the Teflon layer around the aperture. [123]

The formation of a lipid bilayer across an aperture is possible due to the wetting of the material in which the aperture is defined, the septum, by the organic non-polar solvent that is applied to the aperture as part of the bilayer formation protocol (section 2.3.1). Hence, the septum, or at least the surface of the septum, should be sufficiently hydrophobic. Conventional septum materials are listed in Table 1. In plastics like delrin, polysulfone, polymethyl methacrylate (PMMA), Teflon (polytetrafluoroethylene), apertures are usually made by electrical spark discharge or by mechanical means such as microdrilling or laser ablation. But due to the coarse nature of these methods, there is limited control over the size and the geometry of the aperture [124]. This limitation has been overcome by using lithographic techniques with silicon based materials but at the cost of electrical noise performance. Silicon has a very low resistance which allows large background currents and has a high dielectric constant that increases noise. Coating of silicon with an insulating material such as SU8 photoresist can reduce the background current, but there is usually a large shunt capacitance associated with the chips due to thin dielectric films, which restricts the electrical recording bandwidth, which is unfavourable for channels with short-lived open and closed states [117]. Although silicon nitride membranes have a lower dielectric constant than silicon, they are extremely fragile and their fabrication is time consuming. Moreover, the surface of silicon and silicon nitride is hydrophilic and thus requires an additional process step to render the surface hydrophobic [114].

Table 1: Summary of different types of substrate used for the fabrication of apertures that are suitable for the creation of aperture-suspended bilayers by the painting method or the monolayer folding method.

Substrate	Aperture fabrication technique	Dielectric constant[2]	Surface of material	Reference
Teflon	Piercing with hot needle, reactive ion etching	2.1 @ 60 Hz	Hydrophobic	[35, 54, 55, 117, 125, 126]
Poly(p-xylene) (parylene)	Lithographic techniques	2.65-3.15 @ 60 Hz	Hydrophobic	[127, 128]
Silicon nitride	Lithographic techniques	7.5	Surface treatment required to make hydrophobic	[110, 121, 123]
Silicon	Lithographic techniques	11.8	Surface treatment required to make hydrophobic	[114, 119]
Glass	Lithographic techniques	4.84-4.97	Surface treatment required to make hydrophobic	[115, 129, 130]
Photresists- SU8, polyimide	Lithographic techniques	3.25 @1 GHz	Bilayer formation demonstrated with and without surface treatment	[92, 112, 113, 122, 131, 132]
Polymethyl methacrylate, delrin, polyvinylidene chloride, polypropylene	Thermal ablation, piercing with hot needle, CO_2 laser, micro-drilling	2.6, 3.7, 3-6, 2.2-2.6 respectively	Hydrophobic	[78, 94, 133, 134]

3.1.3 Noise analysis

Other than improving bilayer stability, reducing the aperture size also decreases noise in the electrical recordings. There are three major contributors to noise in bilayer recordings [35, 135]:

1. Noise from the interaction of the headstage amplifier that is placed as close as possible to the recording electrodes (e_n, rms noise voltage in headstage amplifier) and the input capacitance (C_t). The spectral density for this noise is given by [35, 135], where *f* is frequency:

$$S_{vc}^2 = 4e_n^2\pi^2C_t^2f^2 \quad [1]$$

[2] Unless specified the frequency is between DC and 1 MHz. Available at http://www.pulsedpower.net/Info/common_dielectrics.htm. Date accessed: 10 September 2013. Zhang 2007 for silicon nitride, product specification sheets for the others

2. Thermal voltage noise from series combination of access resistance (R_a, sum of the resistance of the bath solution, the convergence resistance at each end of the aperture and the resistance of the solution within the aperture) and bilayer capacitance (C_m). The spectral density for this noise is given by [35]:

$$S_{rc}^2 = 4kT \frac{4\pi^2 f^2 R_a^2 C_m^2}{R_a(1+4\pi^2 f^2 R_a^2 C_m^2)} \quad [2]$$

3. Noise from the dielectric materials (D) [35, 135]:

$$S_d^2 = 8kT\pi D C_t f \quad [3]$$

The input capacitance (C_t) is the sum of FET (field effect transistor) input capacitance, lipid bilayer capacitance and stray capacitance, e.g. capacitance from the septum. Equation 1, 2 and 3 show that the noise is directly proportional to the frequency (*f*) or the bandwidth; hence an increase in bandwidth is accompanied by an increase in the noise. Equation 1 and 2 also show a square relationship between capacitance and noise which necessitates careful consideration of the total capacitance of the system. When the capacitance of the septum is kept minimal, the chief contributor to the overall capacitance, and thus the noise, is the capacitance of the lipid bilayer. This capacitance can be reduced by reducing the size of the bilayer, which can be achieved by decreasing the diameter of the aperture across which the bilayer is suspended. The significance of dielectric losses (D) of all the materials to the noise spectrum is shown in equation 3. Since the largest contribution to this type of noise is expected from the septum material, a careful choice of the support material is crucial [35, 36]. The dielectric constant of the septum material should be as low as possible to avoid a significant capacitance. The material with the lowest dielectric constant that can be used for bilayer formation is Teflon (κ=2.1), but its chemical inertness implies that it cannot be wet etched, complicating pattern transfer from an aperture-defining photoresist layer for reproducible aperture fabrication. Hence, researchers have focussed, due to established lithography techniques, on silicon as septum, but its high dielectric constant of ~7-8 has limited its use in ion channel electrophysiology.

3.2 Bilayers in microsystems

3.2.1 Microfluidic chips for formation of bilayers

Various interdisciplinary fields have benefitted from advancements in miniaturized liquid handling systems known as microfluidic systems, and lipid bilayer-related studies are no exception [136]. These microsystems offer several advantages such as faster assays, low volume

consumption and suitability for automation and multiplexing of experimentation [126]. Consequently, these devices open up the possibility for the creation of more and higher-quality targets and leads in the drug discovery process, based on low sample consumption of limited and expensive compound libraries and on reduced analysis times in combination with multiplexing experiments [136]. The numerous microfluidic lipid bilayer platforms that have been developed promise advantages ranging from convenient formation of lipid bilayers [94, 126, 133, 137] for ion channel electrophysiological studies or optical studies of lipid microdomains [134, 138], to low-noise and parallel recordings of ion channel electrophysiology data [132]. Several examples of microfluidic bilayer systems are discussed below.

Rapid and reproducible formation of lipid bilayers has been demonstrated in microfluidic chips made from polymethyl methacrylate (PMMA), which is a non-conductive, low electric constant, transparent and hydrophobic material [139]. Although the aperture across which the bilayer is suspended could either be defined in PMMA or in other materials such as a PMMA-sandwiched delrin or Teflon film, the top and bottom channels are usually made in PMMA [137, 139]. Since these devices allow formation of horizontal bilayers in the apertures, lipid bilayers can be readily observed under an optical microscope (Figure 26). Thinning of the oil-lipid film painted on the horizontally positioned apertures in these microdevices has been shown to be promoted by methods such as pressure application or by air exposure [94, 137, 139]. Recently, instantaneous formation of painted lipid bilayers has been demonstrated with semi-automated procedures, where the entry of buffer into the top and bottom channel, already filled with solvent-lipid solution, is timed to give 100% yield of bilayer formation [126]. Another approach involves the so-called kiss-and-retreat method [138]. Finally, microfluidic platforms have also been developed for bilayer formation with the folding, rather than the painting method [134].

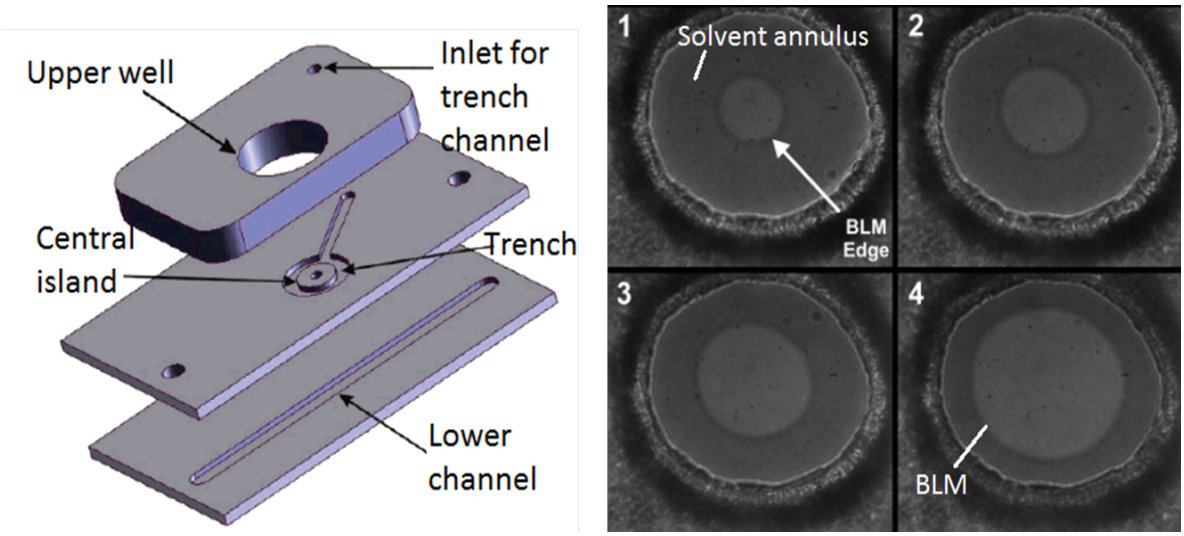

Figure 26: (Left) Microfluidic device design in PMMA for lipid bilayer formation, and (right) series of optical images showing growth of the lipid bilayer (BLM) region by thinning of the oil-lipid film in the central island of the chip. The aperture size is 80-150 µm [137].

Since most of the microfluidic devices described above use conventional macro-size electrodes, which spatially limits the number of recording sites on the microdevice and requires relatively larger volume for electrical contact, one of the other crucial advancements in microdevices for bilayer-related studies has been the integration of miniaturized electrodes into the device [132]. The placement of the electrode closer to the bilayer site allows use of smaller microchannels without increase in the series resistance and compromise in the recording bandwidth. Some research groups have demonstrated successful ion channel recordings with integrated electrodes with a dimension of several hundred micrometers [131, 140]. However Baaken *et al.* achieved low noise (<0.25 pA @ 10 kHz) and high temporal resolution recordings with microelectrode cavity chips with small-volume SU8 compartments that contain electrodes with a size of just ~10 µm and that use short connector strip lines, as shown in Figure 27. The smaller size of the recording sites on these chips also allow highly parallelized recordings from a large number of bilayers [132]. SU8 is a widely used resist in the microelectromechanical systems (MEMS) community and its low cost and favourable properties such as thermal and chemical stability makes it a suitable material for bilayer formation.

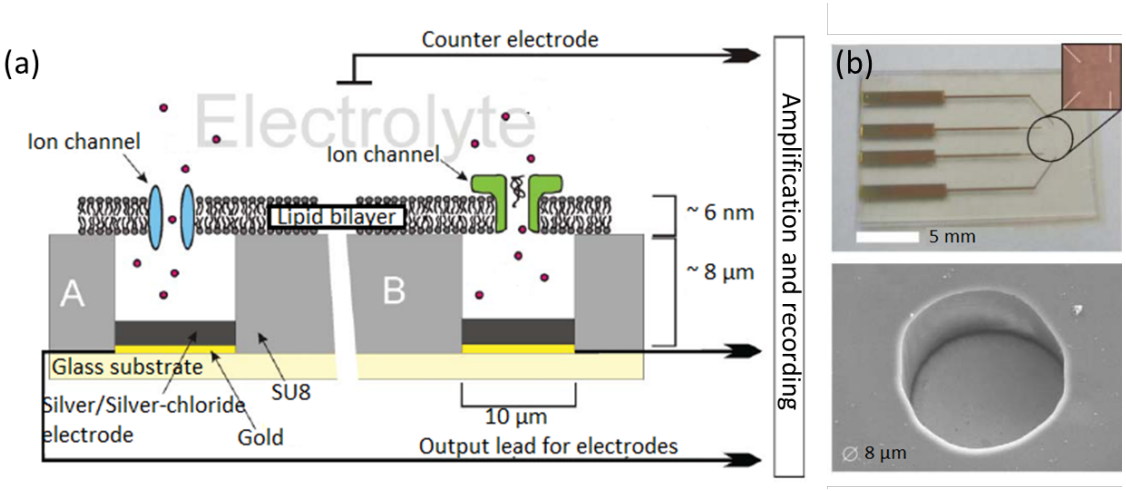

Figure 27: (a) Schematic representation of the planar chip approach for bilayer formation with integrated electrodes. Each chip contains a microcavity defined by SU8 on top of which a bilayer is formed. Inside the microcavity silver/silver-chloride electrodes are present for electrical recordings. Gold acts as conductor lines for the electrode connection to the amplifier. These cavities use a common ground electrode. Bilayers are formed with the painting method. Red dots represents ions in the electrolyte. (b) Photograph of the chip with four microelectrode cavities and a SEM image of a 8 µm diameter SU8 cavity [132].

3.2.2 Interdroplet bilayers

Miniaturization of lipid bilayer recordings could also be achieved by using an alternative approach for the formation of stable bilayers, known as interdroplet bilayers or droplet interface bilayers (DIB) [141, 142]. Interdropet bilayers are bilayers that are suspended between two aqueous droplets, typically approximately 1 µl in volume, submerged in a bulk oil phase. A lipid monolayer is formed at the oil-water interface because the bulk oilphase contains solubilized

lipids, or because lipids are present as vesicles in the aqeuous droplets. When two lipid-monolayer coated droplets are brought into contact, the oil between the droplets is expelled and an interdroplet bilayer is formed (Figure 28a). A variation on this method involves placing a water-in-oil droplet on top of a planar aqueous medium such as a hydrogel, which offers the added advantage of optical imaging of a horizontally oriented suspended bilayer [142-144]. Interdroplet bilayers can have lifetimes of weeks, but the method suffers from limitations such as inconsistent bilayer size due to varying droplet size or position as caused by manual pipetting of the droplets, and difficulty in introducing new compounds into the droplets after the formation of the bilayer. Also, a reduction of droplet size to achieve higher volumetric packaging, and a reduction in bilayer area to achieve lower-noise recordings has not been systematically explored. However, it has been demonstrated that the area of interdroplet bilayers can be modulated by applying pressure on a flexible 'droplet holder'[145] and also by using an aperture in a hydrophobic film that constraints the contact area between an aqueous droplet and the underlying buffer channel (Figure 28b). The latter configuration also permits the perfusion of the solution in the bottom compartment [133, 146].

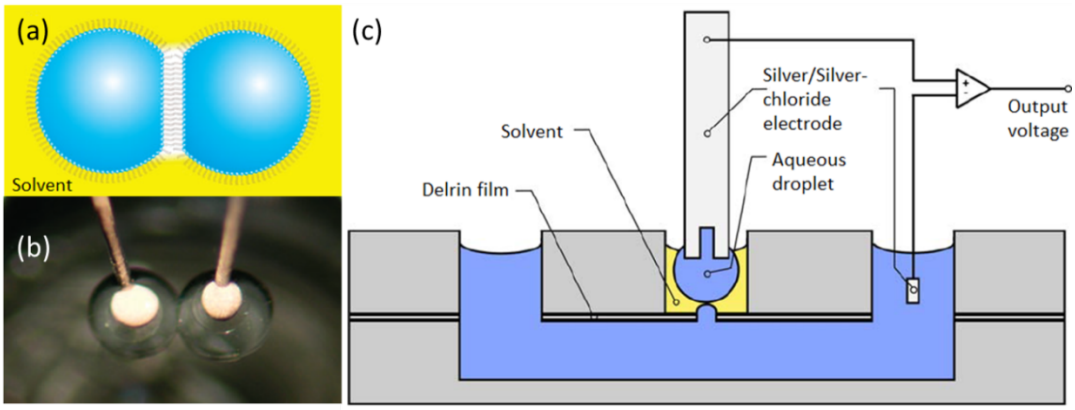

Figure 28: (a) Schematic illustration of an interdroplet lipid bilayer, formed by contacting two lipid monolayer covered aqueous droplets in a bulk oil phase. (b) Photograph of a two droplets hanging from movable electrodes, that can form or pull apart the interdroplet bilayers by moving the droplets towards or away from each other [142]. (c) One of the methods for controlling the area of an 'interdoplet' lipid bilayer is to position a hydrophobic film with an aperture that limit the contact area of a droplet with an aqueous channel [133].

A further refinement in the interdroplet bilayer approach has recently been reported by Kawano *et al.* , who brought two lipid monolayer covered aqueous droplets-in-oil into contact with a polymer sheet containing apertures of 150 µm diameter to restrict the size of the interdroplet bilayers [128]. Their parallel platform with 16 droplet pairs, depicted in Figure **29**b, produced stable bilayers that could be formed with a pipettor robot. The same group also overcame the major drawback that the droplets are essentailly closed compartments of fixed composition by positioning the droplets on top of a substrate with localized micro-holes that are in contact with an underlying aqueous channel, thus enabling droplet solution exchange, or perfusion [127] (Figure **29**c). The applicability of the design was demonstrated by exchanging an

electrolyte-only buffer solution with a solution containg a blocker molecule for the a-hemolysin ion channel. With more extensive validation, this platform could present a powerful tool for electrophysiological ion channel drug screening.

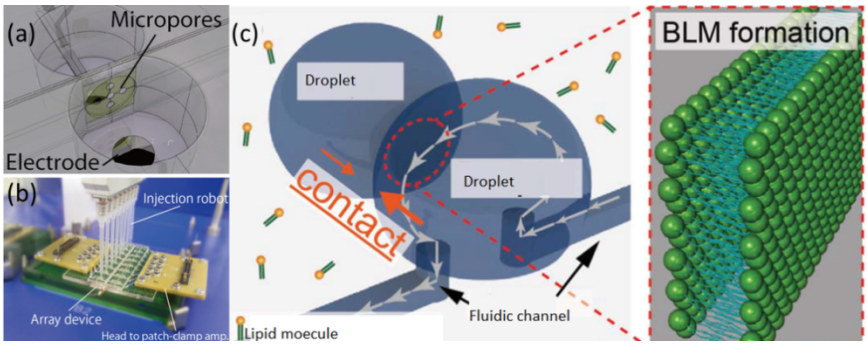

Figure 29: (a) Schematic representation of a device that has a poly-chloro-p-xylylene polymer sheet inbetween two compartments that each contain a droplet submerged in a lipid-oil mixture. (b) Photograph of an automated and parallel approach for a 16 channel platform for interdroplet bilayer formation with the approach depicted in (a), with a pipettor robot for automated interdroplet bilayer formation. (c) Schematic diagram for droplet solution exchange from an underlying microfluidic channel [127, 128].

3.3 Conclusions

Since traditional methods for aperture fabrication use coarse mechanical methods that limit the reproducibility of aperture size, shape, and position in plastic materials, lithographic techniques have been explored for controlled aperture fabrication in silicon-like materials and in photoresists. Various septum materials have been discussed with their associated advantages and disadvantages. Several examples of the application of microfluidic technologies in lipid bilayer and ion channel studies have also been included. This chapter has focused on the interdependency of the stability of suspended lipid bilayers, the noise in electrical recordings of ion channels, and the probability of incorporation of protein ion channels by proteoliposome fusion. Although the bilayer stability and noise characteristics can be improved by reducing the aperture size, the probability of incorporation of ion channels is reduced. A reduction in aperture area also demands a decrease in the thickness of the septum to avoid unstirred layer effects. However, a thinner septum has a higher intrinsic capacitance that limits the bandwidth and increases noise in the recordings. These problems can in principle be addressed by using shaped apertures that are thinned only at the tip of the aperture. Triangle-shaped apertures fabricated in silicon nitride or in a thin photoresist film, SU8 or polyimide, on a silicon support have indeed been shown to give stable bilayers, but with compromised noise performance. Having studied aperture geometry and septum material considerations, it was decided to fabricate shaped apertures in a material with favourable electrical properties, with a sufficiently large internal diameter to enable proteoliposome fusion. The following two chapters discuss fabrication protocols for large diameter (>60 µm) shaped apertures in a low intrinsic capacitance material, the photoresists SU8

and TMMF. The next chapter first describes the fabrication of shaped apertures in SU8 by two-photon absorption lithography.

Table 2: Summary of different aperture sizes and substrates used for aperture-suspended bilayers by the painting method or the monolayer folding method

Material of the aperture/diameter	**Ion channels (if used)**	**Septum capacitance (pF)**	**Bilayer lifetime**	**References**
Teflon/ <5 µm	Gramicidin and voltage gated sodium channel	13		[117, 125]
Silicon nitride/200 nm		466 (including bilayer capacitance)	Upto 4 days	[118]
Polyimide/	Nicotinic acetylcholine receptor	200	50 hours	[113]
Silicon nitride/20-30 µm	Gramicidin	252	15-45 hours	[121]
Silicon nitride/20-30 µm	Gramicidin and alamethicin	40		[123]

Chapter 4 Fabrication of shaped apertures using two-photon polymerisation

Conventional lithography is a planar fabrication technique with little or no freedom of structuring in the vertical dimension. Hence, in this chapter different 3D lithography techniques for making complex geometries are introduced, with a detailed discussion on underlying principles for multi-photon absorption lithography describing its advantages over other methods. Since it is a serial fabrication technique and electrophysiology experiments require a sheet of at least 1 × 1 cm, approaches that reduce the fabrication time have been investigated. Strategies for release of the resist sheet from the substrate and to avoid cracking of the resist film are also discussed.

4.1 Multi-photon polymerisation

Photolithography and its associated processes have been the backbone of the micro- and nano-technology revolution and have provided the ability to define the vast majority of

microdevices with high precision, including microeletronic circuits, micromechanical systems (MEMS), microfluidics and nucleic acid or protein microarrays [147-149]. Fabrication of structures with tailored functionalities, shapes and sizes is also of prime importance for enhancing numerous mechanical, optical, microfluidics and electronics devices[150-154]. However, photolithography is essentially a planar technique which does not provide control in the vertical dimension. Hence the development of new techniques that provide patterning abilities in the third dimension is an active research area.

The history of 3D microfabrication using photopolymers traces back to 1981, when Kodama used photo-hardening polymer, commonly referred to as 'photoresist' or simply 'resist', for patterning, employing a process called stereolithography [155]. Although, the lateral resolution of this technique has increased over the years, the depth of the 3D structures is still limited to several micrometers due to its layer-by-layer nature [153]. Various other techniques that have been used for the fabrication of 3D micro- and nano-structures are listed in Table 3. These include modified lithographic processes [156], direct laser write using multiphoton (usually two-photon) absorption polymerization (MAP) [157], and focused ion beam [153], to name a few. Each technique offers specific advantages, which makes it more suitable for certain applications than others [158]. In this chapter, two-photon polymerization, a technique that has been widely used to make 3D microdevices in resist because of its sub-100 nm resolution and its capability to define complex structures is focussed. It is carried out using a high intensity pulse from a femtosecond laser, which is focussed onto the resin using a high numerical aperture (NA) objective lens to initiate the photochemical reaction and to form the desired structure with ~100 nm resolution [151].

Even though the concept of multi-photon absorption was predicted theoretically in 1931 by Maria Gȍpert-Mayer, the first demonstration of two-photon absorption polymerisation was only carried out in 1997 by Maruo *et al.* [159]. Simultaneous absorption by the photopolymer of two near-infrared photons in a single quantum event correlates to energy in the UV region of the spectrum, to which the photopolymer is sensitive. The critical excitation condition is that the photons should be present simultaneously and should have the same energy. The multi-photon absorption rate for *n* photons is proportional to the concentration or intensity of the photons raised to power *n*, e.g. for two photon absorption, the rate is proportional to the square of the light intensity of the photons. This non-linear dependence of absorption on intensity permits localisation of the excitation [148, 153].

Table 3: Comparison of different 3D patterning technologies [148, 153]

Technology	Features	Limitations
Ink based writing	Ink composed of colloids, polymers or polyelectrolytes. Resolution ~1-100 µm	Arbitrary geometry is not possible because of low rigidity of ink
Self-assembly	Suitable for creation of periodic structures	Arbitrary patterning still in infancy
Layer by layer assembly	Tacking of 2D layers produced with conventional lithography	Mechanical strain imposes geometrical limitations
Modified lithographic processes, e.g. phase mask lithography	Periodic patterns. Mass production. Large scale patterning	Inability to create complex 3D microstructures for certain applications
Focussed ion beam processing	Ultrahigh resolution ~10 nm	Low throughput for mass production
Lithography, electroplating and moulding	X rays patterns with µm resolution and depth > 1 cm. Structures have smooth surface and shared vertical features	Limited 3D complexity owing to line of sigh nature of X ray
Laser chemical machining	Substantial 3D complexity	Slow fabrication and high precision for resin flow

The following equations discuss the reason for the confinement of the excitation in the focal region: Consider a homogenous distribution of the absorbing molecule across the sample. The absorption rate (R) in a transverse section is given by [148]:

$$\boldsymbol{R \propto Intensity\ of\ beam \times No\ of\ absorbing\ molecules\ in\ cross\ section} \quad [\mathbf{1}]$$

where, intensity of the beam (I) and number of absorbing molecules (N) is given by [148]:

$$\boldsymbol{I = \frac{Number\ of\ photons/time}{Area}} \quad [\mathbf{2}]$$

$$\boldsymbol{N \propto Cross\ sectional\ Area} \quad [\mathbf{3}]$$

Substituting the value of equations 2 and 3 in equation 1 gives:

$$\boldsymbol{R \propto \frac{Number\ of\ photons/time}{Area} \times Cross\ section\ area} \quad [\mathbf{4}]$$

$$R \propto \frac{Number\ of\ photons}{time} \qquad [5]$$

Thus, for single photon absorption, the rate is independent of area, hence, the number of absorbing molecules excited by a single photon remains constant in any transverse plane. From the discussion above, the rate for multi-photon absorption is given by:

$$R \propto Intensity^{n} \times Number\ of\ absorbing\ molecules \qquad [6]$$

Substituting the expression for intensity and taking value of *n* as 2 (for two photon absorption):

$$R \propto \left(\frac{Number\ of\ photons/time}{Area}\right)^{2} \times Area \qquad [7]$$

$$R \propto \frac{(Number\ of\ photon/time)^{2}}{Area} \qquad [8]$$

Thus, the absorption rate is inversely proportional to the area, and hence as shown in Figure 30, the absorption is maximised in the region where the laser is most tightly focussed.

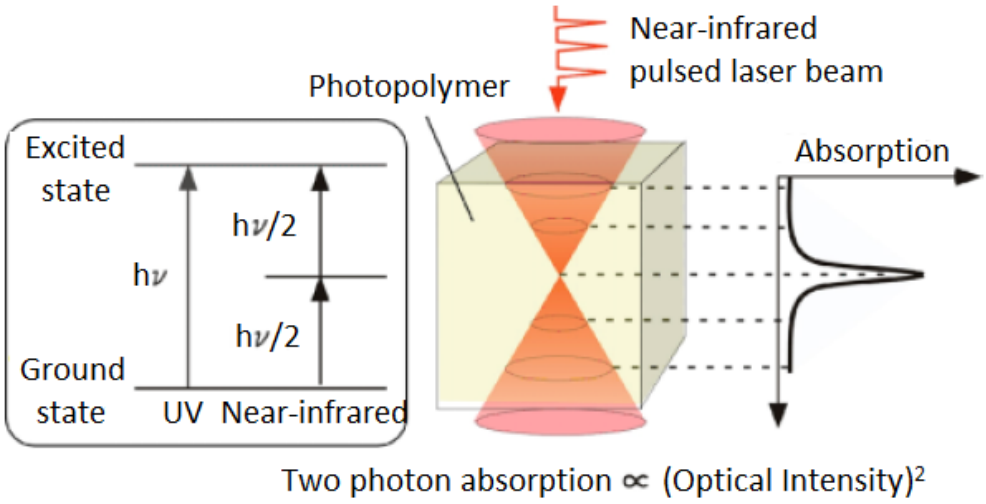

Figure 30: Schematic illustration of the principle for multi-photon polymerisation. The absorption rate is maximal at the focal point of the laser beam. 3D structures can be created by moving the focal point in the resist layer to polymerise it at defined locations and thereby fabricate the desired shape [153]

The resolution of multi-photon absorption depends on the wavelength of the femtosecond laser, the numerical aperture (NA) of the objective lens, the light intensity, the exposure time, and the sensitivity of the photopolymer [153]. Accurate information on focal spots, i.e. the size and

shape of the volume element, also referred to as the voxel, is essential for fabrication of structures with multi-photon absorption [160]. According to linear exposure theory, the voxel dimensions depend on the product of the exposure time and the square of the laser power, if all other parameters are kept constant [148]. Figure 31 shows scanning electron microscope (SEM) images of a complete and isolated voxel, which resembles a spinning ellipsoid with a major-axis to minor-axis ratio (the elongation factor) of 2.4, for an objective lens with NA 1.4. This figure also shows a stronger dependence of the longitudinal size of the voxel on the exposure time than the lateral size. The voxel elongation factor depends on the resist material and is usually in the range 2.5-3.5. It originates from the nature of diffraction and cannot be significantly modified by adjustment of the optical system or by lens design [160]. The shape of the voxel is dependent on the objective used, with a high NA objective providing voxels with a low height-to-width aspect ratio while a low NA objective results in voxels which are more elongated [161].

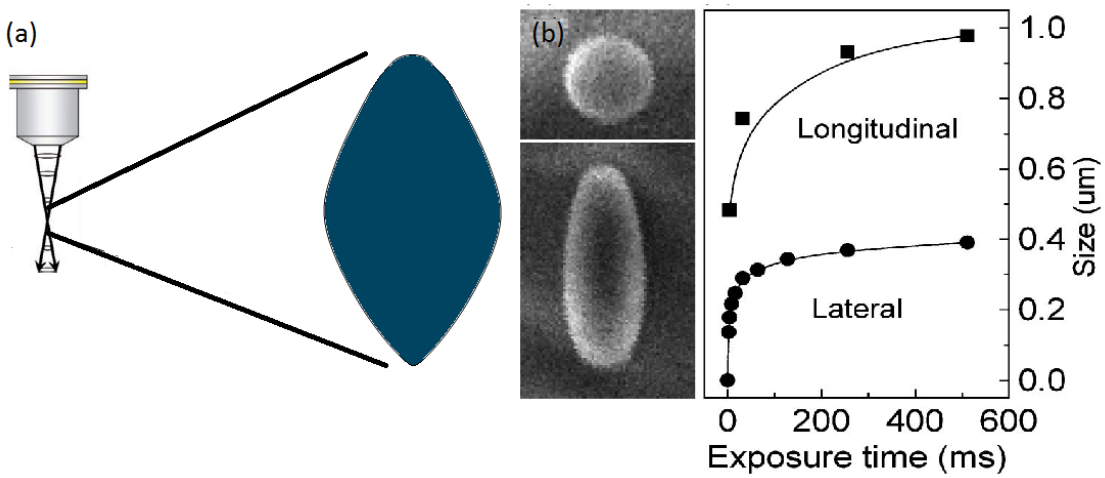

Figure 31: (a) Schematic illustration of voxel elongation along the z-axis. (b) SEM image of an isolated voxel visualized as polymerized resist (left), and a graph (right) of the lateral and longitudinal voxel size as a function of the exposure time for an objective with NA ~1.4 [160].

Resists with conventional photoinitiators were found to exhibit lower photosensitivity due to their low two-photon polymerisation cross section and thus required a high laser power, which is unfavourable. Therefore new photoinitiators for two-photon polymerisation were developed by several groups [162]. Despite such technical challenges, the ability to produce an arbitrary 3D structure with sub-micron resolution has drawn attention from different domains of the micro- and nano-fabrication community. Considerable work has been reported in the fields of photonics and microelectromechanical systems (examples shown in Figure 32), whereas the application of two-photon polymerisation in biology and electronics is also gaining interest [163]. In the field of photonics, it has been used for the fabrication of micro-lenses, couplers, spliters, interferometers, photonic crystals and fiber optics [157, 164]. Direct laser writing has also been employed to

fabricate complex micromachines like microgears, nanotweezers and movable assemblies such as optically driven micropumps [153].

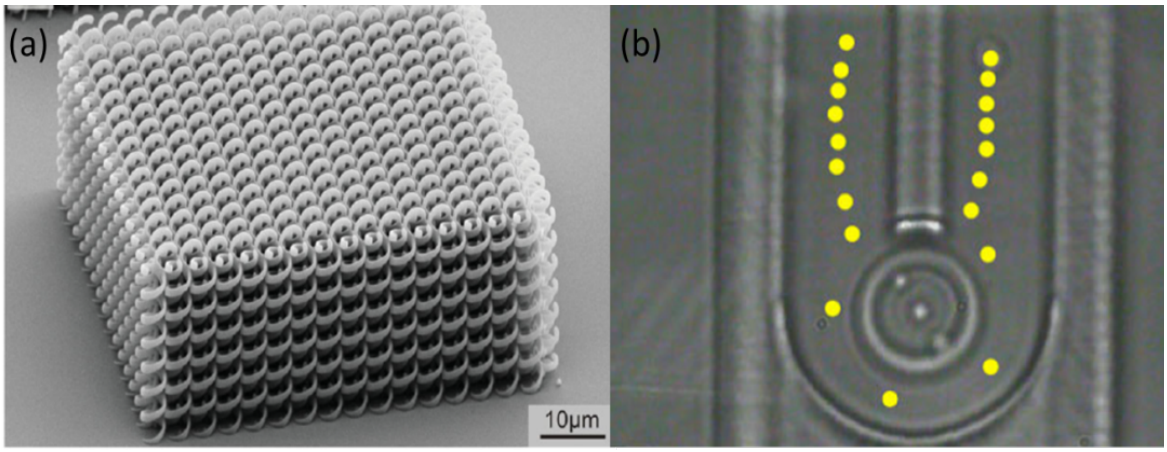

Figure 32: (a) SEM image of a bichiral crystal [165]. (b) A single-disk micropump fabricated using two-photon polymerisation. The disk has a diameter of 10 µm. A sequence of images taken at 2 sec intervals illustrates particle transportation through the channel with the single-disk microrotor being rotated at 27 rpm [166].

4.2 Materials and methods

4.2.1 3D lithography equipment

In this work the “Photonics Professional” from Nanoscribe GmbH (Karlsruhe, Germany) has been used for the fabrication of shaped apertures. It is a state of the art, 3D direct laser write system capable of producing micro- and nano- structures of arbitrary shape in various commercially available resists. The underlying principle of this technology is based on two-photon absorption polymerisation, as discussed in the previous section. The key feature of illumination by the laser beam (780 ± 10 nm, 100 mW) is that a single photon does not provide sufficient energy to cause polymerisation of the resist. However, by tightly focussing the beam in a focal volume, the voxel, its intensity is increased to a level that enables two-photon absorption, which leads to photochemical reactions in the UV sensitive photoresist material. An axial resolution of 800 nm and lateral resolution of 300 nm can be routinely obtained in IP-L resist with this 3D exposure instrument, which is referred to as 'the Nanoscribe'.

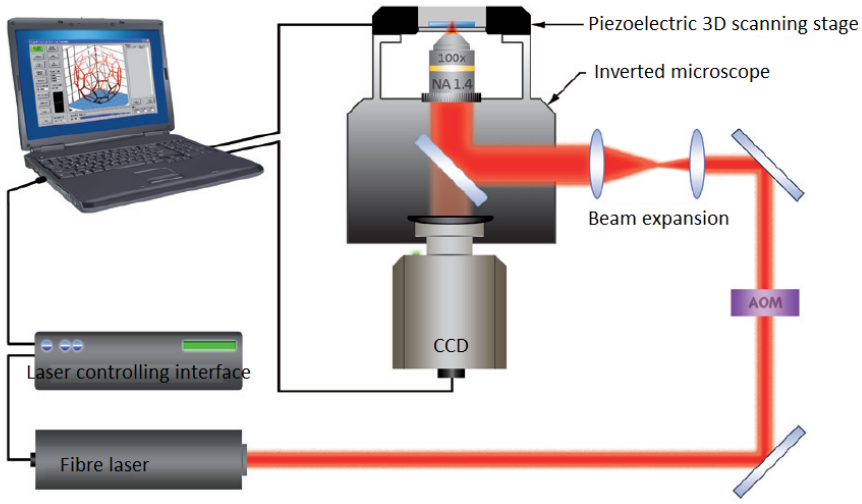

Figure 33: Schematic illustration of the Photonic Professional[3]. The laser beam is focussed by the objective into the resist, which is placed on a motorised stage. The movement of the stage brings the desired regions of the resist in contact with the beam, which gives a 3D structure of laser-polymerized resist.

Figure 33 shows a schematic for Nanoscribe's 3D lithography equipment. The Photonic Professional consists of three major components: a laser and optics cabinet, an inverted microscope, and an electronics rack. The laser and optics cabinet contains the laser head and various optical assemblies to process and monitor the laser beam. The inverted microscope focuses the laser beam for the exposure of the resist at locations defined by the position of the microscope stage. The microscope has three different objectives, 20× (NA 0.5), 63× (NA 0.8) and 100× (NA 1.4, oil immersion objective), but only the 20× (NA 0.5) and 100× (NA 1.4) objectives have been used in this work. These are respectively referred to as the 'low NA' and the 'high NA' objective. The long axis of the ellipsoid shaped voxel is along the optical axis of the beam-focussing microscope objective. The electronics rack consists of the computer system, the electronics cabinet and the laser controller. The computer drives the acousto-optic modulator (AOM) which controls the laser power, and also controls the three-axis piezo electrical scanning stage of the microscope, on which the sample is mounted. The motor stage as well as the piezo stage is mounted on the microscope stand. The piezo stage moves within a range of 300 × 300 × 80 µm[4]. For a writing area larger than 300 × 300 µm, the motorised stage is used, which can move in an area of up to 100 × 100 mm. After writing a structure in a resist layer within the range of the piezo stage, the motorised stage is moved by 300 µm to write another structure by piezo stage movement. The motorised stage has a positional accuracy of 1 µm while the piezo stage has a positional accuracy of 1 nm. Thus, for structures for which a lithographic resolution of ~1 µm accuracy is acceptable, the motorised stage mode can be used to write structures quickly[3].

[3] Manual of Nanoscribe Photonic Professional
[4] With 100× (NA 1.4) objective

4.2.2 Preparation of substrate

30 mm diameter or 22 × 22 mm glass substrates with a thickness of 170 ± 10 µm (Menzel Gläser, Braunschweig, Germany) were first cleaned in fuming nitric acid, followed by cleaning with acetone and isopropanol, and then dried overnight at 210 ^{O}C. For structures built in negative tone IP-L resist (Nanoscribe, Germany), a drop of the resist was placed on the substrate. No prebake or post bake step was performed and the resist was developed in EC solvent for 20 minutes, followed by 10 minutes development in fresh EC solvent and a 10 minute dip in isopropanol. For structures built in SU8 (Microchem), the resist (SU8-50 or SU8-3050) was spin-coated on the glass substrate at 3000 rpm for 30 seconds. SU8-50 was soft baked at 65 ^{O}C for 5 minutes followed by 95 ^{O}C for 15 minutes, while SU8-3050 was baked at 95 ^{O}C for 15 minutes, to obtain a thickness of ~ 50 µm. The substrate was fixed to the substrate holder by applying fixogum (Marabu, Tamm, Germany) around its circumference. The gum was allowed to dry for 15 minutes before putting a drop of IP-L resist , and an oil drop on the opposite side if using the high NA (100×) oil objective. After writing the structure in SU8, the substrate was baked at 65 ^{O}C for 1 minute followed by 95 ^{O}C for 4 minutes, for both the SU8 variants. Structures in SU8 were developed in EC solvent for 5 minutes, followed by rinsing with isopropanol.

4.2.3 Generation of coordinate files

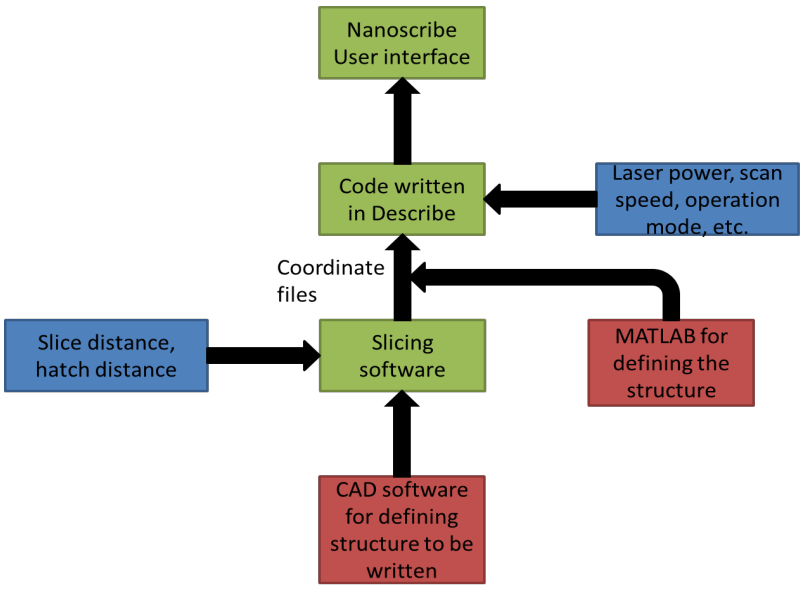

Figure 34: Flow diagram for the generation of code to be exported to the Nanoscribe user interface. The red boxes represents the two options for generation of the coordinate file for the structure, the green boxes represents software specific to the Nanoscribe, and the blue boxes represent the input to the corresponding software

Figure 34 shows the flow diagram for generation of the code that the Nanoscribe takes as input for the writing of 3D structures. First, the structure to be fabricated was defined using a

computerised aided design (CAD) tool such as Solidworks (Dassault Systemes, MA, USA). Once the structure to be written was defined with the CAD tool, it was saved as a '.stl' coordinate file. This file describes the surfaces of the structure by a series of triangles, with each triangle defined by its normal and its vertices. The .stl file thus contains x, y, z coordinates of the vertices of the triangle and their respective normal. The deviation and tolerance defines the smoothness of the curved geometry. Smaller values of tolerance and deviation result in a larger number of triangles, and thus in a smoother surface. Coordinate files were also generated using MATLAB software (Mathworks, Natick, Massachusetts). For complex 3D structures, computer aided design software was used, while for defining less complex structures such as squares and lines the coordinate files were generated with MATLAB.

The dimensions of the structure to be written is given in 'mm' units in SolidWorks, but this is interpreted as 'µm' units by the Nanoscribe slicing software, which provides two coordinate files: *'Solid'* and *'Contour'*. The critical parameters for slicing are the "slice" distance and the "hatch" distance. The slice distance decides the distance at which a slice of the structure is taken along a given direction, while the hatch distance specifies the distance after which coordinate points are taken in a particular slice. Figure 35 illustrates the slicing process for a solid cylinder when the slices are taken along the z-axis and the hatching is done along the y-axis.

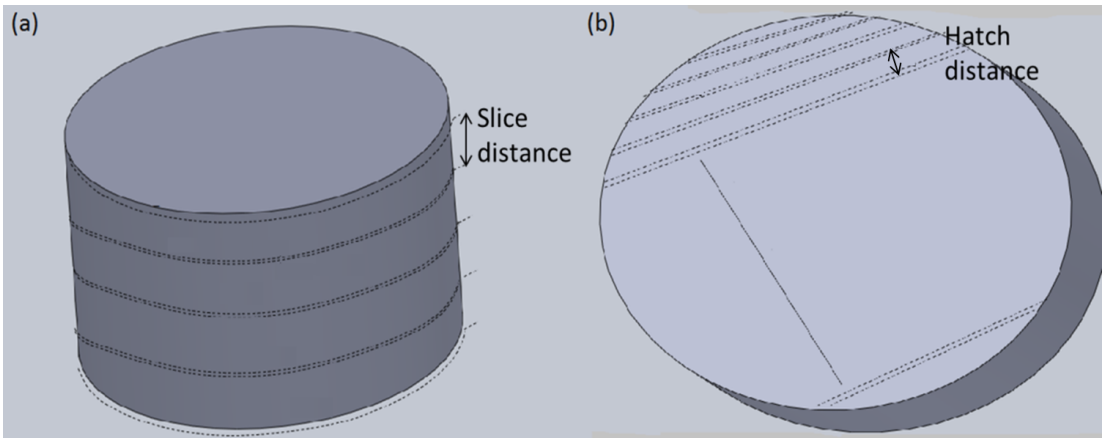

Figure 35: Diagram illustrating the process for generation of coordinate files for the structure to be written with the Nanoscribe using the instrument's slicing software. A solid cylinder has been used as an example to represent slicing at (a) a slice along the z-axis with an inter-slice distance equal to one-fifth of the thickness of the cylinder, and (b) hatching along the y-axis.

The *Contour* file generated by the slicing software contains information about the boundary of the structure while the Solid file contains coordinate values corresponding to its interior. Hence both files should be included in the final code to be exported to the Nanoscribe interface. The user may include slicing and hatching along different axes in case the geometry of the structure is axis dependent, but this would increase the number of coordinate points the laser has to write. Hence, a compromise has to be struck between build time and resolution of the structure

geometry. Infrequently it was observed that extra coordinate points were generated by the slicing software, which were not present in the original structure. In this case, the *Solid* file of the structure was checked and the extra coordinate points such as unwanted hatch lines were deleted. It is vital to determine the correct value for the slicing and hatching distance along the axis of interest, which depends on the shape of the voxel along that axis. For example, if the voxel where two-photon absorption occurs is 1 µm wide (x,y) and 10 µm heigh (z), then a good hatching distance would be 1 µm or less and the slicing distance can be 10 µm or smaller.

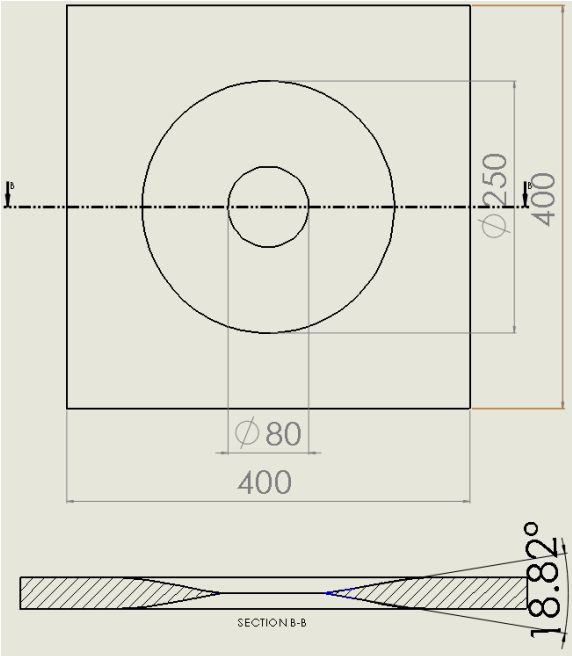

Figure 36: SolidWorks drawing for a beak-shaped aperture, having aperture diameter of 80 µm, in a 400 × 400 µm square. The figure shows top view and cross sectional view along with the dimensions in µm of the final structure built by Nanoscribe in SU8. For all the structures built with Nanoscribe, only the diameter of the aperture was changed, keeping the other details same.

The coordinate files are imported in the instrument's 'Describe' software. This combines information on the laser parameters such as laser power, scan speed, scan mode, and initial positions of the piezo and motorised stage, with the imported coordinates to produce an instruction code for the instrument. This code is then exported to the Nanoscribe user interface for writing the desired structure in the resist at a given position of the substrate.

4.2.4 Double exposure for fabrication of SU8 sheets with shaped apertures

For fabrication of SU8 sheets with shaped apertures, the double exposure strategy depicted in Figure 37 was followed. After writing the aperture edge walls and the immediate surrounding area of the septum as a structure (example shown in Figure 36) in the resist film with the Nanoscribe, the substrate was baked for 2 minutes at 65 ^{O}C to visualize the laser-lithography

exposed area in the resist layer. In a conventional mask aligner (EVG, Austria), the substrate was positioned under a mask in such a way that the already exposed area of the resist was covered by an opaque area on the mask, while the resist outside this area was under the transparent region of the mask. This part of the SU8 film was subsequently exposed at 250 mJ/cm^2, giving a polymerized SU8 sheet of 2 × 2 cm with the laser-lithography defined aperture at the centre position. Post baking of the resist was performed at 65 ^{O}C for 1 minute and at 95 ^{O}C for 4 minutes. The development of the SU8 layer was carried out in EC solvent for 5 minutes, followed by rinsing with isopropanol.

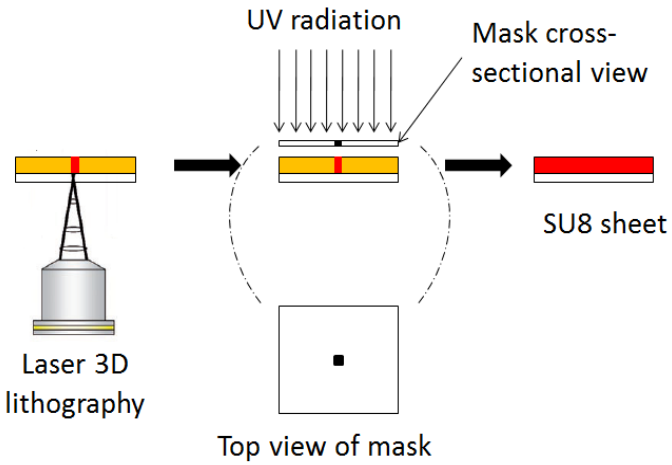

Figure 37: Double exposure fabrication flow for SU8 sheets with tapered apertures. An aperture with a desired geometry was made in an area of 400 × 400 µm using 3D laser lithography, after which the rest of the SU8 sheet was exposed using a conventional mask aligner, while the area already exposed by laser lithography was protected by a photomask. The yellow layer represents unpolymerized SU8 and the red layer represents polymerized SU8.

4.2.4.1 Release of the resist film from the substrate

Three different methods were investigated for the release of resist film. In first method, dextran (20% w/v) was spin coated on the substrate at 1000rpm for 15 seconds and baked at 120 ^{O}C for 2 minutes. In second method, AZ9260 (Microchem) was spin-coated at 3000rpm for 60 seconds and soft baked at 110 ^{O}C for 3 minutes to obtain a thickness of ~8 µm. Development of AZ9260 was carried out in 1:4 AZ400K:water. Third technique involved spin-coating of LOR 7B (Microchem) at 1500 rpm for 60 seconds and soft baked at 150 ^{O}C for 3 minutes. A waiting time of 15 minutes was allowed to cool the substrate before spin coating SU8. AZ 726 MIF developer was used to dissolve LOR 7B (Figure 37). Scanning electron microscopy and optical microscopy were performed with, respectively, EVO LS25 (Carl Zeiss, Jena, Germany) and LV 100 (Nikon, Tokyo, Japan) microscopes.

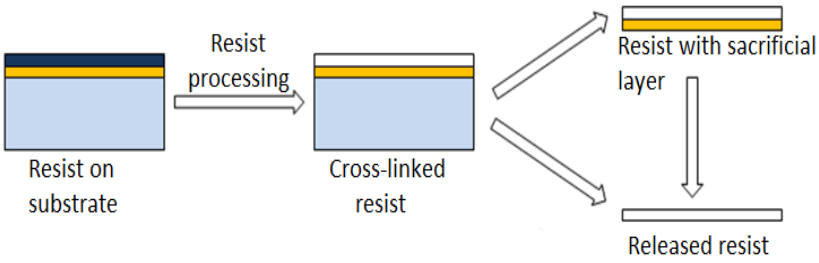

Figure 38: Schematic illustration of the resist (SU8) release strategy from the substrate by employing a sacrificial layer (LOR 7B). Resist was spin-coated on top of the sacrificial layer. After resist processing (exposure, baking and development), the sacrificial layer was dissolved using an appropriate developer (e.g. AZ 726 MIF for LOR 7B). The resist and sacrificial layers could also be released together from the substrate, which was then followed by a final step of dissolution of the sacrificial layer. The dark blue layer represents unpolymerised resist, the white layer represents cross-linked (polymerised) resist and the yellow layer represents the sacrificial layer.

4.3 Results and discussion

4.3.1 Optimisation of fabrication times

This section discusses initial work with two-photon absorption polymerisation to evaluate its applicability for the fabrication of apertures. Since ion channel electrophysiology experiments require clamping of the septum in between two aqueous chambers, the resist sheet with the aperture should have a minimum area of 1 × 1 cm. Because polymerizing resist at the highest resolution (i.e. using the high NA objective) is time-consuming process with a build time of, for example, 3 hours for a micro-bull structure having dimensions 10 µm by 7 µm (size of a red blood cell) [167], the aim of these initial experiments was to optimise the fabrication time for the aperture side walls.

4.3.1.1 Slice and hatch distance

Only inside the voxel is the intensity of the laser beam sufficient to expose the resist by two-photon polymerisation [168]. Consequently, moving the voxel through a spatial geometry polymerises the resist at predefined positions which results in the desired 3D structure. Since the information about the coordinates of the 3D structure to be scanned by the laser is contained in the *Contour* and *Solid* files (see section 4.2.2), the selection of the slice and hatch distances is critical for structure fabrication. This is visualized by the example structure shown in Figure 39, which has a skeletal appearance. Although the structure shows a well-defined contour, the bulk of the structure displays numerous single lines of polymerised resist with an observable gap in between, i.e. the structure does not have a smooth and continuous pattern. As the hatch distance determines the separation between each scan of laser for a given slice, it is apparent that this

structure suffers from a poor selection of hatch distance, with the selected hatch distance being much larger than the lateral dimension, or diameter, of the voxel.

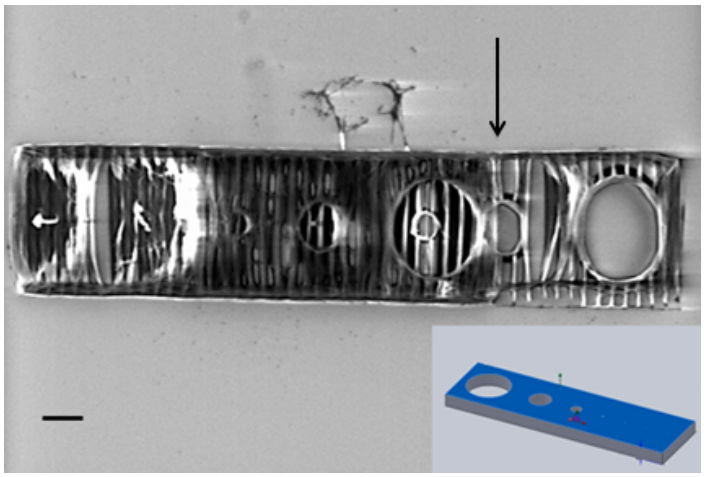

Figure 39: SEM image of a structure built by Nanoscribe using high NA objective in IP-L resist. Slicing was done along z-axis and hatching was done along y-axis. The hatch distance chosen was substantially more than the lateral dimension or diameter of the voxel, hence produced a solid skeleton after washing out of unpolymerised resist due to non-overlapping of the voxels. Inset shows SolidWorks design for the same structure. Arrow on the image shows overlapping of two same structures. The scale bar is 10 µm.

When the smallest details of the desired structure are substantially larger than the voxel and when decreasing the hatching distance is undesirable because of the concomitant increase in build time, a simple solution is to adjust the laser power. Two-photon polymerisation has an energy window within which the voxel diameter can be increased by increasing the input laser power [169, 170]. As a result, a wider strip of resist can be polymerised with each scan of the laser. The lower range of this window is determined by the two-photon polymerisation threshold, below which the resist does not undergo polymerisation, which depends on the chemical composition of the particular resist. Beyond the upper range of the energy window, the resist is damaged or boiled by the laser [162, 169-171], with an example shown in Figure 40.

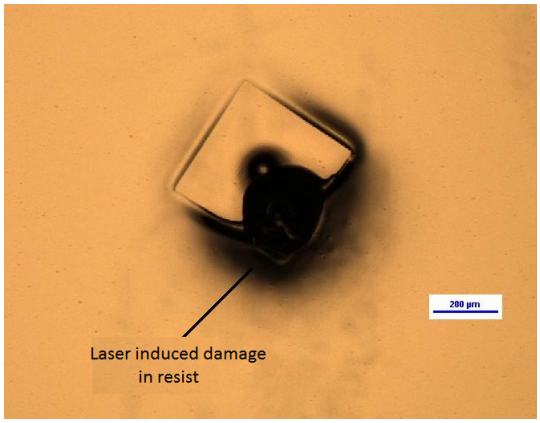

Figure 40: Optical micrograph showing laser induced damage in a structure written by Nanoscribe in negative tone resist, highlighting the effect of using a laser power that is too high. The resist had not been developed, but the imprint of the structure was visible after a bake step. The scale bar is 200 µm.

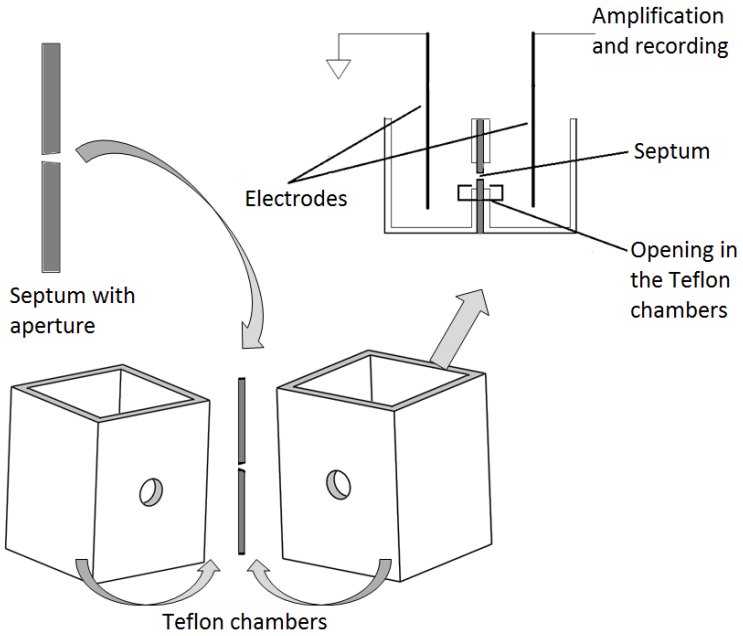

Figure 41: Schematic illustration of clamping of the septum in the Teflon chambers for the formation of electrically accessible suspended bilayers that are vertically oriented. The septum is sealed to the surface of the Teflon chambers such that the aperture is in the middle of the opening in the chamber.

4.3.1.2 Use of low NA objective for reducing fabrication times

Fabrication of structures with sub-micron feature size is not necessary for all applications, and is not required to define shaped apertures for suspended bilayers. Direct laser writing of large structures using small voxels should be avoided because build times can be several days. The definition of large-area, 1 × 1cm, resist sheets that can serve as a septum in an electrophysiology setup (see Figure 41) by two-photon lithography is certainly not practical. Effective methods to reduce the build time are to reduce the number of coordinate points to be scanned by the laser by increasing the slice and the hatch distances, or to increase the laser power, which results in a larger voxel. For example, for a given laser power, scan speed and slice distance, a structure can be written twice as fast if the hatch distance is doubled. However, as shown in Figure 39, this can result in insufficient exposure of the structure or damage to the resist. Since the size of the voxel is also dependent on the focussing optics, we investigated the use of a low NA objective (20×, NA 0.5) for reducing fabrication times [163, 172]. A decrease in NA redistributes the photon energy at the focal volume which increases the voxel size in both the lateral and longitudinal direction [171, 173]. However, intermediate irradiation levels (<5mW) can yield a better lateral resolution with low NA due to distribution of laser power to a larger volume, causing shrinking of the voxel laterally as a result of reduction in the energy below polymerisation threshold [173].

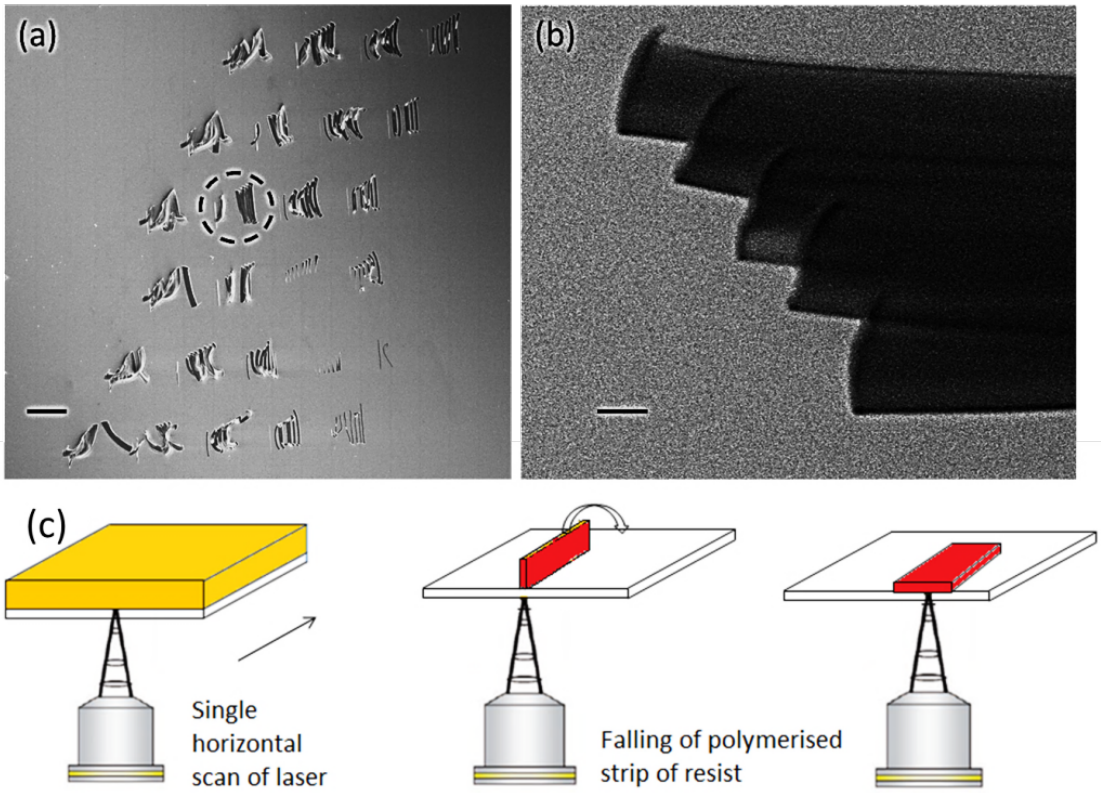

Figure 42: SEM images of sets of isolated linear z-scans of the laser in negative tone resist IP-L, for different laser settings, after exposure and development. (a) left to right line sets: laser power 100, 80, 60, 40, 20 for a given scan speed; top to bottom: scan speed 250, 200, 150, 100, 50, 20 µm/sec. The scale bar is 200 µm. (b) Expanded view of the dotted circle in (a), with a scale bar of 10 µm. (c) Schematic illustration of the use of linear laser scans to evaluate the lateral and longitudinal dimensions of the voxel for the low NA objective. The height of the polymerised rectangle of resist represents the lateral dimension, while its width represents the longitudinal dimension. The yellow colour represents unpolymerised resist and the red colour represents polymerised resist.

Initially, the voxel formed by the low NA objective was characterised by defining single line in the resist at different laser power and scan speed. The interface position, defined as the position at which the voxel is focussed, was also varied to isolate the voxel. The polymerised resist lines indicated that the voxel produced by the low NA objective had a considerably longer longitudinal dimension compared to the lateral dimension, a phenomenon known as voxel elongation [173, 174]. Figure 42 shows SEM images of resist polymerized by single laser passes, after development. The thin long polymerised rectangles of resist had fallen sideways on neighbouring polymerised resist rectangles in a set of lines polymerized at the same laser power and scan speed.

Next, two squares were fabricated by employing a code representing a 2D plane, with different line spacings (Figure 43). The height of the structure was limited by the longitudinal dimension, or height, of the elongated voxel. The code for the first structure consisted of a single pass of parallel horizontal lines with a separation distance of 0.5 µm. A solid square of polymerized resist was obtained after development, containing square apertures that were defined by not exposing the corresponding areas. The second square, fabricated with a line

separation distance of 5 µm, gave a skeletal structure after development, consisting of isolated polymerized resist lines because the voxel position of adjacent lines did not overlap.

Another parameter that was explored was the interface position of the structure that defines the start position for writing in the z-direction. The approximate height of the structure varied with different interface positions as shown in Table 4, where negative values represented movement of the laser spot deep into the resist and positive values means that the laser start position is buried into the glass substrate. When the laser spot was placed deep in the glass substrate, with positive interface positions, the height of the structure after exposure and development was reduced because only the tip of the voxel penetrated out of the glass substrate into the resist layer.

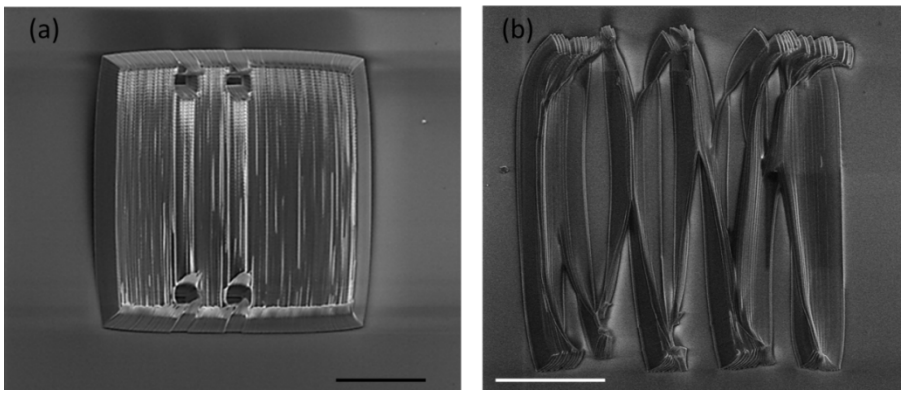

Figure 43: SEM images of squares fabricated in negative tone IP-L resist using a code defining parallel linear laser scans with a separation distance of (a) 0.5 µm or (b) 5 µm. (a) A homogeneous structure is obtained after development, which appears curved because of poor adhesion to the substrate. (b) After development the structure is not homogeneous, consisting of isolated resist strips that have fallen over each other; the voxel diameter was smaller than the distance between the linear scans. Laser power= 80, scan speed= 200 µm/sec and power scaling= 1. The scale bars are 100 µm.

Table 4: Approximate height, measured with tiff annotation software, of the squares (Figure 43a) built with the low NA objective with a separation distance of 0.5 µm and at different glass-resist interface distances, which imply a different writing start position in the z direction.

Interface distance	**Approximate structure height (µm)**
15	1.8
10	9
5	18
0	19
-5	26
-10	33
-20	30

Next, SolidWorks was used to create coordinate files for square structures that contain a shaped aperture, Since the dimension of the voxel depends on resist properties [148], voxel characterisation was also carried out with SU8 resist, which is widely used in the

microelectromechanical systems community, to identify suitable slice and hatch distances. Figure 44 shows two aperture-containing squares written in SU8, with a hatch distance of 1 µm and a slice distance of 0.5 µm, one with the low NA objective and one with the high NA objective. The use of the low NA objective resulted in a full-height structure with a smooth surface, whereas the surface of the structure exposed with the high NA objective displayed discrete lines, which suggest that the voxel diameter was smaller than the hatch distance. Moreover, the latter structure only consisted of a single slice of polymerized resist, indicating that the different slices of the structure were not stitched together because the longitudinal dimension of the voxel was smaller than the slice distance. Because the given hatch and slice distances enable a relatively short build time, the low NA objective lens was preferred for the fabrication of shaped apertures.

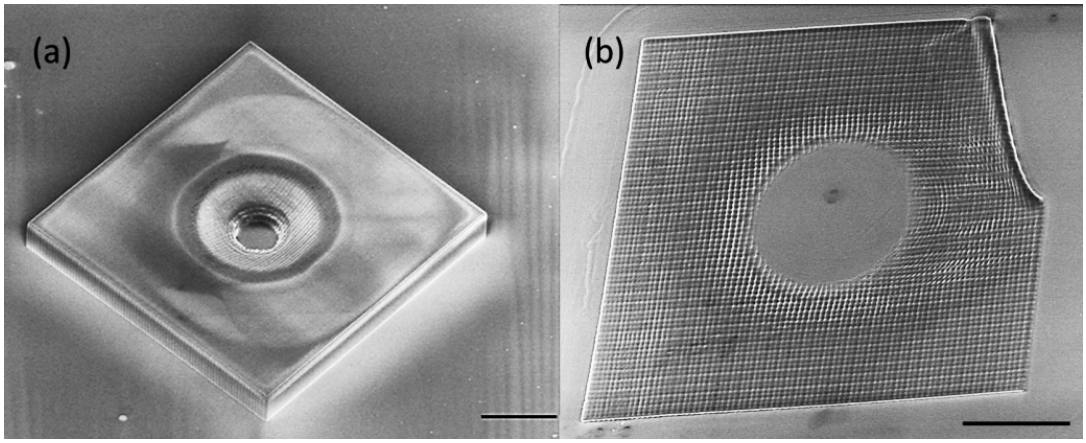

Figure 44: SEM image of a beak-shaped aperture in a square resist area fabricated in SU8 using (a) a low NA (0.5) objective and (b) a high NA (1.4) objective. Both the structures were defined using SolidWorks and sliced and hatched at 0.5 µm and 1 µm, respectively. The wider diameter of the voxel obtained with the low NA objective gave a smooth surface while individual scan lines were apparent with the high NA objective due to its narrower voxel. For the structure built with the high NA objective (b), only the first slice of the structure could be seen after development due to the wide separation between adjoining slices, due to a reduced voxel height, which were thus washed away during development. Laser power= 55, scan speed= 200 µm/sec and power scaling= 1The scale bars are 100 µm.

The SU8 sheets shown in Figure 44a had a thickness of 50 µm even though the input coordinate file specified a thickness of only 25 µm. The elongation of the voxel along the z-axis with the low NA objective allowed the polymerisation of the resist outside the limits of the coordinate file, hence the fabrication time could be further reduced by defining a reduced-height structure in the coordinate file. With optimisation of fabrication times for writing structures with the low NA objective, an area of 400 × 400 µm with a beak shaped aperture could be written in approximately 12 hours.

Since only the side walls of the shaped aperture require 3D lithography, most of the resist sheet of 1 × 1 cm could be exposed in a conventional mask aligner. This method requires careful alignment of the aperture edge built with the Nanoscribe with a suitable mask to avoid re-exposing this area of the resist layer. Since polymerisation is initiated by heat in SU8, a post

exposure bake was done to get the imprint of the aperture built with the Nanoscribe, which enables mask alignment before flood exposure. Figure 45 shows a top view and two cross-sections of a beak-shaped aperture in a SU8 sheet fabricated using this approach, as visualized by confocal laser scanning microscopy with 405 nm excitation, which exploits the absorbance properties of SU8 at lower wavelength [175, 176]. Although confocal microscopy confirmed the fabrication of sloped aperture walls, the thickness of the resist at the tip of the aperture could not be determined due to the low resolution of the fluorescence image.

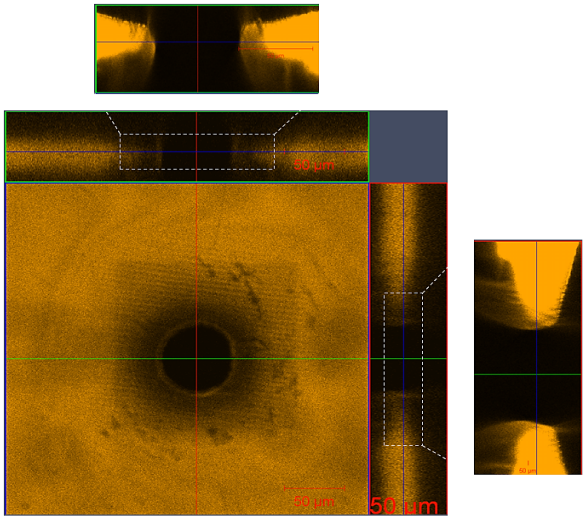

Figure 45: Confocal laser scanning microscopy of a beak-shaped aperture in a 2 × 2 cm sheet of SU8 with 405nm excitation. The darker square in middle of the central image corresponds to the position of the photomask used to protect the Nanoscribe-defined region from flood exposure in the mask aligner. The scale bar is 100 µm.

For detailed information on the aperture cross section, scanning electron microscopy was performed. Top view and cross-section SEM images of shaped apertures, before the release of the SU8 sheet from the glass substrate, are shown in Figure 46. Triangle-shaped and beak-shaped apertures were fabricated successfully, with observed aperture wall profiles closely matching the designed geometries. At the narrowest point, the triangle-shaped and the beak-shaped apertures have an aperture tip thickness of ~2 µm. The intended values of the inner diameters of the apertures were 60 or 80 µm for the triangle-shaped apertures, and 60, 80 or 100 µm for the beak-shaped apertures. The measured diameters were ~10% larger than the design values (Figure 46), which may indicate some overdevelopment. Although the SolidWorks design for the shaped aperture specified a tip thickness of a few hundred nanometers, elongation of voxel hindered fabrication of such thin tips and also the apex of the tip would have washed away during SU8 development due to absence of a support. Hence, voxel elongation with the low NA objective required further optimisation of laser power and scan speed settings to produce shaped apertures with a tip thickness below 2 µm. But because this would have posed fabrication challenges and

also practical problems associated with cleaning of the apertures in between electrophysiology experiments, ultimately restricting overall reusability and reproducibility, this optimisation was not undertaken.

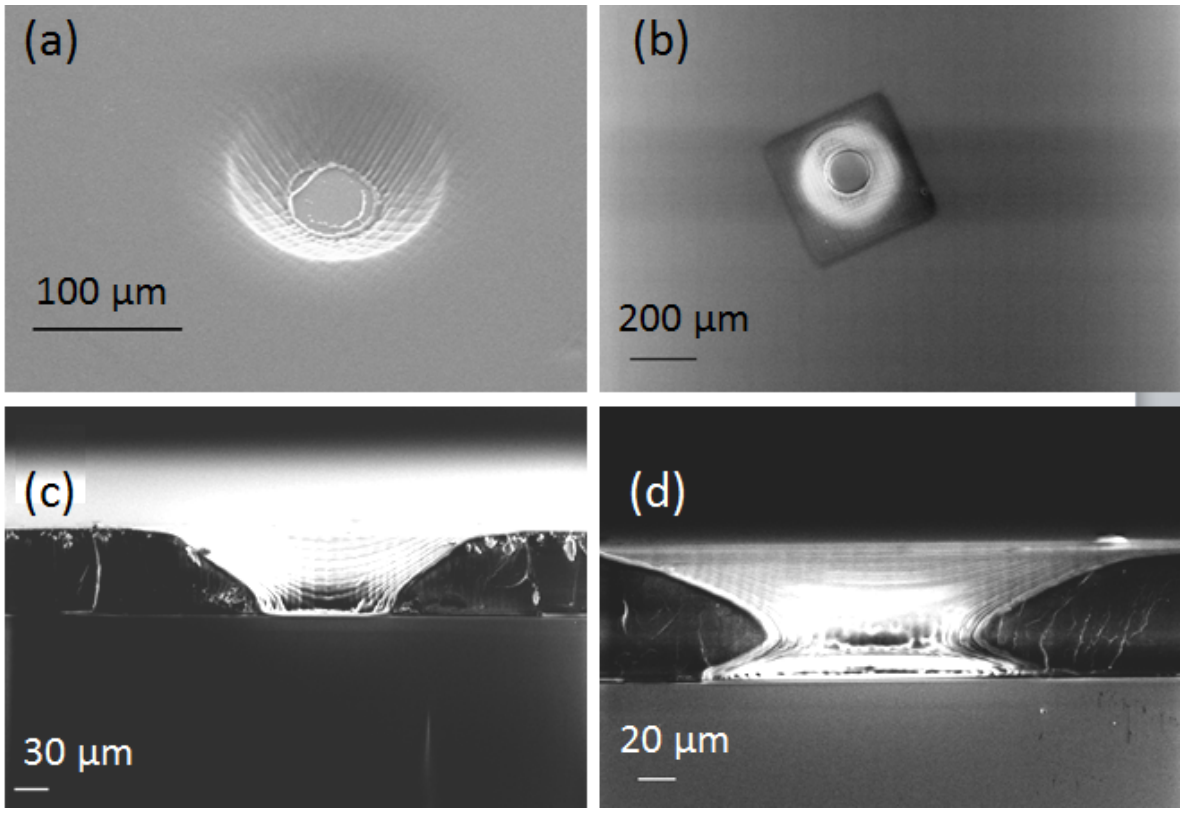

Figure 46: Angled top view (a,b) and cross-section view (c,d) SEM images of shaped apertures in SU8 sheets, still attached to the glass substrate, made using the low NA objective (a,c) triangle-shaped aperture, and (b,d) beak-shaped aperture. The resist outside the immediate vicinity of the aperture has been polymerized by flood exposure in a mask aligner while the Nanoscribe-defined aperture walls were protected by a square mask feature. Laser power= 55, scan speed= 200 µm/sec and power scaling= 1.

To compare the stability of bilayers suspended in shaped and non-shaped apertures, control structures were fabricated as shown in Figure 47: a blunt-beak shaped aperture and a cylindrical aperture with vertical side walls. SU8 sheet with blunt-beak shaped aperture was fabricated with an accelerated writing procedure. The interior of the structure was written with a 5 µm slicing and a 1 µm hatching distance, while the outline of the structure was written with a smaller slicing distance of 0.5 µm and with the same hatching distance of 1 µm. The outline coordinate file with the small slice distance ensured that there were enough coordinate points to obtain the desired shape of the aperture, while the voxel elongation along the z-axis allowed the use of the large slicing distance used for writing the interior region of the structure. Although this blunt-beak aperture was written in just 2 hours, the thickness at the tip of the aperture was ~10µm. The smaller number of coordinate points also gave a step-like appearance to the edge of the aperture (Figure 47a). The third structure shown in Figure 47 is a blocked-beak aperture that was used for calculation of the background capacitance, which will be discussed in Chapter 6.

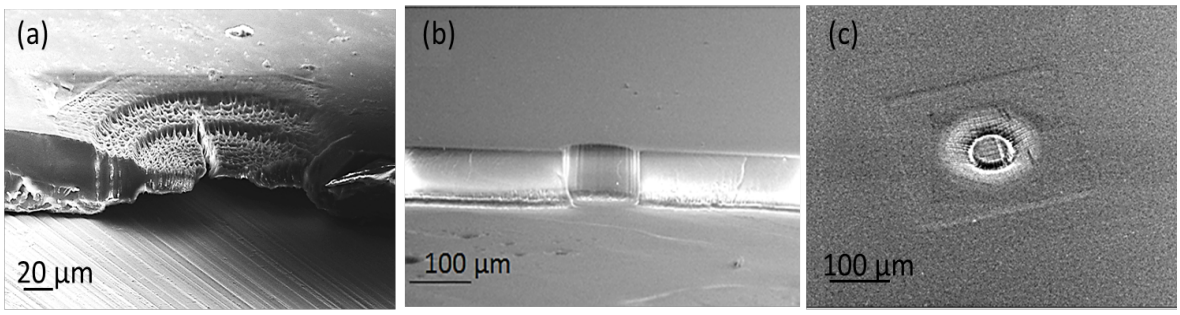

Figure 47: Cross-section view (a,b) and angled top view (c) SEM images of control apertures in SU8 that serve as a control in bilayer stability measurements: (a) blunt-beak shaped aperture, which had cracked during scribing of the cross-section, (b) cylindrical aperture, and (c) blocked-beak shaped aperture. Laser power= 80, scan speed= 140 µm/sec and power scaling= 1 was used for fabricating (a) and laser power= 60, scan speed= 200 µm/sec and power scaling= 1 for b and c.

4.3.2 Resist release strategy

One of the important aspects of the fabrication protocol was the release of the resist sheet from the glass substrate so that it can be clamped inbetween two aqueous chambers for lipid bilayer experiments. Since the laser light has to pass through the substrate to polymerise the resist, a sacrificial layer of opaque materials like titanium and aluminum could not be used, and would also have necessitated toxic etchants [177]. Numerous studies have reported water soluble polymers as sacrificial layer below the resist layer for release of micromachined structures. These polymer molecules can be conveniently spin coated and do not dissolve in developing solvents [177, 178], but are not well suited for the release of larger structures or films because the release process is slow. When water soluble dextran was used as a sacrificial layer in this project, it was found that it took a few days to release the whole sheet of resist (Figure 47), while it was also difficult to obtain a uniform dextran layer.

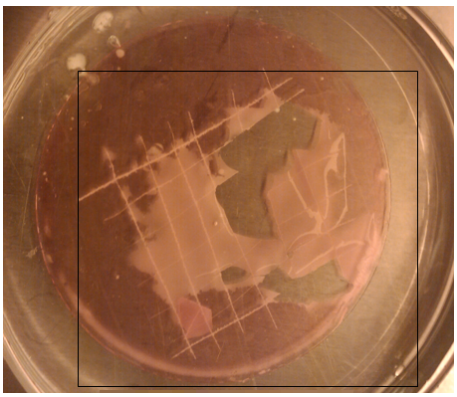

Figure 48: Photograph showing the release of a positive resist layer from the glass surface with dextran as sacrificial layer. The release was facilitated by cutting the resist with a blade in the centre. The resist was not released from the substrate until the centre portion was cut by the blade. The dissolution of dextran in water was quite slow, making release of the resist a tedious process.

Since positive resists becomes soluble to developer on UV exposure, release of structures can be achieved by using exposed positive resists as sacrificial layers [179]. Although AZ9260, a positive tone resist, provided a uniform layer after spin coating on the substrate, the release of SU8 structures was not straightforward. If a positive resist is directly used for SU8 release, a positive resist/SU8 interface is produced which gives rise to effects such as scission and outgassing [179, 180]. Outgassing causes trapping of bubbles at the interface (see Figure 49), while scission causes distortion of the SU8 structures like warping [181]. In general, release strategies involving solutions to dissolve the sacrificial layer are restricted by limited and short distance accessibility, due to diffusion limited lateral supply of developer or etchant underneath the structure [182](see Figure 50). Although this could be alleviated by including numerous release holes in the SU8 layer, this is not desired.

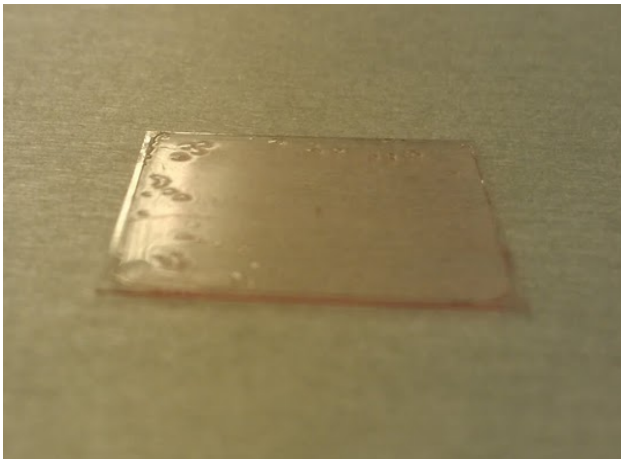

Figure 49: Photograph of a glass substrate (22 × 22 mm) with a SU8 layer spin coated on a sacrificial layer of the positive resist AZ9260. Bubbles can be seen at the surface which is due to the outgassing effect at the SU8/AZ9260 interface.

Different dry release strategies have also been used in various studies to release SU8 structures [182-184], but this was either to release small structures of a few hundred microns or thick SU8 films with a height of several hundred microns. This cannot be employed for thin SU8 films of at most 50 µm thickness, as the use of razor blades or other mechanical means to cut the SU8 sheet from the substrate will damage the SU8 sheet. Hence, another family of resists were used for the release of SU8. LOR is a poly(methyl glutarimide) (PMGI) based resist which does not form any interfacial layer with the top layer of resist and it is resistant to various solvents used for developing resists. LOR 7B and LOR 5A were investigated and LOR 7B was found to be a better choice for release of the SU8 sheet due to the high solubility rates compared with LOR 5A. Choi *et al.* also used LOR 7B to release a SU8 sheet with numerous holes [185], which circumvents the developer diffusion problems. However, in this work, only a single aperture in a 2 × 2 cm SU8 sheet was present, which limits the accessibility of developer to the sub-SU8 LOR 7B layer.

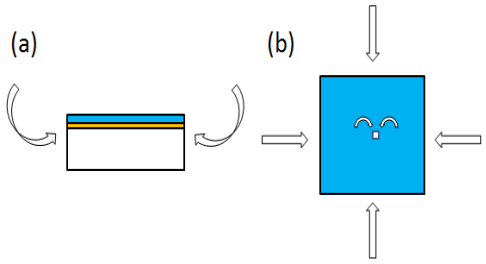

Figure 50: Illustration of diffusion limited accessibility encountered with wet release techniques. The arrows indicate how the solution can access the sacrificial layer i.e. from the edges and through the aperture in the middle of the sheet. (a) Side view and (b) top view of a substrate with a single aperture in the centre as required lipid bilayer applications. The resist structure to be released is shown in blue and the sacrificial layer is shown in yellow.

The glass transition temperature of LOR 7B is around 180-190 ^{O}C, thus the soft baking temperature should be >185 ^{O}C for optimal adhesion to the substrate. In this work, LOR 7B was baked at 150 ^{O}C for 3 minutes and no adhesion promoter was used. Thus, the adhesion of the LOR resist to the glass surface was deliberately reduced. With this approach, the release of the SU8 layer was indeed observed during development of the SU8 with EC solvent. The released SU8 sheet was dipped in AZ 726 MIF to dissolve the LOR sticking to the released SU8 sheet (Figure 51). The release success with this approach was >90%, and for those cases in which release did not occur spontaneously during SU8 development, a dip in alkali developer for LOR released the SU8 sheets within a few hours. AZ 726 MIF was used for dissolving LOR 7B since it is a more aggressive developer than the one recommended by the supplier, facilitating rapid SU8 release. This release strategy is relatively simple and straightforward. However like other techniques, it also has certain limitations. It cannot be used to release of multi-layer SU8 structures, since the release will take place in the first development step. If multi-layer processing is required, soft baking temperatures need to be raised above 185 ^{O}C or a longer soft baking time should be chosen.

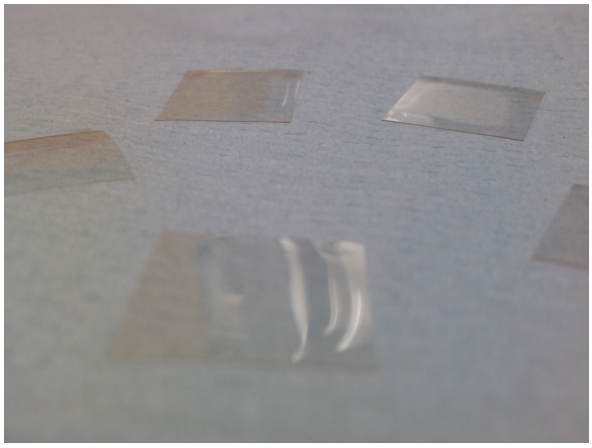

Figure 51: Photograph of 2 × 2 cm SU8 sheets having a single aperture in the centre. The sheets were released from the substrate using LOR 7B as a sacrificial layer. The corrugation near the edge of the sheet was due to the bead effect from resist (in this case SU8) spin coating.

4.3.3 Damage to SU8

One of the problems encountered with the use of SU8 as resist for aperture fabrication was the formation of cracks in the SU8 sheets (see Figure 52) due to the tensile stress which builds up during processing and which is initiated during development of the resist. These cracks could lead to leakage currents in ion channel electrophysiology experiments and thus required considerable attention. Although a hard bake step at 150 ^{O}C helps in annealing surface cracks, it could not be employed because it was observed that this leads to blisters in the released sheet. While some studies reported the optimisation of post exposure bake and soft bake temperatures as a method to avoid cracking due to tensile stress, others reduced the exposure area and prevented sharp concave corners which act as crack nucleation points [186, 187]. It was attempted to avoid the cracks in the SU8 sheet by slowly ramping the temperature during the soft bake and post bake steps up and down, but cracks could still be observed. However, it was established that if the resist was developed 10-12 hours after the post bake steps, cracks did not occur. Additionally, it was found that SU8 from the SU8 3000 series did not require a time gap between the post bake and development steps to circumvent the issue of cracks. Hence, the SU8 3000 series was preferred for fabrication of crack-free resist sheets.

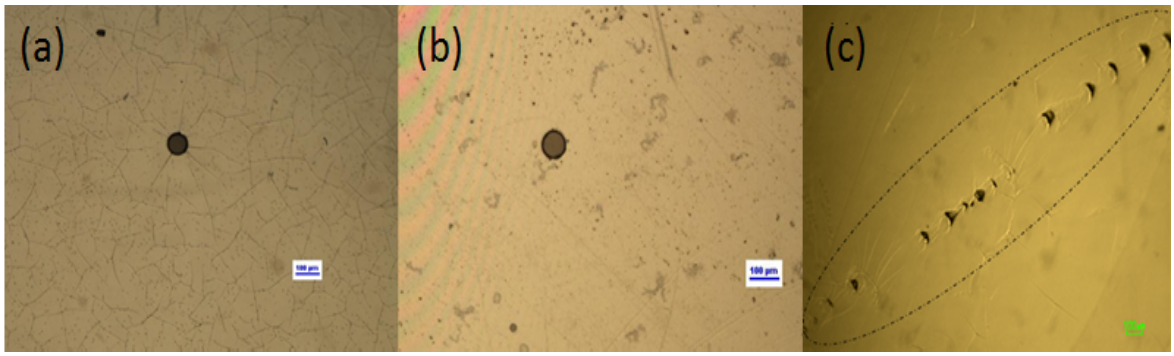

Figure 52: Optical micrographs showing the issue of cracks and fissures in the SU8 layer after development and release from the substrate: (a) cracks associated with tensile stress built in SU8 during processing and released during development, (b) crack-free SU8 when it was developed after 10-12 hours, and (c) fissures associated with non-uniform adhesion of LOR 7B to the glass substrate. The scale bars are 100µm.

However, there were also some discontinuities in the SU8 films, marked by the random presence of fissures in the SU8 sheet, with the same imprint at the same position on the glass substrate. Since these fissures were typically observed when the SU8 sheet was released during development in EC solvent, it was likely that they were associated with the LOR 7B sacrificial layer and not to tensile stress related to SU8 processing. It was anticipated that these fissures could be due to a stronger adhesion of the LOR 7B to the substrate at the fissure locations. Nonetheless, this phenomenon was not observed when a dry film resist, TMMF, laminated onto the LOR 7B layer, was used instead of spin-coated SU8. This observation suggests that the source of these

fissures is associated with spin coating of SU8. It was observed that if the glass substrate was allowed to cool for 15 minutes after baking LOR 7B at 150 ^{O}C, and before spin coating the SU8 layer, these fissures could be avoided, which indicates that the interaction of spin-coated SU8 with the underlying LOR 7B layer is an important parameter.

4.4 Conclusions

This chapter presents a literature review on the two-photon absorption polymerisation technique for fabrication of 3D structures in photoresist. The Photonic Professional from Nanoscribe was used to define shaped apertures with this lithography technique. Methods to optimise build times were investigated to fabricate resist sheets of 1 × 1 cm. The dimensions of the voxel determine the slice and hatch distance that result in the coordinate points to be scanned by the laser, with larger distances resulting in less scan points and a shorter build time. A higher laser power results in a wider voxel which allows for a longer hatch distance but laser induced resist damage should be avoided. Instead, an objective lens of low NA was investigated, and the anticipated increase in the diameter and the height of the voxel was characterized by single-line resist polymerization. Emphasis was placed on the proper selection of the slice and hatch distance, typically 0.5 and 1.0 µm, respectively, to obtain homogeneous structures. This enabled a 400 × 400 µm area of 50 µm thick resist, with a shaped aperture at the centre, to be written in 12 hours. With a double exposure approach the resist outside this area was cross-linked by exposure in a conventional mask aligner, defining a sheet of 2 × 2 cm, suitable as a septum for electrophysiology experiments. The release of this septum from the substrate without crack or fissure formation was problematic but a suitable protocol was eventually identified. The use of LOR 7B as sacrificial layer was found to be quick, simple and reliable provided that a delay of 15 minutes or more was implemented between soft baking of LOR 7B and spin coating of SU8. A waiting time of 10-12 hours between hard bake and development of SU8, and the use of the SU8 3000 series prevented cracks associated with stress build up in SU8. Beak-shaped, triangle-shaped, blunt-beak, blocked-beak and cylindrical apertures were fabricated as test and control shapes for bilayer stability experiments, presented in Chapter 6. Because even with the optimized 3D laser lithography method, the fabrication time is still in excess of 12 hours for a single septum with one shaped aperture, an alternative lithography technique for parallel aperture definition is investigated and discussed in the next chapter.

Chapter 5 High-throughput fabrication of shaped apertures

Although two-photon polymerisation is a powerful method for fabrication of complex 3D structures with high resolution, it is inherently a serial process [148]. Since structures are written on a voxel-by-voxel basis, mass production of 3D structures using this technique is a daunting task. Various groups have investigated different approaches to overcome this serious roadblock such as multipoint fabrication [188] and multibeam interference lithography [189]. Unfortunately, these techniques suffer from limitations such as the requirement for an amplified laser system for multipoint fabrication and creation of periodic structures for both approaches [148]. Nevertheless, the use of software-directed laser lithography to create 3D structures provides an element of flexibility, which was why the 'Nanoscribe' 3D laser lithography tool was used in this project to fabricate apertures and control apertures of various shapes for the study of suspended bilayer stabilisation. However, the low-throughput of aperture fabrication by 3D laser lithography is a bottleneck and will prevent widespread use of these shaped apertures. Possible approaches for the high-throughput fabrication of shaped apertures, imprint lithography and grayscale lithography, are reviewed in this chapter and their applicability for the fabrication of shaped apertures has been experimentally evaluated.

5.1 Imprint lithography

Moulding is a replication method that allows a pattern on a master, also referred to as a mould or a template, to be transferred to a soft material in a parallel manner. Even though

moulding does not directly fabricate patterns, it does replicate the patterns quickly, cheaply and with high fidelity [190]. One of the attractive features of moulding is the fact that its resolution is not limited by the effects of wave diffraction, scattering and interference in the resist or back scattering from the substrate, because it does not use energetic beams. Various moulding methods have been developed over the last decade and these can be classified into the following categories according to the softening or hardening principle involved: (i) temperature based processing (hot embossing) (ii) light-initiated polymerisation (UV imprint lithography), (iii) thermal initiated polymerisation (soft lithography), and (iv) solvent based processing [191]. Initially, the term 'nanoimprint lithography' (NIL) was used as a synonym for hot embossing lithography but its meaning has now been extended to other variations such as UV-NIL, roll imprint process, reverse imprint lithography and related applications. NIL involves the mechanical modification of a thin polymer film due to direct contact between a master with a micro- or nanoscale pattern in a thermo-mechanical or UV curing process (Figure 53) [192]. NIL can either be used for transferring patterns to the substrate with the polymer film acting as a mask, or be applied to add functionality to the imprinted substrate. Its many application areas range from rectilinear patterns for nanowire devices to optical elements for light emitting diodes to bio-devices.

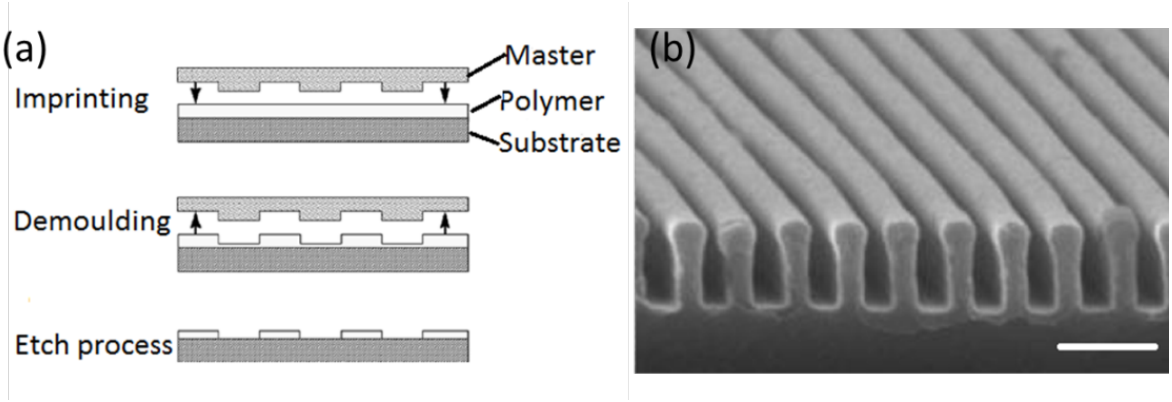

Figure 53: (a) Schematic illustration of the generic NIL process. A master containing nano-features is pressed against a polymer which could either be a thermoplastic polymer or a UV curable resist. For thermoplastic polymers, the substrate is heated above the glass transition temperature of the polymer before bringing the master into contact. The master is removed from the substrate (demoulding) after the substrate has cooled down For UV curable resist, UV light is projected on the resist to polymerise it after the master and substrate are pressed together and resist has filled the cavities. An etch step is performed to remove the residual layer. [149](b) SEM image of 300 nm grating in SU8 resist fabricated using UV NIL. The scale bar is 500 nm [193].

Because it is challenging to remove the thin residual layer of polymer on the bottom of thermally imprinted features [194], this project concentrated on UV-imprint lithography for fabrication of shaped apertures. In UV-NIL, a UV curable resist is pressed against a UV transparent master of a material such as fused silica or quartz. UV irradiation causes the polymerisation or hardening of the patterned resist film that can be demoulded from the template due to shrinking of the resist [191]. It offers the following advantages over thermal NIL: the process (i) can be performed at low pressure and at room temperature, (ii) is rapid, and (iii) allows easy fabrication

of high aspect ratio structures becuase low-viscosity resists are able to fill up high aspect ratio cavities in the master [191]. As an approach that is different from conventional lithographic techniques, nanoimprint lithography faces new issues and challenges [149]. High-throughput replication of patterns with high fidelity depends on two crucial parameters: rheology behaviour of the resist and demould characteristics. Another important factor for imprinting is the imprint time, which has been shown to scale linearly with the viscosity of the imprinted material and quadratically with the pattern size of the master according to the squeeze flow model [149]. For a given pressure the imprint time is thus significantly longer for milli- and micropatterns than for nanopatterns. Larger features on the master also require displacement of the resist over large distances which is a complicating factor [195]. Properties of an ideal UV NIL resist are low viscosity, low surface tension, good adhesion to the substrate, fast cross-linking speed, and high mechanical strength. Rapid advancements in NIL has stimulated research towards development of new NIL materials [149, 196, 197].

The photoresist SU8 is a promising polymer in MEMS that can also remain as a part of the functional micro-device [198], and was employed in the previous chapter for aperture fabrication by 3D laser lithography. Because the resists normally used with UV-NIL are oligomers that are of low viscosity in their uncured state, permitting imprinting at low pressure, using a conventional resist such as SU8 necessitates modifications of the imprinting process. SU8 imprinting has been performed at elevated temperatures of >60 ^{O}C, above the glass transition temperature of this resist [190, 199]. The low glass transition temperature together and the good formability of un-cured SU8 are favourable for imprint lithography [200]. Nonetheless, a lower temperature for imprinting with UV-NIL would reduce stress in the SU8 layer and degradation of the surface of the master. Challenges associated with imprinting in SU8 have been the subject of various studies [190, 201-204].

5.2 Grayscale lithography

Another parallel lithography approach is graytone or grayscale lithography which was introduced in 1994 as an inexpensive and one-step UV lithographic process [205-207]. It provides considerably higher throughput than direct writing methods and also a higher precision compared to multistep lithography. This technique involves localized modulation of the UV intensity received by the photoresist layer by using special masks, called grayscale masks, which contain patterns that affect the transmission of UV light [158]. A variable UV light intensity across the resist surface gives multiple depths of exposed photoresist, and thus different resist heights after development [191] (Figure 54). Sawtooth profile structures for diffractive optical elements [207], 3D microcoils as magnetic sensor [154], microcompressors as turbomachinery applications [156],

deep phase Fresnel lenses [208], spherical microlenses [209], and suspended bridges and cantilevers [210] have all been fabricated by grayscale lithography (examples shown in Figure 55).

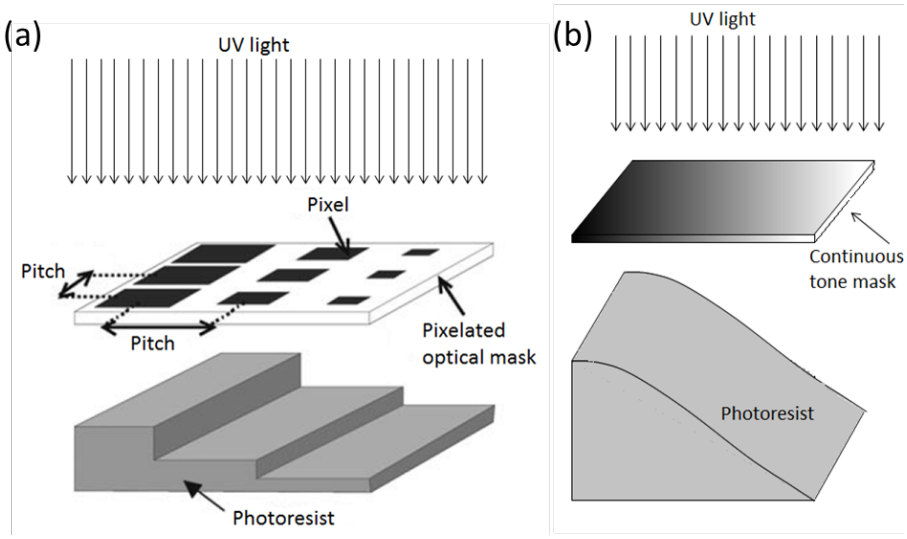

Figure 54: Schematic illustration of the grayscale lithography technique for (a) a three-level grayscale pixelated mask and (b) a continuous-tone mask, and the resulting pattern in positive photoresist. The intensity of UV light received by the resist, and hence the height of the resist remaining after development, depends on the percentage of the opaque area or the density of pixels. In this example, the size of the pixels on the pixelated mask is varied while keeping the pixel density and pitch constant [211].

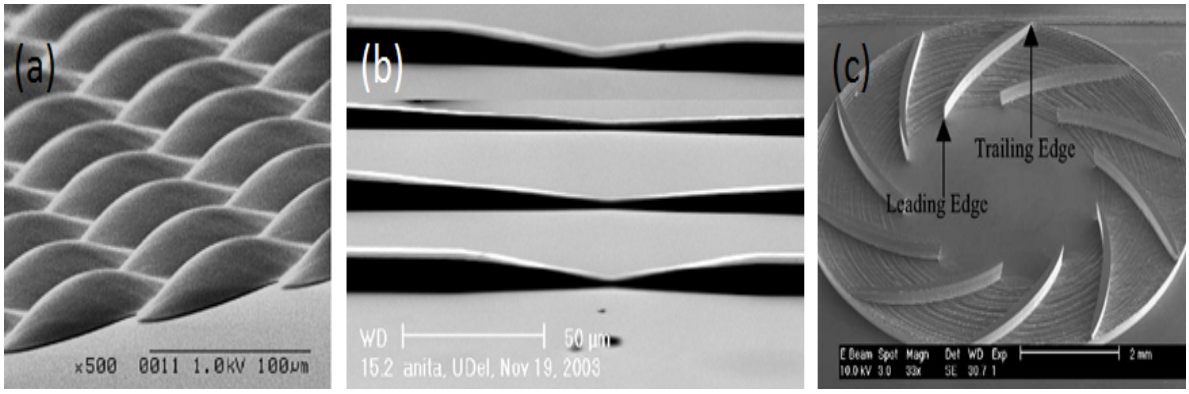

Figure 55: SEM image of structures fabricated using grayscale lithography: (a) spherical microlens array pattern in the positive resist PMER P-LA900PM [209], (b) tapered structures in the resist AZP4620 for efficient coupling from an optical fibre to a chip [212], and (c) variable height micro-compressor etched in silicon using a photoresist patterned with a grayscale lithography as mask [156].

The underlying principle of grayscale lithography concerns the projection optics, which acts as a spatial filter for the UV light diffracted by subresolution pixels on the mask and thus transmit only a diminished UV intensity [158, 206, 213]. Regulation of the UV intensity can be achieved by using either a pixelated, or half-tone, mask or a continuous-tone mask (see Figure 54). Pixelated masks are binary chrome masks with different densities of opaque pixels that are below the resolution of the photolithography tool, on a transparent support such as quartz [158, 191]. Continuous-tone masks consist of high-energy-beam-sensitive (HEBS) glass which has been exposed to controlled doses of a high-energy electron beam to simulate different gray levels by controlling the UV absorption properties of the glass [212, 214]. HEBS glass undergoes a chemical

change upon exposure to high-energy particles that turns it opaque, thus varying glass transparency as a function of high-energy particles energy dose. Although a continuous energy dose variation generates continuous variation of optical intensity of the HEBS mask, fabrication of these masks requires long exposure times [213]. Inexpensive and rapidly reconfigurable continuous-tone masks have also been produced using light absorbing dye in microfluidic channels, where the resist pattern is a function of dye concentration and mask dimensions, as shown in Figure 56. However, this method suffers from various disadvantages such as limitation in fabrication of complex 3D structures, and dependence of the grayscale, i.e. the dye concentration, on the channel length due to diffusion [215]. Pixelated masks are conventional e-beam patterned photomasks that can be realised in two major ways, by either keeping the pitch constant and varying the size of the pixels, or by keeping the size of the pixel constant and varying the pitch. Although the first method requires more patterns to be written by e-beam, thus increasing mask fabrication times, it is more intuitive and easier to attain compared to the second approach due to arrangement of the mask features on a regular mesh [205, 206].

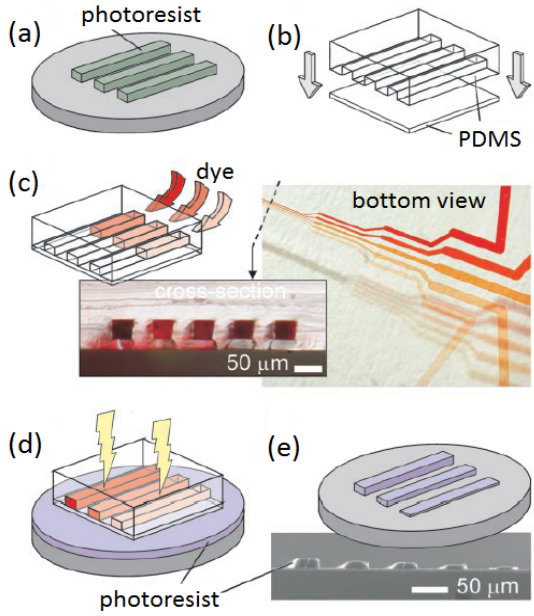

Figure 56: Schematic illustration of the fabrication of a microfluidic dye based grayscale mask. Casting of resist pattern on a wafer (a) gives a PDMS replica which is (b) bonded to a thin layer of PDMS. (c) Microchannels are filled with dye at the desired concentration and (d) placed bottom down on the resist film for UV exposure. (e) The variable-height resist pattern is obtained after development of the resist [215].

The vertical resolution, i.e. the smoothness of the contour of the surface, of this technique is limited by the number of the gray levels that can be realized. For pixelated masks, the vailability of only a finite number of pixel sizes due to mask writing limitations allows only a finite number of gray levels. Hence the vertical resolution provided by pixelated mask is much lower than that of a continuous tone mask. Nevertheless, the vertical resolution for pixelated masks has been demonstrated to be enhanced by the use of a double-exposure technique which combines grayscale lithography with multiple-step photolithography [158]. Multiple-step lithography is

another approach for high throughput fabrication of 3D structures that uses conventional lithography tools. However, the use of multiple masks and issues with alignment make it a tedious process. The time consuming and cost ineffective process of designing, writing and testing grayscale masks for a given set of surface shapes and specific resists has rendered grayscale lithography simulations an indispensable tool [205, 206]. Software pacakages based on a variety of algorithms have been developed to simulate profiles of resists after exposure through a grayscale mask. However, a different mask is still required for each new pattern, which makes grayscale mask design a tedious and costly process. Recent advancements in MEMS technologies have imparted flexibility to grayscale mask design through digital micro-mirror mask technology, where a software-controlled array of micro-mirrors can be rapidly reconfigured to control the amount of time light is reflected onto the resist by an individual micro-mirror [209, 210].

5.3 Materials and methods

5.3.1 Imprinting in SU8

The two protocols proposed and investigated in this work for imprinting in SU8 are shown in Figure 57. One protocol used a UV transparent flexible master from perfluoropolyether, while the other directly used a glass substrate patterned with reflown positive resist as the master. Double coating of AZ9260 (Microchemicals) was performed to get a film thickness of 40 µm. The first layer of AZ9260 was spun at 1000 rpm for 40 seconds and soft baked at 100 ^{O}C for 80 seconds and the second layer was spun at 1000 rpm for 50 seconds and baked at 110 ^{O}C for 240 seconds. The resist was exposed through a mask with circular features at 1150 mJ using a EVG 620TB (EVG, Austria) mask aligner and developed for 6 minutes using a 1:2 (v/v) mixture of AZ400K (Microchemicals) and deionised water. An AZ9260 layer of 22 µm thickness was obtained by spinning the resist at 800 rpm for 30 seconds and baking at 110 ^{O}C for 3 minutes. The substrate was exposed at 550 mJ using the EVG 620TB mask aligner and developed in 1:4 v/v AZ400K/water for 6 minutes. AZ9260 was reflown by baking the wafer at 130 ^{O}C for 3 minutes. The surface of the glass substrate patterned with AZ9260 was made hydrophobic by treatment with (3-aminopropyl)triethoxysilane. The substrate was placed in a vacuum desiccator along with a glass slide with a drop of the silane. The chamber of the desiccator was pumped down for 5 minutes, and the substrate was kept under vacuum for 45 minutes to be exposed to the silane vapour.

For fabrication of the UV transparent flexible master (Figure 57a), a primer was spun on a clean glass wafer and baked for adhesion promotion of the polymer. Perfluoropolyether (PFPE) polymer was poured onto the resist-reflown substrate and the glass wafer coated with primer

was placed on top. The stack of these glass wafers was exposed using the EVG 620TB mask aligner to obtain the UV transparent flexible master.

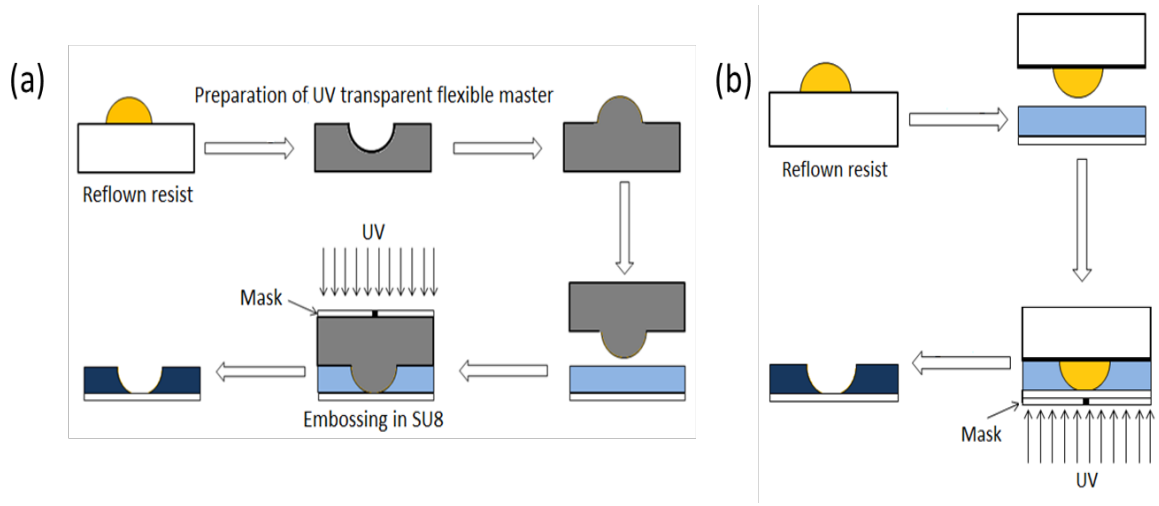

Figure 57: Schematic illustration of two proposed protocols for imprinting in SU8 to obtain shaped apertures. (a) Positive resist AZ9260 is reflown and double casting gives a replica of reflown resist which then acts as the master. Casting is done using perfluoropolyether. SU8 is heated above its glass transition temperature of 90 ^{O}C and the master is imprinted onto the resist to transfer the shape. Exposure is done through a mask that has a circular feature which should coincide with the centre of the hemispherical pattern on the master to give an aperture. (b) In an alternative approach, a positive resist AZ9260 patterned substrate acts as the master which makes contact with SU8. Exposure is done through a mask with a circular feature which should coincide with the centre of the hemispherical pattern on the master to give an aperture. The yellow protrusion is the reflown positive resist AZ9260, the UV transparent flexible master of perfluoropolyether is shown in grey, the light blue layer is non-cured SU8 and the dark blue patterned layer is polymerised SU8 as an aperture geometry.

Glass substrates with a diameter of 4" and a thickness of 700 µm were first cleaned in fuming nitric acid, followed by cleaning with acetone and isopropanol, and then dried overnight at 210 ^{O}C. Ti prime (Microchemicals) was spin-coated at 3000 rpm for 30 seconds and soft baked at 120 ^{O}C for 3 minutes to act as adhesion promoter for SU8. SU8-3050 (Microchem) was spin-coated at 3000 rpm for 30 seconds and soft baked at 95 ^{O}C for 15 minutes to obtain a thickness of ~50 µm. An EVG 501 bonder (EVG, Austria) was used for patterning SU8 according to Figure 57, with the following parameters for imprinting: temperature 90 ^{O}C, force 490 N, pressure 10^{-2} mbar, and time 30 seconds. A substrate coated with SU8 was heated to 90 ^{O}C, the AZ9260 master (Figure 57b) or the PFPE master (Figure 57a) was placed on top of it and force was applied for the given time. The stack of master and SU8 resist was exposed at 320 mJ after which the master was demoulded from the SU8 sample. The SU8 substrate was baked at 65 ^{O}C for 1 minute and at 95 ^{O}C for 4 minutes to crosslink the resist and was subsequently developed in EC solvent (Microposit) for 5 minutes and rinsed with isopropanol.

5.3.2 Grayscale lithography

Glass substrates of 4" diameter with a thickness of 700 µm were cleaned in fuming nitric acid, followed by cleaning with acetone and isopropanol, and then dried overnight at 210 ^{O}C. Ti prime was spin-coated at 3000 rpm for 30 seconds and soft baked at 120 ^{O}C for 3 minutes to act as adhesion promoter for SU8. SU8-3050 (Microchem) was spin-coated at 3000 rpm for 30 seconds and soft baked at 95 ^{O}C for 15 minutes to obtain a thickness of ~50 µm. Exposure was performed at variable energies in an EVG 620TB mask aligner to obtain a contrast curve that shows the variation of the SU8 resist thickness with the energy dosage. Exposure was done from the glass substrate side, not from the resist side of the substrate, to ensure that the resist was still attached to the substrate after development. After exposure, the SU8 substrate was baked at 65 ^{O}C for 1 minute and at 95 ^{O}C for 4 minutes to crosslink the resist and was developed in EC solvent for 5 minutes, followed by rinsing with isopropanol.

Dry film resist, TMMF S2055 (Tokyo Ohka Kogyo Co Ltd, Japan), was laminated on an acid-cleaned glass substrate, a 4" wafer of 700 µm thickness or a 30 mm wafer of 170 µm thickness, at 70 ^{O}C at a lamination speed of 1 m/min as shown in Figure 58. After lamination, the substrate was cut out from the clean room paper using a razor blade or a scalpel. The protective polyester (PET) covering on TMMF resist was removed from the resist and the substrate was soft baked at 60 ^{O}C for 5 minutes. The exposure step was performed at various energies in an EVG 620TB mask aligner. Following UV exposure, post baking was done at 90 ^{O}C for 3 minutes and at 150 ^{O}C for 2 minutes. The TMMF resist was developed in EC solvent for 7 minutes without agitation. For release of the patterned TMMF layer, LOR 7B was used as sacrificial layer (see section 4.2.4).

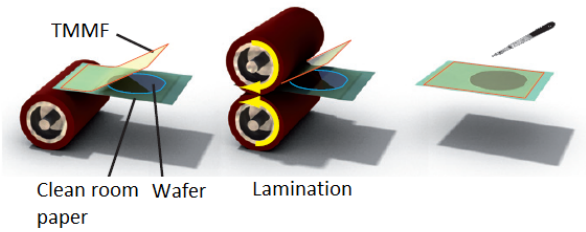

Figure 58: Schematic illustration of TMMF dry film lamination. The TMMF sheet protected by PET film was placed on top of cleanroom paper carrying the wafer substrate and was laminated between the two rubber-coated rolls that are heated to 70 ^{O}C. The laminated wafer was manually cut out using a scalpel or razor blade [216].

Grayscale masks were designed and fabricated by Dr Kian Shen Kiang using GenISys software (Munich, Germany) and the e-beam facility of the Southampton Nanofabrication Center. The final grayscale mask used in this work to define shaped apertures consisted of 6 gray levels each represented by a concentric ring (Figure 59c). The innermost circle had a diameter of 80 µm representing the diameter of the aperture and the diameters of concentric circles for producing

the shaped sidewall were 140 µm, 200 µm, 260 µm and 320 µm. The last zone was a square of 400 × 400 µm which represented the area within which the shaped sidewall of the aperture was obtained. The pixel size of the rings was 750 nm, 600 nm, 500nm, 400 nm, 300 nm and 200 nm, from the centre to the outside of the mask) with a constant pitch of 1 µm. The resist was exposed through the grayscale mask either from the glass substrate side of the glass-resist stack (Figure 59a) or from the resist side (Figure 59b). After the first exposure, second exposure with the same energy was done under another mask in such a way that the grayscale mask feature for shaped aperture area of the resist was covered by an opaque area on the mask, while the resist outside this area was under the transparent region of the mask to further crosslink the septum.

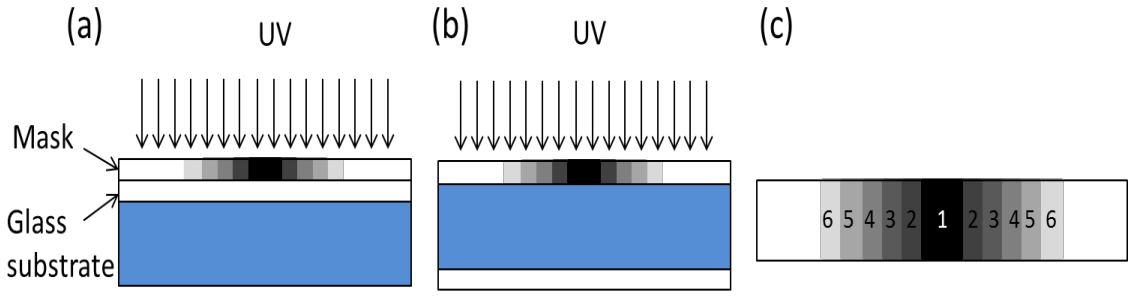

Figure 59: Schematic illustration for the use of the grayscale mask in two different orientations for exposing SU8 or TMMF resist. (a) The resist layer is exposed from the glass substrate side, or (b) the resist layer is exposed from the resist side. (c) Schematic illustration of the cross section of a single grayscale mask feature for producing a shaped aperture, showing 6 different zones that each correspond to a particular gray level.

5.4 Results and discussion

5.4.1 SU8 imprinting

It was shown in Chapter 4 that once the slice and hatch distance had been optimised for a given laser power and scan speed, a change in aperture geometry only required a change in the CAD-generated coordinate file. But the flexibility of aperture fabrication by two-photon lithography comes at the cost of a long build time of ~12 hour per aperture. The UV imprinting method was therefore investigated as a non-laser-lithography technique to achieve high-throughput production of septa with shaped apertures. Since imprint lithography relies on the direct mechanical deformation of a resist layer by the topology of a patterned master, with subsequent UV polymerisarion of the resist, a master with hemi-spherical features was required to obtain apertures with a triangle-shaped cross-section (Figure 57).

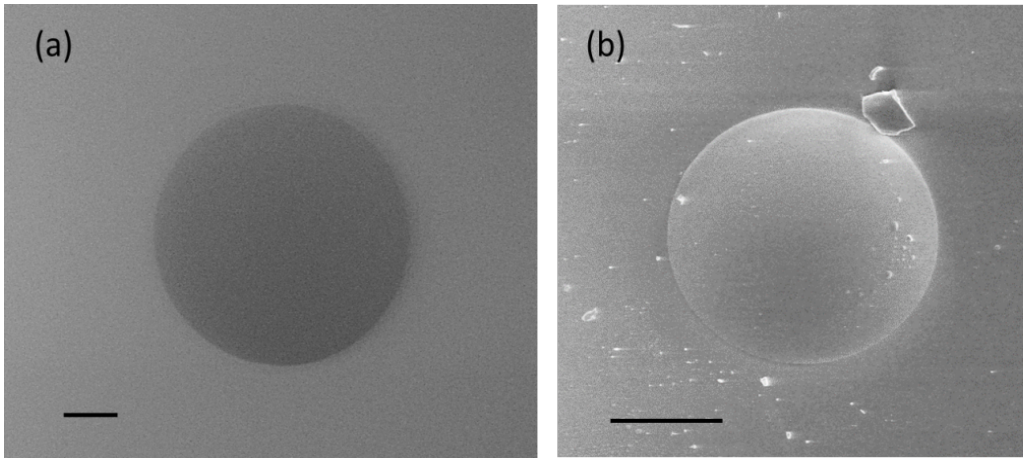

Figure 60: SEM images of positive resist before and after resist reflow: (a) AZ9260 cylinder on a glass wafer after exposure with a circular mask feature and after developent, and (b) after baking the substrate at 130 ^{O}C, which converts the resist cylinder to a resist hemisphere. The width of the base of the resist has been reduced due to evaporation of solvent in the resist during baking. The scale bars are 200 µm.

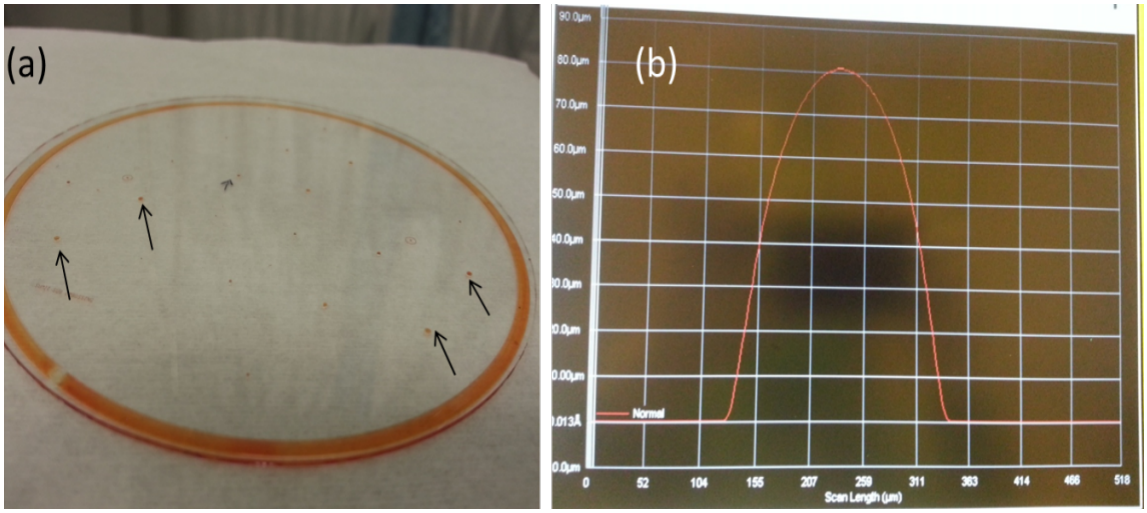

Figure 61: (a) Photograph of a glass wafer with AZ9260 which has been reflown by baking the substrate at 130 ^{O}C . Red dots on the wafer are the AZ9260 cylinders which have been reflown, few of which are pointed out by arrows. (b) Surface profile of 225 µm reflown AZ9260 pattern. The height of the pattern before reflow was 40 µm, which had increased to 80 µm after reflow.

To obtain a master with hemispherical features, thermal softening, or resist reflow, of the positive resist AZ9260 was employed. This process has been widely used in fabrication of microlenses for integration of optical elements [217-219] and fabrication of valves in microfluidics [220]. Figure 60b shows an SEM image of a AZ9260 cylinder after the thermal reflow process during which the solid resist is melted, resulting in a hemispherical shape due to surface tension acting on the original cylindrical pattern [221]. The smoothness of the reflown structure depends on the applied temperature, with higher temperatures giving a higher reflow rate because of an increase in resist fluidity [222]. Since the volume of the resist, except for some solvent evaporation, remains constant while heating, the height of the structure is changed due to the change in shape of the structure [223]. It was found that the height of a cylindrical feature having

a diameter of 225 µm increased from 40 µm to 80 µm after thermal reflow. The evaporation of the solvent in the resist caused constriction of the width of the base of the resist pattern [224], a phenomenon which has also been used for increasing the resolution of optical lithography technique to sub 0.18 µm due to its simplicity [225, 226].

The glass substrate with hemispherical features provided a template for imprinting triangle-shaped apertures in a layer of SU8 resist. According to the process flow shown in Figure 57a, a replica of the original substrate with hemispherical features of AZ9260 was made using the UV transparent polymer perfluoropolyester (PFPE), which would act as a master for imprinting. This flexible polymer master, adhered to a second glass substrate, is chemically inert and has a low interfacial surface energy that reduces irreversible adhesion to the patterned resist [191], here a layer of SU8. The surface of the AZ9260 resist patterned substrate was treated with a hydrophobic silane (section 5.2.1) to lower its surface energy, facilitating demerging of the cross-linked PFPE and AZ9260 layers. However, it was found that full area demerging could not be achieved, producing PFPE master with defects (Figure 62). These defects could either be caused by poor adhesion of PFPE to the glass substrate or by too strong adhesion of PFPE to the AZ9260 resist. However, the use of silane as anti-stick coating and of primer to increase the adhesion of PFPE to the clean glass wafer should have prevented such issues.

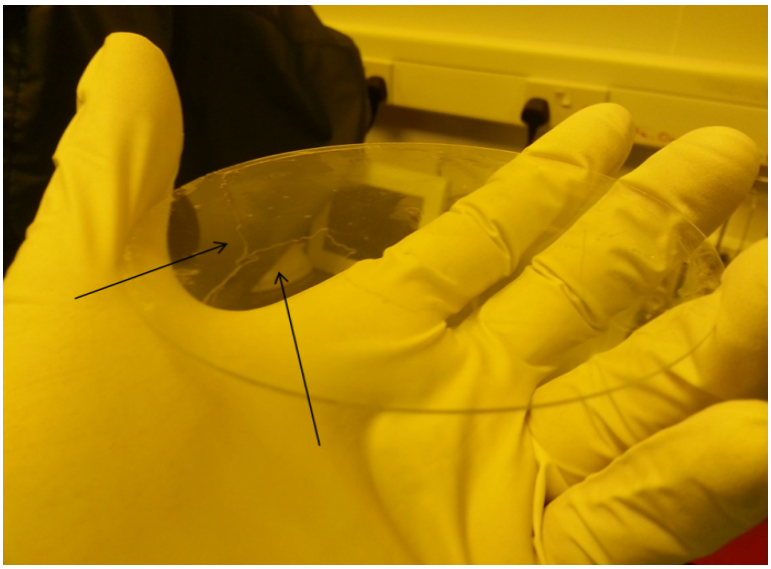

Figure 62: Photograph of a PFPE master, cast from an AZ9260 substrate. The arrows point to defects in this master, where PFPE polymer had stuck to the reflown AZ9260 resist glass substrate during demerging.

Due to difficulties involved with the creation of a defect-free flexible master of PFPE, a modified approach was utilised where the original substrate of reflown AZ9260 on glass was used directly for imprinting (Figure 57b). As shown in Figure 63, bubble defects were observed in the SU8 layer after imprinting with the AZ9260 master. Such defects have also been seen by other groups [199, 200]. Since the master was brought into contact with SU8 at atmospheric pressure, it

is likely that air was entrapped, which would lead to bubble defects, although these can also arise due to the non-perfect flatness of the master and the resist layer [192]. The EVG 501 bonder allows the use of flags for separating the master from the resist, which can be brought into contact when a sufficiently low pressure is realized to avoid bubble defects. However, this method could not be applied because the flags were sticking to the SU8 layer that was heated to 90 ^{O}C, which prevented the master from coming into contact with the resist layer. Once the imprinting process was finished and the AZ9260 and SU layers were demerged, glass-detached segments of AZ9260 were also found stuck in the SU8 film, which suggests that AZ9260 is too soft a master material.

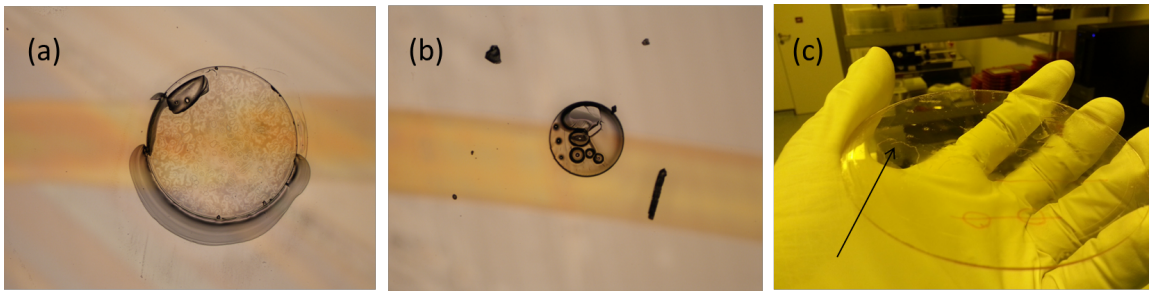

Figure 63: Optical micrographs (a,b) and photograph (c) of the features imprinted in SU8 using the modified approach from Figure 57b where a glass substrate with reflown AZ9260 was used directly as a master for imprinting SU8. (a) Optical micrograph showing imprinted feature in SU8, (b) optical micrograph showing entrapment of air bubbles, and (c) photograph of an imprinted SU8 substrate, with an arrow pointing to an area.where the AZ9260 resist had stuck to the SU8 during demerging.

5.4.2 Grayscale lithography

5.4.2.1 TMMF: a low-contrast resist

Given the various issues encountered with imprint lithography, grayscale lithography was investigated as an alternative method for mass production of shaped apertures. The first step in the grayscale lithography process is the design of the grayscale mask, which requires knowledge of the post-development resist thickness as a function of the exposure energy dose, a relation referred to as the resist contrast curve. The contrast of a resist, defined by the slope of the decay of the resist thickness with a decrease in energy dose, is an ability to distinguish between light and dark portions of the mask[5]. SU8 was exposed with various energy doses (section 5.2.2) and the thickness of the resist after development was measured with a surface profiler. The resulting contrast curve for SU8, depicted in Figure 64, shows two trends: an increase in the thickness of SU8 with a decrease in energy and a sharp decrease in SU8 thickness for an energy dosage <60 mJ. The latter trend represents the high-contrast property of SU8, i.e. below a certain energy

[5] Microchemical website, Available at http://www.microchemicals.com/technical_information/exposure_photoresist.pdf. Date accessed 01/12/2013

dosage, the resist should not polymerise. The former trend is accredited to the problem of swelling in weakly cross-linked SU8 which can cause absorption of developer solvent by the resist [227, 228]. It should be noted that this problem was not observed with two-photon polymerisation because SU8 was completely cross-linked by voxel exposure.

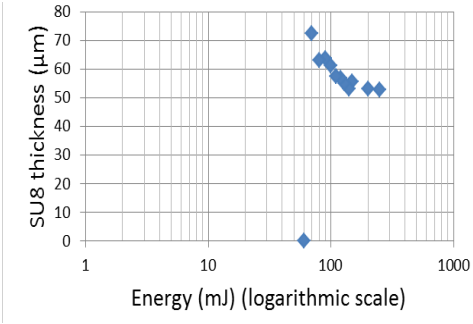

Figure 64: Contrast curve for SU8, obtained by measuring the resist thickness with a surface profiler after exposure and development. The resist was exposed from the glass substrate side of the glass-resist stack. The SU8 thickness increased with a decrease in energy until it reached a dose of ~60 mJ below which polymerisation did not take place. This increase in thickness is due to the swelling of barely cross-linked SU8, while the sharp decrease of the thickness with decrease in energy is typical for a high-contrast resist.

The solvent swelling of SU8 discourages its use in grayscale lithography as it can cause distortion of the shape and size of the structures. It could also cause lift-off of the structures from the substrate due to strain at the interface between the glass substrate and the swollen SU8. Even though the swelling problem can be avoided by hot spin development [227], the high contrast of SU8 renders it of little use in creating grayscale features, which are typically created with low-contrast positive resists [213]. Therefore the epoxy based dry-film resist TMMF was examined. This negative-tone resist has similar properties as SU8 including a low dielectric constant and good mechanical and chemical stability. Experiments at various exposure energies established that TMMF is a low-contrast resist that does not exhibit swelling during development (Figure 65), making it a suitable resist for grayscale lithography.

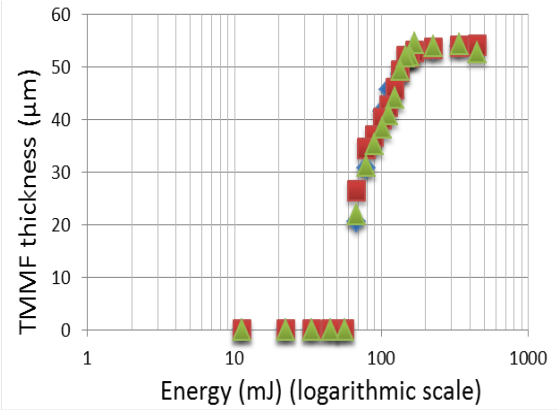

Figure 65: Contrast curve for TMMF, obtained by measuring the resist thickness with a surface profiler after exposure and development. The resist was exposed from the glass substrate side of the glass-resist stack. The gradual decrease in resist thickness with decreasing energy depicts the low-contrast property of TMMF. The green, red and blue data points represent three independent experiments.

5.4.2.2 Fabrication of shaped apertures in TMMF with a grayscale mask

Having obtained the contrast curve for TMMF, a pixelated chrome grayscale mask was designed with GenISys software, with a constant pixel pitch of 1 µm and a pixel size that varied from 750 nm to 200 nm, to regulate the amount of radiation received by the resist [205, 206]. Since a change in the resist or resist process would change the contrast curve which is used for designing the mask, a new mask design would be required if the resist would be changed. Figure 66 shows SEM images of a pixelated mask consisting of multiple rings of different pixel size for the creation of a triangle-shaped aperture in TMMF resist. As discussed in section 5.1.2, the smoothness of the wall of the aperture depends on the number of different gray levels in the mask, which is limited due to mask writing limitations [158]. The final mask designed for this work had six rings (Figure 66c), as determined by the smallest feature size (200 nm) that could be achieved in the Southampton Nanofabrication Centre.

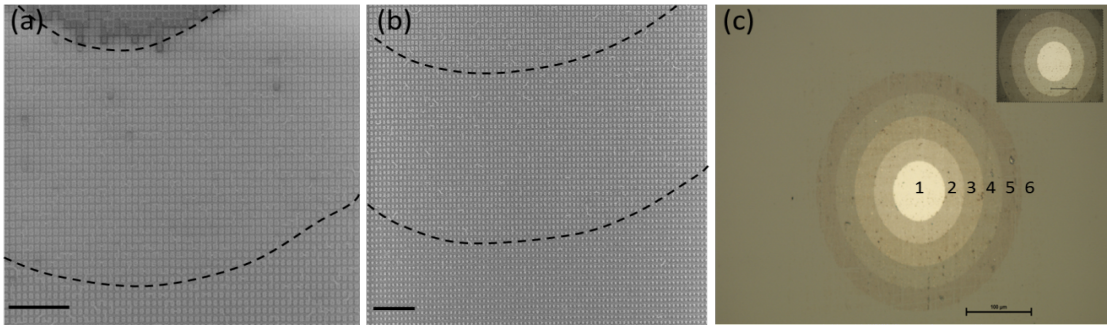

Figure 66: Images of a pixelated grayscale mask, designed using the TMMF contrast curve, to define shaped apertures. (a,b) SEM images of the mask,showing various pixel sizes with a constant pixel pitch of 1 µm. The scale bars are 10 µm. (c) Optical micrograph of the final design of the grayscale mask. Numbers 1 to 6 represent 6 rings, each with a different gray level, obtained by variation of the pixel size from 750 nm for ring 1 to 200 nm for ring 6., The scale bar is 100 µm.

For the mask shown in Figure 66, the ideal structure in the resist should be an aperture with a triangle-shaped cross-section. Triangle-shaped apertures, shown in Figure 67 could indeed be produced in TMMF by exposing the resist through the grayscale mask, from the glass substrate side of the glass-resist stack. The diameter of the aperture was dependent on the diameter of the centre ring, ring 1 in Figure 66, of the grayscale mask, the pixel density of which was high enough to not cause the polymerisation of the resist. The diameter of the outermost ring of the mask determined the point where the tapering of the aperture wall begins. The mask was completely transparent outside these rings, enabling polymerisation of TMMF as 15 × 15 mm sheets, with a shaped aperture at the centre position. For a specific mask, Figure 67 also shows the dependence of the slope of the tapered side-wall on the exposure dose. With an increase in energy, the angle of the slope increased due to increased cross-linking of the resist, necessitating optimisation of the energy dose to obtain an aperture wall tip thickness of approximately 2 µm, as fabricated

using 3D laser lithography (Figure 46). Alternatively, a new grayscale mask could have been designed and fabricated to give this tip thickness at a specified energy dose. For exposure from the glass substrate side, the energy dose for a given shape was found to be almost doubled when LOR 7B was used as a sacrificial release layer, indicating that LOR 7B significantly absorbs at the exposure wavelength of 365 nm.

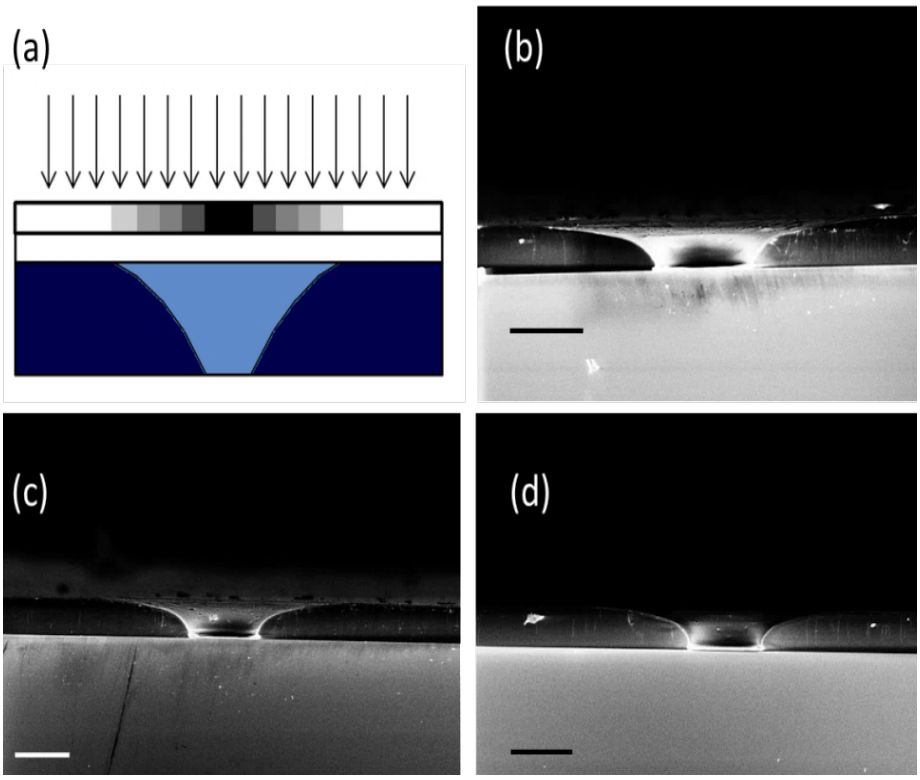

Figure 67: (a) Schematic illustration of the exposure of TMMF resist through a grayscale mask from the glass substrate side, and the cross-sectional TMMF profile expected after exposure. The light blue area represents uncured resist and the dark blue areas represent cross-linked resist. (b-d) SEM cross-section images of shaped apertures fabricated in TMMF using a pixelated grayscale mask and exposure at (b) 180 mJ, (c) 200 mJ, or (d) 210 mJ, through the glass substrate which has a thickness of 700 µm. Varying the energy dose changed the shape of the aperture sidewall. The scale bars are 100 µm.

Since discrete numbers of gray levels were used, the sidewall of the aperture should have been step-like, with the resist thickness of each step being determined by the gray level of the corresponding area of the mask [211]. As a smooth sidewall of the aperture was obtained when the resist was exposed through a 700 µm thick glass substrate (Figure 67), further experiments were carried out to investigate why discrete steps were not observed. It was found that when the resist was exposed through a thinner glass substrate, with a thickness of 170 µm, the aperture wall did have a step-like profile, as shown in Figure 68. The thickness at the tip of the aperture was close to 2 µm, as required, when the resist was exposed through the 170 µm thick glass, whereas for exposure through 700 µm thick glass it was 20 - 30 µm. These observations suggest that when the light passes through a thicker glass substrate, it undergoes deflection from

particular grayscale areas into adjacent areas, causing a more fine-scaled intensity gradient and an increase in exposure intensity for each area.

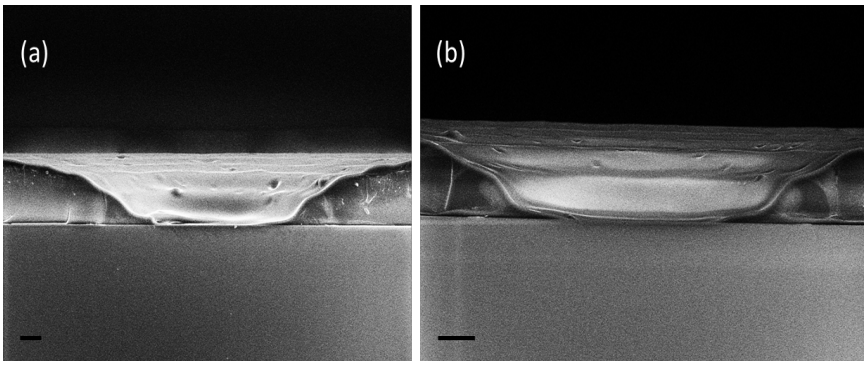

Figure 68: SEM cross-section images of shaped apertures fabricated in TMMF using a pixelated grayscale mask and exposure from the side of the glass substrate, which is 170 µm thick, at an energy dose of (a) 180 mJ or (b) 170 mJ. Varying the energy dose changes the shape of the sidewall of the aperture. Areas of discrete thickness ranges, corresponding to the rings of different pixel sizes on the grayscale mask, are visible. The scale bars are 20 µm.

The dependence of the smoothness of the aperture wall on the thickness of the glass substrate led to an experiment where the TMMF was exposed, through the grayscale mask, from the resist side, hence avoiding the passing of light through the glass. The shape of the sidewall was expected to be the inverted version of the aperture depicted in Figure 68a, i.e. with the aperture tip at the top of the resist layer (Figure 69a). However, as shown in Figure 69b, a beak-shaped aperture was obtained. One of the reasons for obtaining this unexpected shape could be backscattering of UV light from the surface and/or the bottom of the substrate which would produce an interference pattern that could potentially give rise to a beak-shaped intensity profile. However, given that glass substrates were used, such a pronounced reflection from the substrate-resist or substrate-air interface is unlikely. It could also be argued that the beak geometry results from sagging of the aperture tip downwards into the resist layer. However, increasing the post baking time to further cross-link the resist still produced beak-shaped apertures.

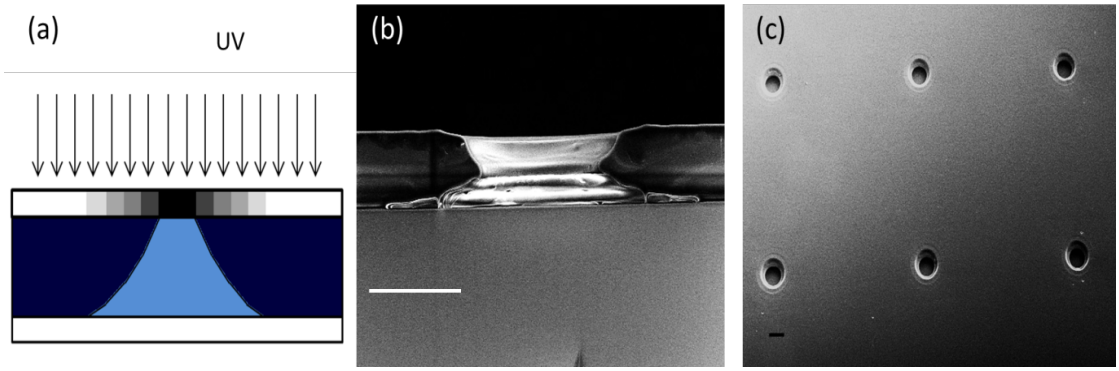

Figure 69: (a) Schematic illustration of the exposure of TMMF through a grayscale mask from the resist side, and the cross-sectional shape expected for this exposure configuration. The light blue area represents uncured resist while the dark blue areas represent cross-linked resist. (b) SEM cross-section image of a beak-shaped aperture and (c) SEM top-view image of a 3 × 3 aperture array obtained in TMMF using a pixelated grayscale mask in this exposure configuration. The scale bars are 100 µm.

Fabrication technique	Aperture shape / diameter designed (μm)	Aperture diameter obtained (μm)	Resist thickness at the tip (μm)
Two-photon lithography	beak/80	88	2.5
Two-photon lithography	triangle/80	90	3
Grayscale lithography	beak/80	90	5
Grayscale lithography	triangle/80	76	3

5.5 Conclusions

To address high-throughput production of shaped apertures, UV imprint lithography (UV NIL) and grayscale lithography were reviewed and experimentally investigated in this chapter. Since UV NIL is based on mechanical deformation of the resist, which is cross-linked with UV radiation while the master and resist are still in contact, it was assumed that triangle-shaped apertures could be obtained if a master with hemispherical structures was used (formed by thermal reflow of a positive resist AZ9260). Although nanoimprint lithography has been widely used for patterning of nano-features in resists, this approach was abandoned for aperture fabrication due to various problems such as the presence of bubble defects in the resist and localized incomplete master-resist demoulding. In grayscale lithography the UV intensity in the resist layer is modulated to produce a 3D structure. The key component of this lithography method is the grayscale mask, the design of which requires knowledge of the relationship between UV intensity and resist thickness. It was demonstrated that SU8, the resist in which shaped apertures were defined by 3D laser lithography (Chapter 4) behaves as a high-contrast resist and that is suffers from solvent swelling, limiting its suitability for grayscale lithography. However, the epoxy-based dry film resist TMMF, which has similar mechanical, chemical and electrical properties as SU8, was demonstrated to be a suitable choice because of its low contrast and absence of solvent swelling. A grayscale mask was designed and fabricated (by Dr Kian Shen Kiang) based on the obtained contrast curve for TMMF. The mask contained six concentric circles, each with a different gray scale value originating from a different pixel size. Grayscale lithography with this mask produced triangle-shaped apertures when the TMMF layer was exposed through the glass substrate. The smoothness of the aperture walls and the thickness of the aperture tip were found to depend on the thickness of the glass substrate, with thinner substrates resulting in an aperture tip thickness of 2 μm. Surprisingly, when the TMMF layer was exposed from the resist side, beak-shaped apertures were produced, the reason for which was not fully understood. Having successfully produced shaped apertures with a high-throughput lithography method, the

next step was the systematic evaluation of lipid bilayers suspended in these shaped apertures, which is the subject of the next chapter.

Chapter 6 Evaluation of bilayer stability in shaped apertures

The issue of fragility of aperture-suspended lipid bilayers and the proposed design of shaped apertures in photoresist for bilayer stabilisation has been discussed in Chapters 1, 2 and 3. Following the successful fabrication of the desired triangle-shaped and beak-shaped apertures in SU8 and TMMF by two-photon lithography and grayscale lithography as described in Chapters 5 and 6, the next step was to test these apertures for bilayer stability. To support the argument of enhancement in bilayer stability due to a change in aperture shape, control apertures with a conventional cylindrical geometry or with a blunted aperture tip were also tested. The results of lifetime and mechanical stability measurements of bilayers suspended in the various apertures are presented and discussed in this chapter.

6.1 Materials and methods

6.1.1 Lipid bilayer formation

The phospholipids, 1,2 dioleoyl-*sn*-glycero-3-phosphocholine (DOPC), 1-palmitoyl-2-oleoyl-*sn*-glycero-3-[phosphor-rac-(1-glycerol)] (POPG), diphytanoylphosphatidylcholine (DPhPC),and 1,2-dioleoyl-*sn*-glycero-3-phosphoethanolamine (DOPE) were purchased from Avanti Polar Lipids (Alabaster, AL, US). Alamethicin ion channel was purchased from Sigma Aldrich (UK). Millipore deionized water was used for all aqueous solutions. All experiments were carried out at room temperature. Teflon (polytetrafluoroethylene, PTFE) sheets of 50 µm thickness were purchased

from Goodfellow Cambridge Ltd (UK) and an aperture was punched in these sheets with a 5 µm tip needle. A septum, either a sheet of SU8, TMMF or Teflon, with an aperture at the centre position was clamped between two chambers of 1.25 ml volume such that it was in contact, with 5 × 7 mm area, with the aqueous phase of both chambers, which were machined from Teflon in the mechanical workshop (Figure 70).

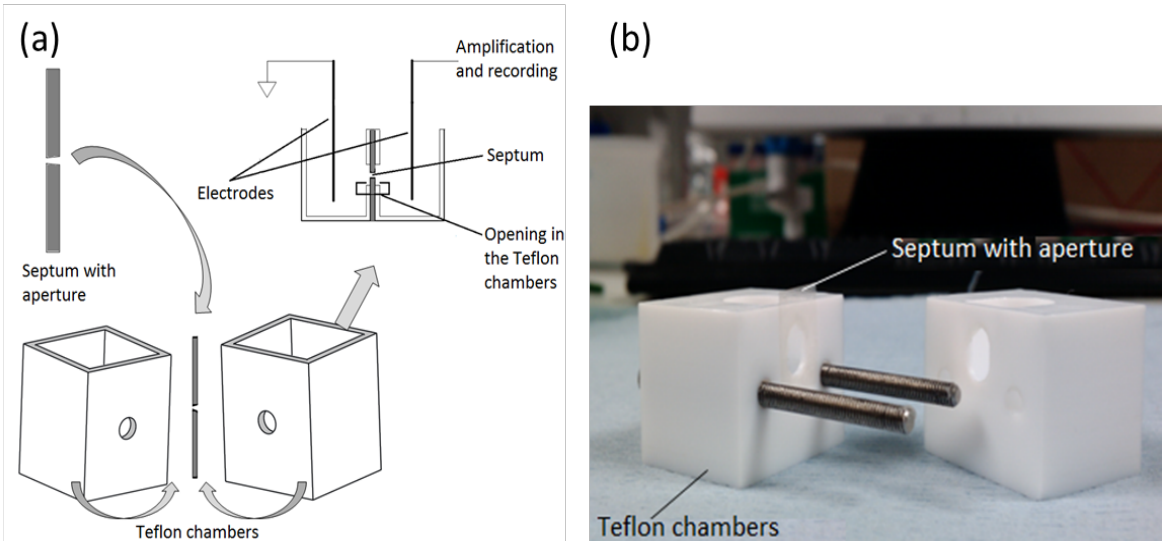

Figure 70: (a) Schematic illustration of clamping of the septum in the Teflon chambers for the formation of electrically accessible suspended bilayers that are vertically oriented. The septum was sealed with Vaseline petroleum jelly to the surface of the Teflon chambers such that the aperture was in the middle of the opening in the chamber. (b) Photograph of the Teflon chambers with a SU8 sheet as septum.

Aperture-suspended bilayers were prepared with the painting or the folding method. For the painting method, lipids were dissolved in decane or nonane at a total lipid concentration of 20 mg/ml by solvent solubilization of a mixed lipid film, obtained by mixing and drying of lipid stock solutions in chloroform using a vacuum desiccator (Nalgene, Thermo Scientific, UK). The lipid-solvent solution was painted on the aperture with a Sable 0000 paint brush, and the buffer-air interface of the buffer solution in each compartment was raised and lowered over the aperture to promote solvent draining and bilayer formation [137]. For the folding method, the aperture was pretreated with 5% hexadecane in hexane. Lipids in volatile solvent, chloroform or hexane, (~7-10 µl of a 20 mg/ml solution or 5.0-7.5 µl of a 40 mg/ml solution) were placed on top of the buffer solution in each compartment and the solvent was allowed to evaporate. The buffer-air interface was then raised and lowered in both compartments over the aperture until a bilayer was formed by monolayer opposition. Typically, a lipid bilayer was formed within 10 aspiration cycles in shaped aperture using monolayer folding technique for any given lipid. The peptide alamethicin was introduced in ethanol in both of the two aqueous chambers giving a concentration of 10 ng/ml and 0.0375 ng/ml respectively.

6.1.2 Capacitance and current measurements

The bilayer cell consisting of the Teflon chambers with a clamped septum was placed in a Faraday cage to minimise electromagnetic interferences. Silver/silver-chloride (Ag/AgCl) wire electrodes were placed in the two aqueous compartments of the Teflon bilayer cell and were connected to one of these two electrical recording systems used for measurement of the bilayer capacitance and the current flowing through the ion channel: (i) a high sensitivity ID562 BLM amplifier (Industrial Developments Bangor, Bangor, UK) with 16 bit, 6036E DAQ card (National instruments, TX, US) for data acquisition at 5 kHz with a home build LabVIEW user interface (National Instruments, TX, US), and (ii) Axopatch 200B amplifier and Axon Digitdata 1440A digitizer (Molecular Devices, CA, US) and for data acquisition at 50 kHz using a 5 kHz 8-pole Bessel filter. Bilayer formation was monitored by capacitance measurements. A linear voltage ramp (triangular wave) was applied, the current signal was displayed on a digital oscilloscope, with a square current waveform indicating bilayer formation, and the value of the capacitance was derived from the current amplitude of this waveform. After successful formation of a lipid bilayer, a DC potential of |100-200 mV| was applied to measure the bilayer current. Bilayer traces were analysed and digitally filtered using a 1 kHz Gaussian filter with Clampfit 10.2 software (Molecular Devices, Sunnyvale, US).

6.1.3 Bilayer stability tests

Bilayer formation was monitored with capacitance measurements. All stability tests in SU8 apertures were carried out on bilayers that had a capacitance values within 1 - 1.5× of the expected capacitance value, which was calculated by assuming a specific bilayer capacitance of 0.5 - 0.7 $\mu F/cm^2$ (32, 12). Bilayers with a smaller capacitance and 'leaky' and unstable bilayers with a sealing resistance less than a few tens of GΩ were rejected. During bilayer lifetime tests, the aqueous solutions in the bilayer chamber were not perturbed and evaporation of the aqueous solution was not prevented. After addition of ion channels to the compartment, the bilayer was kept at DC voltage >|100 mV|. The tests for evaluating bilayer mechanical stability involved raising and lowering of the buffer-air interface over the aperture in either compartment. SU8 sheets were also reused by cleaning the debris inside the aperture at low power agitation in an ultrasonic bath sonicator. If the aperture showed signs of wear around its circumference, the sheet was discarded.

6.1.4 Surface treatment of resist septum

Surface treatment of the resist was performed in the Southampton Nanofabrication Center. Although SU8 is moderately hydrophobic with a contact angle of ~70^{o}, its surface was treated to bring its hydrophobicity closer to that of the conventionally used septum material Teflon, which has a contact angle of ~110 ^{o}. SU8 sheets were dipped in a 5% v/v solution of the fluoropolymer Cytop CTL 809M (AGC Chemicals) in solvent and annealed at 80 ^{o}C and 150 ^{o}C for 45 minutes each, which resulted in a Cytop coating of <1 μm thickness. If the aperture was blocked due to the presence of a thin Cytop film in the aperture, the SU8 sheet was sonicated in an ultrasonic bath for 10 seconds to unblock the aperture. This surface treatment method was later replaced with vapor coating of Parylene C (poly-(para-xylylene)) using a Labcoater 2 Parylene Deposition System (Specialty Coating Systems, Indianapolis, IN). The powdered Parylene precursor is vaporized under vaccum and heated to form a dimeric gas. The gas is then pyrolized in a furnace to give its monomeric form, which is introduced into the deposition chamber at ambient temperature for coating the sample surface. Silane A-174 was used for promoting adhesion of Parylene to the photoresist. 10 ml of the silane was applied to the clean room tissue and applied to the inside of the chamber lid. Silane coats all the surfaces inside the chamber before the Parylene deposition begins.

6.2 Results and discussion

6.2.1 Stability of bilayers in apertures in Teflon

The septum material for bilayer formation should be sufficiently hydrophobic to enable draining of excess solvent, have suitable electrical properties, i.e. high resistivity, low dielectric constant and low dielectric loss, be mechanically strong and chemically compatible with cleaning solutions [35, 36]. Widely used septa for bilayer formation are Teflon sheets of 10-50 μm thickness and locally thinned walls of monolithic polystyrene cuvettes [55] and apertures in these polymers are created by relatively coarse methods such as mechanical punching, microdrilling or electrical spark ablation [35, 91, 116]. Initial experiments for bilayer formation were done with apertures made in Teflon sheets due to the ease of obtaining a punched aperture in a commercially available Teflon sheet. The measurement of the background capacitance from the Teflon septum involved clamping a sheet of 50 μm thickness, without an aperture, in the bilayer cell, which gave a capacitance of 12 pF. Bilayers formed in needle-punched apertures, with a diameter of ~130 μm, in a Teflon septum were stable for only < 3 hours, as previously observed

by other groups [14, 16, 17, 74]. Fine control over the aperture diameter and geometry was not possible with the needle-punch method.

6.2.2 Stability of bilayers in apertures in photoresist

6.2.2.1 Apertures fabricated by two-photon lithography in SU8

Photolithography allows precise control over position and size and has also widely been for production of apertures for bilayer formation. It also allows fabrication of apertures that are substantially smaller, down to hundreds of nanometers, than the conventional micromachined apertures. Teflon has been avoided in lithography based approaches for aperture fabrication because of its chemical inertness. Instead, apertures have been fabricated by lithography in traditional microelectronics materials such as silicon and silicon nitride [114, 121, 229], and also directly in photoresist layers [92, 112, 113, 122, 131, 132]. As discussed in section 3.1.2, because the intrinsic capacitance of silicon and silicon composites is high, apertures in these materials can only be used for single-channel recordings if the capacitance is reduced by a (hydrophobic) coating of a material with a low dielectric constant, an approach that has been demonstrated recently by Niwano and co-workers for triangle-shaped apertures in silicon nitride [110, 123]. In this work, the photoresist SU8 was used, which is a suitable candidate for a septum material for low noise recordings because it has a dielectric constant of only 1.5× that of Teflon and excellent chemical and mechanical properties (section 3.1.2 and section 3.2.1). Another advantage of using SU8, in the context of bilayer stabilization, is that a wide range of aperture shapes can be created by 3D laser lithography (section 4.1), whereas aperture outlines in silicon-type materials are limited by (an)isotropic etching profiles.

Since smaller apertures improve the stability of suspended bilayers (section 3.1.1), the diameter of the aperture could be reduced to improve bilayer stability as has been reported by other groups, for example a bilayer lifetime of 75 hours was demonstrated for 200 nm apertures in silicon nitride [118]. But since fabrication-focused studies tend to verify bilayer suitability for ion channel incorporation with water-soluble ion channels, it is often overlooked that submicron or few-micron bilayers apertures (~<30 μm) are not suitable for proteoliposome fusion with the suspended bilayer [38, 55, 230]. As discussed in section 3.1.1, a reduction in aperture diameter also necessitates a reduction in septum thickness to avoid unstirred layer effects near the bilayer surface and a high convergence resistance at the opening of high aspect ratio apertures [36, 231]. Moreover, based on an analysis of bilayer-to-annulus and annulus-to-septum contact angles, it has been predicted that large-area stable suspended bilayers (i.e. without bilayer destabilization) can be formed when a very thin septum is used [25].

Hence, as discussed in section 3.1.1, reducing the aperture diameter to some extent while thinning the septum as much as possible appears the most promising strategy to obtain stable bilayers that are sufficiently large to facilitate vesicle fusion. But thin septa (<20 µm) are less mechanically robust, and more importantly, increase the septum capacitance and therefore contribute more noise to the electrical recording, which limits the measurement bandwidth [35, 36]. However, the problems of mechanical instability and high septum capacitance can be avoided by only thinning the septum locally, or in other words, by realizing a geometry with a thin aperture wall that tapers out to the full thickness of the bulk septum. Consequently, shaped apertures and control shapes were fabricated using two-photon lithography to evaluate the significance of shaped apertures in stability of lipid bilayers (Figure 71).

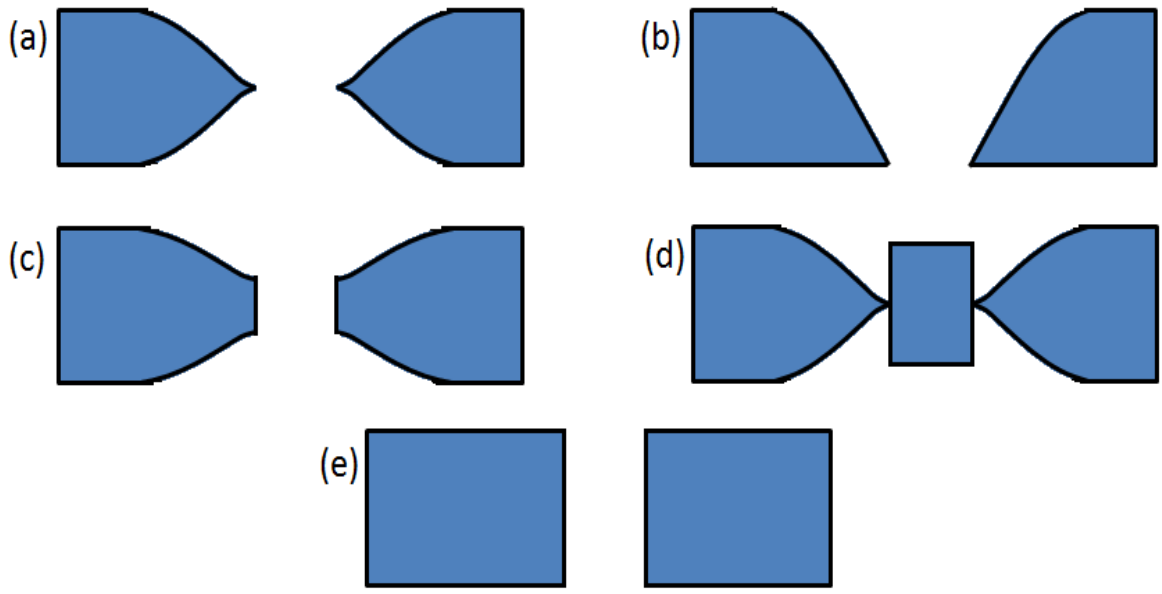

Figure 71: Schematic cross-sectional view of the various fabricated apertures: (a) beak-shaped, (b) triangle-shaped, (c) blunted-beak, (d) blocked-beak control, and (e) cylindrical control.

One of the control shapes is the blocked-beak aperture structure (Figure 71d, Figure 47c), which was fabricated to enable measurement of the capacitance of the SU8 sheet with the shaped apertures. A value of 18 pF was obtained, which is identical, within the accuracy of the measurement, to the capacitance of a clamped 50 µm thick SU8 sheet without an aperture. This indicates that the rather small area, <250 × 250 µm, of the sheet that contains thin (<50 µm thickness) SU8 does not significantly increase the capacitance of the septum, which validates the implementation of a shaped aperture rather than using a cylindrical aperture in a sheet of SU8 of which the entire area is reduced to a thickness of ~2 µm. For comparison, the capacitance of a 50-µm thick sheet of Teflon was measured as 12 pF, reflecting the somewhat smaller dielectric constant of this material. The bilayer stability in a cylindrical SU8 aperture with a diameter of 60 µm (Figure 71e, Figure 47b) was evaluated. These bilayers were stable for up to 1-2 hours and

disintegrated at potentials >|150 mV| (n=8), which is similar to bilayers suspended in a conventional aperture in a Teflon septum [232, 233].

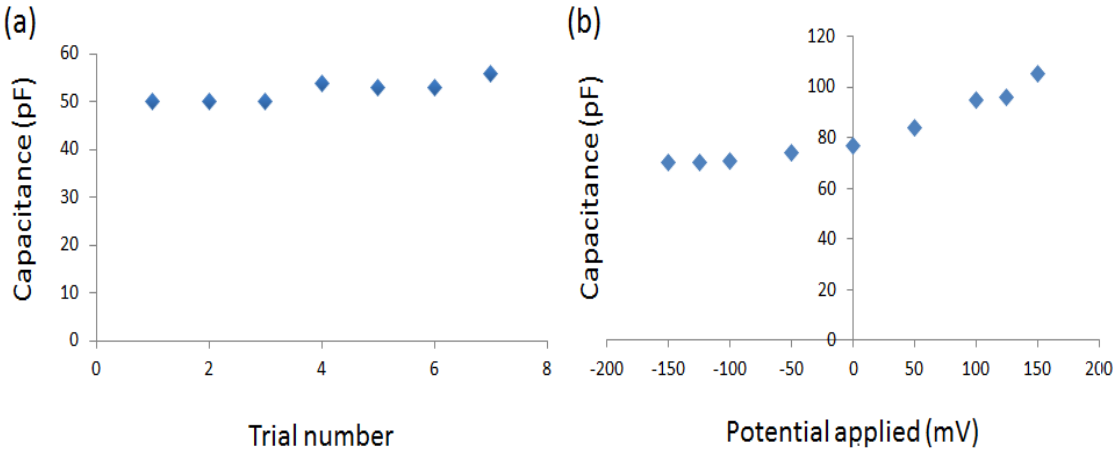

Figure 72: (a) Capacitance of different DOPC:POPG (1:1 molar ratio) bilayers formed with the folding method using a 20 mg/ml chloroform-lipid solution in an 80 µm diameter beak-shaped aperture. (b) Dependence of capacitance on voltage for a DOPC:POPG bilayer (1:1 molar ratio) painted with 20 mg/ml lipid-decane solution in a 100 µm diameter beak-shaped aperture. The apertures were fabricated using two-photon lithography. The background capacitance is 18 pF.

Lipid bilayers were formed in shaped apertures using both the Mueller-Rudin painting method [20] and the Montal-Mueller folding method [52] (section 2.3.1). The total capacitance was measured and the known septum background capacitance of 18 pF was subtracted to obtain the capacitance of the suspended bilayer. As an example, the total capacitance for folded DOPC:POPG bilayers in an 80 µm diameter beak-shaped aperture (Figure 71a) was ~50 pF in eight independent experiments (Figure 72a). Based on a specific bilayer capacitance of 0.7 µF/cm^2 [118] the area of the bilayer was estimated and compared with the area of the narrowest part of the aperture, as determined by microscopy. It was found that for various shaped apertures, the folding method resulted in bilayers that consistently occupied ~85% of the available aperture area. On the other hand, the painting method resulted in a range of bilayer areas, most likely due to varying sizes of the solvent annulus, which is possibly related to the exact amount of oil-lipid solution applied to the aperture. Moreover, unlike the folded bilayers, the capacitance of the painted bilayers showed a dependence on the applied potential (Figure 72b), as previously observed by other groups [54, 55]. However, all the bilayers suspended in beak-shaped and triangle-shaped apertures could easily tolerate potentials up to 200 mV for 1-2 hours.

To determine the position of the suspended lipid bilayer in a shaped aperture, bilayers were painted on horizontally positioned SU8 apertures (results are presented and discussed in detail in Chapter 8), using a PMMA chip with a 170 µm glass coverslip as the bottom layer, rather than the Teflon chambers that clamp SU8 septa in a vertical orientation. Based on the diameter of the decane-lipid annulus and the co-localization of the focal planes of the tip of the aperture and

the bilayer-annulus interface, it was concluded that the bilayer was formed at the narrowest part of the aperture.

Table 5: Lifetime of painted suspended bilayers, for individual experiments, with different lipid composition in shaped apertures using two-photon lithography (single experiments). All experiments had Alamethicin ion channel activity present and ionic solution was buffered at pH 7.

Lipid composition	Solvent	Aperture shape/diameter	Potential applied (mV)	Lifetime (hours)
3:1 DOPC:POPG	decane	cylindrical (60 µm)	100	2
3:1 DOPC:POPG	decane	cylindrical (60 µm)	100	2
3:1 DOPC:POPG	decane	triangle (60 µm)	200, 150, 100	36
1:1 DOPC:POPG	decane	triangle (60 µm)	150, 100	31
1:1 DOPC:POPG	decane	beak (60 µm)	-200, -175, -150, -125	30
1:1 DOPC:POPG	decane	beak (60 µm)	-200, -175,-150	21
3:1 DOPC:POPG	nonane	beak (80 µm)	150, 100	30
1:1 DOPC:POPG	decane	beak (80 µm)	150, 100	30
1:1 DOPC:POPG	decane	beak (80 µm)	-100	21
1:1 DOPC:POPG	decane	beak (100 µm)	100	9

Bilayers were painted with decane or nonane to obtain suspended lipid bilayers with different molar ratios of DOPC and POPG lipids (see Table 5). Painted bilayers in the beak-shaped and triangle-shaped apertures with a tip thickness of ~2 µm were stable for >20 hours at applied potentials of >|100 mV| with continuous alamethicin channel activity as reported in other studies [128] (Figure 73). However, the bilayer lifetime was reduced in the blunted-beak aperture with a tip thickness of ~10 µm (Figure 71c, Figure 47a) to ~14 hours. These experiments highlight the relationship between aperture edge thickness and bilayer stability and suggest that the geometry of the aperture in the vicinity of the tip also has an influence on bilayer stability. Although bilayer stability in the 80 µm beak-shaped aperture was the same when nonane or decane was used as the painting solvent (Table 5), decane was preferred because of its reduced tendency to partition into the lipid bilayer [234].

The diameter of the narrowest part of the beak-shaped aperture was either 60, 80 or 100 µm, keeping the diameter of the widest part of the aperture (i.e. at the septum surface) constant at 250 µm. There was no apparent difference in bilayer stability in the 60 and 80 µm diameter apertures (Table 5) but for the 100 µm diameter aperture, the painted bilayer lifetime was reduced to only a few hours. This suggests that since the 100 µm aperture geometry resembled more closely a cylindrical aperture, the oil annulus gradually drains away, eventually causing bilayer failure [25]. Infrequently, it was also observed that bilayers gave a capacitance around 2-3

times greater than empirically estimated value, which could be due to the formation of the bilayer on the slope of the tapered edge or at the point where the edge starts to taper or due to formation of a cupola shaped bilayer [235]. Such bilayers were not stable and were broken on purpose by agitating the buffer in the chamber by aspiration.

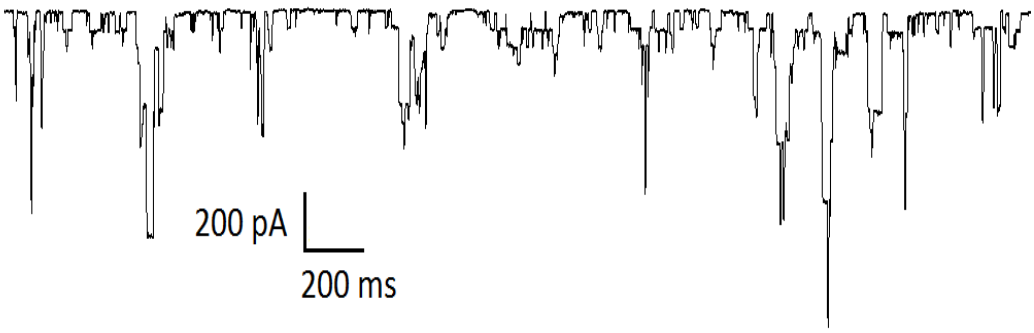

Figure 73: Alamethicin channel activity, 26 hours after bilayer formation, in a DOPC:POPG (1:1 molar ratio) suspended bilayer painted from a lipid-decane solution. The applied potential is -125 mV and the buffer solution is 2M KCl, 10 mM HEPES, pH 7.4. The aperture is beak-shaped using two photon lithography with an inner diameter of 80 µm and an aperture tip thickness of ~2 µm. The trace has been recorded at 5kHz using ID562 BLM amplifier.

Next, the lifetime of folded bilayers was evaluated, which were found to be stable for ~20 hours in triangle-shaped and beak-shaped apertures (Table 6). It was observed that folded bilayers were easier to form in beak-shaped apertures than in triangle-shaped apertures, which may relate to the mechanism of the folding method, where a lipid-air monolayer is brought into contact with each side of the aperture separately. This suggests that tapered side of a triangle-shaped aperture facilitates the formation of a suspended monolayer, whereas the flat side of the aperture does not. Although previous studies with tapered, triangle-shaped, apertures [110, 113, 121-123, 193] have not explored aperture diameter or shape variations and, except for Hirano-Iwata *et al.* [121, 123], have not addressed bilayer mechanical stability, they do report bilayer lifetimes of tens of hours, in full agreement with data presented in this work. However, it is not clear why tapered apertures result in drastically enhanced stability of suspended bilayers.

Although a reduced mismatch between the thickness of a lipid bilayer and the height of the wall of the aperture has been cited for tapered (i.e. thin-edged) apertures, this argument does not seem to apply to the apertures fabricated in this work, which have an edge height that is still 400-fold larger than the bilayer thickness. Moreover, bilayer stability is linked to annulus stability, which in turn relates to favorable contact angles of the solvent with the aperture material [25]. Indeed, Beerlink *et al.* recently obtained a cross-sectional view of the decane annulus of a suspended bilayer in a kapton (polyimide) channel by X-ray propagation imaging, which visualizes how the annulus connects the bilayer to the solid material by wetting tens of micrometers of the kapton channel wall [57]. This suggests that the shaped apertures stabilize the bilayer by

providing an anchor region for the annulus, with the shape and hydrophobicity of the tapered regions preventing excessive drainage or lateral movement of the solvent annulus.

Table 6: Lifetime of folded suspended bilayers, for individual experiments, with different lipid composition in shaped apertures using two photon lithography (single experiments).

Lipid composition	Aperture shape/diameter	Potential applied (mV)	Lifetime (hours)
DPhPC	triangle (60 µm)	100, 150, 200	26
1:1 DOPC:POPG	blunt-beak (60 µm)	100	14
1:1 DOPC:POPG	triangle (80 µm)	100	15
1:1 DOPC:POPG	beak (80 µm)	-100, 100, 125	19
1:1 DOPC:POPG	beak (80 µm)	100	5- 12[6]
1:1 DOPC:POPG	beak (80 µm)	100	21
1:1 DOPC:POPG	beak (80 µm)	100	24[7]
cis DOPC, trans POPG	beak (80 µm)	100	21

Perturbation of the aqueous solution in contact with a lipid bilayer is required to mix a small volume of an added concentrated solution, for example a channel blocker, with the electrophysiology buffer, or to change the buffer solution by successive removal of a fixed volume of the original buffer and addition of the same volume of the new buffer. These procedures are necessary for ion channel screening experiments. In the case of ion channel incorporation by proteoliposome fusion, it has also been observed that moving the buffer-air interface over the aperture promotes liposome fusion with the suspended bilayer [236, 237]. For this reason, the mechanical stability of the suspended bilayers was investigated by counting the number of times that the buffer-air interface could be moved over the bilayer without causing bilayer failure. This procedure was performed by the gentle aspiration of buffer solution from the bottom of an aqueous compartment into a pipette, and then re-introducing the same volume into the compartment. Because painted bilayers have a tendency to change their area, as monitored by capacitance measurements, during such aspiration cycles, this analysis was performed with folded bilayers.

As depicted in Figure 74, DOPC:POPG bilayers (1:1 molar ratio) suspended in the cylindrical SU8 aperture tend to break during the first five aspiration cycles and are hence mechanically unstable. When a bilayer with the same lipid composition is suspended in a beak-shaped aperture of 80 µm diameter, ~37% of the bilayers break within the first five aspiration cycles, while ~25% of the bilayers survive between 6 and 10 cycles, and ~37% of the bilayers are still intact after 15-20

[6] Lifetime reported as ('x'- 'y'), where x is the last time when bilayer was observed and y is the time when bilayer was found to be broken.

[7] Experiment terminated at given time.

aspiration cycles, representing a marked improvement in bilayer stability. Although the bilayer lifetime, in the absence of perturbation of the aqueous compartments, was comparable for triangle-shaped and beak-shaped apertures (see Table 5 and Table 6), the mechanical stability of bilayers suspended in these two apertures is quite different. Remarkably, bilayers in the triangle-shaped apertures could withstand up to 45-60 aspiration cycles in ~30% of 10 experiments and 30-45 cycles in ~30% of the experiments. The ~20% of bilayers that fail within 15-30 cycles are at least as stable as the most stable bilayers in the beak-shaped apertures, with ~30% of the bilayers in the triangle-shaped aperture failing within 15 aspiration cycles.

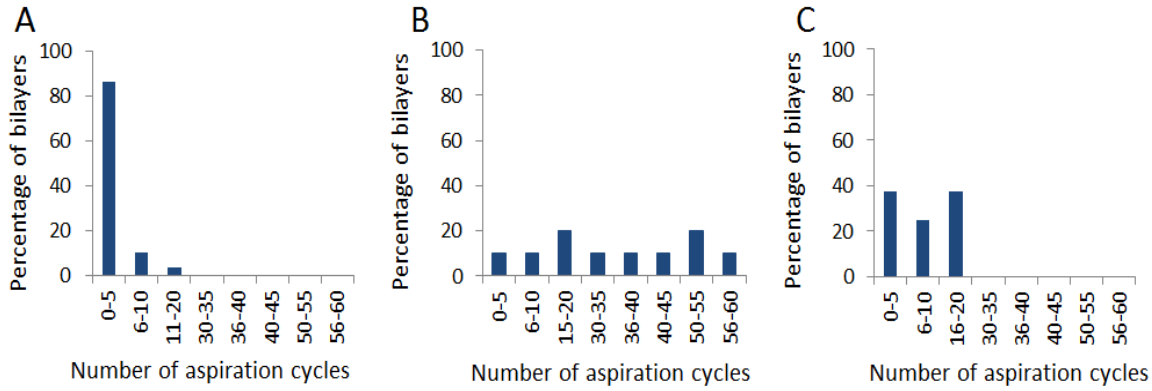

Figure 74: Stability of folded bilayers of DOPC:POPG (1:1 molar ratio) in various apertures fabricated with two-photon lithography, quantified as the number of aspiration cycles that leads to bilayer failure, in (a) Cylindrical aperture of 80 µm diameter (n=19), (b) triangle-shaped aperture of 80 µm diameter (n=10), and (c) beak-shaped aperture of 80 µm diameter (n=8).

6.2.2.2 Apertures fabricated by grayscale lithography in TMMF

Having established that triangle-shaped and beak-shaped apertures fabricated by two-photon laser lithography substantially increase bilayer stability, shaped apertures fabricated using grayscale lithography were tested. As discussed in the previous chapter, the use of SU8 with this lithography technique posed technical challenges which led to the use of TMMF. This resist, like SU8, has a low dielectric constant and is mechanically and chemically stable. Similar to bilayer experiments with shaped apertures fabricated with two-photon lithography, the position of the suspended lipid bilayer in a shaped aperture obtained with grayscale lithography was determined by painting bilayers on horizontally positioned TMMF apertures, using a PMMA chip with a 170 µm glass coverslip as the bottom layer. Again, it was concluded that the bilayer was formed at the narrowest part of the aperture, as discussed in detail in Chapter 8.

The aperture size in the grayscale mask was set to 80 µm because apertures with this diameter resulted in stable bilayers which also supported protein ion channel activity delivered with vesicle fusion, as discussed in Chapter 7. With the grayscale lithography shaped apertures in

TMMF, both bilayer formation methods were used and similar results were obtained as with the two-photon lithography shaped apertures in SU8. Bilayers prepared with the folding method in triangle-shaped TMMF apertures had a lifetime of ~20 hours (Table 7), similar to the bilayer lifetime experiments listed in Table 6 for SU8 apertures. As it could be argued that the bilayer lifetime could vary from one aperture to another, lipid bilayers were also formed in nine apertures simultaneously, using a septum with a 3 × 3 array of triangle-shaped TMMF apertures. The nine bilayers in this array collectively were stable for ~20 hours, for both the painting and the folding method (Table 7), demonstrating that all nine shaped apertures effectively enhanced the lifetime of a suspended bilayer.

Table 7: Lifetime of folded suspended bilayers, for individual experiments, with different lipid composition in triangle-shaped apertures fabricated with grayscale lithography (single experiments). A potential of 100 mV was applied to all of the bilayers.

Lipid composition	Aperture shape/diameter	Lifetime (hours)
DOPC	triangle (80 μm)	23
DOPC	triangle (80 μm)	22
DOPC	triangle (80 μm)	23

Table 8: Lifetime of suspended bilayers, for individual experiments, with different lipid composition in triangle-shaped apertures fabricated with grayscale lithography (single experiments).

Lipid composition	Preparation method/ potential applied	Aperture shape/diameter	Lifetime (hours)
1:1 DOPC:POPG	painting/100 mV	3 × 3 triangle (80 μm)	16 - 20[6]
1:1 DOPC:POPG	painting/100 mV	3 × 3 triangle (80 μm)	14
1:1 DOPC:POPG	painting/100 mV	3 × 3 triangle (80 μm)	27[7]
DOPC	folding/50 mV, 100 mV	3 × 3 triangle (80 μm)	19

The mechanical stability of the suspended bilayers prepared by the folding method in triangle-shaped and beak-shaped TMMF apertures was investigated by counting the number of times that the buffer-air interface could be moved over the bilayer without causing bilayer failure. As depicted in Figure 74, when a DOPE:POPG bilayer was suspended in a triangle-shaped aperture of 80 μm diameter, ~40% of the bilayers broke within the first ten aspiration cycles, while ~35% of the bilayers survived between 21 and 30 cycles, and ~14% of the bilayers were still intact after 31-70 aspiration cycles, representing a marked improvement in bilayer stability. However, the mechanical stability of bilayers suspended in beak-shaped apertures was remarkably different , with more than 50% of the bilayers being able to withstand 90-100 aspiration cycles, while >30% of the bilayers survived up to 50-90 aspiration cycles. It should be noted that the aspiration of the buffer was stopped after 100 cycles to limit the experimental time, and that the data in Figure 6 was collected by Mr Jiajun Wang.

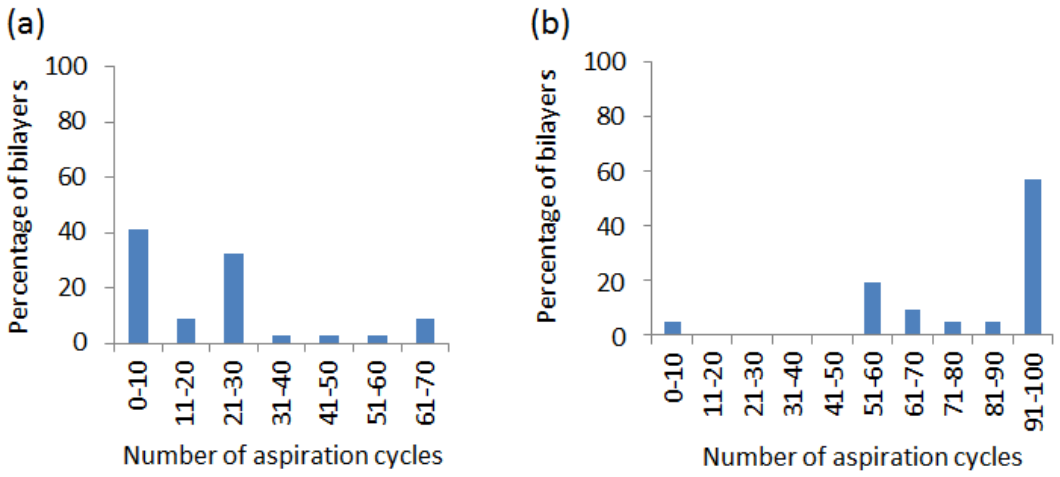

Figure 75: Stability of folded bilayers of DOPE:POPG (1:1 molar ratio) in apertures fabricated using grayscale lithography, quantified as the number of aspiration cycles that leads to bilayer failure in (a) a triangle-shaped aperture of 80 µm diameter (n=34) and (b) a beak-shaped aperture of 80 µm diameter (n=21). (Measurements done by Mr Jiajun Wang)

This mechanical stability behaviour is opposite to what was observed for bilayers suspended in apertures fabricated by two-photon lithography in SU8, where triangle-shaped apertures gave more stable bilayers than beak-shaped apertures (Figure 74b,c). Although the overall geometry of the aperture walls is very similar with both fabrication methods and the surface of both materials was coated with Parylene, the apertures fabricated using grayscale lithography in TMMF have sidewalls with discrete thickness steps (Figure 68 and Figure 69) that originate from the discrete zones on the grayscale mask, whereas the walls of the two-photon lithography apertures in SU8 have a continuous thickness gradient (Figure 46). Another difference is that the two-photon lithography apertures have a distinct surface topology that follows the write direction of the laser voxel, whereas the surface of the TMMF aperture walls is more smooth. This suggests that the detailed geometry and surface roughness of aperture walls could also affect the stability of aperture-suspended bilayers, opening an interesting research area for future investigation.

6.3 Conclusions

The shaped apertures fabricated by two-photon lithography and by grayscale lithography were used for the formation of suspended lipid bilayers. For a given aperture diameter, bilayers suspended in beak-shaped or triangle-shaped apertures with a tip thickness of ~2 µm typically had a lifetime of ~20 hours, while bilayers in a cylindrical aperture in a 50 µm thick septum of the same material failed after ~2 hours. The bilayer lifetime was reduced when the aperture diameter was increased to 100 µm or when the tip thickness of the shaped aperture was increased to 10 µm. The mechanical stability of the bilayer, assessed by the number of times the buffer-air interface can be raised and lowered over the bilayer without causing bilayer failure, was also

increased to several tens of cycles by the use of shaped apertures compared to the cylindrical control aperture. Similar bilayer lifetimes of typically ~20 hours were obtained with shaped apertures fabricated with grayscale lithography. However, the mechanical stability of the bilayer was better in triangle-shaped apertures than in beak-shaped apertures when the apertures were fabricated by two-photon lithography, while bilayers formed in beak-shaped apertures fabricated by grayscale lithography were of superior stability, being able to withstand up to 100 aspiration cycles. The likely dependence of bilayer stability on details of the aperture wall geometry and surface roughness highlights the crucial role of the aperture design on bilayer stability. Nonetheless, the clear conclusion from the results obtained in this chapter is that apertures with a thin tip of ~2 µm, give substantially more stable suspended bilayers than conventional cylindrical apertures in a septum that is tens of micrometers thick. Since the stability of the bilayer is enhanced by shaping of the aperture, a reduction in diameter of the aperture can be avoided, which is favourable for vesicle fusion with the suspended bilayer. The next chapter discusses electrophysiology measurements of ion channels delivered with vesicle fusion to the bilayers formed in shaped apertures.

Chapter 7 Protein ion channel electrophysiology

After demonstrating the enhancement in lifetime and mechanical stability of lipid bilayers suspended in shaped apertures, the ability of these model membranes to support protein ion channel activity was evaluated. In this chapter, protocols for the reconstitution of detergent-solubilised ion channels into vesicles, or proteoliposomes, are outlined.The potassium channels, KcsA and $hERG_{S5\text{-}S6}$, and the pore domain of the sodium channel Na_vSp, introduced in Chapter 2, were incorporated into the suspended bilayer via proteoliposome fusion, while the water-soluble protein toxin α-hemolysin was able to self-insert from aqueous solution. Current-voltage plots for KcsA, hERG and Na_vSp are presented, and the importance of the aperture size for facilitating proteoliposome fusion is discussed

7.1 Materials and methods

7.1.1 Ion channel reconstitution into the bilayers

The potassium channel KcsA was expressed and purified according to previously published procedures [97] by Dr Andrew M. Powl (Birkbeck College, University of London, UK). The Na_vSp pore was also expressed, purified and reconstituted into lipid vesicles by Dr Andrew M. Powl. The

hERG pore domain, $hERG_{S5-S6}$ was expressed and purified by Ms Maiwenn Beaugrand (Université du Québec à Montréal, Canada). Reconstitution of proteins into lipid vesicles was performed by detergent depletion. Bio-Beads SM-2 (Biorad Laboratories, Hemel Hempstead, UK) were cleaned in methanol for 30 mins followed by thorough rinsing with electrophysiology buffer (150 mM KCl, 10 mM HEPES, pH 7.4). Phospholipid solutions in chloroform were mixed in the desired combination (3 µmol total lipid) and dried onto the walls of a glass vial as a mixed lipid film. The lipid film was subsequently dissolved in 1 ml of reconstitution buffer (40 mM β-D-octyl glucoside, 150 mM KCl, 10 mM HEPES, pH 7.4), with bath sonication to clarity for at least 30 min. KcsA in detergent solution (1.9 mg/ml in dodecyl β-D-maltoside (Sigma Aldrich) (20 µg or 60 µg protein)) was added to achieve a 10000:1 or 3333:1 molar ratio of lipid to KcsA tetramer. 100 µg of $hERG_{S5-S6}$ in detergent (1.12 mg/ml) was added to achieve a 2000:1 molar ratio of lipid to $hERG_{S5-S6}$ tetramer. The β-D-octyl glucoside detergent (SIgma Aldrich, St. Louis, MO) was gradually removed by an initial one-hour incubation with 80 mg of washed biobeads, followed by a second one-hour incubation with 80 mg of fresh biobeads. The dispersion of proteoliposomes was then removed from the biobeads and stored at +4 ^{o}C until use. α-Hemolysin powder (Sigma Aldrich) was solubilized in electrophysiology buffer (150 mM, 10 mM HEPES, pH 7.4) to obtain a concentration of 0.5 mg/ml. A suspended lipid bilayer was formed using the protocol described in Chapter 6. Ion channel incorporation in the bilayer was initiated by adding several microliters of a proteoliposome solution or of the α-hemolysin solution to one of the aqueous chambers.

7.1.2 Single-channel measurements

For KcsA and α-HL measurements, the bilayer capacitance and current flowing through the ion channel were measured with the ID562 BLM amplifier described in section 6.1.2, while the hERG and Na_vSp pore measurements were performed with the Axopatch 200B described in the same section. Resist sheets with shaped apertures were clamped in the bilayer cell shown in Figure 70. After successful formation of a lipid bilayer, a DC potential of |50-200mV| was applied to measure the bilayer current at 5 kHz (ID562) or 50 kHz (Axopatch) acquisition. Bilayer traces were analysed and digitally filtered using Clampfit 10.2 software following the application of a 1 kHz Gaussian filter. Drift in baseline was adjusted using baseline correction feature in Clampfit 10.2.

7.2 Results and discussions

7.2.1 KcsA ion channel electrophysiology

The KcsA potassium channel, as discussed in section 2.5.2.2, is a well-characterized ion channel that is suitable for demonstrating the functionality of lipid bilayers, i.e. the ability to obtain single-channel current traces typical for KcsA by the proteoliposome fusion method for ion channel incorporation. Since it is activated by a sufficiently high proton concentration, one of two aqueous compartments separating the bilayer with reconstituted KcsA contained buffer solution of pH 4.0 [96, 97, 238]. Initially, a lipid:protein (L:P) ratio of 10,000:1 in the proteoliposome was used as previously used by Marius *et al.* for obtaining single-channel activity of KcsA, and lipid bilayers of pure POPG were used since they increase the open probability of the channel [97]. However, characteristic gating events of KcsA could not be obtained under these conditions. The amount of protein in the vesicles was subsequently increased threefold to a lipid:protein ratio of 3333:1. When protein activity was not observed after addition of proteoliposome solution to the buffer, a larger amount of the proteoliposome was added. If this also did not result in ion channel activity, the bilayer was broken and reformed in the presence of the proteoliposomes, a method previously employed by Marius *et al.* [97].

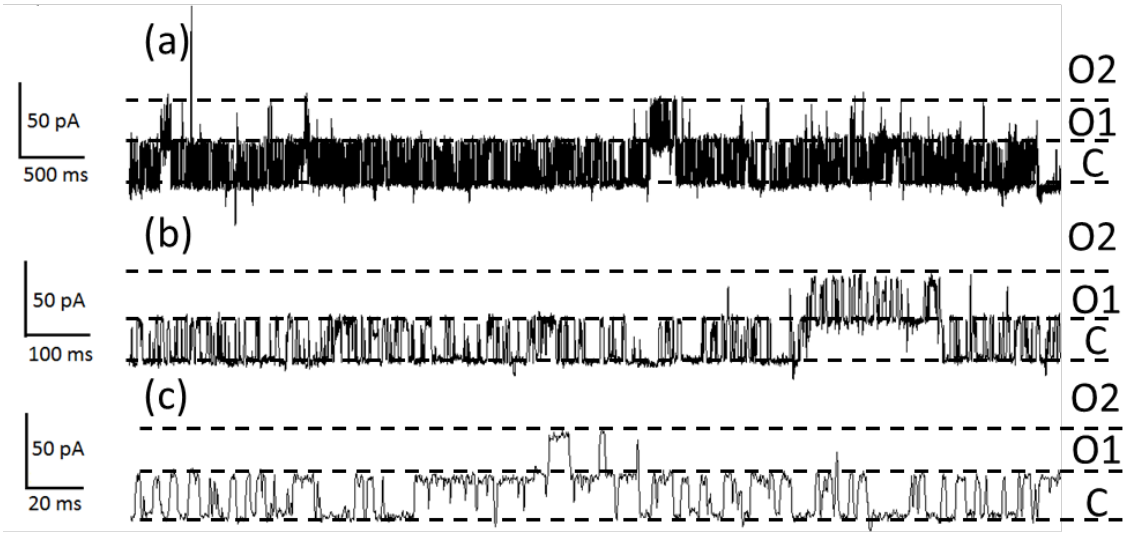

Figure 76: (a) KcsA ion channel activity in a POPG bilayer painted with a decane-POPG solution on a beak-shaped aperture in SU8 with an inner diameter of 60 µm and a tip thickness of ~2 µm (150 mV potential, 150 mM KCl, pH 4.0 in one compartment and pH 7.4 in the second compartment), and (b,c) zoomed views of the same bilayer trace, depicting individual gating events. Current level 'C' corresponds to a closed channel and current levels 'O' correspond to open channels.

Figure 76 shows KcsA channel activity in a POPG bilayer painted on a 60-µm shaped aperture with an inner diameter of 60 µm. These bilayer current steps are characteristic for KcsA gating and demonstrate that the KcsA has been incorporated in the suspended lipid bilayer by

proteoliposome fusion [98]. As seen in Figure 76 a burst of ion channel activity was obtained in the POPG bilayer voltage-clamped at +150 mV. The amplitude of the current events was 27.4 ± 0.86 pA and the open probability of the channel was 0.63. These values are in agreement with the literature on KcsA gating, with the open probability corresponding to the so-called 'flicker mode' of KcsA [97, 239]. The trace also shows incorporation of more than one active ion channel into the bilayer which is represented by current level O2, which originates from current level O1.

When the total capacitance was smaller than 40 pF, KcsA ion channel activity was never observed, implying that bilayers that are smaller than ~60 µm in diameter did not readily support KcsA incorporation through proteoliposome fusion. This observation is consistent with other studies that mention the dependence of incorporation of an active ion channel on lipid bilayer area [14, 37, 38, 55]. This highlights the need to verify novel bilayer stabilization strategies with proteoliposome-delivered channels rather than exclusively with channels such as gramicidin, alamethicin and α-hemolysin, which can self-insert into a bilayer from aqueous solution. In this context it should also be emphasized that aperture-suspended bilayers formed with the painting method gave bilayers of variable areas, whereas the folding method consistently produced bilayers of a similar size (section 6.2.2).

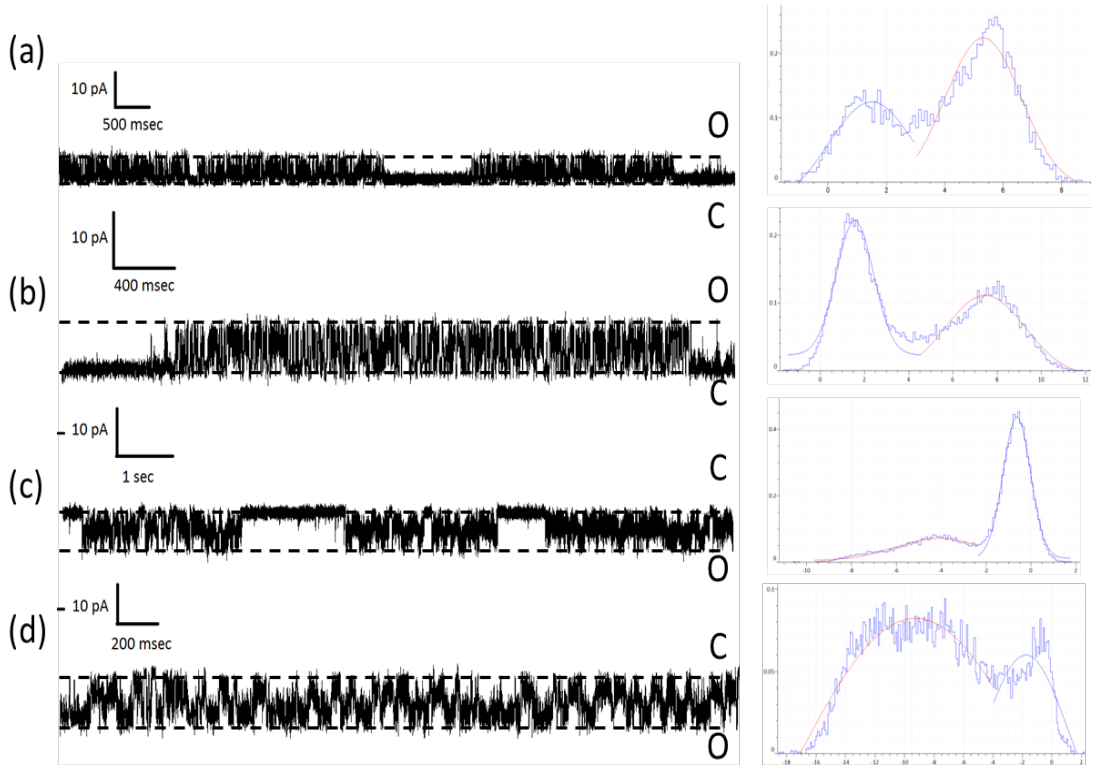

Figure 77: KcsA ion channel activity in a POPG bilayer painted with a decane-POPG solution on a beak-shaped aperture in SU8 with an inner diameter of 80 µm and a tip thickness of ~2 µm (150 mM KCl, pH 4.0 in one compartment and pH 7.4 in the second compartment) at an applied potential of (a) 50 mV, (b) 75 mV (c) -50 mV, and (d) -75 mV. The panels on the right side are histograms of the adjacent current trace, where the y-axis represents normalised count and the x-axis the current signal in pA units. Current level 'C' corresponds to a closed channel and current level 'O' corresponds to an open channel.

To consistently obtain a total capacitance exceeding 40 pF, i.e. to obtain sufficiently large bilayers for proteoliposome fusion, shaped apertures with an inner diameter of 80 µm were fabricated. Figure 77 shows KcsA ion channel activity in a POPG bilayer painted across an 80 µm shaped aperture at four different potentials. At negative potentials, the open channel current of KcsA showed excessive noise as previously noted by other groups [98]. A current voltage (I-V) plot based on more traces is shown in Figure 78. This I-V plot depicts the mild rectification typical for the KcsA channel [97, 98]. It was also observed that bilayers painted from nonane rather than decane did not display KcsA current events, neither in 60 µm nor in 80 µm diameter beak-shaped apertures, indicating that nonane modulated the properties of the phospholipid bilayer [62, 63].

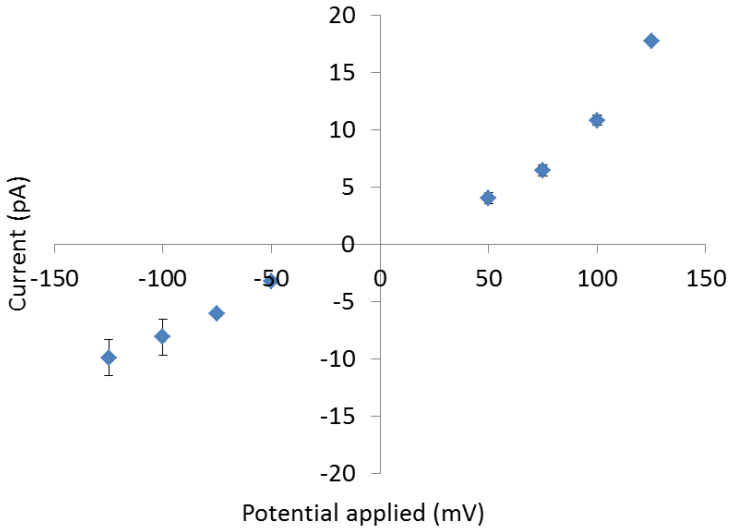

Figure 78: I-V plot for KcsA in a suspended bilayer of pure POPG painted from a lipid-decane solution in a shaped aperture with an inner diameter of 80 µm and a tip thickness of ~2 µm (150 mM KCl, pH 4.0 in one compartment and pH 7.4 in the second compartment). The data were obtained from three different measurements, from which the standard deviation was calculated.

7.2.2 Na_vSp pore domain electrophysiology

After demonstrating of functionality of suspended bilayers in shaped apertures using the well-characterised KcsA channel, other channels were investigated, for which the single-channel electrophysiology is less well described. Despite the importance of voltage gated sodium channels for human (patho)physiology, there are no X-ray or NMR structures of eukaryotic sodium channels. Since prokaryotic sodium channel pore domains (see section 2.5.2.3) can be expressed and purified and have recently been demonstrated to self-assemble as a tetrameric channel when incorporated into lipid bilayers [102], the pore domain of Na_vsp from *Silicibacter pomeroyi* was selected for electrophysiology experiments with bilayers suspended in shaped apertures. A 1:1 mixture of POPE and POPG lipids was selected because the activity of the Na_vSp has been shown to depend on the presence of negatively charged lipids [240].

First, the dependence of the channel on the pH of the buffer solution was investigated by placing solutions of different pH, but the same ionic strength, on either side of the bilayer. As shown in Figure 79 and Figure 80, different single-channel current steps and different gating behaviour (i.e. different open probabilities) were observed for a symmetrical pH of 3.5, 4.5 and 7.0. Moreover, the use of a pH 3.5 / 6.0 pH gradient significantly increased the gating frequency of the channel (Figure 80). These are interesting observations because full-length Na_vSp is a voltage-gated channel that has not been reported to show any dependence on pH. Although a pH gradient could give rise to voltage changes due to the Nernst potential[8], the voltage sensing domain has been dissected, hence the Na_vSp pore domain is not expected to exhibit a (pH gradient mediated) voltage sensitivity.

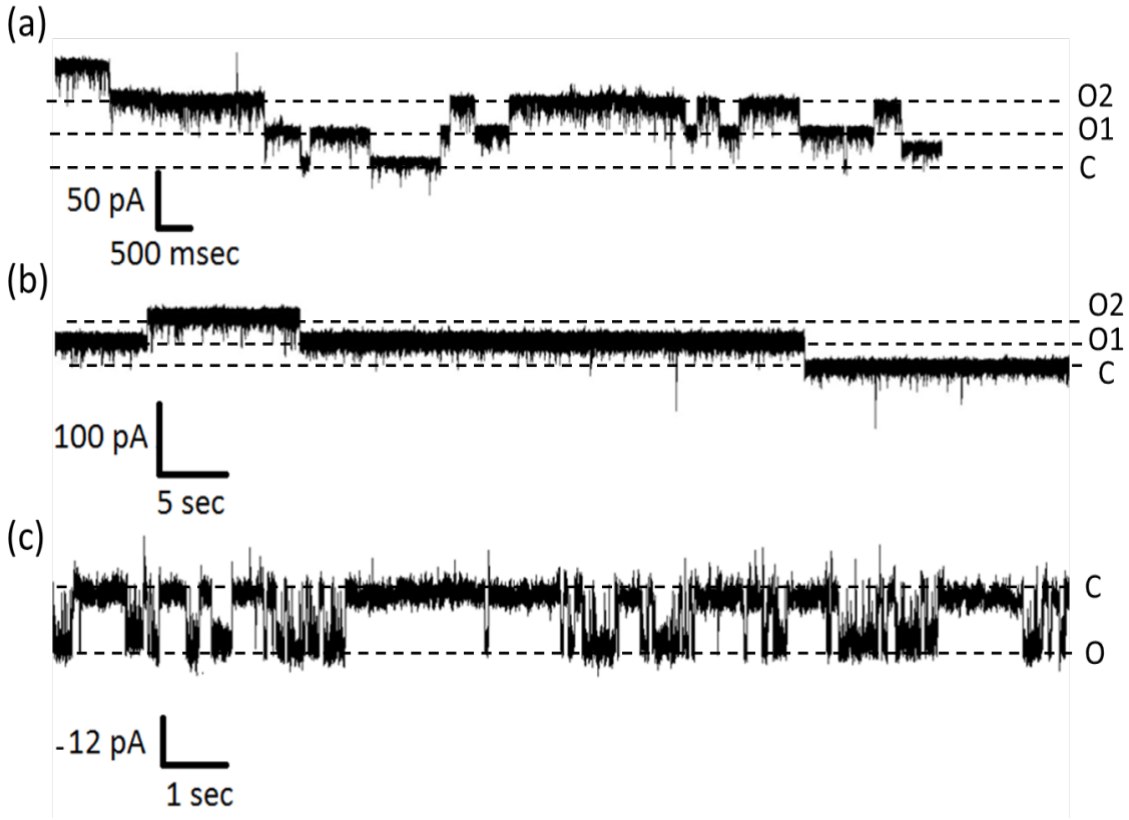

Figure 79: Na_vSp pore domain ion channel activity in a POPE:POPG (1:1 molar ratio) bilayer formed with the folding method in a shaped aperture with an inner diameter of 80 µm (500 mM NaCl, 20mM HEPES) at different pH values: (a) buffered at pH 3.5 in both compartments, at an applied potential of 100 mV, (b) buffered at pH 4.5 in one compartment and pH 7 in the other, at an applied potential of 100 mV, and (c) buffered at pH 7 in both compartments, at an applied potential of -100 mV. Current level 'C' corresponds to a closed channel and current levels 'O' correspond to open channels.

[8] The Nernst potential is an equilibrium potential for a given ion and is calculated using the Nernst equation, based on the charge of the ion and its concentration gradient across the membrane. It is also affected by temperature. (Physiologyweb.com)

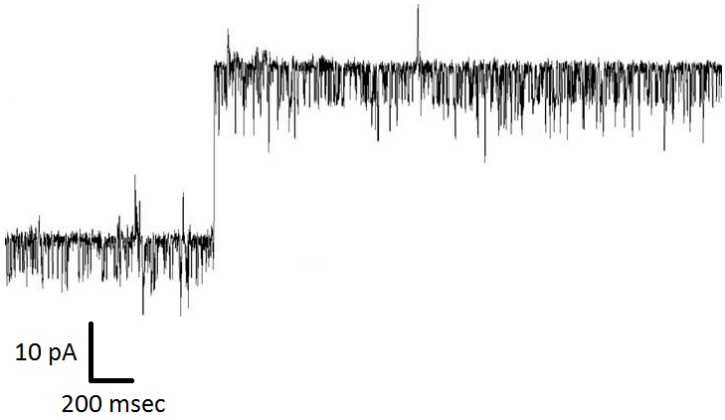

Figure 80: Na_vSp pore domain ion channel activity in a POPE:POPG (1:1 molar ratio) bilayer formed with the folding method in a shaped aperture with an inner diameter of 80 µm (500 mM NaCl, 20mM HEPES) buffered at pH 3.5 in one compartment and pH 6 in the other compartment, at an applied potential of 100 mV.

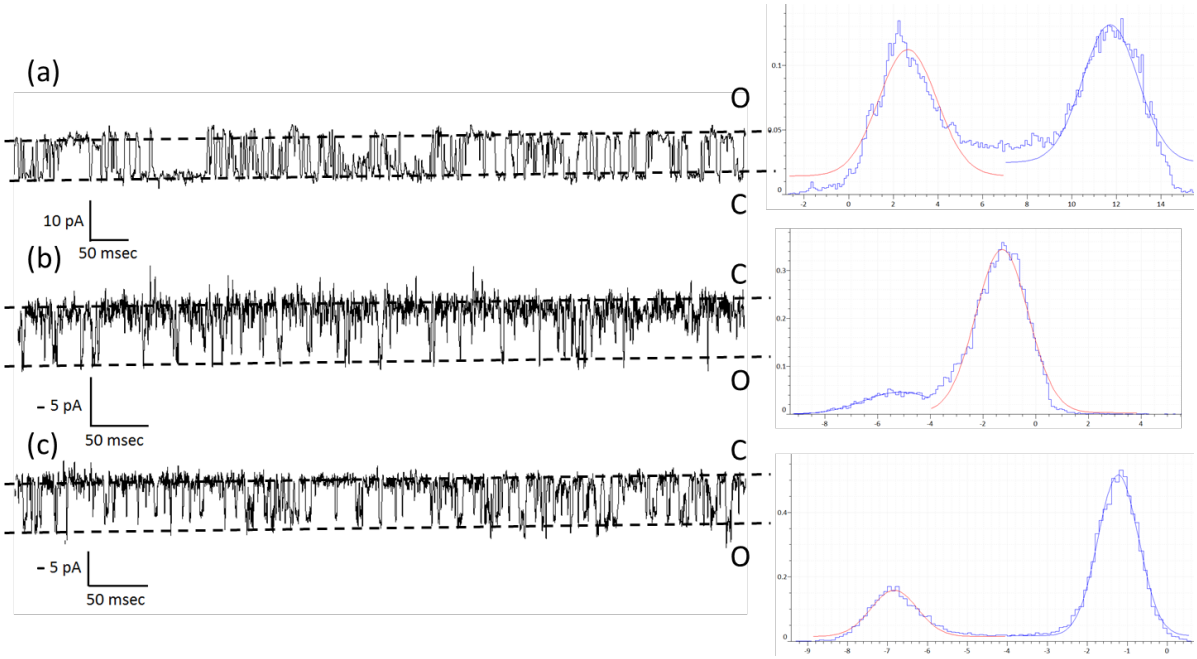

Figure 81: Na_vSp pore domain ion channel activity in a POPE:POPG (1:1 molar ratio) bilayer formed with the folding method in a shaped aperture with an inner diameter of 80 µm (500 mM NaCl, pH 4.0 in one compartment and pH 7.4 in the second compartment) at an applied potential of (a) 125 mV, (b) -125 mV, and (c) -150 mV. The panels on the right side are histograms of the adjacent current trace, where the y-axis represents normalised count and the x-axis the current signal in pA units. Current level 'C' corresponds to a closed channel and current level 'O' correspond to an open channel.

Since the channel was found to readily gate when a pH gradient was used, the voltage dependence of the Na_vSp pore was investigated with a pH 7.4 / pH 4.0 gradient. Traces displaying single-channel activity are shown in Figure 81 for 125 mV, -125 mV and -150 mV applied potential, together with a histogram analysis, while an I-V plot based on a larger range of voltages is shown in Figure 82. Rapid gating is observed for all fixed-value applied potentials, indicating that the Na_vSp pore domain is indeed not gated by voltage. Analysis of the data results in a conductance of 86.9 ± 0.3 pS at 100 mV for the Na_vSp pore domain under the given conditions of pH and ionic strength. The only reported single-channel conductance in the literature, obtained with patch clamp electrophysiology of Na_vSp pore domain constructs reconstituted into DPhPC giant

unilamellar vesicles [102], is a value of 31.1 ± 1.4 pS. This is 2.8-fold lower than the conductance value found determined in the present work, however the measurement conditions are not the same: Shaya *et al.* used asymmetric salt solutions, 110 mM KCl and 200 mM NaCl, at a symmetric pH of 7.0, while this work used a 3.2-fold higher 'average' salt concentration of 500 mM in both compartments, but with a pH gradient. Moreover, the activity of Na_vSp for Na^+ uptake experiments has shown to be low for PC-only vesicles that lack net negatively charged lipid species such as PG [240]. Although a direct comparison with the single-channel electrophysiology data of Shaya *et al.* could be achieved by additional experiments, with matching buffer solutions and lipid composition, the Na_vSp pore domain traces obtained with the bilayers in shaped apertures are in general agreement with the small number of published studies [102]. Moreover, a calcium channel blocker, nifedipine, which also blocks sodium channels [241, 242] was added to the aqueous chamber of the bilayer cell and inhibited the reconstituted Na_vSp pore (Figure 83). Due to insertion of multiple channel pores, the baseline was elevated to higher current value showing few closing events (Figure 83a), the frequency of these closing events increased with addition of drug (Figure 83b) until the baseline became flat (Figure 83c). It is noteworthy that the addition of the drug and perturbation of the aqueous solution following aspiration cycles to mix the drug did not result in bilayer failure. This highlights the applicability of the stable lipid bilayers formed in the shaped apertures for increasing the experimental throughput of the drug screening applications.

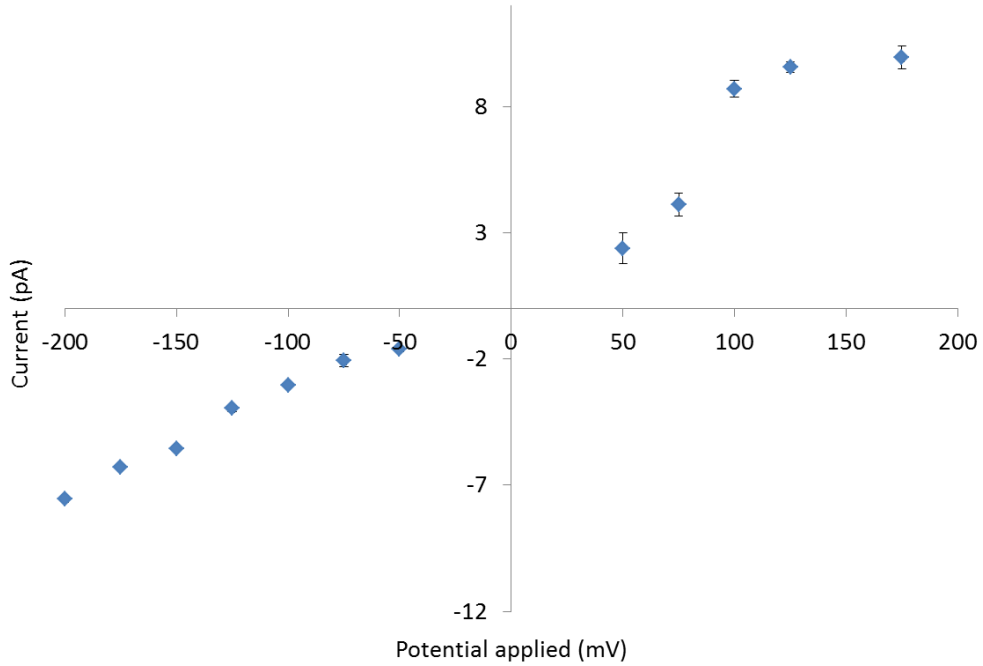

Figure 82: I-V plot for Na_vSp pore domain ion channel activity in a POPE:POPG (1:1 molar ratio) bilayer formed with the folding method in a shaped aperture with an inner diameter of 80 µm (500 mM NaCl, pH 4.0 in one compartment and pH 7.4 in the second compartment). The data were obtained from three different measurements, from which the standard deviation was calculated.

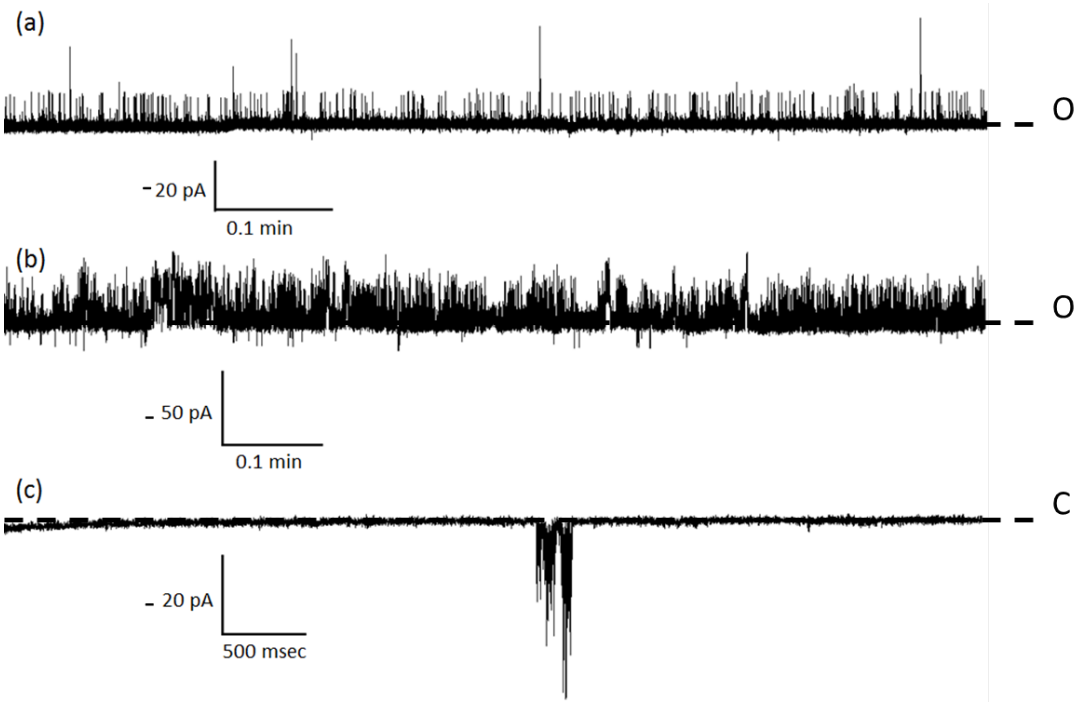

Figure 83: Effect of durg, nifedipine, on Na_vSp pore domain ion channel activity in a POPE:POPG (1:1 molar ratio) bilayer formed with the folding method in a shaped aperture with an inner diameter of 80 µm (500 mM NaCl, pH 4.0 in one compartment and pH 7.4 in the second compartment) at an applied potential of -100 mV. (a) no drug, (b) 1 µl, and (c) 3 µl of nitrendipine. The channel activity went from an elevated baseline with few closing events (a) to rigorous closing (b) to a quiet baseline (c) on addition of drug. Current level 'C' corresponds to a closed channel and current level 'O' corresponds to an open channel.

7.2.3 hERG ion channel electrophysiology

The pore domain, $hERG_{S5\text{-}S6}$, of the voltage-gated potassium channel hERG (section 2.5.2.4) was also reconstituted into the suspended bilayers using proteoliposome fusion. As for Na_vSp, there is only limited literature data on single-channel hERG or $hERG_{S5\text{-}S6}$ activity. As a starting point, a symmetrical buffer of 150 mM KCl buffered at pH 7 was used to study this protein, with a lipid composition of the suspended bilayer of POPC:POPG (1:1 molar ratio), as employed in used in previous studies of the KcsA potassium channel [97]. The current recordings obtained for $hERG_{S5\text{-}S6}$ are shown in Figure 84, with the current-voltage plot, derived from a larger number of recordings, in Figure 85. The trend of the I-V plot represents rectifying behaviour of $hERG_{S5\text{-}S6}$, which has also been reported in patch clamp electrophysiology studies for full-length hERG [109, 111] (refer to Figure **85** legend for analysis hypothesis). A single-channel conductance of 406.9 pS at 100 mV, and 123 pS at -100 mV, was obtained under the specified experimental conditions. The I-V plot reported by Kiehn *et al.* for full-length hERG (Figure 23a) is a mirror image of the I-V plot obtained here (Figure 85), which suggests that the $hERG_{S5\text{-}S6}$ was incorporated in the bilayer in the opposite orientation, giving the higher conductance at positive potential and the lower conductance at negative potential. However, the similarity of the I-V plots is striking, with the

conductance increasing linearly at one potential (inward direction) and reaching a plateau at the other potential (outward direction).

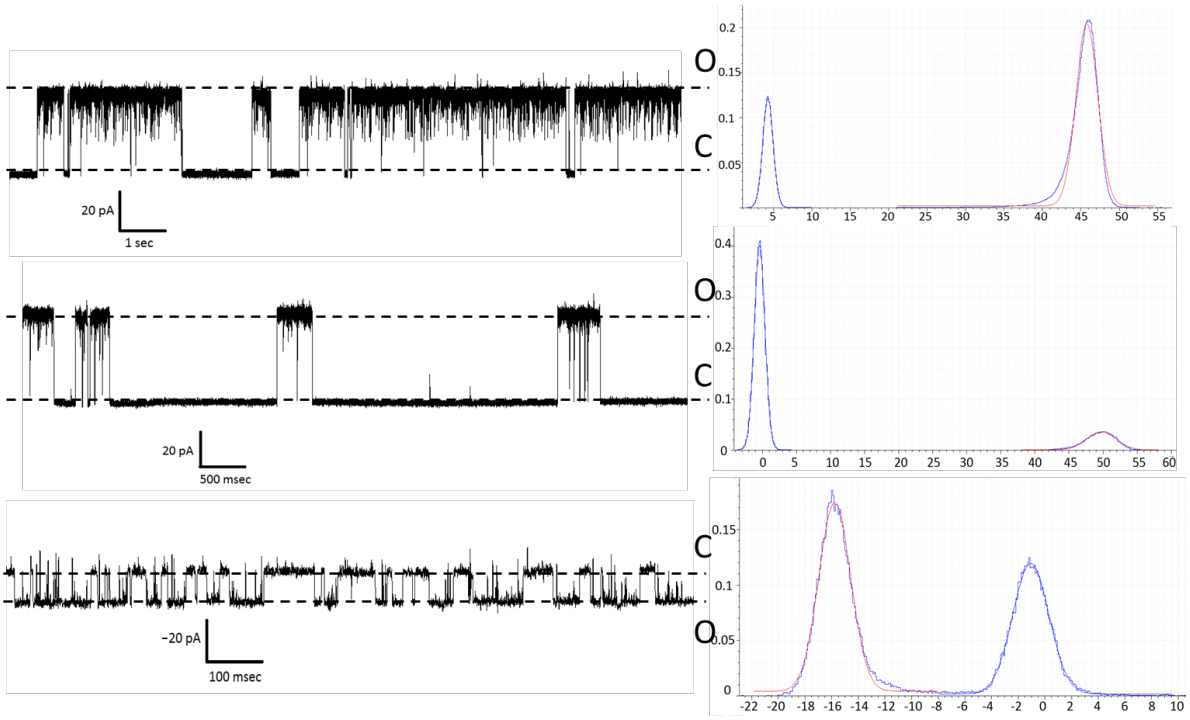

Figure 84: Single-channel activity of $hERG_{S5\text{-}S6}$ in a POPC:POPG (1:1 molar ratio) bilayer formed with the folding method in a shaped aperture with an inner diameter of 80 µm and a tip thickness of ~2 µm (150 mM KCl, 10 mM HEPES, pH 7.4) at an applied potential of (a) 100 mV, (b) 125 mV, and (c) -125 mV. The panels on the right side are histograms of the adjacent current trace, where the y-axis represents normalised count and the x-axis the current signal in pA units. Current level 'C' corresponds to a closed channel and current level 'O' corresponds to an open channel.

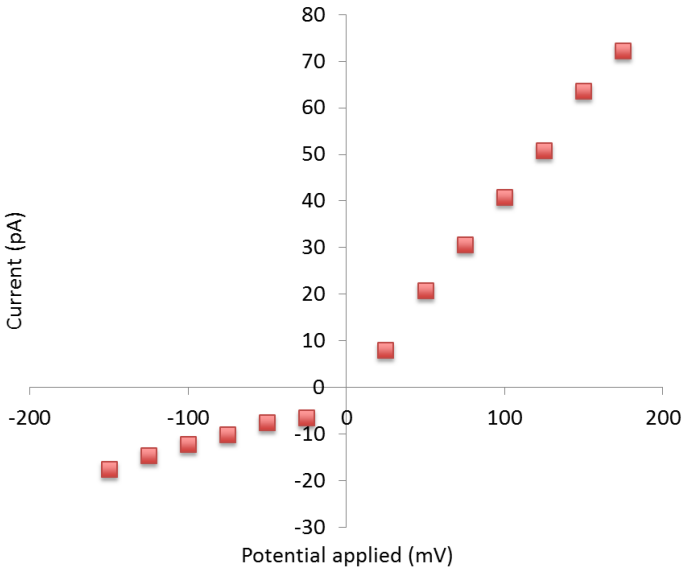

Figure 85: I-V plot for $hERG_{S5\text{-}S6}$ ion channel activity in a POPC:POPG (1:1 molar ratio) bilayer formed with the folding method in a shaped aperture with an inner diameter of 80 µm (150 mM KCl, 10mM HEPES, pH 7.4). In this analysis, the large current amplitude events have been considered for the positive potential and small current amplitude events have been considered for the negative potential.

Nevertheless, the conductance values obtained for $hERG_{S5\text{-}S6}$ are approximately 40-fold higher than the value of 9.7 pS determined for the full-length hERG channel with patch clamp

electrophysiology of *Xenopus* oocytes at 100 mM K^+ [109] and the value of 10 pS obtained with guinea pig atrial cells at 150 mM K^+ [111]. Recent studies with planar lipid bilayers also reported similar low conductances in PC:PE:cholesterol suspended bilayers for full-length channel hERG [110]. However, this study involved the hERG pore domain, $hERG_{S5\text{-}S6}$, rather than the full-length channel. In a preliminary characterization of $hERG_{S5\text{-}S6}$, Friddin *et al.* reported a single-channel conductance of 243 ± 29 pS at 150 mM KCl but also observed a smaller conductance of 37 ± 4 pS, obtained with cell-free expression of $hERG_{S5\text{-}S6}$, which self-inserted into an interdroplet bilayer of asolectin lipids [243]. A direct comparison between these data and the conductance obtained with the bilayers suspended in shaped apertures would require additional experiments with the same lipid composition. However it appears that the hERG pore domain by itself, i.e. dissected from the voltage sensing and other non-pore domains (Figure 22), gives a channel with a considerably higher conductance than the full-length hERG channel.

It was noted that the $hERG_{S5\text{-}S6}$ pore displayed some voltage dependence, as the application of a potential regularly initiated channel gating, as shown in Figure 86. Although this could potentially be explained by the fact that the sequence of the $hERG_{S5\text{-}S6}$ construct (residues 540-673 from UniProtKB sequence database entry Q12809) overlaps to some extent with the voltage sensing domains of full-length hERG, the exact boundaries of these domains are unknown and identification of the sites that contribute to voltage sensing requires a set of pore domains that have been dissected at different positions in the protein sequence. As with the experiments on the Na_vSp pore domain, it should be emphasized that the stable bilayers in the developed shaped apertures enabled collection of a substantial data set in a relatively short amount of time.

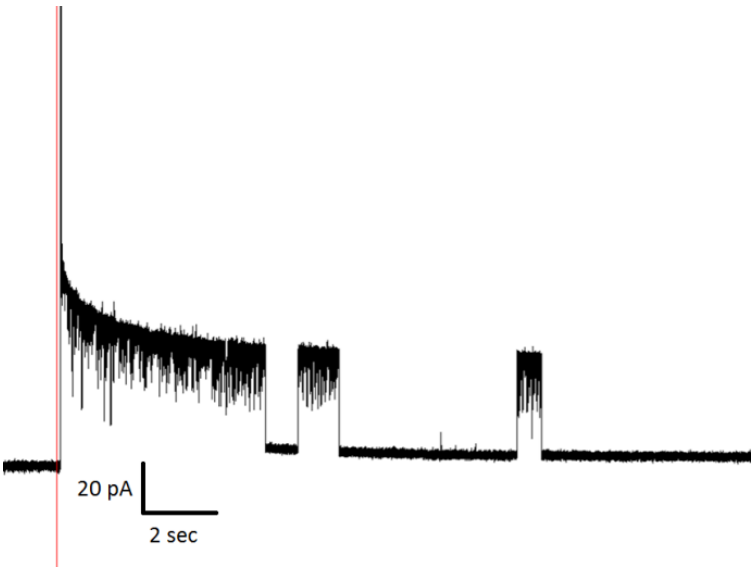

Figure 86: Voltage dependence of $hERG_{S5\text{-}S6}$ ion channel activity in a POPC:POPG (1:1 molar ratio) bilayer formed with the folding method in a shaped aperture with an inner diameter of 80 µm and a tip thickness of ~2 µm (150 mM KCl, 10 mM HEPES, pH 7.4) at an applied potential of 100 mV. The red line marks the application of the potential.

7.2.4 α-Hemolysin electrophysiology

Finally, the water-soluble α-hemolysin channel was introduced in one of the two aqueous compartments. A stepwise increase in bilayer current was observed, typical for sequential insertion of multiple non-gating α-hemolysin nanopores. The trace in Figure 87 shows six current steps, representing a single-pore conductance of 1.64 nS, in agreement with literature values for the conductance of this well-characterised toxin [244].

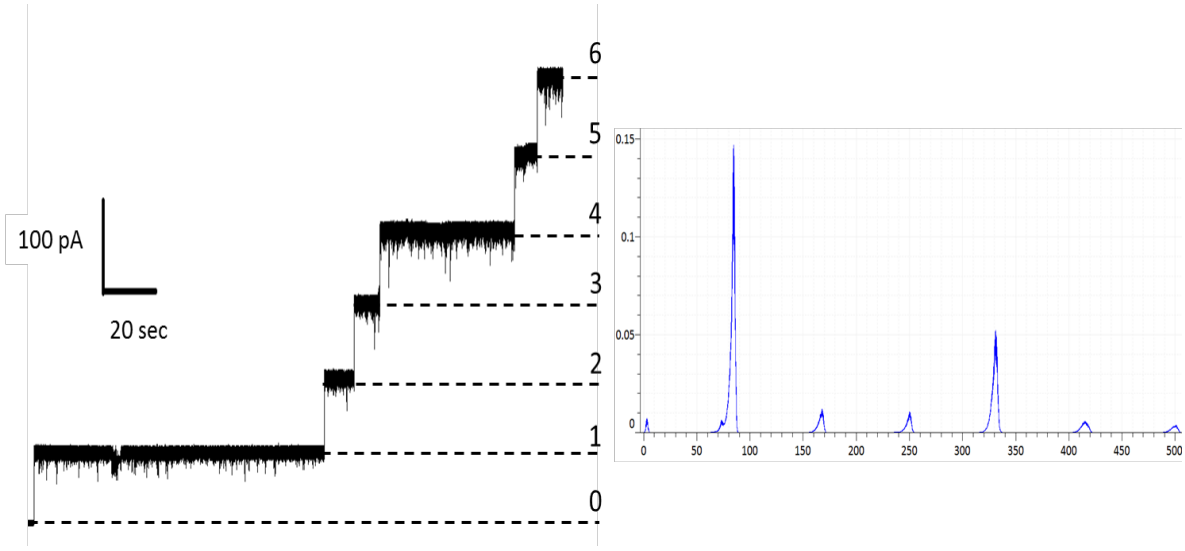

Figure 87: α-Hemolysin single-channel activity in a POPC:POPG (1:1 molar ratio) suspended bilayer painted with a lipid-decane solution on a shaped aperture with an inner diameter of 80 µm and a tip thickness of ~2 µm. The applied potential is 50 mV and the buffer solution is 2 M KCl, 10 mM HEPES, pH 7.4. The trace shows formation of six channels in the bilayer, each having a typical current step of 82 pA. The panel on the right shows the normalised histogram of the current trace, with current (pA) on the x-axis and data point counts on the y-axis.

7.3 Conclusions

While the previous chapter demonstrated that the developed shaped apertures enabled the formation of stable suspended bilayers, it was investigated in the present chapter whether these bilayers were suitable for protein ion channel electrophysiology. First, a well understood potassium ion channel, KcsA, was reconstituted into the bilayer by proteoliposome fusion, resulting in bilayer traces with single-channel activity. Analysis of these revealed a conductance, open probability, and voltage-current relationship of KcsA that were all in agreement with the literature. It has been suggested that bilayers with a diameter smaller than approximately 30 µm do not support proteoliposome fusion and hence that integral ion channels such as KcsA cannot be incorporated in bilayers that are too small [14, 245-247], which may be due to unstirred layer effects in high aspect ratio apertures [248]. This relation between bilayer size and ion channel activity was indeed observed with the shaped apertures: bilayers in 80 µm diameter apertures more readily gave KcsA channel activity than smaller bilayers in 60 µm diameter apertures. Hence,

for further electrophysiological studies, shaped apertures with an internal diameter of 80 µm were used. Two channels were characterised, with the main aim of obtaining a substantial data set for these 'novel' constructs, i.e. the pore domains of the Na_vSp sodium channel and of the hERG potassium channel, and to compare the data with the small number of relevant electrophysiology publications. Single-channel traces for both pore domains were readily obtained, enabling the exploration of several electrophysiology parameters. The Na_vSp pore showed a pronounced dependence of the gating activity on pH, while the hERG pore had a substantially larger single-channel conductance than reported for full-length hERG, but there is no literature that contradicts these findings and from a general perspective these sodium and potassium channel pore domains displayed expected behaviour in the suspended bilayers, as did the water soluble protein toxin α-hemolysin. Application of the stable lipid bilayers formed in shaped apertures for enhancing the experimental throughput of drug screening was demonstrated by introduction of a channel blocking drug for Na_vSp into the aqueous chamber of the bilayer cell without bilayer failure. Because aperture-suspended bilayers are also suitable for optical, rather than electrical, studies of biomembranes, the use of shaped apertures in an optically accessible configuration was also explored, which is the subject of the next chapter.

Chapter 8 Optically accessible lipid bilayers

Ion channel studies can also be performed with optical techniques, but these require that the bilayer is optically accessible, which is not the case for standard electrophysiology chambers. This chapter describes the development of a chip implemented in the transparent polymer PMMA that enables optical microscopy of aperture-suspended bilayers. The bilayer and the solvent annulus could be visualized inside shaped apertures and channel-tracking trial experiments were performed with KcsA labeled with a fluorescent quantum dot.

8.1 Materials and methods

8.1.1 Fabrication of PMMA chips

For optically accessible bilayers, the resist sheet was clamped in a home-made microfluidic chip of poly(methyl methacrylate) (PMMA) as shown in Figure 88, giving a distance from the aperture to the surface of the glass coverslip of ~300 µm. The bottom PMMA layer of the chip contained a microfluidic channel of 700 µm width and 18 mm length in a layer of 200 µm thick PMMA which was coated with 467MP adhesive tape (3M, USA) on both sides. The top PMMA layer, of 3 mm thickness and coated on one side with adhesive tape, contained a compartment of 10 × 5 mm and access holes that connect to the start and end of the channel in the bottom layer. The PMMA sheets, including channel, compartment and access holes, were cut using a mini laser

system (Epilog, USA) operating in vector mode. The bottom channel was cut with a laser power of 100%, scan speed of 70% and frequency of 5 kHz, while the top compartment was cut with a lower scan speed of 5%. After cutting the top compartment and the bottom channel, the protective coating was removed to expose the sticky side of the tape. A resist film with a shaped aperture was carefully aligned such that the aperture was in the centre of the bottom channel. The PMMA chip was mounted on a Zeiss Axiovert 200 inverted fluorescence microscope for optical imaging of the painted horizontal bilayer. Customised filter blocks were used for imaging the quantum dot labelled KcsA.

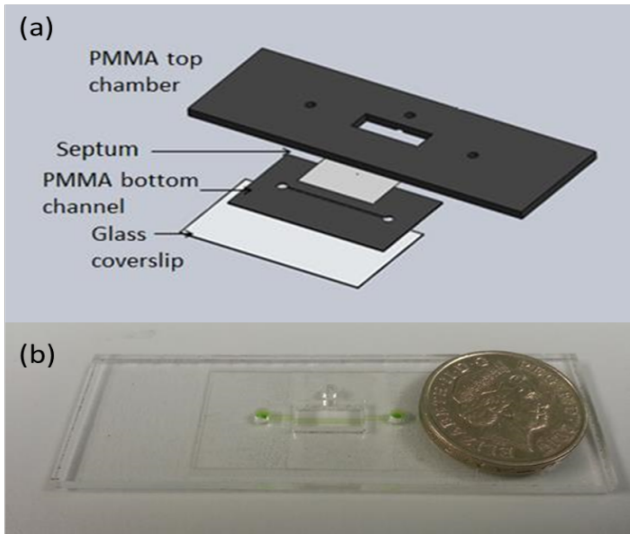

Figure 88: (a) Schematic deconstructed view of the PMMA chip for the formation of horizontally oriented optically accessible aperture-suspended bilayers. Double-sided adhesive tape, attached to the PMMA layers, was used to clamp the resist sheet with the aperture inside the chip. The distance of the aperture from the surface of the glass coverslip was ~300 µm. (b) Photograph of the PMMA chip with a SU8 sheet clamped in the chip. The bottom channel is filled with a green dye.

8.1.2 Bilayer formation

Aperture-suspended bilayers were prepared with the painting method. Lipids were dissolved in decane at a total lipid concentration of 20 mg/ml by solvent solubilization of a mixed lipid film, obtained by mixing and drying of lipid stock solutions in chloroform. The lipid-solvent solution was painted on the aperture, accessed through the top compartment, with a Sable 0000 paint brush after the top compartment and the bottom channel were filled with buffer. To promote solvent draining and bilayer formation, the buffer solution in the top compartment was aspirated into a 1 ml disposable pipette and then reintroduced into the compartment [137].

8.1.3 Proteoliposomes with quatum dot labelled KcsA

The potassium channel KcsA was expressed, purified, labelled with a pegylated quantum dot (Qdot® 800 ITK™ amino (PEG) quantum dots, Lifetechnologies, USA) and reconstituted into lipid vesicles by Dr Andrew M. Powl (Birkbeck College, University of London, UK). The quantum dots had a size of 21 nm, extinction coefficient measured at 550 nm of 1,700,000 M^{-1} cm^{-1} and emission maxima of 800 nm. Each KcsA subunit was labelled with a quantum dot, giving four quantum dots per tetrameric KcsA channel. Reconstitution of proteins into lipid vesicles was performed by detergent depletion, as described in section 7.1.1. Bio-Beads SM-2 (Biorad Laboratories, Hemel Hempstead, UK) were cleaned in methanol for 30 mins followed by thorough rinsing with electrophysiology buffer (150 mM KCl, 10 mM HEPES, pH 7.4). Phospholipid solutions in chloroform were mixed in the desired combination and dried onto the walls of a glass vial as a mixed lipid film. The lipid film was subsequently dissolved in 1 ml of reconstitution buffer (β-D-octyl glucoside, 150 mM KCl, 10 mM HEPES, pH 7.4), with bath sonication to clarity for at least 30 min. KcsA in detergent solution was added to achieve a 6000:1 molar ratio of lipid to KcsA tetramer. The β-D-octyl glucoside detergent (SIgma Aldrich, St. Louis, MO) was gradually removed by an initial one-hour incubation with 80 mg of washed biobeads, followed by a second one-hour incubation with 80 mg of fresh biobeads. The dispersion of proteoliposomes was then removed from the biobeads and stored at -85 ^{o}C until use.

8.2 Results and discussion

8.2.1 Optical microscopy of lipid bilayer

Before the formation of a lipid bilayer in the PMMA chip, the aperture was imaged without and with buffer solution in the chip. Figure 89 shows optical micrographs of a beak-shaped aperture , taken with a 20× objective lens having NA of 0.6. The images show the aperture when the chip is empty, with buffer solution in the bottom channel, and with buffer solution in the channel and the top compartment. The grid pattern on the septum surface, typical for two-photon lithography apertures, is clearly visible while the aperture itself does not show any features.

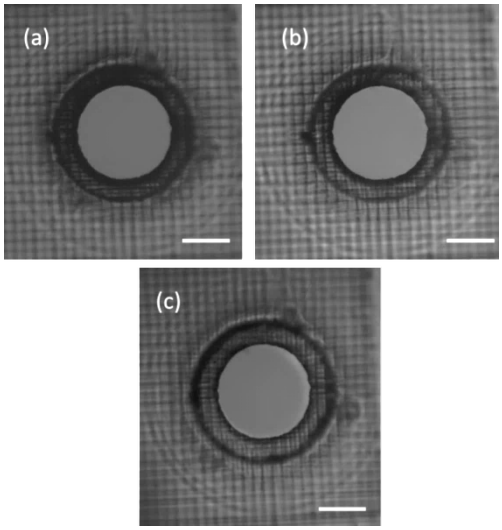

Figure 89: Bright field optical micrograph of a beak-shaped SU8 aperture mounted in the PMMA chip, with (a) no buffer in both the compartments, (b) buffer only in the bottom compartment, and (c) buffer in both the top and bottom compartment. The scale bars are 50 µm.

Figure 90 shows four different bilayers formed by the painting method in the PMMA chip: different experiments result in bilayers of different size, with smaller bilayers being surrounded by a wider solvent annulus. It should be noted that the thinning of the lipid-oil mixture to form a lipid bilayer (section 2.3.1) was not always spontaneous and was promoted by the air exposure technique [137]. As mentioned in Chapter 6 and 7, and as can be seen in these images, bilayers formed with the painting method are of variable area, consistent with other studies [55].

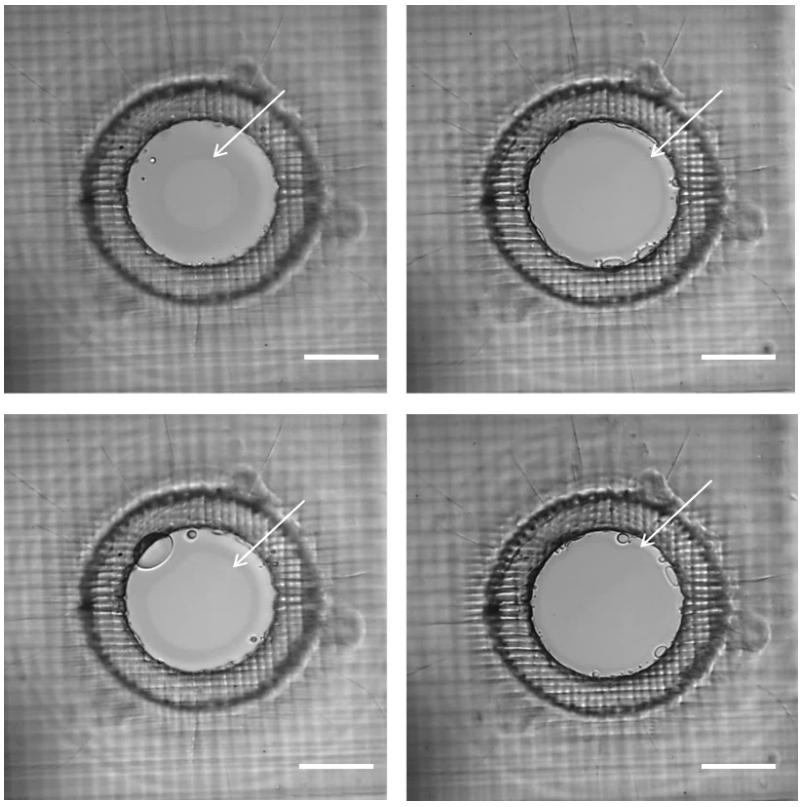

Figure 90: Optical micrograph of a beak-shaped SU8 aperture mounted in the PMMA chip showing bilayers of different area (light grey), with the surrounding solvent annulus (dark grey), with the arrows pointing to the circumference of the lipid bilayer. The bilayers were painted with a DPhPC/fluo-DOPE/decane mixture. The scale bars are 50 µm.

Figure 4 a and b show bright field and fluorescence images of a painted bilayer. The bright field image shows the interface between the bilayer and the decane annulus as a transition from a lighter to a darker region. Because the lipid-oil mixture also contained a fraction of fluorescent lipids, the decane annulus, with solubilized lipids, is clearly visible in the fluorescent image. The slope of the fluorescence intensity profile (Figure 4 b, inset) reflects the gradient in thickness of the annulus, with thicker regions containing more fluorescent lipid. Based on the diameter of the decane-lipid annulus and the co-localization of the focal planes of the tip of the aperture and the bilayer-annulus interface, it was concluded that the bilayer was formed at the narrowest part of the aperture.

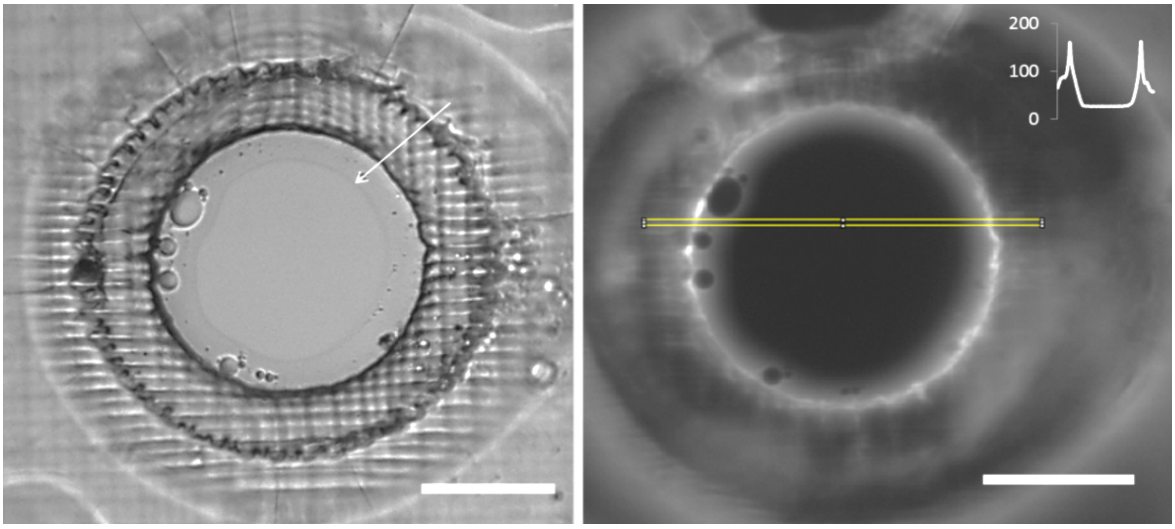

Figure 91: (a) Bright field and (b) fluorescence image of a beak-shaped SU8 aperture in a PMMA chip painted with a DPhPC/fluo-DOPE/decane mixture. The arrow points to the circumference of the lipid bilayer in the bright field image (a), while the yellow box is the area from which the fluorescence intensity cross-section (inset) is taken in the fluorescence image (b).. The scale bars are 50 µm.

Next, horizontally oriented lipid bilayers were formed in apertures fabricated with grayscale lithography. In contrast to the apertures produced with two-photon lithography, distinct surface features were not apparent but the aperture walls appear to consist of discrete rings (Figure 92), which probably correspond to the thickness steps in the SEM cross-section depicted in Figure 69. The aperture itself does not show any features in the absence of a painted bilayer. When lipid a solution was painted on the aperture, different experiments resulted in different bilayer areas as shown in Figure 93 where the circumference of the formed bilayer, or the bilayer-annulus boundary, is indicated by arrows.

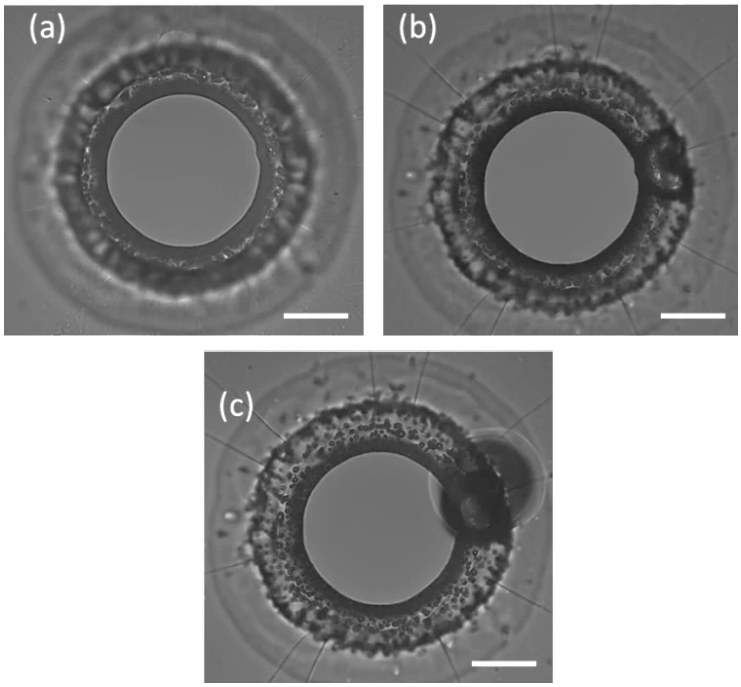

Figure 92: Optical micrographs of a beak-shaped TMMF aperture mounted in the PMMA chip, with (a) no buffer solution in the compartments, (b) buffer only in the bottom compartment, and (c) buffer in both the top and bottom compartments. The dark circle in (c) is an air bubble. The scale bar are 50 μm.

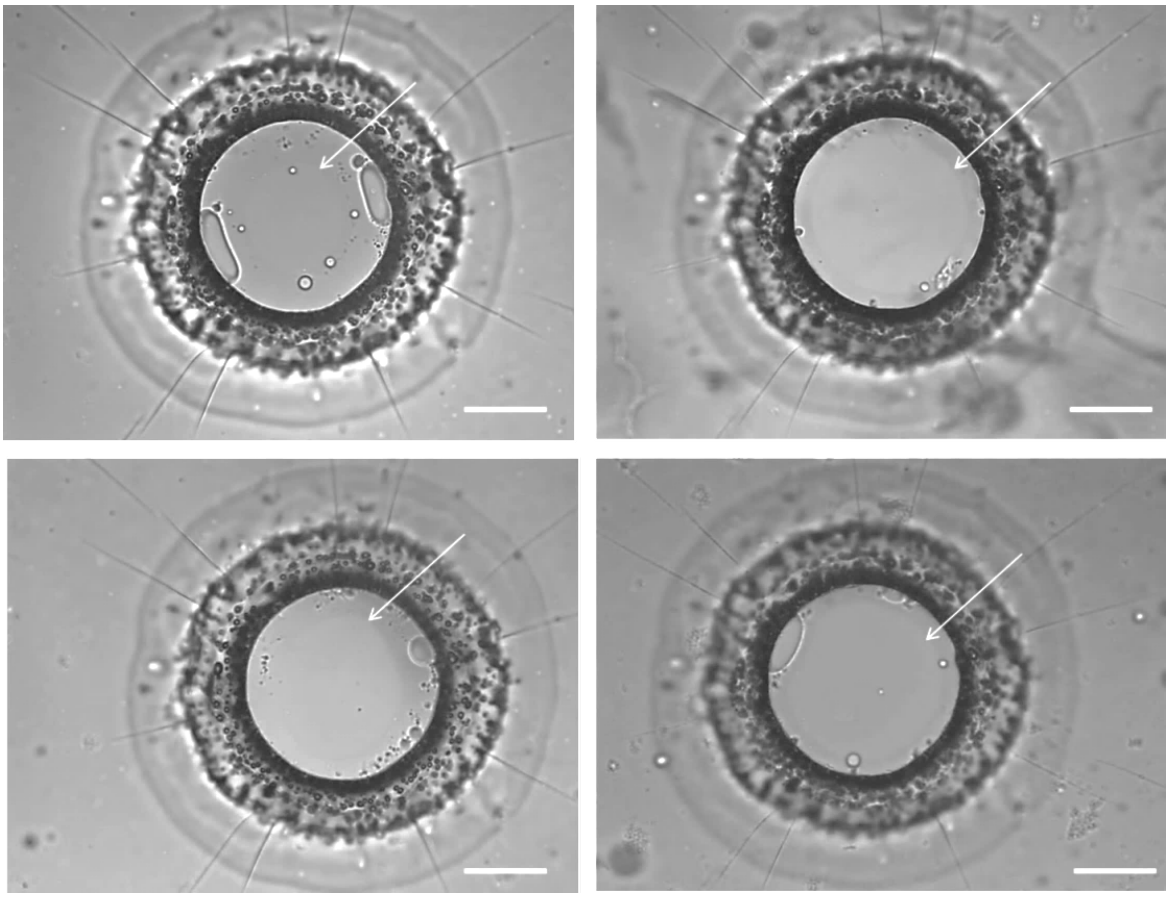

Figure 93: Optical micrograph of a beak-shaped TMMF aperture in TMMF mounted in a PMMA chip. Bilayers are painted with a POPC:POPG (1:1 molar ratio) lipid mixture in decane. Four different experiments each result in a different bilayer area. The arrows point out the circumference of the lipid bilayer. The scale bars are 50 μm.

8.2.2 Quantum dot labelled KcsA

There are many questions in membrane research that can be addressed by tracking of (fluorescently labeled) proteins or protein subunits in a lipid bilayer [249, 250]. Of particular interest for the lipid bilayer electrophysiology technique is the incorporation of ion channels in the lipid bilayer by vesicle fusion. Although various methods have been developed to promote the fusion of proteoliposomes with planar lipid bilayers [77], the mechanism of protein delivery is not understood in detail. The number of vesicles added to the aqueous compartment is in the order of 10^9-10^{10}, with each vesicle typically carrying tens of ion channels, but still only a handful of active channels are observed in the bilayer [251]. To visualize KcsA proteoliposomes and bilayer-incorporated KcsA channels, KcsA monomers in detergent solution were labelled with quantum dots (Qdots) by Dr Andrew Powl following the conjugation protocol of the supplier, but the effectiveness of this procedure was not verified. Ideally, after reconstitution in a proteoliposome, KcsA would be present as tetrameric channels that were each labelled with four quantum dots through PEG polymer linkages. Qdots were used instead of chemical fluorophores as they offer several advantages such as a higher signal to noise ratio due to brighter emission and reduced photobleaching, which makes them suitable for continuous tracking studies [252].

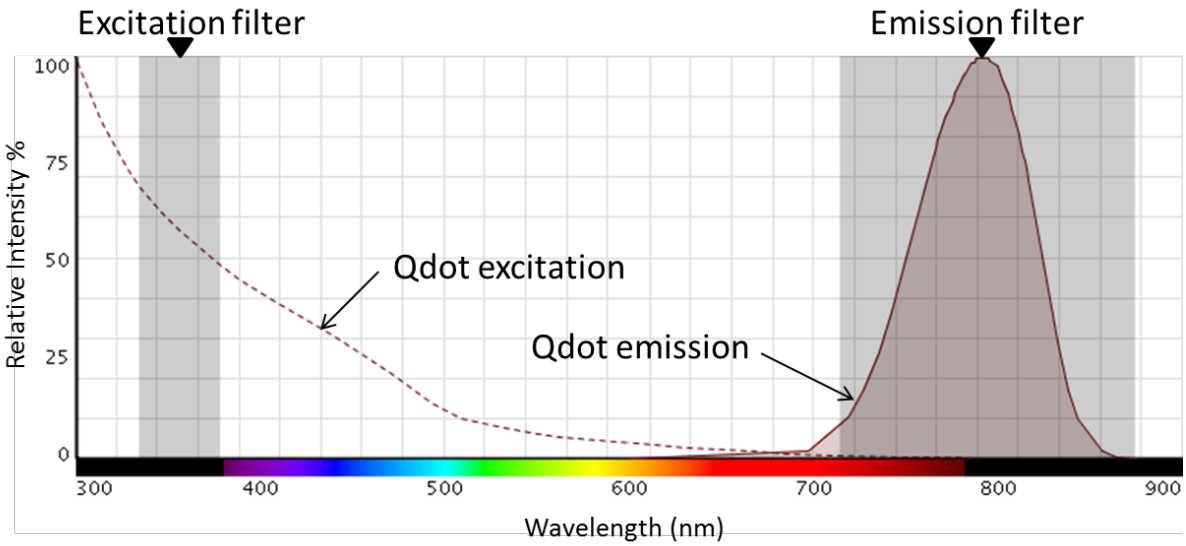

Figure 94: Plot of relative intensity vs wavelength showing excitation and emission of Qdot 800 ITK. Greyed out regions represents the excitation and emission spectra of filter block used for imaging the signal, overlapping most of the emission spectra of the Qdot.

Figure 94 depicts the excitation and emission bands of the employed Qdot. The emission peak is well-defined but in order to attain a high signal to noise ratio between fluorescence light and background light, the selection of appropriate filters is crucial. While the excitation filter passes wavelength of light necessary for excitation of the Qdot, the emission filter transmits light

of the emitted fluorescence wavelength and blocks any excitation light[9]. A filter cube was assembled an excitation band pass of 337-377 nm and an emission band pass of 714-874 nm.

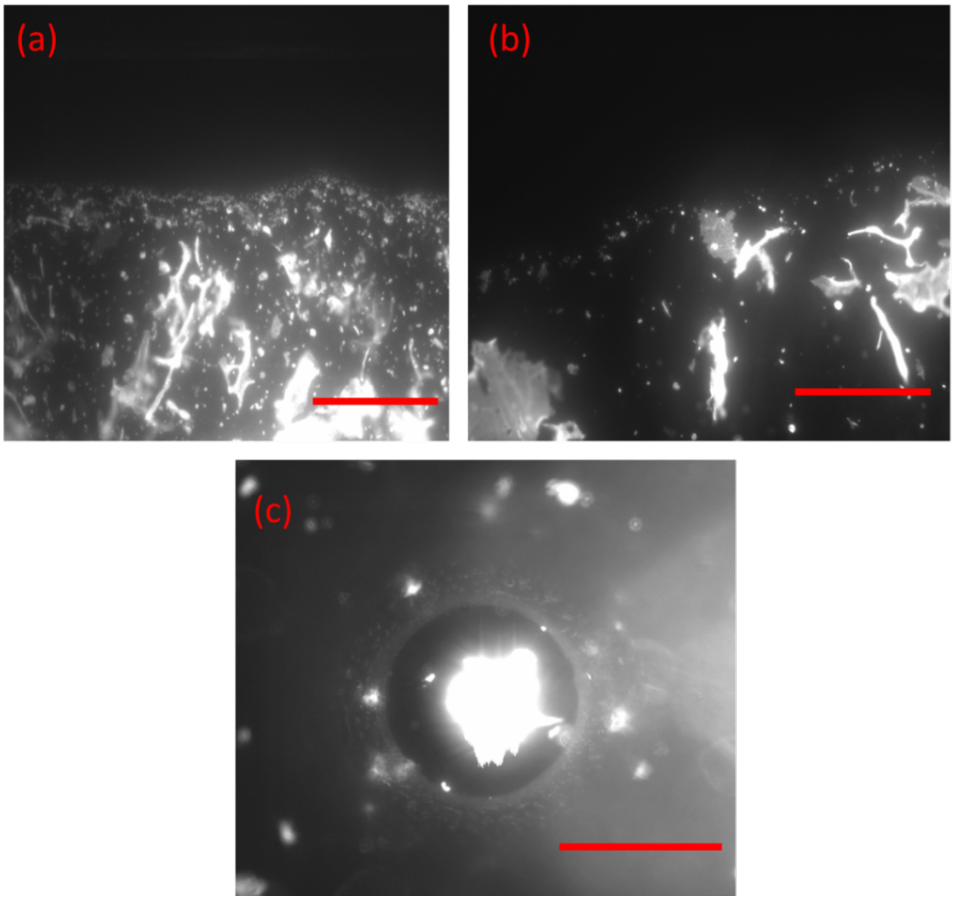

Figure 95: Fluorescence images of a drop of Qdot-KcsA proteoliposome suspension on a glass slide: (a) no dilution, and (b) 10-fold dilution in water. (c) Fluorescence image after addition of 1 µl of undiluted proteoliposome suspension into the top compartment of a PMMA chip having a lipid bilayer painted on a TMMF beak-shaped aperture. The scale bars are 100 µm.

First, a suspension of Qdot-KcsA proteoliposome was imaged to confirm the suitability of the assembled filter cube for imaging of the Qdots. A drop of proteoliposome suspension was placed on a glass slide and, as shown in Figure 95, a strong fluorescence signal was observed. The suspension was diluted in an attempt to visualize individual Qdot-KcsA proteoliposomes, but it appeared that the Qdots were present in an aggregated state. Assuming that the Qdots were all attached to the proteoliposomes, either the liposome-protruding Qdots themselves were prone to aggregation, or the proteoliposomes had a tendency to aggregate. Qdots functionalised with amine-derivatized PEG were used and it is known that encapsulation of the quantum dots in a polymer like poly(ethylene glycol) (PEG) reduces aggregation [253, 254], but this would have to be verified for Qdots suspended in electrophysiology buffer in the absence of liposomes. However, these control experiments were not performed due to the small volume of the Qdot stock solution.

[9] Nikon website. http://www.nikon.com/products/instruments/lineup/option/filters/. Date accessed 12/11/2013

When the proteoliposome suspension was added to the top compartment of the PMMA chip, the suspended bilayer failed within a few tens of minutes. This bilayer stabilization could have been caused by a variety of factors, including deposition of Qdot-KcsA proteoliposome aggregates on the bilayer or deposition of (free) Qdot aggregates on the bilayer. In general, a horizontally oriented bilayer will be susceptible to sedimenting aggregates, whereas a vertically oriented bilayer, as in a typical bilayer electrophysiology configuration, is not. However, non-conjugated mono-disperse nanoparticles, if present, could also permeabilize the lipid bilayer [255]. Although aggregation of Qdots can be avoided by employing basic conditions [256], it could not be used because KcsA is a proton-activated ion channel and thus requires acidic conditions for combined optical-electrical studies.

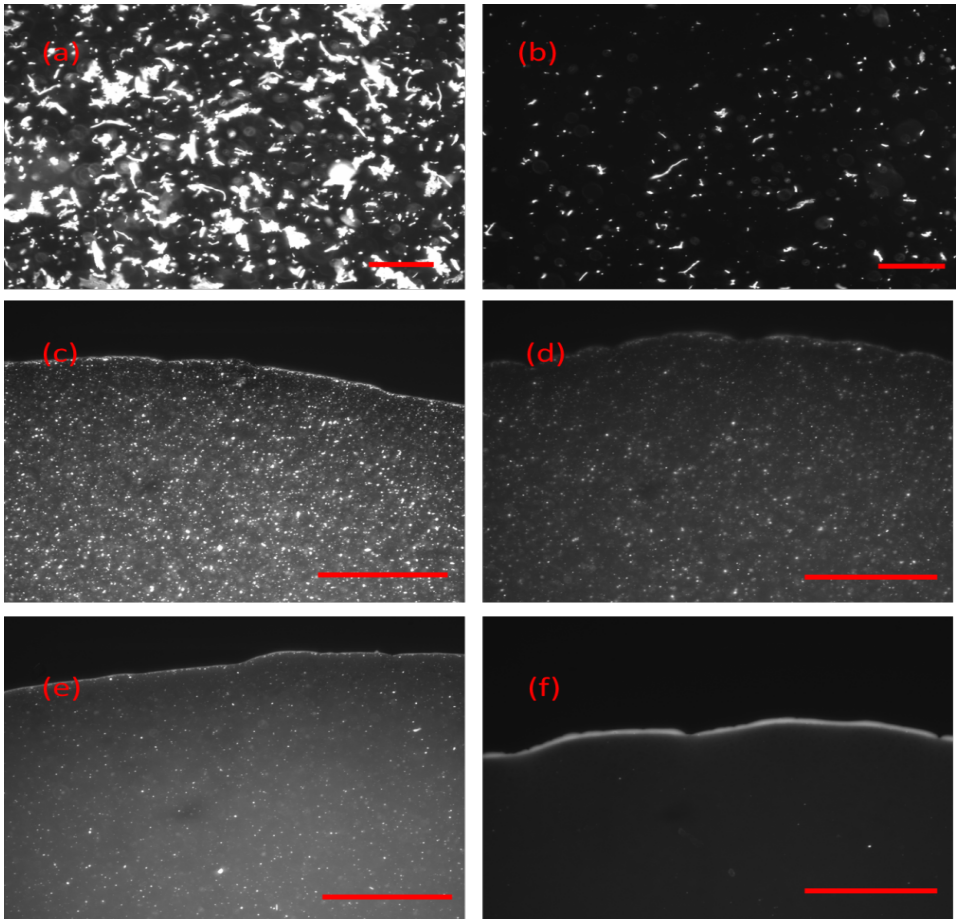

Figure 96: Fluorescence images of a drop of Qdot-KcsA proteoliposome suspension on a glass slide: (a) 10x dilution of original proteoliposome suspension (150 mM KCl) in a solution of 1 M KCl, (b) 10x dilution of original suspension in 20 mM KCl, (c) 10x dilution of original suspension in 1 M KCl with 30 sec bath sonication, (d) 10x dilution of original suspension in 20 mM KCl with 30 sec bath sonication, (e) 10x dilution of original suspension in 1 M KCl with 120 sec bath sonication, and (f) 10x dilution of original suspension in 20 mM KCl with 120 sec bath sonication. The scale bars in (a,b) are 50 µm and the scale bars in (c-f) are 200 µm.

Therefore, the Qdot-KcsA proteoliposome suspension in 150 mM KCl was diluted in a high-salt solution (1 M KCl) and also in a low-salt solution (20 mM KCl). It was found that when both these dilutions were sonicated, most of the aggregates were dispersed, as shown in Figure 96. Since an increase in ionic strength shields the particle surface charge, allowing the particles to approach each other until the attractive forces such as the Van der Waals force become strong

enough to cause agglomeration of the particles [257], dilution in low ionic strength solution in combination with sonication was preferred.

An optically mono-disperse Qdot-KcsA proteoliposome suspension was introduced into the top compartment of the PMMA chip after the formation of a suspended lipid bilayer, and bright field and fluorescence images were taken. As shown in Figure 96, when the lipid bilayer was in bright field focus, a single point source could be observed in fluorescence mode in the lipid bilayer. This point source slowly moved towards the periphery of the bilayer. It could not be established whether this point source was a free non-conjugated Qdot, or KcsA-conjugated KcsA, or a Qdot-KcsA proteoliposome adsorbed to the surface of the bilayer. If this signal originated from Qdot-labelled KcsA incorporated in the bilayer, these images would represent a slow migration of the channel from the bilayer towards the annulus. As the channel would not be functional in the annulus oil film, such outward diffusion could explain why despite addition of a large number of vesicles only a few active ion channels are observed in the bilayer. However, these trial experiments require extensive control experiments and the preliminary data presented here serve only to illustrate potential optical studies with stable bilayers in horizontally oriented bilayers suspended in shaped apertures.

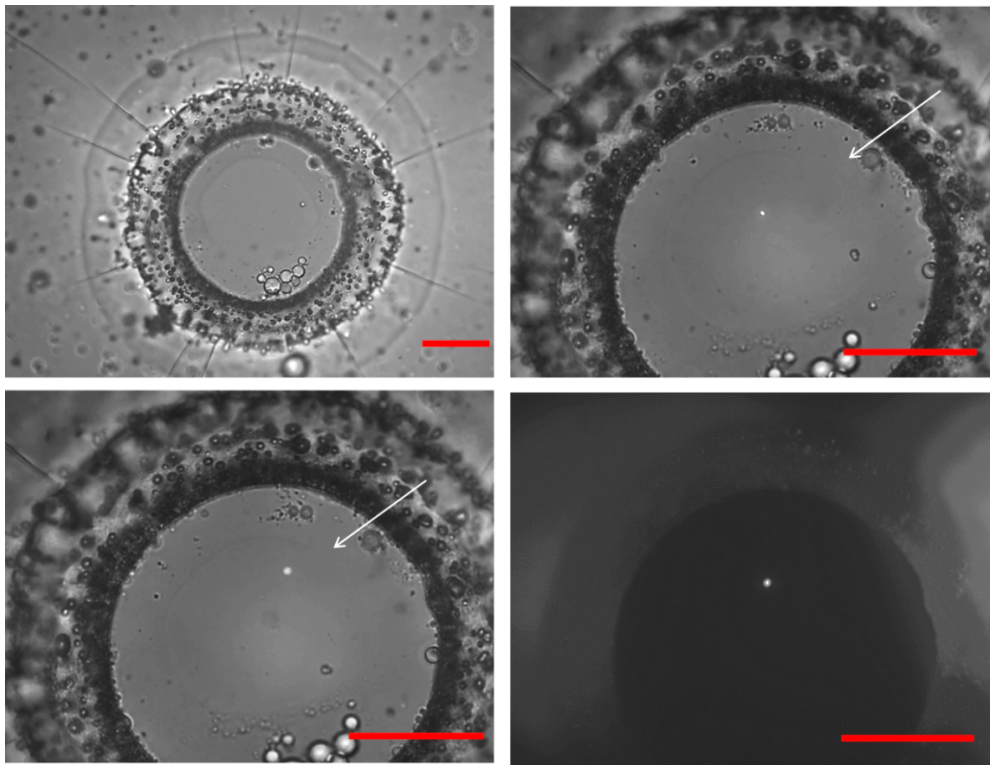

Figure 97: Bright field image with fluorescence signal and only fluorescence (bottom right) image of a lipid bilayer painted with a POPC:POPG (1:1 molar ratio) lipid mixture in decane, in a beak-shaped TMMF aperture in a PMMA chip. The Qdot-Kcsa proteoliposome suspension was 10x diluted in 20 mM KCl and sonicated before addition to the top compartment. A fluorescence point source was visible in the plane of the bilayer. The arrows point to the circumference of the bilayer. The scale bars are 50 µm.

8.3 Conclusions

Ion channel studies, and membrane protein studies in general, can also be performed with optical techniques, but these require that the bilayer is optically accessible, which is not the case for standard electrophysiology chambers. In this chapter a PMMA chip was developed in which shaped apertures were clamped for formation of horizontally oriented bilayers that could be visualized with an optical microscope. Lipid bilayers, formed by the painting method, could be visualized together with the surrounding solvent annulus. Consistent with previous studies and with the electrophysiology experiments discussed in Chapters 6 and 7, different bilayer areas were observed for different bilayer formation experiments, confirming the limited reproducibility of the painting method. Optical microscopy of proteoliposome suspensions, with Qdot-labelled KcsA, showed extensive aggregates, and addition of this suspension to the top compartment of the PMMA chips led to bilayer failure within tens of minutes. Breaking of the bilayer could either be a general problem of horizontally oriented bilayers, which are exposed to sedimenting aggregates, or could be a result of the interaction of free Qdots with the bilayer. Regardless, extensive aggregation was not apparent after 10-fold dilution of the Qdot-KcsA proteoliposome suspension in a low ionic strength solution of 20 mM KCl, followed by mild bath sonication. Following addition of this optically mono-disperse sample to the top compartment of the PMMA chip, a single point source could be observed in the plane of the bilayer, which diffused towards the annulus. Although further experiments are required to confirm that such signals originate from bilayer incorporated Qdot-labeled KcsA channels, this preliminary work demonstrates the use of stable aperture-suspended bilayers for optical studies, which could also be combined with electrical measurements of ion channel activity.

Chapter 9 Conclusions and Future outlook

9.1 Summary

Biological membranes define boundaries in living cells and sub-cellular organelles [32] and represent the first point of contact between host receptors and foreign agents such as antibiotics and viruses [41]. Membranes also function as scaffolds for membrane proteins, including the ion channels that allow exchange of ions across an otherwise insulating biological membrane [6]. Since ion channels play an important role in various physiological processes as highlighted in Chapter 1 and 2, they are fundamental to biology and medicine. However, the development of a platform for ion channel characterisation has been particularly challenging because the channels should be present in an experimentally accessible membrane [14]. Electrophysiology, in particular the patch clamp method, has been the gold standard for ion channel characterisation because it is capable of measuring the ion flow through the channel and is suitable for activating voltage-gated channels. However, the inherently complex multi-component nature of natural membranes has been a limiting factor for their utility in many technological and industrial applications [41]. As a consequence, simplified artificial model membrane systems, as described in section 2.3, have been developed for membrane studies in general and ion channel studies in particular.

This thesis concerns the fragility of lipid bilayers that are suspended over apertures in a hydrophobic septum, a configuration in which current flowing over the model membrane, through incorporated ion channels can readily be measured. In Chapter 3, the interdependence of various parameters such as aperture diameter, septum thickness, bilayer stability and protein

delivery has been outlined and the development of shaped apertures in a photoresist septum was proposed. In shaped apertures, as opposed to conventional cylindrical apertures, bilayers could be stabilised by a micrometer thin aperture edge rather than a decrease in aperture area, which is important for proteoliposome-facilitated ion channel incorporation in the bilayer. Based on the desired properties of a septum material, outlined in section 3.1.2, films of 50 µm thickness of the resists SU8 and TMMF were selected, the electrical, chemical and mechanical properties of which are similar to the conventional septum material Teflon. As described in Chapter 4, beak- and triangle-shaped apertures were fabricated in SU8 films by two-photon laser lithography. Although slow and low-throughput, this flexible 3D patterning technique enabled initial bilayer stability measurements and identification of suitable aperture geometries. A parallel, higher throughput, grayscale lithography process for the fabrication of triangle- and beaked-shaped apertures was subsequently developed in Chapter 5.

A remarkable enhancement in lifetimes and mechanical stability of the lipid bilayers was demonstrated in Chapter 6 for shaped apertures with a tip thickness of 2 µm. Bilayer stability in these apertures was not affected when the diameter of the aperture was increased from 60 to 80 µm, which is important because the ion channel measurements in Chapter 7 highlighted that ion channel incorporation by proteoliposome fusion occurs more readily with bilayers in the larger, 80 µm diameter, apertures. The stable aperture-suspended bilayers enabled the collection of substantial data sets of high-quality current recordings of the KcsA potassium channel and of pore domains of the hERG potassium channel and the Na_vSp sodium channel. Further exploiting the enhanced bilayer stability, drug modulation of the Na_vSp activity, which involves perturbation of the aqueous solution, was measured in section 7.2.2. Finally, a PMMA chip was developed in Chapter 8 to visualise horizontally oriented aperture-suspended bilayers with optical microscopy. This chip was used to obtain preliminary data with a fluorescently labelled KcsA protein, aimed at addressing the efficiency of proteoliposome-facilitated delivery of ion channels to suspended bilayers.

9.2 Recommendations for future work

Although long-lifetime and mechanically stable lipid bilayers could be formed with the shaped apertures developed in this work, the exact relationship between aperture geometry and bilayer stability is not known. It would therefore be of interest to evaluate bilayer stability for a wider range of apertures than those described in Chapter 4 and 5, including variations of the aperture tip angle, aperture wall smoothness and septum hydrophobicity.

The experimental throughput of lipid bilayer electrophysiology could be increased because the shaped apertures provided more stable bilayers than conventional apertures, but as highlighted in section 2.2.1, drug screening applications necessitate parallel recordings sites, as provided by automated patch clamp instruments. Hence, lipid bilayer platforms are required that enable multiplexed recordings, for example by placing multiple bilayer cells with an aperture-containing septum next to each other, in combination with integrated electronics and a robotic pipettor for automated formation of folded lipid bilayers. Several groups have been working on arrayed lipid bilayers [128, 132, 258] but not in combination with the shaped aperture methodology. Moreover, the aqueous compartments could be miniaturized by fabricating the apertures inside a microfluidic chip, based on the microcavity array approach of Baaken *et al.*, with a process flow as described in (Figure 98).

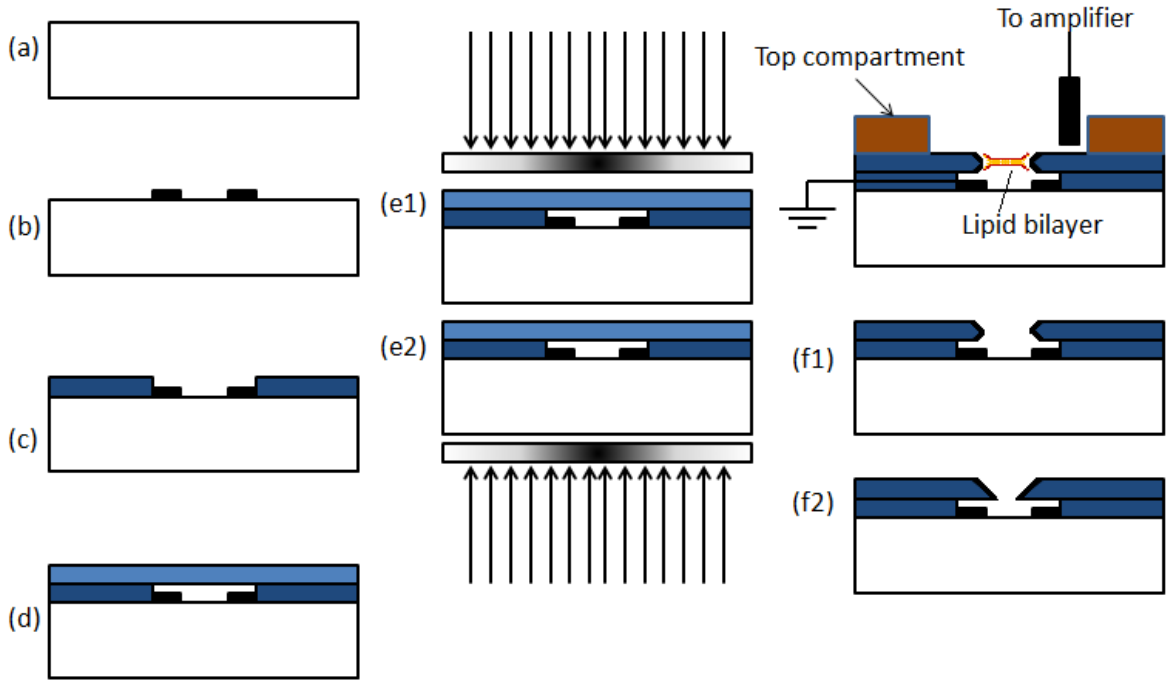

Figure 98: Schematic of fabrication process for a shaped aperture in resist using grayscale lithography with integrated electrodes for parallel electrophysiology. The electrodes are in the form of a ring to allow exposure of resist from the substrate side. This platform can potentially be used for parallel electrophysiology with multiple and individually electrically addressable bilayers. Black colour represents electrodes, light blue represents unpolymerised TMMF, dark blue represents polymerised TMMF and brown colour represents top compartment made by a laser cut polymer adhered to TMMF.

Furthermore, as discussed in Chapter 8, ion channel incorporation through proteoliposome fusion is not an efficient methodology, requiring addition of ~10^9 vesicles with incorporated channels to the aqeuous compartment. With more stable aperture-suspended bilayers, ion channel incorporation in the bilayer constitutes the next bottleneck for lipid bilayer electrophysiology. Insight in proteoliposome fusion with the suspended bilayer and the location of incorporated channels in the solvent-suspended bilayer could be gained from optical studies, which could lead to more efficient incorporation protocols.

9.3 Publications arising from this work

A publication regarding enhancement of stability of lipid bilayer with shaped apertures fabricated using two-photon lithography in photoresists has been accepted with minor revisions in Biophysical Journal. The data presented in Chapter 4 about use of low NA objective for optimisation of fabrication times and in Chapter 5 about use of grayscale lithography technique for mass production of shaped apertures together with its stability data will be published in two separate journals. Publications about the electrophysiological data in Chapter 7 will be done by the groups who provided with the ion channels, which is currently in preparation.

References

1. Engel, A. and H.E. Gaub, *Structure and mechanics of membrane proteins*, in *Annual Review of Biochemistry*. 2008. p. 127-148.
2. Bezanilla, F., *How membrane proteins sense voltage.* Nature Reviews Molecular Cell Biology, 2008. **9**(4): p. 323-332.
3. Chan, Y.H.M. and S.G. Boxer, *Model membrane systems and their applications.* Current Opinion in Chemical Biology, 2007. **11**(6): p. 581-587.
4. van Meer, G., D.R. Voelker, and G.W. Feigenson, *Membrane lipids: where they are and how they behave.* Nature Reviews Molecular Cell Biology, 2008. **9**(2): p. 112-124.
5. Kongsuphol, P., K.B. Fang, and Z.P. Ding, *Lipid bilayer technologies in ion channel recordings and their potential in drug screening assay.* Sensors and Actuators B-Chemical, 2013. **185**: p. 530-542.
6. Bagal, S., A.D. Brown, P.J. Cox, K. Omoto, R.M. Owen, D.C. Pryde, B. Sidders, S.E. Skerratt, E.B. Stevens, R.I. Storer, and N.A. Swain, *Ion Channels as Therapeutic Targets: A Drug Discovery Perspective.* Journal of Medicinal Chemistry, 2013. **56**(3): p. 593-624.
7. Hubner, C.A. and T.J. Jentsch, *Ion channel diseases.* Human Molecular Genetics, 2002. **11**(20): p. 2435-2445.
8. Dunlop, J., M. Bowlby, R. Peri, D. Vasilyev, and R. Arias, *High-throughput electrophysiology: an emerging paradigm for ion-channel screening and physiology.* Nature Reviews Drug Discovery, 2008. **7**(4): p. 358-368.
9. Cooper, E.C. and L.Y. Jan, *Ion channel genes and human neurological disease: Recent progress, prospects, and challenges.* Proceedings of the National Academy of Sciences of the United States of America, 1999. **96**(9): p. 4759-4766.
10. Xie, M., M.H. Holmqvist, and A.Y. Hsia *Ion channel drug discovery expands into new disease areas*. 2004.
11. Barr, C.S., A. Naas, M. Freeman, C.C. Lang, and A.D. Struthers, *QT dispersion and sudden unexpected death in chronic heart-failure.* Lancet, 1994. **343**(8893): p. 327-329.
12. Finlayson, K., H.J. Witchel, J. McCulloch, and J. Sharkey, *Acquired QT interval prolongation and hERG: implications for drug discovery and development.* European Journal of Pharmacology, 2004. **500**(1-3): p. 129-142.
13. Keller, S.H., O. Platoshyn, and J.X.J. Yuan, *Long QT syndrome-associated I593R mutation in HERG potassium channel activates ER stress pathways.* Cell Biochemistry and Biophysics, 2005. **43**(3): p. 365-377.
14. Demarche, S., K. Sugihara, T. Zambelli, L. Tiefenauer, and J. Voros, *Techniques for recording reconstituted ion channels.* Analyst, 2011. **136**(6): p. 1077-1089.
15. Tanaka, M. and E. Sackmann, *Polymer-supported membranes as models of the cell surface.* Nature, 2005. **437**(7059): p. 656-663.
16. Reimhult, E. and K. Kumar, *Membrane biosensor platforms using nano- and microporous supports.* Trends in Biotechnology, 2008. **26**(2): p. 82-89.
17. Bally, M., K. Bailey, K. Sugihara, D. Grieshaber, J. Voros, and B. Stadler, *Liposome and Lipid Bilayer Arrays Towards Biosensing Applications.* Small, 2010. **6**(22): p. 2481-2497.
18. Escriba, P.V., J.M. Gonzalez-Ros, F.M. Goni, P.K.J. Kinnunen, L. Vigh, L. Sanchez-Magraner, A.M. Fernandez, X. Busquets, I. Horvath, and G. Barcelo-Coblijn, *Membranes: a meeting point for lipids, proteins and therapies.* Journal of Cellular and Molecular Medicine, 2008. **12**(3): p. 829-875.
19. Achalkumar, A.S., R.J. Bushby, and S.D. Evans, *Cholesterol-based anchors and tethers for phospholipid bilayers and for model biological membranes.* Soft Matter, 2010. **6**(24): p. 6036-6051.
20. Mueller, P., D.O. Rudin, H.T. Tien, and W.C. Wescott, *Reconstitution of cell membrane structure in vitro and its transformation into an excitable system.* Nature, 1962. **194**((4832)): p. 979-980.
21. Tien, H.T. and A.L. Ottova, *The lipid bilayer concept and its experimental realization: from soap bubbles, kitchen sink, to bilayer lipid membranes.* Journal of Membrane Science, 2001. **189**(1): p. 83-117.
22. Overbeek, J.T.G., *Black soap films.* The Journal of Physical Chemistry, 1960. **64**(9): p. 1178-1183.
23. Ottova, A. and H. Ti Tien, *The 40th anniversary of bilayer lipid membrane research.* Bioelectrochemistry, 2002. **56**(1–2): p. 171-173.

24. Tien, H.T., *Thermodynamics of bimolecular (black) lipid membranes at the water-oil-water biface.* The Journal of Physical Chemistry, 1968. **72**(8): p. 2723-2729.
25. White, S.H., *Analysis of torus surrounding planar lipid bilayer membranes.* Biophysical Journal, 1972. **12**(4): p. 432-&.
26. Tien, H.T., *Black Lipid Membranes at bifaces : formation characteristics, optical and some thermodynamic properties.* The Journal of general physiology, 1968. **52**(1): p. 125-44.
27. Heimburg, T., *Lipid ion channels.* Biophysical Chemistry, 2010. **150**(1-3): p. 2-22.
28. Hodgkin, A.L. and A.F. Huxley, *Currents carried by sodium and potassium ions through the membrane of the giant axon of Loligo.* The Journal of physiology, 1952. **116**(4): p. 449-72.
29. Neher, E. and B. Sakmann, *Single-channel currents recorded from membrane of denervated frog muscle-fibers.* Nature, 1976. **260**(5554): p. 799-802.
30. Franciolini, F. and A. Petris, *Single channel recording and gating function of ionic channels.* Experientia, 1988. **44**(3): p. 183-188.
31. Feng, Q., *Principle of single-channel kinetic analysis*, in *Patch-clamp methods and protocols*, P. Molnar and J.J. Hickman, Editors. 2007, Humana Press Inc.: NewYork.
32. Nielsen, C.H., *Biomimetic membranes for sensor and separation applications.* Analytical and Bioanalytical Chemistry, 2009. **395**(3): p. 697-718.
33. *Planar lipid bilayers and their applications*. Membrane science and technology Series 7, ed. H.T. Tien and A. Ottova. 2003, Amsterdam: Elsevier.
34. Rossi, S., G. Waton, and M.P. Krafft, *Phospholipid-coated gas bubble engineering: key parameters for size and stability control, as determined by an acoustical method.* Langmuir, 2010. **26**(3): p. 1649-1655.
35. Mayer, M., J.K. Kriebel, M.T. Tosteson, and G.M. Whitesides, *Microfabricated Teflon membranes for low-noise recordings of ion channels in planar lipid bilayers.* Biophysical Journal, 2003. **85**(4): p. 2684-2695.
36. Wonderlin, W.F., A. Finkel, and R.J. French, *Optimizing planar lipid bilayer single-channel recordings for high resolution with rapid voltage steps.* Biophysical Journal, 1990. **58**(2): p. 289-297.
37. Studer, A., S. Demarche, D. Langenegger, and L. Tiefenauer, *Integration and recording of a reconstituted voltage-gated sodium channel in planar lipid bilayers.* Biosensors & Bioelectronics, 2011. **26**(5): p. 1924-1928.
38. Kresak, S., T. Hianik, and R.L.C. Naumann, *Giga-seal solvent-free bilayer lipid membranes: from single nanopores to nanopore arrays.* Soft Matter, 2009. **5**(20): p. 4021-4032.
39. Xu, J., X.B. Wang, B. Ensign, M. Li, L. Wu, A. Guia, and J.Q. Xu, *Ion-channel assay technologies: quo vadis?* Drug Discovery Today, 2001. **6**(24): p. 1278-1287.
40. White, S.H., *Analysis of the torus surrounding planar lipid bilayer membranes.* Biophys J, 1972. **12**: p. 14.
41. Belegrinou, S., S. Menon, D. Dobrunz, and W. Meier, *Solid-supported polymeric membranes.* Soft Matter, 2011. **7**(6): p. 2202-2210.
42. Eeman, M. and M. Deleu, *From biological membranes to biomimetic model membranes.* Biotechnologie Agronomie Societe Et Environnement, 2010. **14**(4): p. 719-736.
43. Futaki, S., *Peptide ion channels: Design and creation of function.* Biopolymers, 1998. **47**(1): p. 75-81.
44. Armstrong, C.M., *Voltage-gated K channels.* Science's STKE : signal transduction knowledge environment, 2003. **2003**(188): p. re10.
45. Clare, J.J., *Targeting Ion Channels for Drug Discovery.* Discovery Medicine, 2010. **46**: p. 253-260.
46. Hille, B., *Ion channels of excitable membranes*. 2001, Massachusetts: Sinauer Associates.
47. Trapani, J.G. and S.J. Korn, *Control of ion channel expression for patch clamp recordings using an inducible expression system in mammalian cell lines.* Bmc Neuroscience, 2003. **4**.
48. Zhao, Y., S. Inayat, D.A. Dikin, H. Singer, R.S. Ruoff, and J.B. Troy, *Patch clamp technique: review of the current state of the art and potential contributions from nanoengineering.* Proceedings of the Institution of Mechanical Engineers, Part N (Journal of Nanoengineering and Nanosystems), 2008. **222**(1): p. 1-11.
49. Thei, F., *A hybrid technology for parallel recording of single ion channels*. 2011, Università di Bologna.
50. Kornreich, B.G., *The patch clamp technique: principles and technical considerations.* Journal of veterinary cardiology : the official journal of the European Society of Veterinary Cardiology, 2007. **9**(1): p. 25-37.
51. Benz, R., *Investigation of substrate-specific porin channels in BLMs*, in *Planar lipid bilayers (BLMs) and their applications*, H.T.T.a.A. Ottova-Leitmannova, Editor. 2003, Elsevier: Amsterdam.

52. Montal, M. and P. Mueller, *Formation of biomolecular membranes from lipid monolayers and a study of their electrical properties.* Proceedings of the National Academy of Sciences of the United States of America, 1972. **69**(12): p. 3561-3566.
53. White, S.H., D.C. Petersen, S. Simon, and Masaoyafuso, *Formation of planar bilayer membranes from lipid monolayers. A critique.* Biophysical Journal, 1976. **16**(5): p. 481-489.
54. White, S.H., *The physical nature of planar lipid bilayer*, in *Ion channel reconstitution*, C. Miller, Editor. 1986, Plenum Press: New York.
55. Williams., A.J., in *Microelectrode techniques*, D.C. Odgen, Editor. 1994, The Company of Biologists: Cambridge.
56. Pelzer, D.J., T.F. McDonald, and S. Pelzer, in *Methods in Pharmacology*, H. Glossmann and J. Striessnig, Editors. 1993, Plenum Press: New York.
57. Beerlink, A., S. Thutupalli, M. Mell, M. Bartels, P. Cloetens, S. Herminghaus, and T. Salditt, *X-Ray propagation imaging of a lipid bilayer in solution.* Soft Matter, 2012. **8**(17): p. 4595-4601.
58. Andrews, D.M. and D.A. Haydon, *Electron microscope studies of lipid bilayer membranes.* Journal of Molecular Biology, 1968. **32**(1): p. 149-150.
59. Requena, J., D.A. Haydon, and S.B. Hladky, *Lenses and compression of black lipid membranes by an electric field.* Biophysical Journal, 1975. **15**(1): p. 77-81.
60. Henn, F.A. and T.E. Thompson, *Properties of lipid bilayer membranes separating two aqueous phases: Composition studies.* Journal of Molecular Biology, 1968. **31**((2)): p. 227-235.
61. Hendry, B.M., B.W. Urban, and D.A. Haydon, *The blockage of the electrical conductance in a pore-containing membrane by the n-alkanes.* Biochimica et Biophysica Acta (BBA) - Biomembranes, 1978. **513**(1): p. 106-116.
62. Fettiplace, R., D.M. Andrews, and D.A. Haydon, *Thickness, composition and structure of some lipid bilayers and natural membranes.* Journal of Membrane Biology, 1971. **5**(3): p. 277-&.
63. McIntosh, T.J., S.A. Simon, and R.C. MacDonald, *The organisation of normal n-alkanes in lipid bilayers.* Biochimica et Biophysica Acta, 1980. **597**(3): p. 445-463.
64. Rudnev, V.S., L.N. Ermishkin, L.A. Fonina, and Y.G. Rovin, *The dependence of the conductance and lifetime of gramicidin channels on the thickness and tension of lipid bilayers.* Biochimica et Biophysica Acta (BBA) - Biomembranes, 1981. **642**(1): p. 196-202.
65. Chernyshev, A., K.M. Armstrong, and S. Cukierman, *Proton transfer in gramicidin channels is modulated by the thickness of monoglyceride bilayers.* Biophysical Journal, 2003. **84**(1): p. 238-250.
66. Andersen, O.S. and R.E. Koeppe, II, *Bilayer thickness and membrane protein function: An energetic perspective*, in *Annual Review of Biophysics and Biomolecular Structure*. 2007. p. 107-130.
67. Tien, H.T. and A.L. Ottova, *The bilayer lipid membrane (BLM) under electrical fields.* IEEE Transactions on Dielectrics and Electrical Insulation, 2003. **10**(5): p. 717-727.
68. Hanai, T., D.A. Haydon, and J. Taylor, *Polar group orientation and the electrical properties of lecithin bimolecular leaflets.* J Theor Biol, 1965. **9**((2)): p. 278-296.
69. Thompson, M., R.B. Lennox, and R.A. McClelland, *STRUCTURE AND ELECTROCHEMICAL PROPERTIES OF MICRO-FILTRATION FILTER LIPID-MEMBRANE SYSTEMS.* Analytical Chemistry, 1982. **54**(1): p. 76-81.
70. Berti, D., G. Caminati, and P. Baglioni, *Functional liposomes and supported lipid bilayers: towards the complexity of biological archetypes.* Physical Chemistry Chemical Physics, 2011. **13**(19): p. 8769-8782.
71. Sugihara, K., J. Voros, and T. Zambelli, *A Gigaseal Obtained with a Self-Assembled Long-Lifetime Lipid Bilayer on a Single Polyelectrolyte Multilayer-Filled Nanopore.* Acs Nano, 2010. **4**(9): p. 5047-5054.
72. Schmitt, E.K., C. Weichbrodt, and C. Steinem, *Impedance analysis of gramicidin D in pore-suspending membranes.* Soft Matter, 2009. **5**(17): p. 3347-3353.
73. Kleefen, A., D. Pedone, C. Grunwald, R. Wei, M. Firnkes, G. Abstreiter, U. Rant, and R. Tampe, *Multiplexed Parallel Single Transport Recordings on Nanopore Arrays.* Nano Letters, 2010. **10**(12): p. 5080-5087.
74. Kumar, K., L. Isa, A. Egner, R. Schmidt, M. Textor, and E. Reimhult, *Formation of Nanopore-Spanning Lipid Bilayers through Liposome Fusion.* Langmuir, 2011. **27**(17): p. 10920-10928.
75. Buchholz, K., A. Tinazli, A. Kleefen, D. Dorfner, D. Pedone, U. Rant, R. Tampe, G. Abstreiter, and M. Tornow, *Silicon-on-insulator based nanopore cavity arrays for lipid membrane investigation.* Nanotechnology, 2008. **19**(44).
76. Seddon, A.M., P. Curnow, and P.J. Booth, *Membrane proteins, lipids and detergents: not just a soap opera.* Biochimica Et Biophysica Acta-Biomembranes, 2004. **1666**(1-2): p. 105-117.

77. de Planque, M.R.R., G.P. Mendes, M. Zagnoni, M.E. Sandison, K.H. Fisher, R.M. Berry, A. Watts, and H. Morgan, *Controlled delivery of membrane proteins to artificial lipid bilayers by nystatin-ergosterol modulated vesicle fusion.* Iee Proceedings-Nanobiotechnology, 2006. **153**(2): p. 21-30.
78. Zagnoni, M., M.E. Sandison, P. Marius, A.G. Lee, and H. Morgan, *Controlled delivery of proteins into bilayer lipid membranes on chip.* Lab on a Chip, 2007. **7**(9): p. 1176-1183.
79. Andersen, O.S., *Ion movement through gramicidin A channels. Single channel measurements at very high potentials.* Biophysical Journal, 1983. **41**(2): p. 119-133.
80. Kelkar, D.A. and A. Chattopadhyay, *The gramicidin ion channel: A model membrane protein.* Biochimica Et Biophysica Acta-Biomembranes, 2007. **1768**(9): p. 2011-2025.
81. Andersen, O.S., R.E. Koeppe, and B. Roux, *Gramicidin channels.* Ieee Transactions on Nanobioscience, 2005. **4**(1): p. 10-20.
82. Veatch, W.R. and E.R. Blout, *Aggregation of gramicidin A in solution.* Biochemistry, 1974. **13**(26): p. 5257-5264.
83. Woolley, G.A. and B.A. Wallace, *Model ion channels- gramicidin and alamethicin.* Journal of Membrane Biology, 1992. **129**(2): p. 109-136.
84. Duclohier, H. and H. Wroblewski, *Voltage-dependent pore formation and antimicrobial activity by alamethicin and analogues.* Journal of Membrane Biology, 2001. **184**(1): p. 1-12.
85. Gordon, L.G.M. and D.A. Haydon, *Potential dependent conductances in lipid membranes containing alamethicin.* Philosophical Transactions of the Royal Society of London Series B-Biological Sciences, 1975. **270**(908): p. 433-447.
86. Keller, S.L., S.M. Bezrukov, S.M. Gruner, M.W. Tate, I. Vodyanoy, and V.A. Parsegian, *Probability of alamethicin conductance states varies with non lamellar tendency of bilayer phospholipids.* Biophysical Journal, 1993. **65**(1): p. 23-27.
87. Aguilella, V.M. and S.M. Bezrukov, *Alamethicin channel conductance modified by lipid charge.* European Biophysics Journal with Biophysics Letters, 2001. **30**(4): p. 233-241.
88. Cafiso, D.S., *Alamethicin: A Peptide Model for Voltage Gating and Protein-Membrane Interactions.* Annual Review of Biophysics and Biomolecular Structure, 1994. **23**(1): p. 141-165.
89. Gouaux, E., *α-Hemolysin fromStaphylococcus aureus:An Archetype of β-Barrel, Channel-Forming Toxins.* Journal of Structural Biology, 1998. **121**(2): p. 110-122.
90. Noskov, S.Y., W. Im, and B. Roux, *Ion permeation through the alpha-hemolysin channel: theoretical studies based on Brownian dynamics and Poisson-Nernst-Plank electrodiffusion theory.* Biophys J, 2004. **87**(4): p. 2299-309.
91. Maglia, G., A.G. Heron, D. Stoddart, D. Japrung, and B. H., *Analysis of single nucleic acid molecules with protein nanopores*, in *Methods in enzymology*, G.W. Nils, Editor. 2010, Academic Press: Massachusetts.
92. Baaken, G., N. Ankri, A. Schuler, J. Ruehe, and J.C. Behrends, *Nanopore-Based Single-Molecule Mass Spectrometry on a Lipid Membrane Microarray.* Acs Nano, 2011. **5**(10): p. 8080-8088.
93. Gu, L. and J.W. Shim, *Single molecule sensing by nanopores and nanopore devices.* Analyst, 2010. **135**(3): p. 441-451.
94. Suzuki, H., K.V. Tabata, H. Noji, and S. Takeuchi, *Electrophysiological recordings of single ion channels in planar lipid bilayers using a polymethyl methacrylate microfluidic chip.* Biosensors & Bioelectronics, 2007. **22**(6): p. 1111-1115.
95. McCoy, J.G. and C.M. Nimigean, *Structural correlates of selectivity and inactivation in potassium channels.* Biochimica et Biophysica Acta (BBA) - Biomembranes, 2012. **1818**(2): p. 272-285.
96. Seeger, H.M., L. Aldrovandi, A. Alessandrini, and P. Facci, *Changes in Single K+ Channel Behavior Induced by a Lipid Phase Transition.* Biophysical Journal, 2010. **99**(11): p. 3675-3683.
97. Marius, P., M. Zagnoni, M.E. Sandison, J.M. East, H. Morgan, and A.G. Lee, *Binding of anionic lipids to at least three nonannular sites on the potassium channel KcsA is required for channel opening.* Biophysical Journal, 2008. **94**(5): p. 1689-1698.
98. LeMasurier, M., L. Heginbotham, and C. Miller, *KcsA: It's a potassium channel.* Journal of General Physiology, 2001. **118**(3): p. 303-313.
99. Bolivar, J.H., N. Smithers, J.M. East, D. Marsh, and A.G. Lee, *Multiple binding sites for fatty acids on the potassium channel KcsA.* Biochemistry, 2012. **51**(13): p. 2889-2898.
100. McCusker, E.C., N. D'Avanzo, C.G. Nichols, and B.A. Wallace, *Simplified Bacterial "Pore" Channel Provides Insight into the Assembly, Stability, and Structure of Sodium Channels.* Journal of Biological Chemistry, 2011. **286**(18).
101. Koishi, R., H.X. Xu, D.J. Ren, B. Navarro, B.W. Spiller, Q. Shi, and D.E. Clapham, *A superfamily of voltage-gated sodium channels in bacteria.* Journal of Biological Chemistry, 2004. **279**(10): p. 9532-9538.

102. Shaya, D., M. Kreir, R.A. Robbins, S. Wong, J. Hammon, A. Brueggemann, and D.L. Minor, Jr., *Voltage-gated sodium channel (Na-V) protein dissection creates a set of functional pore-only proteins.* Proceedings of the National Academy of Sciences of the United States of America, 2011. **108**(30): p. 12313-12318.
103. Charalambous, K. and B.A. Wallace, *NaChBac: The Long Lost Sodium Channel Ancestor.* Biochemistry, 2011. **50**(32): p. 6742-6752.
104. Yang, N., *Cardiac Drug Safety and hERG channel.* Trends in bio/pharmaceutical industry, 2007. **50**: p. 30-35.
105. Zhang, Y., P. Thai, J. Dunlop, and J. Dalziel, *hERG ion channel pharmacology: cell membrane liposomes in porous-supported lipid bilayers compared with whole-cell patch-clamping.* European Biophysics Journal with Biophysics Letters, 2012. **41**(11): p. 949-958.
106. Sanguinetti, M.C. and M. Tristani-Firouzi, *hERG potassium channels and cardiac arrhythmia.* Nature, 2006. **440**(7083): p. 463-469.
107. Hausammann, G.J. and M.G. Grütter, *Chimeric hERG channels containing a tetramerization domain are functional and stable.* Biochemistry, 2013. **52**(51): p. 9237-9245.
108. Gravel, A.E., A.A. Arnold, E.J. Dufourc, and I. Marcotte, *An NMR investigation of the structure, function and role of the hERG channel selectivity filter in the long QT syndrome.* Biochimica Et Biophysica Acta-Biomembranes, 2013. **1828**(6): p. 1494-1502.
109. Kiehn, J., A.E. Lacerda, and A.M. Brown, *Pathways of hERG inactivation.* American Journal of Physiology-Heart and Circulatory Physiology, 1999. **277**(1): p. H199-H210.
110. Oshima, A., A. Hirano-Iwata, H. Mozumi, Y. Ishinari, Y. Kimura, and M. Niwano, *Reconstitution of Human Ether-a-go-go-Related Gene Channels in Microfabricated Silicon Chips.* Analytical Chemistry, 2013. **85**(9): p. 4363-4369.
111. Vandenberg, J.I., M.D. Perry, M.J. Perrin, S.A. Mann, Y. Ke, and A.P. Hill, *hERG K+ Channels: structure, function and clinical significance.* Physiological Reviews, 2012. **92**(3): p. 1393-1478.
112. Liu, B.W., D. Rieck, B.J. Van Wie, G.J. Cheng, D.F. Moffett, and D.A. Kidwell, *Bilayer lipid membrane (BLM) based ion selective electrodes at the meso-, micro-, and nano-scales.* Biosensors & Bioelectronics, 2009. **24**(7): p. 1843-1849.
113. Eray, M., N.S. Dogan, L.J. Liu, A.R. Koch, D.F. Moffett, M. Silber, and B.J. Vanwie, *Highly stable bilayer lipid membranes (BLMs) formed on microfabricated polyimide apertures.* Biosensors & Bioelectronics, 1994. **9**(4-5): p. 343-351.
114. Goryll, M. and N. Chaplet, eds. *Miniaturized silicon apertures for lipid bilayer reconstitution experiments*. Materials and Strategies for Lab-on-a-Chip - Biological Analysis, Cell-Material Interfaces and Fluidic Assembly of Nanostructures, ed. S.K. Murthy, et al. Vol. 1191. 2009. 79-84.
115. Fertig, N., C. Meyer, R.H. Blick, C. Trautmann, and J.C. Behrends, *Microstructured glass chip for ion-channel electrophysiology.* Physical Review E, 2001. **64**(4).
116. O'Shaughnessy, T.J., J.E. Hu, J.L. Kulp, III, S.M. Daly, and F.S. Ligler, *Laser ablation of micropores for formation of artificial planar lipid bilayers.* Biomedical Microdevices, 2007. **9**(6): p. 863-868.
117. Kitta, M., H. Tanaka, and T. Kawai, *Rapid fabrication of Teflon micropores for artificial lipid bilayer formation.* Biosensors & Bioelectronics, 2009. **25**(4): p. 931-934.
118. Han, X.J., A. Studer, H. Sehr, I. Geissbuhler, M. Di Berardino, F.K. Winkler, and L.X. Tiefenauer, *Nanopore arrays for stable and functional free-standing lipid bilayers.* Advanced Materials, 2007. **19**(24): p. 4466-+.
119. Weiskopf, D., E.K. Schmitt, M.H. Kluehr, S.K. Dertinger, and C. Steinem, *Micro-BLMs on highly ordered porous silicon substrates: rupture process and lateral mobility.* Langmuir, 2007. **23**(18): p. 9134-9139.
120. Romer, W. and C. Steinem, *Impedance analysis and single-channel recordings on nano-black lipid membranes based on porous alumina.* Biophysical Journal, 2004. **86**(2): p. 955-965.
121. Hirano-Iwata, A., K. Aoto, A. Oshima, T. Taira, R.T. Yamaguchi, Y. Kimura, and M. Niwano, *Free-Standing Lipid Bilayers in Silicon Chips-Membrane Stabilization Based on Microfabricated Apertures with a Nanometer-Scale Smoothness.* Langmuir, 2010. **26**(3): p. 1949-1952.
122. Eray, M., N.S. Dogan, S.R. Reiken, H. Sutisna, B.J. Vanwie, A.R. Koch, D.F. Moffett, M. Silber, and W.C. Davis, *A Highly stable and selective biosensor using modified nicotinic acetylcholine-receptor (nAChR).* Biosystems, 1995. **35**(2-3): p. 183-188.
123. Oshima, A., A. Hirano-Iwata, T. Nasu, Y. Kimura, and M. Niwano, *Mechanically stable lipid bilayers in Teflon-coated silicon chips for single-channel recordings.* Micro and Nanosystems, 2012. **4**(1): p. 2-7.
124. Peterman, M.C., J.M. Ziebarth, O. Braha, H. Bayley, H.A. Fishman, and D.M. Bloom, *Ion channels and lipid bilayer membranes under high potentials using microfabricated apertures.* Biomedical Microdevices, 2002. **4**(3): p. 231-236.

125. Phung, T., Y.L. Zhang, J. Dunlop, and J. Dalziel, *Bilayer lipid membranes supported on Teflon filters: a functional environment for ion channels.* Biosensors & Bioelectronics, 2011. **26**(7): p. 3127-3135.
126. Stimberg, V.C., J.G. Bomer, I. van Uitert, A. van den Berg, and S. Le Gac, *High Yield, Reproducible and Quasi-Automated Bilayer Formation in a Microfluidic Format.* Small, 2013. **9**(7): p. 1076-1085.
127. Tsuji, Y., R. Kawano, T. Osaki, K. Kamiya, N. Miki, and S. Takeuchi, *Droplet-based lipid bilayer system integrated with microfluidic channels for solution exchange.* Lab on a Chip, 2013. **13**(8): p. 1476-1481.
128. Kawano, R., Y. Tsuji, K. Sato, T. Osaki, K. Kamiya, M. Hirano, T. Ide, N. Miki, and S. Takeuchi, *Automated Parallel Recordings of Topologically Identified Single Ion Channels.* Scientific Reports, 2013. **3**.
129. Sondermann, M., M. George, N. Fertig, and J.C. Behrends, *High-resolution electrophysiology on a chip: transient dynamics of alamethicin channel formation.* Biochimica Et Biophysica Acta-Biomembranes, 2006. **1758**(4): p. 545-551.
130. Sandison, M.E., M. Zagnoni, M. Abu-Hantash, and H. Morgan, *Micromachined glass apertures for artificial lipid bilayer formation in a microfluidic system.* Journal of Micromechanics and Microengineering, 2007. **17**(7): p. S189-S196.
131. Cheng, Y.L., R.J. Bushby, S.D. Evans, P.F. Knowles, R.E. Miles, and S.D. Ogier, *Single ion channel sensitivity in suspended bilayers on micromachined supports.* Langmuir, 2001. **17**(4): p. 1240-1242.
132. Baaken, G., M. Sondermann, C. Schlemmer, J. Ruehe, and J.C. Behrends, *Planar microelectrode-cavity array for high-resolution and parallel electrical recording of membrane ionic currents.* Lab on a Chip, 2008. **8**(6): p. 938-944.
133. Portonovo, S.A. and J. Schmidt, *Masking apertures enabling automation and solution exchange in sessile droplet lipid bilayers.* Biomedical Microdevices, 2012. **14**(1): p. 187-191.
134. Kendall, E.L., C.R. Shao, and D.L. Devoe, *Visualizing the Growth and Dynamics of Liquid-Ordered Domains During Lipid Bilayer Folding in a Microfluidic Chip.* Small, 2012. **8**(23): p. 3613-3619.
135. Levis, R.A. and J.L. Rae, *The use of quartz patch pipettes for low-noise single-channel recording.* Biophysical Journal, 1993. **65**(4): p. 1666-1677.
136. Pihl, J., M. Karlsson, and D.T. Chiu, *Microfluidic technologies in drug discovery.* Drug Discovery Today, 2005. **10**(20): p. 1377-1383.
137. Sandison, M.E., M. Zagnoni, and H. Morgan, *Air-exposure technique for the formation of artificial lipid bilayers in microsystems.* Langmuir, 2007. **23**(15): p. 8277-8284.
138. Shao, C., E.L. Kendall, and D.L. DeVoe, *Electro-optical BLM chips enabling dynamic imaging of ordered lipid domains.* Lab on a Chip, 2012. **12**(17): p. 3142-3149.
139. Suzuki, H., K.V. Tabata, H. Noji, and S. Takeuchi, *Highly reproducible method of planar lipid bilayer reconstitution in polymethyl methacrylate microfluidic chip.* Langmuir, 2006. **22**(4): p. 1937-1942.
140. Hromada, L.P., B.J. Nablo, J.J. Kasianowicz, M.A. Gaitan, and D.L. DeVoe, *Single molecule measurements within individual membrane-bound ion channels using a polymer-based bilayer lipid membrane chip.* Lab on a Chip, 2008. **8**(4): p. 602-608.
141. Funakoshi, K., H. Suzuki, and S. Takeuchi, *Lipid bilayer formation by contacting monolayers in a microfluidic device for membrane protein analysis.* Analytical Chemistry, 2006. **78**(24): p. 8169-8174.
142. Bayley, H., B. Cronin, A. Heron, M.A. Holden, W.L. Hwang, R. Syeda, J. Thompson, and M. Wallace, *Droplet interface bilayers.* Molecular Biosystems, 2008. **4**(12): p. 1191-1208.
143. Gross, L.C.M., O.K. Castell, and M.I. Wallace, *Dynamic and Reversible Control of 2D Membrane Protein Concentration in a Droplet Interface Bilayer.* Nano Letters, 2011. **11**(8): p. 3324-3328.
144. Gross, L.C.M., A.J. Heron, S.C. Baca, and M.I. Wallace, *Determining Membrane Capacitance by Dynamic Control of Droplet Interface Bilayer Area.* Langmuir, 2011. **27**(23): p. 14335-14342.
145. Sarles, S.A. and D.J. Leo, *Regulated Attachment Method for Reconstituting Lipid Bilayers of Prescribed Size within Flexible Substrates.* Analytical Chemistry, 2010. **82**(3): p. 959-966.
146. El-Arabi, A.M., C.S. Salazar, and J.J. Schmidt, *Ion channel drug potency assay with an artificial bilayer chip.* Lab on a Chip, 2012. **12**(13): p. 2409-2413.
147. Bratton, D., D. Yang, J.Y. Dai, and C.K. Ober, *Recent progress in high resolution lithography.* Polymers for Advanced Technologies, 2006. **17**(2): p. 94-103.
148. LaFratta, C.N., J.T. Fourkas, T. Baldacchini, and R.A. Farrer, *Multiphoton fabrication.* Angewandte Chemie-International Edition, 2007. **46**(33): p. 6238-6258.
149. Guo, L.J., *Nanoimprint lithography: Methods and material requirements.* Advanced Materials, 2007. **19**(4): p. 495-513.
150. Moon, J.H. and S. Yang, *Creating three-dimensional polymeric microstructures by multi-beam interference lithography.* Journal of Macromolecular Science-Polymer Reviews, 2005. **C45**(4): p. 351-373.

151. Lee, K.S., D.Y. Yang, S.H. Park, and R.H. Kim, *Recent developments in the use of two-photon polymerization in precise 2D and 3D microfabrications.* Polymers for Advanced Technologies, 2006. **17**(2): p. 72-82.
152. Moon, J.H., J. Ford, and S. Yang, *Fabricating three-dimensional polymeric photonic structures by multi-beam interference lithography.* Polymers for Advanced Technologies, 2006. **17**(2): p. 83-93.
153. Maruo, S. and J.T. Fourkas, *Recent progress in multiphoton microfabrication.* Laser & Photonics Reviews, 2008. **2**(1-2): p. 100-111.
154. Woytasik, M., J.P. Grandchamp, E. Dufour-Gergam, J.P. Gilles, S. Megherbi, E. Martincic, H. Mathias, and P. Crozat, *Two- and three-dimensional microcoil fabrication process for three-axis magnetic sensors on flexible substrates.* Sensors and Actuators a-Physical, 2006. **132**(1): p. 2-7.
155. Kodama, H., *Automated method for fabricating a 3-dimensional plastic model with photo-hardening polymer.* Review of Scientific Instruments, 1981. **52**(11): p. 1770-1773.
156. Waits, C.M., B. Morgan, M. Kastantin, and R. Ghodssi, *Microfabrication of 3D silicon MEMS structures using gray-scale lithography and deep reactive ion etching.* Sensors and Actuators a-Physical, 2005. **119**(1): p. 245-253.
157. Staude, I., G. von Freymann, S. Essig, K. Busch, and M. Wegener, *Waveguides in three-dimensional photonic-bandgap materials by direct laser writing and silicon double inversion.* Optics Letters, 2011. **36**(1): p. 67-69.
158. Mosher, L., C.M. Waits, B. Morgan, and R. Ghodssi, *Double-Exposure Grayscale Photolithography.* Journal of Microelectromechanical Systems, 2009. **18**(2): p. 308-315.
159. Maruo, S., O. Nakamura, and S. Kawata, *Three-dimensional microfabrication with two-photon-absorbed photopolymerization.* Optics Letters, 1997. **22**(2): p. 132-134.
160. Sun, H.B., T. Tanaka, and S. Kawata, *Three-dimensional focal spots related to two-photon excitation.* Applied Physics Letters, 2002. **80**(20): p. 3673-3675.
161. Honegger, T., T. Elmberg, K. Berton, and D. Peyrade, *Visible microlaser two-photon polymerization in a microfludic cell: a resist study.* Microelectronic Engineering, 2011. **88**(8): p. 2725-2728.
162. Cumpston, B.H., S.P. Ananthavel, S. Barlow, D.L. Dyer, J.E. Ehrlich, L.L. Erskine, A.A. Heikal, S.M. Kuebler, S.I.-Y. Lee, D. McCord-Maughon, J. Qin, H. Rockel, M. Rumi, X. Wu, S.R. Marder, and J.W. Perry, *Two-photon polymerization initators for three-dimensional optical data storage and microfabrication.* Nature, 1999. **398**: p. 51-54.
163. Gittard, S.D. and R. Narayan, *Laser direct writing of micro- and nano-scale medical devices.* Expert Review of Medical Devices, 2010. **7**(3): p. 343-356.
164. von Freymann, G., A. Ledermann, M. Thiel, I. Staude, S. Essig, K. Busch, and M. Wegener, *Three-Dimensional Nanostructures for Photonics.* Advanced Functional Materials, 2010. **20**(7): p. 1038-1052.
165. Thiel, M., M.S. Rill, G. von Freymann, and M. Wegener, *Three-Dimensional Bi-chiral Photonic Crystals.* Advanced Materials, 2009. **21**(46): p. 4680-+.
166. Maruo, S. and H. Inoue, *Optically driven viscous micropump using a rotating microdisk.* Applied Physics Letters, 2007. **91**(8).
167. Kawata, S., H.B. Sun, T. Tanaka, and K. Takada, *Finer features for functional microdevices - Micromachines can be created with higher resolution using two-photon absorption.* Nature, 2001. **412**(6848): p. 697-698.
168. Witzgall, G., R. Vrijen, E. Yablonovitch, V. Doan, and B.J. Schwartz, *Single-shot two-photon exposure of commercial photoresist for the production of three-dimensional structures.* Optics Letters, 1998. **23**(22): p. 1745-1747.
169. Sun, H.B., S. Matsuo, and H. Misawa, *Three-dimensional photonic crystal structures achieved with two-photon-absorption photopolymerization of resin.* Applied Physics Letters, 1999. **74**(6): p. 786-788.
170. Sun, H.B., T. Kawakami, Y. Xu, J.Y. Ye, S. Matuso, H. Misawa, M. Miwa, and R. Kaneko, *Real three-dimensional microstructures fabricated by photopolymerization of resins through two-photon absorption.* Optics Letters, 2000. **25**(15): p. 1110-1112.
171. Teh, W.H., U. Durig, U. Drechsler, C.G. Smith, and H.J. Guntherodt, *Effect of low numerical-aperture femtosecond two-photon absorption on (SU-8) resist for ultrahigh-aspect-ratio microstereolithography.* Journal of Applied Physics, 2005. **97**(5).
172. Correa, D.S., L. De Boni, A.J.G. Otuka, V. Tribuzi, and C.R. Mendonca, *Two-photon polymerization fabrication of doped microstructures*, in *Polymerization*, A.D.S. Gomes, Editor. 2012, InTech: Rijeka.
173. Sun, H.B., M. Maeda, K. Takada, J.W.M. Chon, M. Gu, and S. Kawata, *Experimental investigation of single voxels for laser nanofabrication via two-photon photopolymerization.* Applied Physics Letters, 2003. **83**(5): p. 819-821.

174. Kawata, S. and H.B. Sun, *Two-photon photopolymerization as a tool for making micro-devices.* Applied Surface Science, 2003. **208**: p. 153-158.
175. Marie, R., S. Schmid, A. Johansson, L.E. Ejsing, M. Nordstrom, D. Hafliger, C.B.V. Christensen, A. Boisen, and M. Dufva, *Immobilisation of DNA to polymerised SU-8 photoresist.* Biosensors & Bioelectronics, 2006. **21**(7): p. 1327-1332.
176. Sikanen, T., L. Heikkila, S. Tuornikoski, R.A. Ketola, R. Kostiainen, S. Franssila, and T. Kotiaho, *Performance of SU-8 microchips as separation devices and comparison with glass microchips.* Analytical Chemistry, 2007. **79**(16): p. 6255-6263.
177. Linder, V., B.D. Gates, D. Ryan, B.A. Parviz, and G.M. Whitesides, *Water-soluble sacrificial layers for surface micromachining.* Small, 2005. **1**(7): p. 730-736.
178. Cortese, B., G. Gigli, and M. Riehle, *Mechanical Gradient Cues for Guided Cell Motility and Control of Cell Behavior on Uniform Substrates.* Advanced Functional Materials, 2009. **19**(18): p. 2961-2968.
179. Li, D.Z., S. Tumkor, S. Manoochehri, K. Pochiraju, and Asme. *Fabrication of polymeric and polymeric nano-composite MEMS structures*. in *Asme International Mechanical Engineering Congress and Exposition*. 2010.
180. Bao, X.Q., T. Dargent, and E. Cattan, *Micromachining SU-8 pivot structures using AZ photoresist as direct sacrificial layers for a large wing displacement.* Journal of Micromechanics and Microengineering, 2010. **20**(2).
181. Luo, C., A. Govindaraju, J. Garra, T. Schneider, R. White, J. Currie, and M. Paranjape, *Releasing SU-8 structures using polystyrene as a sacrificial material.* Sensors and Actuators a-Physical, 2004. **114**(1): p. 123-128.
182. Cheng, M.C., A.P. Gadre, J.A. Garra, A.J. Nijdam, C. Luo, T.W. Schneider, R.C. White, J.F. Currie, and M. Paranjape, *Dry release of polymer structures with anti-sticking layer.* Journal of Vacuum Science & Technology A, 2004. **22**(3): p. 837-841.
183. Haefliger, D., M. Nordstrom, P.A. Rasmussen, and A. Boisen, *Dry release of all-polymer structures.* Microelectronic Engineering, 2005. **78-79**: p. 88-92.
184. Nordstrom, M., S. Keller, M. Lillemose, A. Johansson, S. Dohn, D. Haefliger, G. Blagoi, M. Havsteen-Jakobsen, and A. Boisen, *SU-8 cantilevers for bio/chemical sensing; fabrication, characterisation and development of novel read-out methods.* Sensors, 2008. **8**(3): p. 1595-1612.
185. Choi, J., A. Roychowdhury, N. Kim, D.E. Nikitopoulos, W. Lee, H. Han, and S. Park, *A microfluidic platform with a free-standing perforated polymer membrane.* Journal of Micromechanics and Microengineering, 2010. **20**(8).
186. Bystrova, S., R. Luttge, and A. van den Berg, *Study of crack formation in high-aspect ratio SU-8 structures on silicon.* Microelectronic Engineering, 2007. **84**(5-8): p. 1113-1116.
187. Anhoj, T.A., A.M. Jorgensen, D.A. Zauner, and J. Hubner, *The effect of soft bake temperature on the polymerization of SU-8 photoresist.* Journal of Micromechanics and Microengineering, 2006. **16**(9): p. 1819-1824.
188. Formanek, F., N. Takeyasu, T. Tanaka, K. Chiyoda, A. Ishikawa, and S. Kawata, *Three-dimensional fabrication of metallic nanostructures over large areas by two-photon polymerization.* Optics Express, 2006. **14**(2): p. 800-809.
189. Jeon, S., V. Malyarchuk, J.A. Rogers, and G.P. Wiederrecht, *Fabricating three dimensional nanostructures using two photon lithography in a single exposure step.* Optics Express, 2006. **14**(6): p. 2300-2308.
190. Cannistra, A.T. and T.J. Suleski, *Characterization of hybrid molding and lithography for SU-8 micro-optical components.* Journal of Micro-Nanolithography Mems and Moems, 2010. **9**(1).
191. del Campo, A. and E. Arzt, *Fabrication approaches for generating complex micro- and nanopatterns on polymeric surfaces.* Chemical Reviews, 2008. **108**(3): p. 911-945.
192. Lan, H. and Y. Ding, *Nanoimprint lithography*, in *Lithography*, M. Wang, Editor. 2010, InTech: Rijeka.
193. Liu, R., B.R. Lu, S.Q. Xie, J. Wan, Z. Shu, X.P. Qu, and Y. Chen, *Optical Nanostructures Fabricated by SU-8 based Nanoimprint Lithography.* Journal of the Korean Physical Society, 2009. **55**(3): p. 1290-1294.
194. Zhu, X.L. and T.H. Cui, *Fabrication of polymer via holes by a combination of hot embossing and indentation processes.* Journal of Micromechanics and Microengineering, 2011. **21**(4).
195. Cheng, X. and L.J. Guo, *One-step lithography for various size patterns with a hybrid mask-mold.* Microelectronic Engineering, 2004. **71**(3-4): p. 288-293.
196. Zhang, J.Z., X. Hu, J. Zhang, Y.S. Cui, C.S. Yuan, H.X. Ge, Y.F. Chen, W. Wu, and Q.F. Xia, *A fast thermal-curing nanoimprint resist based on cationic polymerizable epoxysiloxane.* Nanoscale Research Letters, 2012. **7**.

197. Shin, Y.J., Y.K. Wu, and L.J. Guo, *Nanoimprinting ultrasmall and high-aspect-ratio structures by using rubber-toughened UV cured epoxy resist.* Nanotechnology, 2013. **24**(25).
198. Abgrall, P., V. Conedera, H. Camon, A.-M. Gue, and N.-T. Nguyen, *SU-8 as a structural material for labs-on-chips and microelectromechanical systems.* Electrophoresis, 2007. **28**(24): p. 4539-4551.
199. Wang, X.D., Y. Chen, S. Banu, H. Morgan, S.J. Fu, and Z. Cui, *High density patterns fabricated in SU-8 by UV curing nanoimprint.* Microelectronic Engineering, 2007. **84**(5-8): p. 872-876.
200. Youn, S.W., A. Ueno, M. Takahashi, and R. Maeda, *Microstructuring of SU-8 photoresist by UV-assisted thermal imprinting with non-transparent mold.* Microelectronic Engineering, 2008. **85**(9): p. 1924-1931.
201. Skjolding, L.H.D., G.T. Teixidor, J. Emneus, and L. Montelius, *Negative UV-NIL (NUV-NIL) - A mix-and-match NIL and UV strategy for realisation of nano- and micrometre structures.* Microelectronic Engineering, 2009. **86**(4-6): p. 654-656.
202. Dhima, K., A. Mayer, S. Wang, S. Moellenbeck, and H.-C. Scheer, *A novel processing procedure for T/UV-NIL with negative tone resists.* Microelectronic Engineering, 2013. **110**: p. 85-89.
203. Scheer, H.C., M. Wissen, N. Bogdanski, S. Moellenbeck, and A. Mayer, *Potential and limitations of a T-NIL/UVL hybrid process.* Microelectronic Engineering, 2010. **87**(5-8): p. 851-853.
204. Hu, W., B. Yang, C. Peng, and S.W. Pang, *Three-dimensional SU-8 structures by reversal UV imprint.* Journal of Vacuum Science & Technology B, 2006. **24**(5): p. 2225-2229.
205. Wagner, B., H.J. Quenzer, W. Henke, W. Hoppe, and W. Pilz, *Microfabrication of complex surface topographies using grey-tone lithography.* Sensors and Actuators a-Physical, 1995. **46**(1-3): p. 89-94.
206. Henke, W., W. Hoppe, H.J. Quenzer, P. Staudt-Fischbach, and B. Wagner, *Simulation and experimental study of gray-tone lithography for the fabrication of arbitrarily shaped surfaces.* Proceedings IEEE Micro Electro Mechanical Systems. An Investigation of Micro Structures, Sensors, Actuators, Machines and Robotic Systems (Cat. No.94CH3404-1), 1994: p. 205-10.
207. Oppliger, Y., P. Sixt, J.M. Stauffer, J.M. Mayor, P. Regnault, and G. Voirin, *One step 3D shaping using a gray-tone mask for optical and microelectronic applications.* Microelectronic Engineering, 1994. **23**(1-4): p. 449-454.
208. Morgan, B., C.M. Waits, and R. Ghodssi, *Compensated aspect ratio dependent etching (CARDE) using gray-scale technology.* Microelectronic Engineering, 2005. **77**(1): p. 85-94.
209. Totsu, K., K. Fujishiro, S. Tanaka, and M. Esashi, *Fabrication of three-dimensional microstructure using maskless gray-scale lithography.* Sensors and Actuators a-Physical, 2006. **130**: p. 387-392.
210. Rammohan, A., P.K. Dwivedi, R. Martinez-Duarte, H. Katepalli, M.J. Madou, and A. Sharma, *One-step maskless grayscale lithography for the fabrication of 3-dimensional structures in SU-8.* Sensors and Actuators B-Chemical, 2011. **153**(1): p. 125-134.
211. Waits, C.M., A. Modafe, and R. Ghodssi, *Investigation of gray-scale technology for large area 3D silicon MEMS structures.* Journal of Micromechanics and Microengineering, 2003. **13**(2): p. 170-177.
212. Sure, A., T. Dillon, J. Murakowski, C.C. Lin, D. Pustai, and D.W. Prather, *Fabrication and characterization of three-dimensional silicon tapers.* Optics Express, 2003. **11**(26): p. 3555-3561.
213. Cui, Z., J.L. Du, and Y.K. Guo, *Overview of greyscale photolithography for microoptical elements fabrication*, in *Micromachining Technology for Micro-Optics and Nano-Optics*, E.G. Johnson, Editor. 2003. p. 111-117.
214. Dillon, T., A. Sure, J. Murakowski, and D. Prather, *Process development and application of grayscale lithography for efficient three-dimensionally profiled fiber-to-waveguide couplers*, in *Lithographic and Micromachining Techniques for Optical Component Fabrication Ii*, E.B. Kley and H.P. Herzig, Editors. 2003. p. 123-131.
215. Chen, C.C., D. Hirdes, and A. Folch, *Gray-scale photolithography using microfluidic photomasks.* Proceedings of the National Academy of Sciences of the United States of America, 2003. **100**(4): p. 1499-1504.
216. Wangler, N., L. Gutzweiler, K. Kalkandjiev, C. Mueller, F. Mayenfels, H. Reinecke, R. Zengerle, and N. Paust, *High-resolution permanent photoresist laminate TMMF for sealed microfluidic structures in biological applications.* Journal of Micromechanics and Microengineering, 2011. **21**(9).
217. Ruffieux, P., T. Scharf, I. Philipoussis, H.P. Herzig, R. Voelkel, and K.J. Weible, *Two step process for the fabrication of diffraction limited concave microlens arrays.* Optics Express, 2008. **16**(24): p. 19541-19549.
218. Li, F., S. Chen, H. Luo, Y. Zhou, J. Lai, and Y. Gao, *Fabrication and characterization of polydimethylsiloxane concave microlens array.* Optics and Laser Technology, 2012. **44**(4): p. 1054-1059.

219. Roy, E., B. Voisin, J.F. Gravel, R. Peytavi, D. Boudreau, and T. Veres, *Microlens array fabrication by enhanced thermal reflow process: Towards efficient collection of fluorescence light from microarrays.* Microelectronic Engineering, 2009. **86**(11): p. 2255-2261.
220. Fordyce, P.M., C.A. Diaz-Botia, J.L. DeRisi, and R. Gomez-Sjoberg, *Systematic characterization of feature dimensions and closing pressures for microfluidic valves produced via photoresist reflow.* Lab on a Chip, 2012. **12**(21): p. 4287-4295.
221. Popovic, Z.D., R.A. Sprague, and G.A.N. Connell, *Technique for monolithic fabrication of microlens arrays.* Applied Optics, 1988. **27**(7): p. 1281-1284.
222. Emadi, A., H. Wu, S. Grabarnik, G. de Graaf, and R.F. Wolffenbuttel, *Vertically tapered layers for optical applications fabricated using resist reflow.* Journal of Micromechanics and Microengineering, 2009. **19**(7).
223. Shinill, K., *Patterning technology for micro/nanomold fabrication*, in *Micro/nano replication. Processes and applications*. 2012, John Wiley and Sons Inc. : New Jersey.
224. Choi, J.S., Y. Piao, and T.S. Seo, *Fabrication of a circular PDMS microchannel for constructing a three-dimensional endothelial cell layer.* Bioprocess and Biosystems Engineering, 2013. **36**(12): p. 1871-1878.
225. Hishiro, Y., *Resist pattern and reflow technology*. 2008, Micron Technology, Inc: US.
226. Kim, S.K., H.K. Oh, I. An, S.M. Lee, C.K. Bok, and S.C. Moon, *Bulk effects of thermal flow resists.* Journal of the Korean Physical Society, 2005. **46**(6): p. 1439-1444.
227. Afromowitz, M.A., *3-D structures with smoothly varying topographical features in photo-sensitive epoxy resists*. 2003, Afromowitz, M. A.: US.
228. Wouters, K. and R. Puers, *Diffusing and swelling in SU-8: insight in material properties and processing.* Journal of Micromechanics and Microengineering, 2010. **20**(9).
229. Wilk, S.J., M. Goryll, G.M. Laws, S.M. Goodnick, T.J. Thornton, M. Saraniti, J. Tang, and R.S. Eisenberg, *Teflon (TM)-coated silicon apertures for supported lipid bilayer membranes.* Applied Physics Letters, 2004. **85**(15): p. 3307-3309.
230. *Introduction to the BLM workstation*.
231. Niles, W.D. and F.S. Cohen, *Video fluorescence microscopy studies of phospholipid vesicle fusion with a planar lipid phospholipid membrane.* Journal of General Physiology, 1987. **90**(5): p. 703-735.
232. Cassiday, L., *A portable protein nanopore.* analytical chemistry, 2007. **79**(11): p. 3979.
233. Costa, J.A., D.A. Nguyen, E. Leal-Pinto, R.E. Gordon, and B. Hanss, *Wicking: A Rapid Method for Manually Inserting Ion Channels into Planar Lipid Bilayers.* Plos One, 2013. **8**(5): p. e60836.
234. McIntosh, T.J., S.A. Simon, and R.C. MacDonald, *The organization of n-alkanes in lipid bilayers.* Biochimica et Biophysica Acta (BBA) - Biomembranes, 1980. **597**(3): p. 445-463.
235. Antonov, V.F., E.V. Shevchenko, E.Y. Smirnova, E.V. Yakovenko, and A.V. Frolov, *Stable cupola shaped bilayer lipid membranes with mobile plateau gibbs border: explansion- shrinkage of membrane due to thermal transitions.* Chemistry and Physics of Lipids, 1992. **61**(3): p. 219-224.
236. Akabas, M.H., F.S. Cohen, and A. Finkelstein, *Separation of the osmotically driven fusion event from vesicle-planar membrane attachment in a model system for exocytosis.* Journal of Cell Biology, 1984. **98**(3): p. 1063-1071.
237. Cohen, F.S., in *Ion channel reconstitution*, C. Miller, Editor. 1986, Plenum Press: New York.
238. McCoy, J.G. and C.M. Nimigean, *Structural correlates of selectivity and inactivation in potassium channels.* Biochimica Et Biophysica Acta-Biomembranes, 2012. **1818**(2): p. 272-285.
239. Chakrapani, S., J.F. Cordero-Morales, and E. Perozo, *A quantitative description of KcsA Gating II: single-channel currents.* Journal of General Physiology, 2007. **130**(5): p. 479-496.
240. D'Avanzo, N., E.C. McCusker, A.M. Powl, A.J. Miles, C.G. Nichols, and B.A. Wallace, *Differential lipid dependence of the function of bacterial sodium channels.* Plos One, 2013. **8**(4).
241. Ren, D.J., B. Navarro, H.X. Xu, L.X. Yue, Q. Shi, and D.E. Clapham, *A prokaryotic voltage-gated sodium channel.* Science, 2001. **294**(5550): p. 2372-2375.
242. Nurani, G., M. Radford, K. Charalambous, A.O. O'Reilly, N.B. Cronin, S. Haque, and B.A. Wallace, *Tetrameric bacterial sodium channels: characterization of structure, stability, and drug binding.* Biochemistry, 2008. **47**(31): p. 8114-8121.
243. Friddin, M.S., N.P. Smithers, M. Beaugrand, I. Marcotte, P.T.F. Williamson, H. Morgan, and M.R.R. de Planque, *Single-channel electrophysiology of cell-free expressed ion channels by direct incorporation in lipid bilayers.* Analyst, 2013. **138**(24): p. 7294-7298.
244. Bhattacharya, S., J. Muzard, L. Payet, J. Mathe, U. Bockelmann, A. Aksimentiev, and V. Viasnoff, *Rectification of the current in alpha-Hemolysin pore depends on the cation type: the alkali series probed by molecular dynamics simulations and experiments.* Journal of Physical Chemistry C, 2011. **115**(10): p. 4255-4264.

245. Williams, A.J., *An introduction to the methods available for ion channel reconstitution*, in *Microelectrode techniques*, D.C.Odgen, Editor. 1994, The company of biologist: Cambridge. p. 79-99.
246. A. Studer, S.D., D. Langenegger, L. Tiefenauer, *Integration and recording of a reconstituted voltage-gated sodium channel in planar lipid bilayers.* Biosens Bioelectron, 2011. **26**: p. 5.
247. *Introduction to the BLM Workstation*.
248. Zhu, Z.W., Y. Wang, X. Zhang, C.F. Sun, M.G. Li, J.W. Yan, and B.W. Mao, *Electrochemical impedance spectroscopy and atomic force microscopic studies of electrical and mechanical properties of nano-black lipid membranes and size dependence.* Langmuir, 2012. **28**(41): p. 14739-46.
249. Borisenko, V., T. Lougheed, J. Hesse, E. Fureder-Kitzmuller, N. Fertig, J.C. Behrends, G.A. Woolley, and G.J. Schutz, *Simultaneous optical and electrical recording of single gramicidin channels.* Biophysical Journal, 2003. **84**(1): p. 612-622.
250. Rajapaksha, S.P., X. Wang, and H.P. Lu, *Suspended lipid bilayer for optical and electrical measurements of single ion channel proteins.* Analytical chemistry, 2013. **85**(19): p. 8951-5.
251. Woodbury, D.J. and C. Miller, *Nystatin induced liposome fusion. A versatile approach to ion channel reconstitution into planar bilayers.* Biophysical Journal, 1990. **58**(4): p. 833-839.
252. Gao, X.H., L.L. Yang, J.A. Petros, F.F. Marshal, J.W. Simons, and S.M. Nie, *In vivo molecular and cellular imaging with quantum dots.* Current Opinion in Biotechnology, 2005. **16**(1): p. 63-72.
253. Dubertret, B., P. Skourides, D.J. Norris, V. Noireaux, A.H. Brivanlou, and A. Libchaber, *In vivo imaging of quantum dots encapsulated in phospholipid micelles.* Science, 2002. **298**(5599): p. 1759-1762.
254. Lei, S., *Biocompatible polymer/quantum dots hybrid materials: current status and future developments.* Journal of Functional Biomaterials, 2011. **2**(4): p. 355-72.
255. de Planque, M.R.R., S. Aghdaei, T. Roose, and H. Morgan, *Electrophysiological characterization of membrane disruption by nanoparticles.* Acs Nano, 2011. **5**(5): p. 3599-3606.
256. Zhang, Y., L. Mi, P.N. Wang, J. Ma, and J.Y. Chen, *pH-dependent aggregation and photoluminescence behavior of thiol-capped CdTe quantum dots in aqueous solutions.* Journal of Luminescence, 2008. **128**(12): p. 1948-1951.
257. Sperling, R.A. and W.J. Parak, *Surface modification, functionalization and bioconjugation of colloidal inorganic nanoparticles.* Philosophical Transactions of the Royal Society a-Mathematical Physical and Engineering Sciences, 2010. **368**(1915): p. 1333-1383.
258. Thei, F., M. Rossi, M. Bennati, M. Crescentini, F. Lodesani, H. Morgan, and M. Tartagni, *Parallel recording of single ion channels: a heterogeneous system approach.* IEEE Transactions on Nanotechnology, 2010. **9**(3): p. 295-312.